CHEMICAL REVIEWS

pubs.acs.org/CR

Review

Large-Area Interfaces for Single-Molecule Label-free Bioelectronic Detection

Eleonora Macchia,[§] Fabrizio Torricelli,[§] Paolo Bollella, Lucia Sarcina, Angelo Tricase, Cinzia Di Franco, Ronald Österbacka, Zsolt M. Kovács-Vajna, Gaetano Scamarcio, and Luisa Torsi*

Cite This: *Chem. Rev.* 2022, 122, 4636–4699

Read Online

ACCESS | Metrics & More | Article Recommendations

ABSTRACT: Bioelectronic transducing surfaces that are nanometric in size have been the main route to detect single molecules. Though enabling the study of rarer events, such methodologies are not suited to assay at concentrations below the nanomolar level. Bioelectronic field-effect-transistors with a wide (μm^2–mm^2) transducing interface are also assumed to be not suited, because the molecule to be detected is orders of magnitude smaller than the transducing surface. *Indeed, it is like seeing changes on the surface of a one-kilometer-wide pond when a droplet of water falls on it.* However, it is a fact that a number of large-area transistors have been shown to detect at a limit of detection lower than femtomolar; they are also fast and hence innately suitable for point-of-care applications. This review critically discusses key elements, such as sensing materials, FET-structures, and target molecules that can be selectively assayed. The amplification effects enabling extremely sensitive large-area bioelectronic sensing are also addressed.

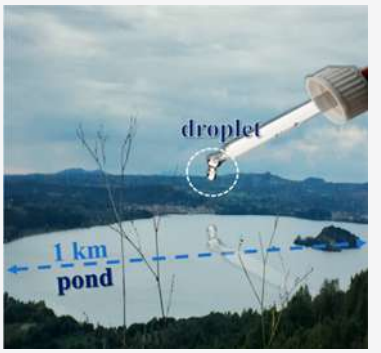

CONTENTS

Special Issue: Organic Bioelectronics

Received: April 7, 2021
Published: January 25, 2022

https://doi.org/10.1021/acs.chemrev.1c00290
Chem. Rev. 2022, 122, 4636–4699

1. INTRODUCTION

This review aims to show that label-free ultrasensitive detections, down to the single-molecule ultimate limit, are possible with large micrometer/millimeter wide, bioelectronic devices based on field-effect-transistor transducers. These are high-performing, stable, and reliable systems that exhibit most of the ideal features necessary to conveniently serve in point-of-care testing systems. They can also be produced with cost-effective large-area technologies. The so-called *near-field* approach to single-molecule detection has been extensively studied, and many reviews[1−3] can be found. Herein, this aspect will be recalled only to clarify the differences between the single-molecule approaches involving nanometric transducing interfaces and those involving micrometric or even millimetric wide devices. We will also not mention the plethora of organic-based transistors that can perform chemical and biochemical detections at limit-of-detections higher than femtomolar that were also recently reviewed.[4]

Herein, the focus is on label-free bioelectronic sensors that are large-area and that can detect a given target analyte (*e.g.*, proteins, peptides, DNA/RNA/PNA, virus, or bacteria) present in a solution or possibly in a real fluid with minimal sample pretreatment and at a concentration below a few femtomolar (fM, 10^{-15} mol L^{-1}). The devices are also endowed with high selectivity conferred by integrating suitable recognition elements at the detecting/transducing electronic interface. Specifically, the review is structured into the following sections, each containing many exemplary cases:

In section 1 a general introduction to single-molecule sensing is given, briefly recalling the different approaches that over the years have been developed. Eventually the focus is shifted to single-molecule sensing at a large detecting interface by using an electronic transducer.

In section 2 the toolbox to correctly operate a biosensor and apply the needed analytical validation strategies to the assays performed with ultrasensitive bioelectronic devices is provided. This enables gathering data with a given qualitative (including yes/no type of response) and quantitative reliability. Typical biosensor figures of merit, such as sensitivity, selectivity, limit-of-detection (LOD), limit-of-identification (LOI), and limit-of-quantification (LOQ), that are relevant to proceed with the validation of a new biosensor platform are operatively defined.

Section 3 presents an extensive review of the state-of-the-art of ultrasensitive (namely, the technologies exhibiting LODs lower than fM) and single-molecule bioelectronic sensors engaging different technologies from MOSFET, including extended gates, to electrolyte-gated field-effect transistors. Relevant aspects such as the stability and the role of the Debye length are addressed as well. A very detailed overview of the different materials engaged, from high electron mobility inorganic materials to organic semiconductors and graphene-based channels, is also provided. For the device technologies and the different materials used, tables summarizing the sensors' main figures of merit are conveniently provided.

In section 4 the main biofunctionalization strategies to provide the devices with high selectivity are reviewed. The strategies generally comprise the grafting of a chemical self-assembled monolayer to the transducing interface (*i.e.*, gate or channel) to which the recognition elements are stably attached. Moreover, the plethora of different types of target analytes that can be detected are also described with examples and tables.

In section 5 the most relevant spectroscopic approaches for *in situ* and *operando* sensing devices characterizations are reviewed. To this end, two main classes of optical probes have been selected, namely, (i) surface plasmon resonance and (ii) surface-enhanced infrared absorption spectroscopy. These approaches set the groundwork for independent characterization tools to be used, eventually, directly *in situ* and *operando* on bioelectronic devices. The aim of this section is hence to present tools that will enable reaching, in the near future, a better understanding of how the sensing occurs in large-area, single-molecule bioelectronic sensing.

Section 6 highlights the essential differences between the near-field and the large-area single-molecule label-free bioelectronic detections. The former is the workhorse and is plagued by the diffusion-barrier issue that prevents its use for detecting below nanomolar concentration. Conversely, it is shown how large-area bioelectronic approaches can provide, very much like cells do, a sufficiently large signal-to-noise ratio when sensing at the ultimate limit.

As in large-area single-molecule detections, amplification effects need to be in place. Section 7 presents an overview of the possible sensing mechanisms that enable a significantly high signal-to-noise ratio even when the detecting interface has many orders of magnitude larger area than the footprint of the single molecules to be detected. To this end, the electronic amplification of the FET is considered along with collaborative collective electrostatic effects that generate a domino-like propagation effect. A comparison of the bioelectronic transduction and the propagation effects demonstrated in liquid crystals is proposed to better elucidate the strength and generality of the effects underpinning large-area, single-molecule bioelectronic detections.

1.1. Prologue on Why Single-Molecule Sensing Is Important

Until a few decades ago, almost all the studies on chemical and biochemical sensing encompassed the interrogation of an ensemble (or bulk collection of molecules) comprising millions or billions of molecules in the inspected volume. In these studies, the measured output integrates the signals coming from many molecules of the ensemble; therefore, the contribution of every single molecule to the whole output signal could not be distinguished. The characteristic features of the molecules whose behavior is similar to that of the majority are, hence, duly represented, while those producing rarer features inevitably fall in the background noise. In other words, rarer features and events are lost to the ensemble as they are submerged in the noise.

It has become more and more evident how the phenomena underpinning a complex system's behavior are not necessarily associated with a characteristic feature shared by most of the molecules. Instead, a few of them or even just a single molecule behaving not like the majority of the other molecules may trigger a process that induces a specific performance of the whole ensemble. This means that a rare event involving one single molecule or biomolecule can determine the fate of the whole system. This is the reason why the detection of single-molecule

https://doi.org/10.1021/acs.chemrev.1c00290
Chem. Rev. 2022, 122, 4636−4699

events is foreseen to have a high impact on clinical diagnosis. More generally, identifying proteins, peptides, and genomic single-markers is deemed as more and more important to achieve a better understanding of the ethiology and also for the early diagnosis of progressive, life-threatening, and life-quality-affecting diseases. Indeed, biomedical research and clinical practice progress depend mainly on developing powerful methodologies for the accurate and sensitive detection of biomolecules. The availability of such systems will provide clinicians with the attacker advantage over many diseases that will be treated at the earliest possible stage with more chances to defeat them.

A paradigmatic example of how relevant single-molecule detection can occur in clinical diagnosis is given by cells. Proteins, DNA, RNA, and other cellular biomolecules are in continuous motion, and hence, a large number of different and very complex dynamic interactions and conformational states originate, which are essential for the correct functioning of the system.[5] Therefore, 3D protein structures and dynamics can provide critically relevant information to identify a cancer driver gene that is essential to fully unleash the potential of precision medicine in fighting such diseases.[6] Single-molecule technologies can be essential in this endeavor as it is now clear, for instance, how a tumor and other progressive diseases can be triggered by a mutation involving a single-cell genome. Targeting and profiling that given cell can be the key to the right cure.

Tracking these features at the single-cell and/or single-molecule level can be performed nowadays by established technologies, such as the next-generation sequencing (NGS)[7] capable of sequencing single-molecules (copies) of DNA markers, so that very high diagnostic sensitivity and specificity are within reach. This is not yet possible for protein or peptide markers because an equally high-performing technology for their detection at the single-molecule level is still lacking. This is indeed an issue because, compared to the human genome, the proteome is considered a better indicator of an individual health profile. Yet, while thousands of human genomes have been sequenced, the proteome is still largely unexplored. This is because the proteome has manifold protein variants due to functional diversification enabling processes such as post-translational modifications. However, presently less than 20% of the different species populating the human proteome are known. This happens because, at a given overall concentration of proteins in a biofluid, more diversified species are found when the protein concentration drops beyond the detection limits of currently available clinical analytical methods. Indeed, the signal related to the detection of peptide biomarkers is hidden by the large signal generated by the much more abundant proteins usually present in human blood plasma. In Figure 1 the large dynamic range of the concentration of proteins and peptides in human blood plasma is illustrated. In particular, a substantial amount of albumin in a typical sample is known to be an issue for the successful identification of lower-abundance biomarkers in many proteomic studies. Hence, the iceberg metaphor recalls the fact that the most diversified species of our proteome (which are also the least abundant) are not easily accessible when assayed with approaches that detect the whole ensemble rather than a single or few molecules.

The most sensitive approach to genomic markers is the elicited NGS.[7] When it comes to the supersensitive detection of proteins, the effort undertaken by Quanterix since 2013 to lead the way by introducing a technology named Single-Molecule-

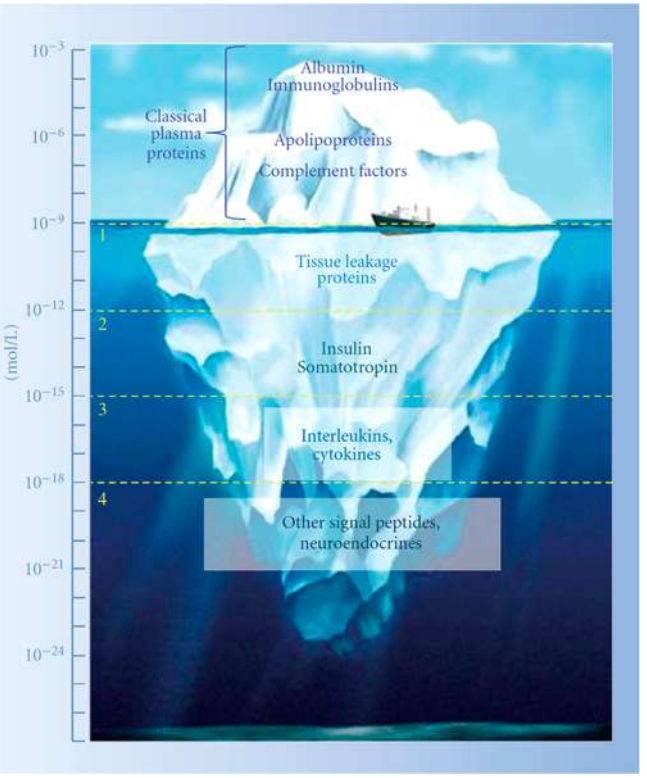

Figure 1. Iceberg metaphor featuring the large dynamic range of the concentration of proteins and peptides found in blood, detailing some of the more representative classes. At the tip of the iceberg the most abundant plasma proteins in 1 μL of a sample are shown. The metaphor represents these species to be the most "visible" ones because indeed they are easier to spot or detect with standard approaches. This does not mean that the most abundant species are also the most important to serve as markers for the early diagnosis of progressive diseases. Much less abundant are the tissue leakage proteins. Peptides/proteins like insulin and somatotropin are present at concentrations that are at least 3 orders of magnitude less. This means that Poisson sampling statistics needs to be used to precisely quantify such an extremely low level of molecules. Interleukins and other cytokines drive state-of-the-art analysis systems (*e.g.*, mass spectrometry) toward the limit of their sensitivity. In contrast, other peptides, such as those producing neuro-secretory signals, are present at such a low concentration that they can be detected only by mass-spectroscopy after a preconcentration step. Reprinted with permission from ref 12. Copyright 2011 Hindawi under Creative Commons Attribution 4.0 License (http://creativecommons.org/licenses/by/4.0/).

Array (Simoa)[8−10] is worth noting. At that time, visionaries were already convinced that single-molecule assays could elucidate the etiology of progressive diseases such as cancer, including the relapse after therapy. This was revolutionary because the established view was that no protein or genomic molecule could serve as a marker if it was present in a given biofluid, below a nanomolar (nM) or picomolar (pM) concentration. Below a given concentration, no reliable correlations could be found between the concentration of a given molecule and the progression (at its very early stage) of a disease. In 2017 Quanterix played the crucial pioneering role of clarifying that detection limits of specific proteins into the low fg/mL range (*ca.* $1-10 \times 10^{-18}$ M, aM) can be useful in oncology, neurology, inflammation, and infectious diseases.[8−10]

Another very important advantage is the use of supersensitive devices for minimally invasive assays capable of detecting

https://doi.org/10.1021/acs.chemrev.1c00290
Chem. Rev. 2022, 122, 4636−4699

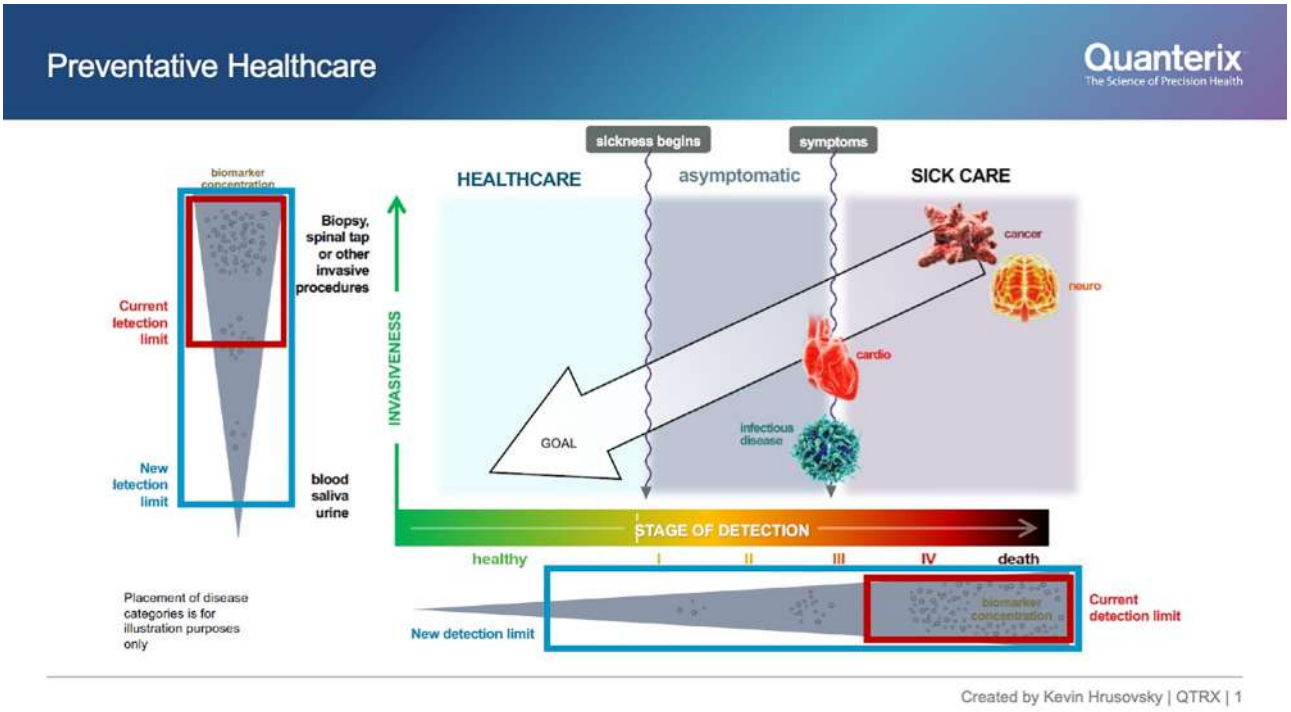

Figure 2. An improved limit of detection enables preventive healthcare. The "stage-of-detection" bar shows the early stage in green that marks the region of homeostasis. The yellow area describes the region of presymptomatic illness. Screening with Simoa assays with a low limit of detection is often useful here. The red region is typical of the performance of symptom-triggered healthcare using a workhorse such as the enzyme-linked immunosorbent assay (ELISA) technology. Reproduced with the permission of Kevin Hrusovsky and Quanterix.

markers in peripheral body fluids (*e.g.*, peripheral blood, saliva, interstitial fluid, *etc.*), where their concentration can be very low.[11] This is a further advantage of ultrasensitive clinical analysis methods that will allow for a biopsy to be carried out in a minimally invasive way.

Moreover, the availability of the so far discussed supersensitive detection systems would enable the transition from the so-called *reactive sick care* to the truly *preventive healthcare regime*, as schematically illustrated in Figure 2. Here, the horizontal color bar shows the transition going from homeostasis (green) passing through the presymptomatic (yellow) and ending with the full-blown (red) disease. The intervention of a clinician at the red stage means working in the regime of reactive sick care where the chances of curing the patients are often very low. Indeed, the earlier the diagnosis, the earlier the definition of the prognosis, the better the chances to effectively cure the patient. The region represented by enzyme-linked immunosorbent assay (ELISA),[13] the workhorse for 40 years in immunometric detections, is in the red boxes in the upper left and bottom right portions of the figure. It is clear the ELISA diagnostic tool (the only available till a few years ago for immunoassay-based protein detection) is able to spot a disease protein marker only when the patient is in the sick-care regime. The blue box illustrates how improved detection limits (and hence improved sensitivity) increase the possibility to detect a marker when present at much lower concentrations (below pM). This provides clinicians with the attacker advantage, enabling the possibility of making a diagnosis much before symptoms appear. The transition to a truly preventive healthcare system that can save many more lives and much money is hence accomplished.

On a more general level, an interesting perspective for single-molecule detection foresees in the future a transition from an *analog* to a *digital* reading of the molecular content in a solution.[14] This concept is illustrated in Figure 3. To assess the concentration of a solution through a fluorescent optical

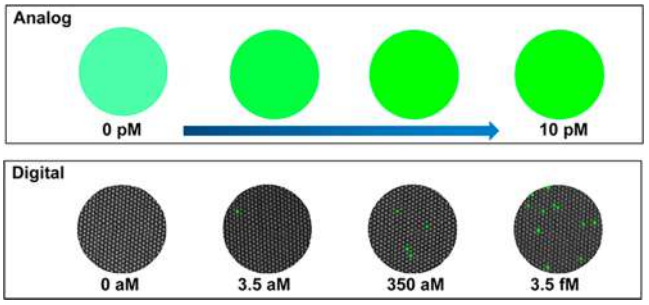

Figure 3. In the top panel, an example of analog measurement is shown. Here, the increasing intensity of an optical signal, coming for instance from a solution of a fluorophore with increasing concentration, is schematically reported. In the bottom panel, a digital measurement carried out with a Simoa array (*vide infra*) is shown. Each pixel of the array gives an independent signal that is intense enough to be counted as "plus-one", and hence the quantification simply relies on a one/zero or yes/no (presence/absence) signal readout. Reprinted with permission from ref 14. Copyright 2013 American Chemical Society.

imaging technique, the proportionality between the concentration and the intensity of the signal is needed for calibration purposes. This engages the reading of an analog signal coming from the solution (Figure 3, top panel). In contrast, the measurement of a single-molecule returns a binary zero-or-one digit. Hence, so long as each single molecule shows a signal that is bright enough to be discriminated from the background noise, this event can be added as a "plus-one" to the counting of the whole ensemble of molecules (Figure 3, bottom panel). Measuring the presence (one) or the absence (zero) of a

https://doi.org/10.1021/acs.chemrev.1c00290
Chem. Rev. 2022, 122, 4636−4699

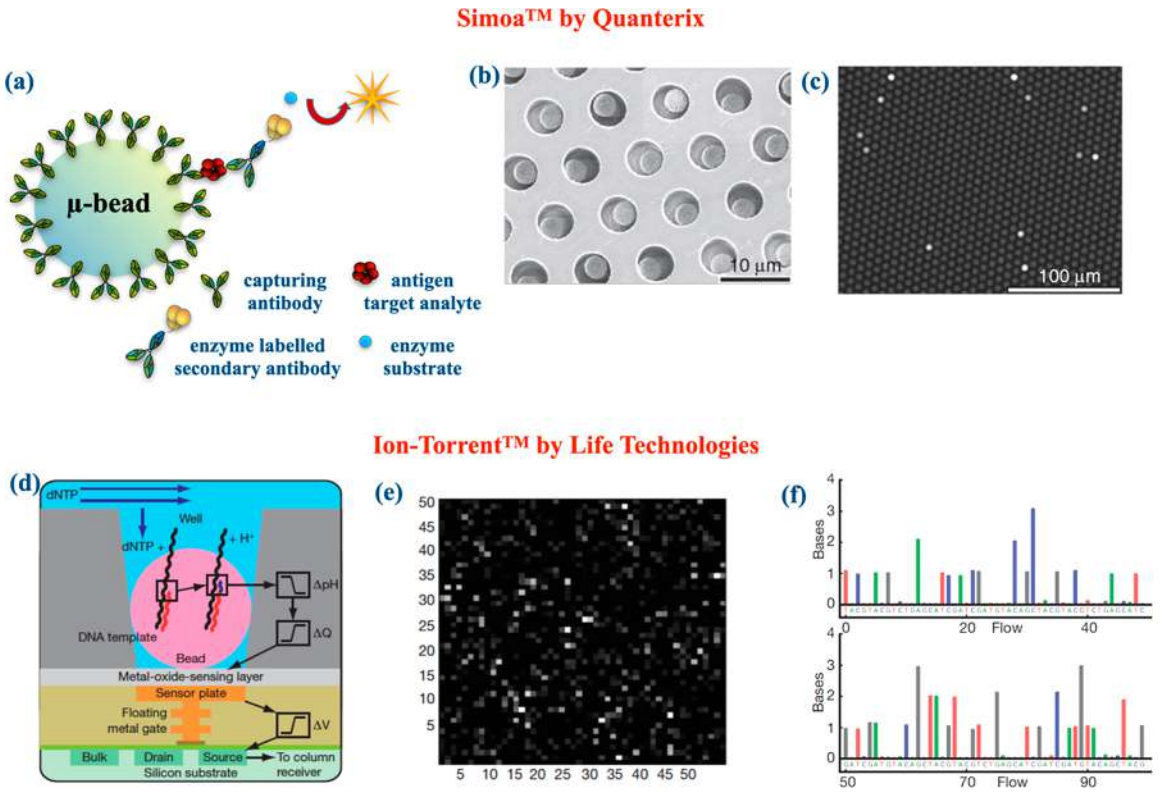

Figure 4. Examples of two wide-field capturing technologies, namely, Simoa and next-generation sequencing. (a) A microbead functionalized with antibodies capturing their affinity antigen. A secondary antibody linked to an enzyme is captured by the target antigen that is detected as a result of the interaction between the enzyme and its fluorogenic substrate. (b) A scanning electron micrograph of few size-exclusion microwells (with a volume of a femtoliter) of a Simoa array when the microbeads are loaded. In one of the wells the bead can be seen. (c) Fluorescence image of a typical Simoa array taken with a CCD camera showing the bright signals coming from a single microbead confined in its hosting well. (Panels b and c are reprinted with permission from ref 23. Copyright 2010 Springer Nature.) (d) Illustrative replica of an Ion Torrent pixel, which is fully described in the text. (e) Picture of a typical NGS plate showing the wells producing a signal whose brightness can be correlated with the number of DNA nitrogenous bases incorporated when one of the four nucleotides is provided. (f) A plot showing the number (from one to hundreds) of subsequent nucleotide solutions flooding the NGS plate versus the number of nucleotides actually attached to the bead in the well; the color code describes the different nitrogenous basis: thymine (T, red), adenine (A, green), cytosine (C, blue), and guanine (G, gray). [Panels d–f are reprinted with permission from ref 7. Copyright 2011 Springer Nature under Creative Commons Attribution-NonCommercial-Share Alike license (http://creativecommons.org/licenses/by-nc-sa/3.0/).]

sufficiently intense signal is therefore more convenient than measuring the level of an analog signal. This is because such a level can be turned into a meaningful quantification of a given parameter (*e.g.*, the analyte concentration) only after comparison with an *ad hoc* devised and measured calibration curve. In other words, counting is easier as it can be quantitative with no need for a calibration curve.

In conclusion, detecting a protein and a genomic marker at the single-molecule level can change the way molecular interactions are studied and can have a remarkably beneficial effect on the possibility of performing early detection of biomarkers, hence enabling early diagnosis.

1.2. Why Sense at the Physical Limit with a Large Interface?

In this section an introduction to the main rationale for why detecting a single molecule with a nanometric interface is less appealing, from a technological and application point of view, than detecting a single molecule with a large interface is explained, starting from a historical perspective.

Single-molecule studies were proposed for the first time more than 60 years ago, and in this respect it is worth mentioning the seminal work by Boris Rotman carried out at Stanford Medical School.[15] In this study, a solution containing the β-galactosidase enzyme along with its florescent substrate was dispersed by spraying it into a silicon-based oil. Eventually, oil droplets formed that were small enough and the enzyme concentration was high enough so that each droplet statistically entrapped a single enzyme. A statistical study based on the fluorescent intensity measured from single droplets of different sizes enabled deriving information on individual enzyme activity. Relevantly, a single enzyme becomes visible because it can turn over thousands of fluorescent substrates. This catalytic activity acts as the amplification mechanism that allows measuring a sufficiently high signal-to-noise ratio when studying a single enzyme. Thomas Hirschfield performed a more direct measurement in 1976.[16] Here, the single molecule of globulin, labeled with approximately 100 fluorescein dyes, was observed while passing through a focused laser. The labeled proteins were illuminated with a sufficiently high-power laser to photobleach the labeled molecules by employing the total internal fluorescence detection approach. By carrying out the detection at given calibrated concentrations, each single molecule was separately observed.

Afterward many other studies were successfully performed, and nanotechnologies seemed to offer the privileged pathway to accomplish the difficult task of reliably performing label-free single-molecule detections. Besides the very early endeavors

https://doi.org/10.1021/acs.chemrev.1c00290
Chem. Rev. 2022, 122, 4636−4699

previously noted, it is relevant to mention those detections that were carried out in the so-called *near-field* regime with a nanoscopic sensing interface.[17,18] Typically, they involved the inspection of a small volume (*e.g.*, femtoliter) including the single molecule to be detected. As an example, these endeavors involved tip-enhanced imaging of the single-molecule interactions, alone or combined with spectroscopic techniques. Indeed, the tip used was nanometric in size. In these configurations, the probing tip apexes act as plasmonic nanofocusing antennae that withstand strong, highly localized field enhancement restrained within a few nanometers from the sensing surface. Such an occurrence enables the imaging and the detection of single-molecule events. Generally, the *near-field* label-free approach to single-molecule sensing involves a probing/detecting interface that is nanometric in size, hence holding dimensions of the same order of magnitude of the single molecule to be detected. This ensures a high signal-to-noise ratio.[19] An example of a bioelectronic system that works in the *near-field* approach will be proposed in section 6 (Figure 32A). Relevantly, a *near-field* approach measures generally a *telegraph-noise-like* signal with each of the fluctuations being associated with a single-molecule interaction that can be addressed and studied independently. Therefore, a *near-field* detection is not any longer about measuring a large signal that integrates the contributions generated by many molecules of an ensemble. In the latter case, the output integrated-signal features the majority of the molecules sharing the same status while it disregards the few discrete signals coming from the much fewer molecules exhibiting rarer features. In this respect, the *near-field* approach can be highly relevant to track the whole Gaussian distribution of the features characterizing an interaction, from the more probable (shared by many molecules of the ensemble) to the less probable ones shared by only a few molecules. However, the *near-field* approach is affected, like all nanoscale transducing interfaces, by an intrinsic limitation generally addressed as the *diffusion-barrier* issue. This problem occurs when a nanoscale interface is placed in a large volume (10−100 μL) where there is just one molecule to be detected. Indeed, the encounter between the detecting interface and the species to be assayed is very improbable. As an example, it has been proven that several days are needed for 10 molecules, out of $\sim 10^6$ in 100 μL of a femtomolar (fM) concentrated solution, to be collected and assayed at a nanometric transducing interface immersed in the same solution.[20] A similar limitation is observed with nano-transducers,[19] such as nanopores[21] or nanotransistors,[22] engaged in detection in the picomolar (pM) range or larger. Therefore, nanointerfaces cannot be used to detect markers below a concentration in the order of pM because the detecting time would be extremely long because of the low probability that a few molecules in a large volume (*e.g.*, 10−100 μL) have to encounter a nanometric interface that is submerged in the same large volume. This is indeed addressed as the *diffusion-barrier issue*.

To overcome this limiting factor, several different methodologies were proposed, and among them, particularly successful are those relying on *wide-field sampling* principles.[17] The idea here is that if you throw a large number of biofunctionalized micro beads (μ-beads) in the volume you want to assay, the chance that a μ-bead can bump into one of the few molecules to assay is very large. This is the basis of *wide-field sampling*. A schematic illustration of the functioning principles of two paradigmatic examples of *wide-field sampling*, *e.g.*,Simoa and NGS, is given in Figure 4.

They are both commercially available, and while NGS[7] can detect genomic markers at the ultimate limit, ultrasensitive protein detections can be carried out with Simoa.[8−10] More specifically, Simoa can detect the proteomic marker at a limit of detection of 10 attomolar (aM, 10^{-18} mole·L^{-1}) or lower.[23] Thousands of molecules are present in 100 μL of a 10 aM solution; hence, the Simoa technology reaches higher detection limits as compared to NGS. The latter, in fact, can spot a single molecule (a single copy of a DNA marker) in a comparable volume. In these technologies, the *wide-field sampling* (overcoming the diffusion barrier issue) is implemented thanks to several microbeads that are paramagnetic in nature. These are biofunctionalized with recognition/capturing elements (*e.g.*, antibodies, Figure 4a) that can find the marker (*e.g.*, the antigen) and bind it.[10,19] The magnetic microbeads are dispersed into the biofluid to be assayed, to seek and bind the few targeted markers. The magnetic beads are then collected through an applied magnetic field and dispersed on the Simoa array. This is composed of microwells with an internal volume just slightly larger than the bead itself, so each well can lodge either zero or one bead at most. In Figure 4b a size-exclusion well plate is shown where into some of the wells a bead can be seen. As it is clear each size-exclusion well can contain either no or one bead. More specifically, in the Simoa protein assay, as many as 2×10^5 μ-beads biofunctionalized with 2.5×10^5 recognition elements (capturing antibodies) are engaged. The concentration of the antibodies that capture the target antigens in the assay volume is as high as nanomolar. Therefore, the antigen−antibody interaction cross section is high enough that the few antigens are efficiently captured by the cognate antibodies (Figure 4a) in a few minutes. Then, the ELISA-type[13] detecting strategy is implemented as schematically shown in Figure 4a. Notably, a second antibody, quantitatively conjugated with an enzyme, binds to the biomarker. As anticipated, afterward, the beads are collected with a magnetic device and dispersed on the elicited Simoa array where each well can host only zero or one bead (Figure 4b).

The microwells are coated with a wax lid making sure that the fluorophore substrate of the enzyme, serving as the label (Figure 4a), is also present inside the wells. As is typical of ELISA-based detecting procedures, the florigenic substrate molecule is activated only in the presence of the enzyme that is attached to the marker. Hence, the spot at each well becomes bright only when the bead hosted has captured at least one target proteomic marker. The assessment of the number of hosted beads is accomplished by counting the fluorescent spots (associated with the wells) with a CCD camera (Figure 4c). As long as the fluorogenic signal is sufficiently intense, the quantification of the few protein biomarkers can be achieved by counting the bright spots in the CCD camera image. As anticipated in section 1.1, this quantification method needs no calibration curve.

The other class of ultrasensitive assays is the also mentioned NGS platform that can sequence the whole genome of a single cell, being sensitive to one single genomic copy. In this case, the genomic strand of a marker is adsorbed and amplified by polymerase chain reaction (PCR) on the surface of microbeads that are also hosted into a plate (a chip in fact), comprising size-exclusion wells with a pH-sensitive metal oxide semiconductor field-effect transistor (MOSFET) system array placed at the bottom (Figure 4d). A genomic template is present so as to trigger the sequencing process through the polymerase DNA synthesis; the genomic marker is present too. The chip is sequentially exposed to abundant solutions of one of the four

https://doi.org/10.1021/acs.chemrev.1c00290
Chem. Rev. 2022, 122, 4636−4699

nucleotide bases, namely, thymine, adenine, cytosine, and guanine. In the sequencing process, once a given nucleotide recognizes its complimentary base, it is integrated into the growing complementary strand. The hydrolysis of the integrated nucleotide takes place that necessarily involves the releases of protons. The solution's pH changes significantly as the process involves all the PCR-generated replicates of the markers. The sensible pH change provokes, a change in the surface chemistry composition and hence of the surface electrochemical potential of the metal-oxide-sensing layer which in turn triggers a measurable shift the MOSFET threshold voltage. This is the electronic signal that is detected when a single copy of a genomic marker is present in the solution to be assayed. In Figure 4e a picture of the size-exclusion wells of an NGS plate is shown with the pixel intensity representing the number of bases integrated per well when one of the four nucleotide solution is flooding the chip. In Figure 4f, the number of nucleotides integrated in the chip after each flooding is shown. Being a sequencing technique, NGS enables the identification of the whole genomic material present in a given cell. Such an aspect is very relevant information, but it is a lengthy and sometimes unnecessary process when a genomic marker with a known sequence is to be assayed and not sequenced. Also, this wide-field capturing technique is label-based as the polymerase-enzyme is necessary for the sequencing process. More details about the NGS and the Simoa can be found in ref 19.

Large-area or *wide-field*[17] transducing interfaces provide a higher geometrical cross section to the few molecules present in the solution. This is hence a very interesting solution to overcome the diffusion barrier. The signals collected from an ensemble of molecules are an average of many molecules' interactions with the detecting surface. In contrast, a large-area sensor detects a signal that is originated from each protein or bioentity interacting with the capturing interface. Hence, it has become possible to study a single molecule through the recognition process that holds the features that are typical of each and every process involving just two binding partners. Such a heterogeneity of information is indeed averaged off when an ensemble of molecules is assayed. One example is the method that enables the study of single protein complexes that reside in a cell. It is called *single-molecule pull-down*[24] because macromolecular complexes that are typical of a given physiological setting are dragged down from for an extraction of cells or tissues directly into the imaging surface of single-molecule fluorescence microscopy, enabling a very sensitive analysis of such complexes.

A more recent development in ultrasensitive detections involves the assay of markers, proteins in particular, with a large area (μm^2 to mm^2 wide) interface at an aM or even 10^{-20} zM limit of detection. Thus, corresponding in a volume of 100 μL, to a hundred or one single molecules, respectively. The detection is carried out with electronic biosensors whose millimeter-wide detecting interface is biofunctionalized with many recognition elements (10^{11}–10^{12} cm^{-2}). It is important to note that this is also when the detection is label-free, meaning that the output signal is directly associated with a change of an intrinsic property (*e.g.*, electrostatic or dielectric ones) of the complex formed once a biomarker interacts with its recognition element. Combining these two aspects, the large interface and the direct label-free detection, results in the interesting bioelectronic systems reviewed in sections 3 and 4 that involve MOSFET devices, including extended gates, as well as electrolyte-gated field-effect transistors. The potential is to develop ultrasensitive, fast, highly reliable, and low-cost diagnostic systems for the early diagnosis of diseases like tumors and viral and bacterial infections. Among the different platforms that are reviewed here, the single-molecule with a large transistor (SiMoT) technology[25] was the first one to detect proteins at the 10 zM limit of detection. In fact, it detects both proteins (HIV-p24, CRP, IgG, IgM)[25−28] and genomic markers[29] also in serum at the physical limit. Recently, other technologies could reach this ultimate limit, as single-molecule chiral detection was also proposed with a large-area, fast-responding cyclodextrin derivative-functionalized organic FET.[30] Moreover, COVID virus[31] as well as aptamers[32] have been detected at the single-molecule level with interesting bioelectronic approaches.

Despite the great potential, the full development of these platforms has been affected so far by two ingrained beliefs. It is believed that large-area detecting interfaces cannot offer a sufficiently high signal-to-noise ratio because the few binding markers engage a too-small portion of the sensitive area. Furthermore, the diffusion of a marker in a large volume (*e.g.*, 10−100 μL) is too slow and therefore affected by the diffusion barrier issue, as happens in a nanometric interface. Indeed, these assumptions rely on the view that one or even a few markers cannot reach by Brownian motion (diffusion) the large gate electronic area in a few minutes. Another aspect perceived as critical is the following: the single-molecule event involves only one recognition element over the trillions populating the millimeter-wide interface, and spotting the effects of such an interaction would be like seeing the surface of an approximately 1 km-wide pond that changes because a droplet of water falls and impinges on it. The evidence that a single molecule impacting and interacting with a millimeter-wide transducing interface can generate a sufficiently high signal clearly implies that amplification effects should be in place. In wide-field sampling technologies, amplification effects are indeed in place: in Simoa, a signal enhancement is connected with the labeling enzyme catalytic activity, while in NGS, the polymerase chain reaction amplification and the pH-sensitive MOSFET amplified transduction synergically contribute to enhance the output signal. The wide-field bioelectronic sensors here reviewed take advantage of the field-effect transistor (FET) amplification effects proven to contribute with a factor of 10^3 to the signal enhancment.[33] Such an enhancement is indeed not sufficient to grant that a single binding event results in a sufficiently high signal. Hence, another amplification phenomenon needs to be involved. While the detailed explanation of such an effect remains elusive at this stage, a possible mechanism was proposed in a model based on the results gathered with the SiMoT technology.[25] Eventually it was found to be conceptually similar to the process involved in liquid crystal film-based biodetection conceived by Abbott and co-workers[34] to selectively detect proteins *via* their capture of antibodies attached at a surface. The binding event is transduced into an amplified optical output. To this end, self-assembled surfaces were conceived so that proteins, upon binding to their capturing antibodies attached to a transducing surface, provoked changes in the orientations of micrometer-thick films of liquid crystals. For each protein binding, a reorientation of millions of liquid crystal molecules (mesogen) was proven to occur. This binding-induced reorientation of a huge number of liquid crystal molecules per bound protein significantly changes the intensity of light transmitted through the liquid crystal film so that the effect was easily seen with the unaided eye.[34] These aspects will be better elucidated in section 7.

https://doi.org/10.1021/acs.chemrev.1c00290
Chem. Rev. 2022, 122, 4636−4699

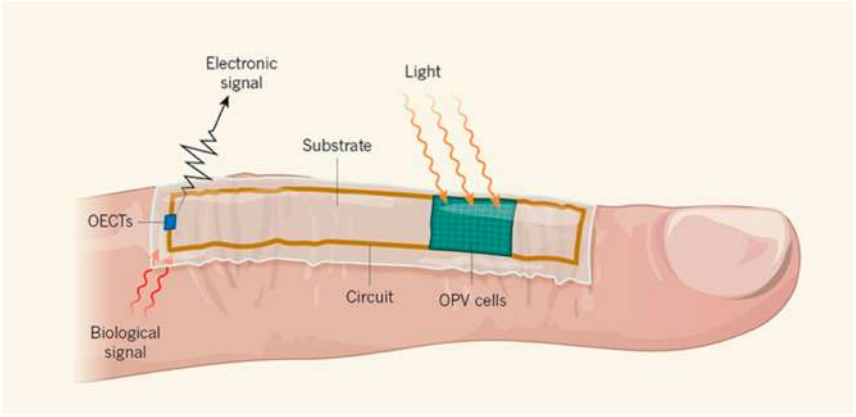

Figure 5. A self-powered ultraflexible biosensor. Park *et al.*[36] have demonstrated a platform to detect physiological signals that are turned into electronic voltage shifts. The system is ultraflexible and is not required to be biased by an external power source. It is based on a circuit comprising organic electrochemical transistors (OECTs) and solar cells labeled in the sketch as organic photovoltaic (OPV) cells. These circuit elements are attached to a micrometer thin conformable plastic substrate. The technological platform is biased *via* OPV cells that are irradiated with LEDs. Reprinted with permission from ref 38. Copyright 2018 Springer Nature.

1.3. Why Sense with Electronic Devices

Electronic and optoelectronic devices offer many very relevant advantages in biosensing applications. They are generally label-free, fast, and easier to operate. The acquired data are also, conveniently, already digitalized. Data transfer and storing into a cloud system for remote processing is also favored. Moreover, electronic sensing systems can be fabricated through mass-manufacturable, large-area compatible, scalable techniques, including printing and other direct-writing processes.

As anticipated, presently, diagnostic tests carried out routinely are based on the quantification of a given biomarker and/or of a specific biochemical parameter of a patient that is performed in a centralized facility, such as a clinical lab. Because of the sometimes complex logistics, the output of the assay becomes available only after several hours or even days, depending on a number of factors. Miniaturization of diagnostic tools along with the availability of high- performing point-of-care testing (POCT) technologies[35] can be a game changer to reliably perform the diagnosis as well as the monitoring of a disease not only at the patient's house or the doctor's office but also in emergency rooms and in resource-limited areas that are otherwise difficult to reach. Electronic devices offer a perfect fit for POCT. Among the main benefits are the possibility to assay low-volume samples and to use less reagents, the convenience of the system portability because of small form factors, and the rapid response. Electronic emerging technological innovations in healthcare also offer full self-testing to patients that, besides requiring no visit to central facilities, allow the test results (that are already in a digital form) to be immediately sent to healthcare providers *via*, for instance, a WiFi connection. An electronic POCT platform that also enables self-testing, which requires in principle minimal human intervention in all the operational phases, also reduces possible human errors; other desirable characteristics include being user-friendly, for instance by implementing easy-to-manage human−system interfaces. Moreover, it will also likely be characterized by a high clinical sensitivity, specificity, and accuracy. Such an occurrence will provide the clinician the ability to provide an immediate clinical assessment while being in a remote connection. Such a POCT technology is still not available; a fully integrated platform that clearly shows the high potential of bioelectronics is discussed in the following. It comprises self-powered ultraflexible electronics, including an organic photovoltaic cell that fuels a bioelectronic sensor integrated into a conformable substrate that the patient can wear.[36] It is a fact that most biomedical devices, particularly those that are meant for to be worn, must be endowed with characteristics such as being sufficiently flexible or conformable to very well adapt to human skin or maybe even to the irregular shape of an organ. They must also be self-powered. The idea is that such a system becomes integrated with the human body or another living organism to precisely and continuously control and asses a number of physiological parameters. Flexible photovoltaics could provide self-powering functionality that can be integrated into unevenly shaped 3D biological tissues and organs. The integration of such power sources with electronic and electrical circuital elements, encompassing also sensors, was demonstrated by the Someya group[36] that studied and developed a self-powered electronic system capable of assessing biometric signals when attached to a tissue or the skin. Specifically, an organic electrochemical transistor served as sensor while an organic photovoltaic cell provided the needed electrical power, and they both were accommodated on an extremely thin (μm thick) and hence ultraflexible substrate. In Figure 5, a schematic for the proof-of-principle system proposed by the Someya group is shown. As can be seen, this is an ultraflexible and self-powered system that is shown to work as an extremely performing cardiac sensor. To demonstrate such a challenging application, the system is attached to the finger's skin while a wireless connected gel-based electrode is attached to the chest to detect the patient's heartbeats. Each time the patient's heart produces a beat a voltage shift is registered because each beat causes ions to move in the person's body. Such a voltage shift is an extremely weak signal that cannot be easily detected. This platform managed to read such a weak signal with a high signal-to-noise ratio as a result of the high signal enhancement that was possible because of the use of the elicited organic electrochemical transistor (OECT).[37] The potential shift measured between the gel-based electrode that catches the heartbeats from the chest and the OECT ion-sensor channel allocated on the finger changes the organic channel electronic conductance.

Very well readable biological signals were measured under light-emitting diode (LED) illumination because of good adhesion of the ultraflexible platform to the skin. The recorded

https://doi.org/10.1021/acs.chemrev.1c00290
Chem. Rev. 2022, 122, 4636−4699

cardiac signal intensity and standard deviation peaked in an estimated signal-to-noise ratio 3-fold higher than previously reported. The mechanical flexibility and biocompatibility make it possible for the device to be attached directly to a rat heart's exposed surface. The electrocardiographic recorded when the heart-action-evoked potential was transduced by the self-powered OECT devices was assayed under the illumination of a simple LED light source, showing very strong electrocardiographic signals.

2. RELIABLY DETECTING A FEW OR A SINGLE BIOLOGICAL ANALYTE

In this section the toolbox to correctly operate a biosensor and apply the needed analytical chemistry validation strategies to the assays performed with ultrasensitive bioelectronic devices is provided. This enables gathering data with a given qualitative (including YES/NO type of response) and quantitative reliability. Typical biosensor figures of merit, such as sensitivity, selectivity, limit of detection (LOD), limit of identification (LOI), and limit of quantification (LOQ), are operatively defined (relevant to proceeding with the validation of a new biosensor platform).

The reliable and sensitive detection of an analyte has been the main focus of the biosensing community since the 1970s or 1980s with the development of the first commercial prototypes of glucose sensors and lateral flow-based devices, such as pregnancy tests.[17,39] Despite the continuous development of novel advances reported in the biosensing community, for instance new bioreceptors or transducers, glucose sensors and pregnancy tests still remain the most commercialized devices.[40] However, the attention of many researchers is currently being rerouted toward new goals such as the reliable detection of a few single biological analyte molecules (*e.g.*, low or ultralow limit of detection or quantification).[41] Figure 6 shows the possibility of sensing an analyte at different dimensional levels going from millimeter size (*e.g.*, tissues) down to few nanometers (*e.g.*, few molecules), finally achieving single-molecule detection.[42−44]

The single-molecule detection concept has been developed considering the possibility of mimicking natural processes like the ultrasensitive detection of pheromones by using vomeronasal neurons as a chemoreceptive platform transducing the pheromone concentration into an electrical signal.[45] Moreover, the downsizing of biological entities to be analyzed has been progressing in parallel with the development of new biosensing devices.

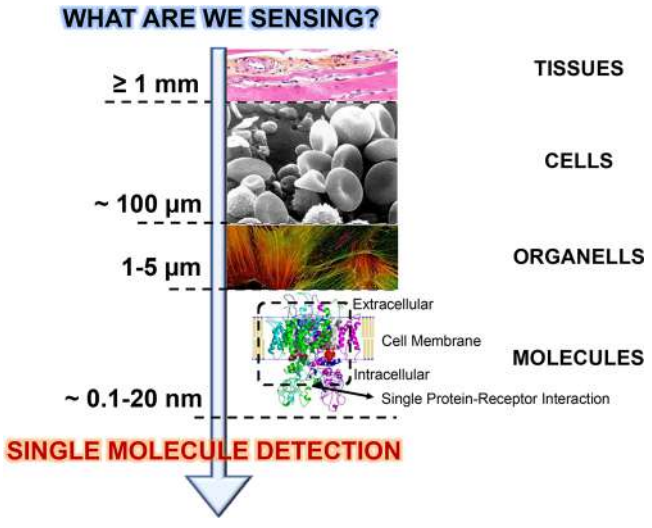

Figure 6. Schematic representation of the dimensional downsizing of biological analytes going from millimeter size (*e.g.*, tissues) down to few nanometers (*e.g.*, few molecules), finally achieving single-molecule detection.

In this section, the most relevant information on what is a biosensor and what is the correct way to operate it, but most relevantly, what are the figures of merit that need to be estimated to correctly characterize the level of performance of the device, is presented.

2.1. What is an Electronic Biosensor?

A biosensor is an analytical device able to convert information related to a biochemical interaction to produce a digital electronic signal quantitatively that is a function of the target analyte concentration.[46,47] To observe a specific biochemical interaction, biological recognition elements are usually immobilized or intimately incorporated onto the surface of the transducing interface. Hence, the information about the biochemical interaction can be transformed into a chemical or physical signal output.[48]

The structure of a biosensor is schematically reported in Figure 7. Notably, a variety of biorecognition elements (*e.g.*, antibody, DNA/RNA strands, aptamers, *etc.*) can be immobilized onto the detecting interface, forming stable complexes through the selective interaction with analytes such as antigens, viruses, microorganisms, complementary DNA/RNA strands, *etc.* The scheme also shows a selection of transducers that can be used to convert the biological signal into a quantifiable output. The list of transducers has been purposely limited to optical (*e.g.*, surface plasmon resonance, fluorescence, *etc.*), electrochemical (*e.g.*, amperometry, voltammetry, electrochemical impedance spectroscopy, *etc.*), and electronic (*e.g.*, field-effect transistor-based) because of their ability to achieve low and ultralow detection limits.[49]

2.2. Biosensor Figures of Merit

Despite the large amount of literature available on biosensing, in the interdisciplinary field of bioelectronics it is important to shed light on the analytical validation of these assays in order to gather data with a given qualitative and quantitative reliability. In this regard, one should be able to assess typical biosensor figures of merit, such as sensitivity, selectivity, limit of detection (LOD), limit of identification (LOI), limit of quantification (LOQ), *etc.*, to proceed with the validation of the new biosensor platform.[50] For convenience, Table 1 provides a complete list of the typical biosensors' figures of merit with a clear "take-home" message (operative definition) on how to use or calculate these parameters toward a rigorous validation of the analytical method. The performance of a biosensor (comparison with others or toward a reference method) can be quantitatively evaluated by using the aforementioned figures of merit.

Among the typical biosensors' figures of merit, sensitivity and selectivity deserve particular attention. The sensitivity of bioanalytical quantitative determination is usually defined as the slope of the calibration function $y = f(x)$. The calibration curve is obtained by recording the response signal for several concentrations, usually within the linear dynamic range. Thus, the sensitivity can be defined also as the differential quotient between two signal responses (Δy) and the corresponding concentrations difference ($\Delta[M]$), as shown in Figure 8A. In certain cases, sensitivities can be calculated over a larger or narrower range of concentrations; thus, it would be a good idea

https://doi.org/10.1021/acs.chemrev.1c00290
Chem. Rev. 2022, 122, 4636−4699

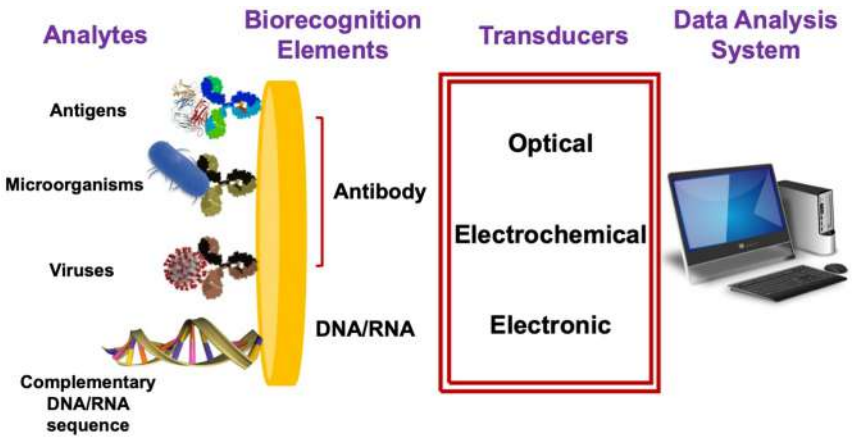

Figure 7. Structure of a typical biosensor.

Table 1. Typical Biosensor Figures of Merit

Figure of Merit	Operative Definition
Sensitivity	Identifies the slope, α, of the calibration curve with the equation $Y = \alpha[M] + \alpha_0$. It is calculated as $\alpha = \Delta y/\Delta[M]$.
Selectivity	A biosensor platform is able to distinguish the analyte of interest from other molecules present in the sample assayed.
Limit of detection (LOD)	Matches the lowest [M] that can be reliably detected at $3s_B$ units from the blank signal.
Limit of identification (LOI)	Matches the lowest [M] that can be reliably identified at $6s_B$ units from the blank signal.
Limit of quantification (LOQ)	Matches the lowest [M] that can be reliably quantified at $10s_B$ units from the blank signal.
Dynamic linear range	Identifies the concentration range where the correspondence between the signal recorded and the analyte concentrations is represented by $Y = \alpha[M] + \alpha_0$ (calibration curve).
Accuracy	Indicates how much the result of an experiment agrees with a "true" or expected value. It can be defined as an absolute error (difference between the two values) or as a percentage relative error (absolute error normalized by the expected value).
Precision	Measures the variability between the different trials for a single concentration of analyte or how much closer the agreement is between individual analyses on a certain sample.
Robustness	Qualitatively defines how much the analytical method is free from possible interference (if you can use a biosensor in any sample matrix).
Ruggedness	Qualitatively defines how much the analytical method is able to resist possible variations of the experimental conditions (*e.g.*, temperature, pressure, *etc.*).

to report the sensitivity with the corresponding dynamic linear range in order to perform accurate comparisons between different biosensor platforms.[51]

Consistent with the International Union of Pure and Applied Chemistry (IUPAC) definition, the selectivity can be defined as the possibility of distinguishing the analyte of interest from other molecules present in the analyzed sample. Some attempts have been made to quantify the selectivity, for example, considering a sensitivity factor matrix (K) that includes n sensors for m components (a matrix like $K[n, m]$). However, scientists are still using qualitative grades like good, excellent, poor, *etc*. Moreover, there is a very unfortunate problem about the misleading concept that "selectivity" and "specificity" are the same thing. The difference between "selectivity" and "specificity" is that the first can be graded while the second cannot. Thus, scientists should try to avoid creating unnecessary confusion, using preferably the term "selectivity".[52]

Other figures of merit, such as LOI, LOQ, calibration curve, and dynamic linear range, are discussed in detail in the following sections.

2.3. Qualitative ON/OFF or YES/NO Detection at the Limit of Detection (LOD)

A qualitative analysis aims at detecting if a given species is present (signal-ON) or absent (signal-OFF) in the sample to be assayed. This is the reason why it is also named *ON/OFF-type* or *YES/NO-type* detection because a signal is *ON* when the analyte is present although no information on the actual concentration is available at a sufficiently high level of confidence. These detections are performed taking the LOD level as threshold to discriminate the *ON* from the *OFF* state. Indeed, according to IUPAC recommendation, the limit of quantification (LOD) has been defined as the minimum concentration (or amount) of analyte that could be statistically distinguished from the blank (no analyte present) in terms of signal response.[53,54] In Figure 8A a typical calibration curve is shown.

However, several issues have arisen especially considering the term "statistically different". In this regard, the error magnitude associated with measuring of a certain concentration of analyte (C_A) can be generally described by using a Gaussian distribution or bell-shaped function, also known as a normal distribution. The bell-shaped function is centered at the mean value of the responses for a certain analyte concentration ($\overline{y}_A$) and spreads out for k units of standard deviation (σ), as shown in the inset of Figure 8B. The area underlying the bell function can be described in terms of the probability that response values (y_x) measured for an x concentration of analyte would fall somewhere under the curve. Hence, the probability that a newly measured value (y_E) would be k units of standard deviation from the mean response value ($\overline{y}_A$) is the probability that $y_E \geq \overline{y}_A + k\sigma$.[51] This can be graphically represented by the

https://doi.org/10.1021/acs.chemrev.1c00290
Chem. Rev. 2022, 122, 4636−4699

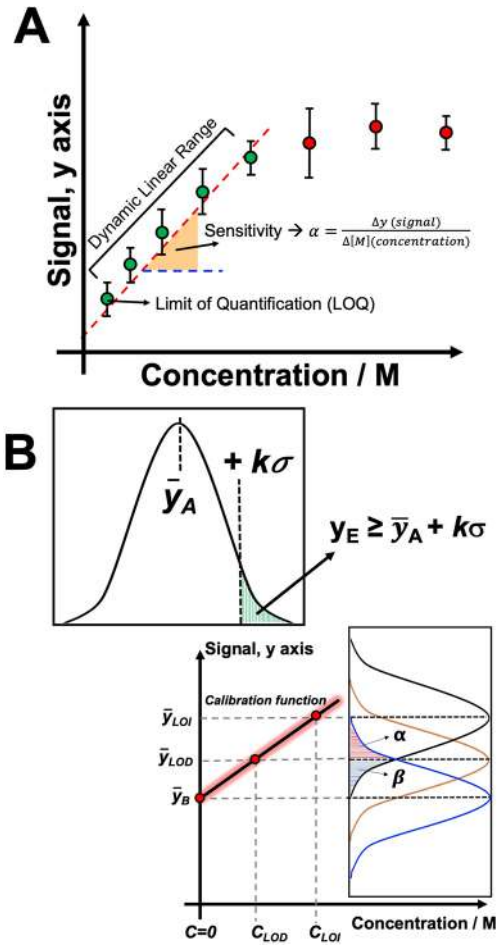

Figure 8. (A) Schematic representation of dynamic linear range (green data points) over a larger range of concentrations used to perform the calibration curve. The first green data point is the lowest [M] that can be accurately quantified, defined as limit of quantification (LOQ). The orange shaded area represents the calibration slope also defined sensitivity of the analytical method. (B) Calibration function that allows the statistical definition of blank signal, limit of detection (LOD), and limit of identification (LoI) with the corresponding statistical distributions. The red and blue shaded areas (α and β) represent the probability of obtaining a false positive or false negative outcome in the proximity of the LOD signal response. Inset: Scheme of a normal distribution.

green shaded area on the right of the dashed line (inset of Figure 8B) as

$$P = \frac{1}{2\pi}\int_{k}^{\infty} \exp\left(\frac{-k^2}{2}\right)dk \tag{2.1}$$

where the y_E value is $k\sigma$ from $\overline{y}_A$ (*i.e.*, $(y_E - \overline{y}_A)/\sigma = k$). This prologue on the statistical definition of the error correlated with a measurement can help in the explanation of the IUPAC definition of the LOD. When determining LOD, a certain number of measurements on the blank needs to be taken. However, two questions have to be answered up front: "What is the blank?" and "How well are these y_B values known?".[55] First, the blank is a sample containing zero analyte concentration. The second answer proceeds through the calculation of mean value of blank responses ($\overline{y}_B$) as

$$\overline{y}_B = \frac{\sum_{j=1}^{n_B} y_{Bj}}{n_B} \tag{2.2}$$

and the standard deviation as

$$s_{BB}^2 = \frac{\sum_{j=1}^{n_B} (y_{Bj} - \overline{y}_B)^2}{(n_B - 1)} \tag{2.3}$$

for n_B observations. In a normal set of measurements, 20 (or more) blank readings would be taken.

In this case, the variance (s_B) can be considered as an indicator of standard deviation of the blank (σ_B). By using a normal distribution for the error correlated with the blank measurements, the probability that the minimum concentration (or amount) of analyte (C_{LOD}) could be statistically distinguished from the blank and not an odd fluctuation of the blank depends on how many units of standard deviation $\overline{y}_{LOD}$ is away from $\overline{y}_B$ (mean value of blank responses). If $\overline{y}_{LOD}$ were $3s_B$ units away from $\overline{y}_B$, $\overline{y}_{LOD}$ would fall in the red shaded area (α), meaning a 0.13% probability that the signal $\overline{y}_{LOD}$, corresponding to C_{LOD}, is a random oscillation of the blank signal (99.87% probability high chance that $\overline{y}_{LOD}$ is a true value). This probability fulfils the requirements of the term "statistically different". In compliance with the IUPAC recommendation

$$\overline{y}_{LOD} = \overline{y}_B + ks_B \tag{2.4}$$

where k is a numerical value based on the confidence level desired. Thus, C_{LOD} could be defined as a function of $\overline{y}_{LOD}$

$$C_{LOD} = \frac{(\overline{y}_{LOD} - \overline{y}_B)}{m} \tag{2.5}$$

where m is the sensitivity of the analytical assay (*e.g.*, biosensors). Using eq 2.5, it is possible to obtain

$$C_{LOD} = \frac{ks_B}{m} \tag{2.6}$$

This definition is graphically represented in Figure 8B. The LOD can be determined by expressing ks_B as a certain concentration value divided by the slope of the calibration curve (solid line highlighted in red) obtained from the linear regression analysis.

According to the normal distribution, considering $k = 3$, a confidence level of 99.86% that $\overline{y}_{LOD} \geq \overline{y}_B + 3s_B$ is granted. However, many problems have been encountered in the definition of the LOD, especially considering all the expressions of standard deviation of the blank (σ_B) that could be used. This may result in a variety of $\overline{y}_{LOD}$ values calculated according to equations that are different from the one recommended by IUPAC.[56]

To help define the trueness of LOD values, another concept has been introduced in $\overline{y}_{LOD}$ estimation, namely, the limit of identification (LOI, $\overline{y}_I$) defined as

$$\overline{y}_I = \overline{y}_{LOD} + ks_I \tag{2.7}$$

where s_I is the error correlated with the measurement of $\overline{y}_I$. If $s_I = s_B$, eq 2.7 can be replaced by

$$\overline{y}_I = \overline{y}_{LOD} + ks_B \tag{2.8}$$

as graphically shown in Figure 8B. Thus, combining eqs 2.4 and 2.8, it is possible to obtain

$$\overline{y}_I = \overline{y}_B + 2ks_B \tag{2.9}$$

which for $k = 3$ would be

https://doi.org/10.1021/acs.chemrev.1c00290
Chem. Rev. 2022, 122, 4636−4699

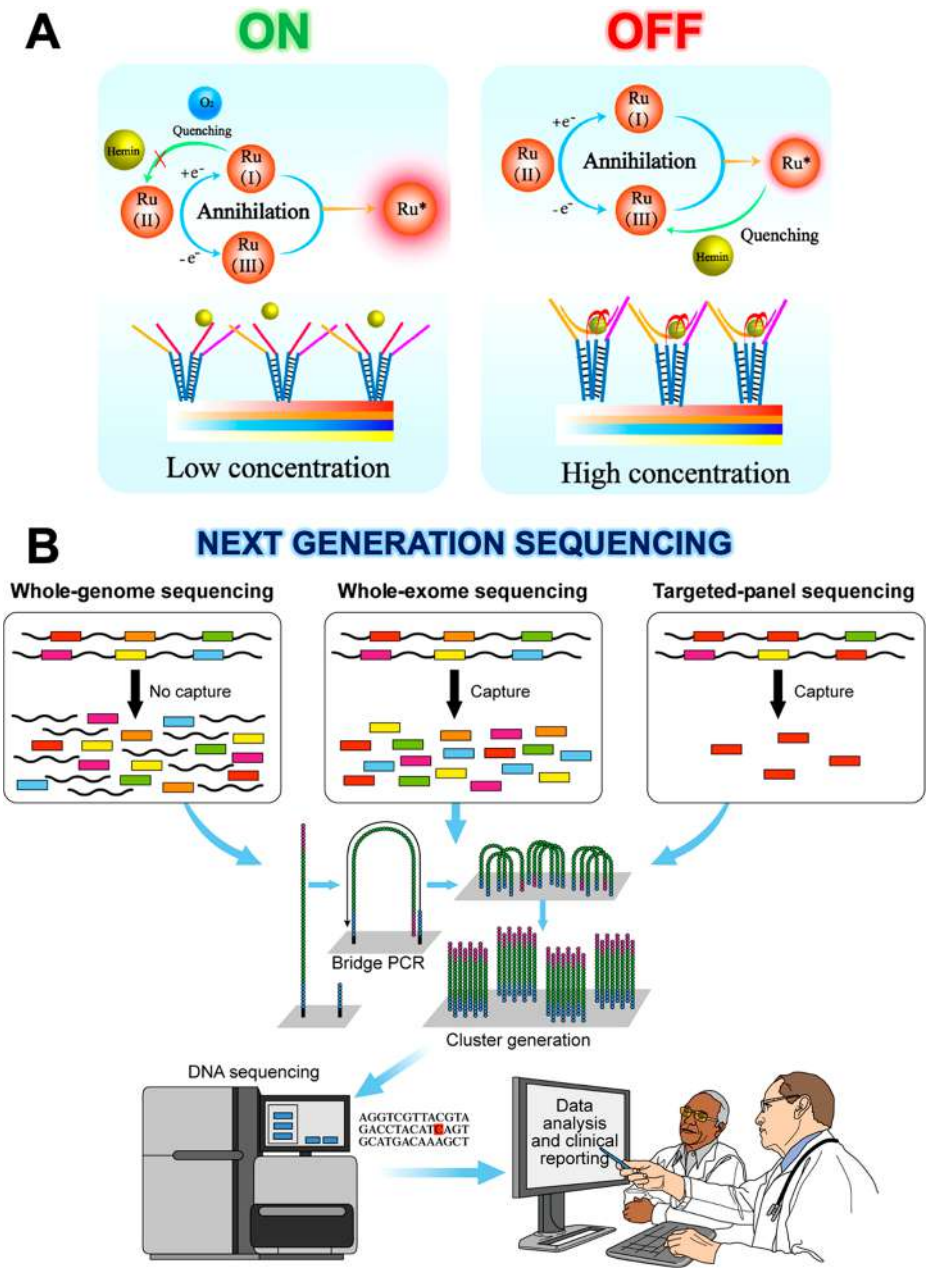

Figure 9. (A) Scheme of an ultrasensitive "ON/OFF" ECL biosensor for the detection of PML/RARα. (B) Scheme of the sequencing revolution by NGS though whole-genome sequencing, whole-exosome sequencing, and targeted-panel sequencing. After the capture of specific genome portions, they are amplified through bridge-PCR and cluster generation. Finally, the selected DNA fragments are sequenced and analyzed. Panel A is adapted with permission from ref 62. Copyright 2019 American Chemical Society. Panel B is reprinted with permission from ref 64 . Copyright 2017 Elsevier Ltd.

$$\overline{y}_{II} = \overline{y}_B + 6s_B \tag{2.10}$$

which means that the limit of identification (LOI, $\overline{y}_I$) is $k_I = 6$ units of s_B away from $\overline{y}_B$.[57]

However, sometimes it is not possible to perform a large number of replicates mainly because of financial (*e.g.*, high cost of the biosensor platform to perform the analysis) and technical reasons (*e.g.*, low volume or amount of sample available).[58] Thus, the normal distribution cannot be applied for the statistical analysis of the measurements recorded because of the limited number of replicates available (*e.g.*, 3 or greater), while the Student's *t*-distribution results would be more appropriate. In the *t*-distribution, the variance (s_B) would need to be replaced by the standard error ($\overline{s}_B$), expressed by

$$\overline{s}_B = \frac{s_B}{\sqrt{n_B}} \tag{2.11}$$

while the *k* factor is replaced by t_α (these values are tabulated for different degrees of freedom and according to the confidence level desired), which is determined for a certain number of readings (n) that corresponds to $\nu = n - 1$ degrees of freedom. Thus, eq 2.4 would be rearranged as

$$\overline{y}_{LOD} = \overline{y}_B \pm t_\alpha \frac{s_B}{\sqrt{n_B}} \tag{2.12}$$

which is used to calculate the confidence interval. To obtain a confidence level of 99.87% corresponding to $k = 3$, we would

https://doi.org/10.1021/acs.chemrev.1c00290
Chem. Rev. 2022, 122, 4636−4699

need to use an $\alpha = 0.0005$ (meaning a 99.9% confidence level for a two-tailed *t*-distribution).[59]

On the basis of previous equations, if y_X were at least $3s_B$ units below $\overline{y}_D$, it would fall in the blue shaded area (β) below $\overline{y}_{LOD}$; hence, $P = 0.13\%$ that y_X is not a true signal. By considering that the red and blue shaded areas are the same (0.0013), as reported in Figure 8B, the probability that a reading y_X (related to C_X approximately close to C_{LOD}) would fall in one of the two areas is 50%. Hence, it is possible to introduce the concepts of *false positive* (falling in the red area, α), when a test result indicates the presence of a certain analyte while it is not present, and *false negative* (falling in the blue area, β), which is the opposite error occurring when the test fails to indicate the presence of a certain analyte while it is present in reality.[60] These concepts are the two kinds of errors occurring in a binary classification that are the base of a qualitative detection as "YES/NO" or "ON/OFF" answer in several biosensing platforms. This cannot be considered a "true" quantification because the signal response obtained has a numerical (or statistical) significance below the LOQ, which is usually set at $10s_B$ units away from $\overline{y}_B$.

There are plenty of biosensing platforms based on the qualitative detection as "YES/NO" or "ON/OFF" outcomes, but we will review only a few cases where the LOD is approaching the femtomolar range, including also some insights on the detection based on the NGS. Jing and co-workers detected matrix metalloproteinase 2 (MMP-2) by using a signal "ON/OFF" electrochemical peptide-based biosensor.[61] The assay was based on target-induced cleavage of the specific peptide immobilized on DNA-porous platinum nanoparticles (S1-pPtNPs-P1).

To detect MMP-2, the modified surface underwent hybridization chain reaction to embed the electroactive thionine. In the presence of H_2O_2, the intensity of the electrochemical signal depended on H_2O_2 reduction catalyzed by pPtNPs, thus being significantly amplified (ON state corresponding to the absence of substrate). After the cleavage operated by MMP-2 (analyte), pPtNPs and the electroactive thionine would leave the electrode surface, conveying a remarkable drop of the electrochemical signal (OFF state corresponding to the presence of analyte). This biosensing platform exhibited an LOD of 0.32 pg mL^{-1}, setting the threshold for the "ON/OFF" detection in the femtomolar range (5.1 fM based on the molecular weight of MMP-2). Bian *et al.* developed an enzyme-free "ON/OFF" electrochemiluminescence (ECL) biosensor detecting the fusion gene PML/RARα (promyelocytic leukemia, retinoic acid receptor α) as a biomarker of acute promyelocytic leukemia.[62]

The sensing mechanism is based on a simple target-switched DNA nanotweezer combined with hemin as response amplifier, as shown in Figure 9A. In the absence of the analyte, the nanotweezer was in the open state, leading to a low concentration of hemin in solution that results in an enhanced $Ru(bpy)_3^{2+}$ electrochemiluminescence signal (ON state, absence of analyte). On the other hand, in the presence of PML/RARα, the nanotweezer in its closed conformation can capture hemin, quenching the electrochemiluminescence signal (OFF state, presence of analyte). With this amplification, the authors were able to set the "ON/OFF" threshold for PML/RARα detection at 0.125 fM. Moreover, a biosensor platform that combines electrochemiluminescence as amplification mechanism and molecular imprinted polymers for trace detection of dopamine was realized by Wang and co-workers.[63] In this platform, the authors combined CdSeTe/ZnS quantum dots with a molecularly imprinted polymer based on o-phenylenediamine which was templated with dopamine. In the absence of dopamine, the electrochemiluminescence response was quite significant (ON state, no analyte is present).

First, the glassy carbon electrode was modified with zinc sulphide quantum dots responsible for the photoelectric signal denoted as "ON1". Next, the immobilized hairpin DNA1 was used. The selective detection of dopamine (rebinding mechanism) was further amplified from the quenching effect of dopamine on the electrochemiluminescence reaction of quantum dots in the presence of potassium persulfate as coreactant (OFF state, analyte is present), thus achieving an LOD of 3.3 fM, which was considered as a threshold value for the qualitative detection of dopamine.

In a similar approach, Mo and co-workers reported on the development of microRNA assay for the early diagnosis of a variety of diseases.[65] This biosensing platform was conceived as enzyme-free "ON1-OFF-ON2" photoelectrochemical biosensor for the sensitive detection of microRNA141. In this case, manganese-doped cadmium sulphide coupled with zinc sulphide quantum dots and manganese porphyrin have been used as photoelectric material and photosensitizer, respectively.

The modified electrode was used to target microRNA141 (at different concentrations) through a mechanism of the unfolding of hairpin DNA1. At this point, the catalytic hairpin amplification was occurring through the interaction with a complementary sequence of DNA, namely, hairpin DNA2, which was displacing microRNA141, making it readily available for the next binding interaction (target recycling). The as-modified electrode was further hybridized with DNA1 and DNA2. After the catalytic hairpin amplification process and further hybridization, the photocurrent value recorded was quite low compared to the previous step. This step can be identified as the "OFF" state. Then, the electrode was incubated with manganese porphyrin, recovering the photocurrent signal because of the photocatalysis and photosensitization of manganese porphyrin, denoted as "ON2". This quadradic amplification process using target recycling and photoactive materials allowed placing the LOD threshold for a qualitative detection of microRNA141 at 3.3 fM.

Another electrochemical biosensor was developed by de la Escosura-Muñiz and co-workers that realized a nanochannel-based immunoassay able to filter and detect proteins in whole blood without any particular pretreatment.[66] The biosensor platform was realized depositing an anodized aluminum oxide nanoporous structure, including a specific antibody in the nanochannel. In the absence of substrate (ON state), a redox probe was diffused toward the electrode surface, resulting in a high electrochemical signal, while after the interaction with the antigen, the diffusion was hindered, lowering the electrochemical signal (OFF state). The as-modified system did not allow achieving ultralow LOD, but after completing the affinity sandwich with a gold nanoparticles (AuNPs)-labeled antibody, the sensitivity was extremely increased, allowing the ultrasensitive detection of CA15-3 in blood with an LOD of 600 fM.

Despite the electrochemical platforms, solid-state nanopores and nanopipettes have been used to develop new biosensing devices. In particular, the detection method involves measuring ionic current variations associated with the electrolyte solution swap during the application of voltages between two chambers filled with ionic solutions.[67] At constant potential, the target molecule in one chamber would move through the nanopore, producing a transient variation in the ionic current. Both

https://doi.org/10.1021/acs.chemrev.1c00290
Chem. Rev. 2022, 122, 4636−4699

techniques allow the detection of a target analyte at the single-molecule level without any labeling procedure. In this regard, Yu and co-workers reported the monitoring of an immunoreaction between the α-fetal protein and its antibody at the single-molecule level by using a quartz nanopipette ($d \approx 30$ nm). The discrimination was based on different current blockages produced in the presence of only antigen and antigen−antibody complex (variation of conductivity).[68]

Recently, many researchers focused their attention on a new type of solid-state nanopores, defined as plasmonic nanopores, which allowed moving to the next level of information behind the single-molecule detection, notably single-molecule sequencing.[69] This technology can play a significant role in building a portable sequencing technology ("fourth" generation sequencing), as part of NGS, that is defined as large fragment single-molecule aiming at sequencing long DNA (and RNA) molecules. This technology is increasingly being applied in clinical testing (*e.g.*, neurodegenerative diseases that are mostly related to monogenetic causes).[70] To date, three NGS approaches have been explored: whole-genome sequencing, whole-exosome sequencing, and targeted-panel sequencing, as displayed in Figure 9B. Whole-genome sequencing is achieved when the sequencing and the associated data analysis of the entire genome are performed, comprising roughly 3 billion base pairs (bp) of DNA. Despite being a huge source of information, whole-genome sequencing certainly exhibited some limiting factors, such as incomplete coverage [*e.g.*, analyzing the whole-genome sequencing of individuals, some important genes (variants), considered as biomarkers for pathological conditions, might not be covered (or sequenced)], the sequencing cost (*e.g.*, whole-genome sequencing is 3/5-fold more expensive than whole-exome sequencing offering a larger but incomplete coverage), the complexity of data processing for whole-genome sequencing considering the different levels of information, and the sample size required (*e.g.*, sometimes the sample size does not allow having a large number of replicates). Alternatively, whole-exome sequencing covers all protein-coding regions of the human genome, restricting the sequencing process down to 50 million bp (1.5% of the whole human genome). Herein, there are also some problems related to the coverage and the high processing cost. Hence, targeted-panel sequencing might be most appropriate when a given pathologic state has already been diagnosed. In this case, depending on the disease, the coverage might be downsized to 10^2-10^6 bp (*i.e.*, ∼0.5−5% of an exosome). To amplify specific genomic regions, targeted-panel sequencing undergoes a target-enrichment step. Despite the advantage of the deepness of information for a specific disease, the main limitation of this approach is the new gene discovery (most of the new diseases are related to genes, whose sequence still needs to be uncovered). Finally, the parallel sequencing occurs through bridge PCR where the primers are immobilized on the surface of a flow cell (dense layer) allowing the attachment of complementary DNA strands at one end first and later to the other primer. Afterward, the enzymes create the double strands DNA that are further denatured to generate separate DNA fragments. This process is repeated *n*-fold in order to obtain clusters of identical strands that allow DNA sequencing through different technologies (*e.g.*, 454 pyrosequencing, reversible terminator sequencing, illumina, *etc.*).[64]

In this section, we have reported so far only two general cases of statistical analysis applied to collected data, notably the normal distribution (considering the case $s_I = s_B$ for a large number of data gives 50% probability of trueness of the recorded response) and the *t*-distribution (considering the case of a small number of replicates for a certain measurement). However, to make the picture clearer for the readers, we should mention two other cases: the first one frequently occurring within the biosensing community, while the other one is mainly regarding single-molecule detection.

In the first case, we will consider a case of normal distribution with $s_I \neq s_B$ (different number of replicates performed for the blank and $\overline{y}_I$) where the probability that a reading y_X would be a false positive or a false negative will be different because of the different variance (standard error) associated with the measurements. In the other case, regarding the single-molecule detection, the normal distribution (or *t*-distribution) would be unable to analyze experiments with an indefinitely large number of trials and a limited probability that an event is likely to occur at each trial. The Poisson distribution as a special case of the binomial distribution can be a valid alternative. For example, we might consider the number of bacteria growing on a Petri dish. In this case, there are many tiny spots on the dish where bacteria may or may not grow (little probability of the event to occur in each spot).[71−73]

2.4. Quantitative Detection at the Limit of Quantification

Quantitative detection is the assay that enables giving the exact concentration of a given analyte with a sufficiently high level of confidence. To this end the level of quantification (LOQ) needs to be used. Despite the great attention devoted to operatively define the limit of detection (LOD), as previously discussed, IUPAC did not give any particular recommendation for the limit of quantification (LOQ) that was numerically defined for the first time by the American Chemical Society (ACS).[57] Because LOD was not fulfilling any quantitative analysis minimum requirements, ACS introduced LOQ as an additional statistical distance between the blank and sensing signal distributions. Hence, LOQ is the minimum analyte concentration that can be quantitatively detected with a given degree of reliability, as shown in Figure 8A. In compliance with the aforementioned definition and considering a data set that follows a normal distribution

$$\overline{y}_{LOQ} = \overline{y}_I + ks_Q \tag{2.13}$$

where s_Q is the variance associated with the measurement of $\overline{y}_{LOQ}$. If $s_Q = s_I = s_B$, eq 2.13 can be replaced by

$$\overline{y}_{LOQ} = \overline{y}_I + ks_B \tag{2.14}$$

which combined with eq 2.8 gives

$$\overline{y}_{LOQ} = \overline{y}_B + 2ks_B + ks_B \tag{2.15}$$

rearranged as

$$\overline{y}_{LOQ} = \overline{y}_B + 3ks_B \tag{2.16}$$

which means that the limit of quantification (LOQ, $\overline{y}_{LOQ}$) is $k_Q = 3k = 9$ units of s_B away from $\overline{y}_B$. The fact of selecting $k_Q = 9$ (95% probability) or $k_Q = 10$ (99% probability) depends on the confidence level desired. During a set of experiments, only a restrained number of blank signals are registered. Thus, considering eq 2.12 and its boundary conditions, we can define

$$\overline{y}_{LOQ} = \overline{y}_B \pm 3t_\alpha \frac{s_B}{\sqrt{n_B}} \tag{2.17}$$

which can be used to calculate the confidence range for LOQ according to *t*-distribution.

https://doi.org/10.1021/acs.chemrev.1c00290
Chem. Rev. 2022, 122, 4636−4699

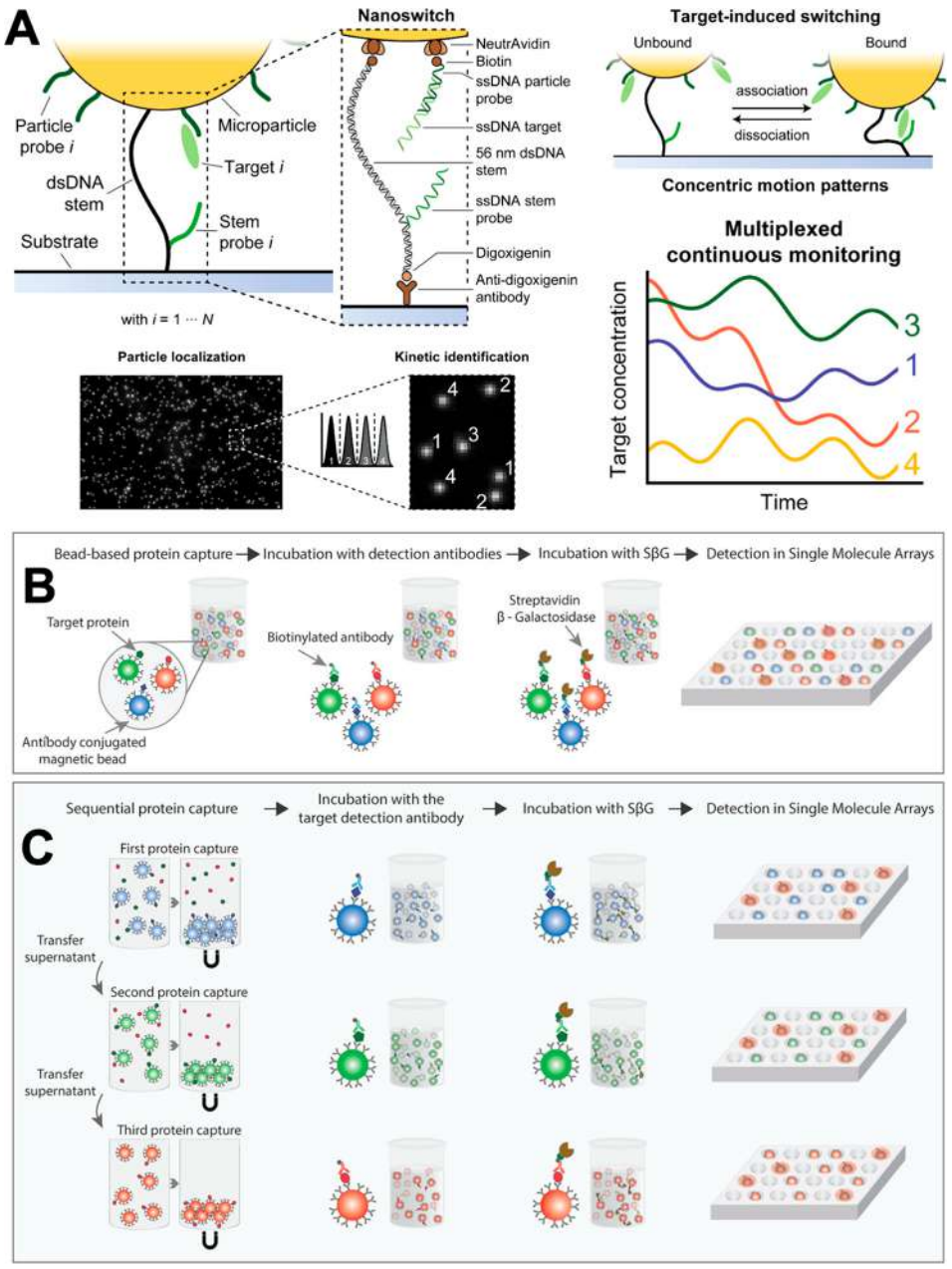

Figure 10. (A) Scheme of a binary nanoswitch for multiplexed continuous biomolecular monitoring at the single-molecule level. This includes three components: a single double-stranded DNA stem linking the particle to the surface, a single stem probe, and several particle probes (immobilized on the surface of the microparticle). The DNA-based nanoswitch is connected to the microparticle through the affinity complex neutravidin−biotin and to the surface through the complex between digoxigenin and its antibody. The binding of the target molecule binding to the nanoswitch can be detected because the particles exhibit different motion patterns in the bound (low mobility) and unbound states (high mobility). Hence, it is possible to kinetically detect the single molecule as well as following the time traces. (B) Scheme of a standard Simoa assay without magnetic separation. (C) Scheme of the procedure of a sequential multiplex Simoa assay by using sequential magnetic separation. Panel A is adapted with permission from ref 78. Copyright 2020 American Chemical Society. Panels B and C are adapted with permission from ref 81. Copyright 2021 Wiley.

In addition to the definition of LOQ, the calibration curve is also a key element within quantitative analysis, establishing a one-to-one correspondence between the signal recorded (y_x) with the x concentrations for a certain analyte. Pure substances can be exploited as calibrating standard. The goal of a calibration curve goes far behind the mere construction of the transfer function, evaluating the error throughout the measurement range (error associated with the deviation of the transfer function from its true value). The construction of a calibration curve encompasses the following steps:

- preparation and certification of the standardized mixtures;
- recording of analytical signal for each certified concentration value of the standardized mixtures;
- monitoring of the uniformity and dispersion of analytical responses in the concentration range chosen for the calibration procedure;
- model the calibration curve;
- calculate the parameters of the calibration curve based on the least-squares method and verification of its accuracy;
- evaluate the confidence limits desired for each concentration on the basis of their signal response.

https://doi.org/10.1021/acs.chemrev.1c00290
Chem. Rev. 2022, 122, 4636−4699

Considering the procedure just discussed for the construction of a calibration curve, one should be able to obtain a transfer function like the one reported in Figure 8A. By selecting k standardized mixtures corresponding to k concentrations, the transfer function (calibration curve) in its dynamic linear range (red dashed line within the range of the green data points) would be represented by

$$Y = \alpha[M] + \alpha_0 \tag{2.18}$$

where α is the slope or the sensitivity of the analytical methods and α_0 the intercept.[74]

Herein, we would like to review a few examples about quantitative analysis at the single-molecule level. Thrift and co-workers reported on the possible combination of single-molecule detection and imaging methods.[75] In particular, the authors demonstrated the possibility of combining surface-enhanced Raman scattering spectroscopy (SERS) with convolutional neural network CNN. The analysis of SERS spectra with a convolutional neural network model allowed determining single-molecule events' distribution. To achieve the single-molecule detection, SERS spectra are bundled into (8×8)-pixel maps and processed by using a nonnegative matrix factorization chosen by using principal component analysis (PCA). This allowed quantifying many metabolites down to 10 fM as LOQ.

Another approach that showed promising features toward single-molecule quantification was reported by Cheng and co-workers.[76] The detection of microbial nucleic acids is currently considered the most reliable technique to rapidly diagnose many infectious diseases. The authors developed a new culture-free method based on the single-molecule tethering mechanism to detect microorganisms in body fluids at the single-molecule level. The sensing platform is modified with an oligonucleotide sequence (Oligo-3) that is able to capture the DNA-machinery. After the lysis of a microbial cell, there is the release of RNA in a solution containing the oligonucleotide sequence (Oligo-2), a long DNA-probe, and a micrometer-sized bead modified with an oligonucleotide sequence (Oligo-1, complementary to Oligo-2) which were able to form the DNA machinery. Finally, the DNA machinery was captured on the modified capillary surface. The ultrasensitive quantification was obtained by measuring the displacement of micrometer-sized beads bound to DNA probes. The authors demonstrated the possibility of using the single-molecule tethering technology to quantify microbial nucleic acids directly in human fluids at subfemtomolar concentrations.

We have discussed the calculation of several analytical parameters (*e.g.*, limit of detection, limit of quantification, dynamic linear range, *etc.*) considering only one analyte. Currently, to circumvent the labor-intensive and time-consuming single-analyte determination, many scientists have started to develop analytical methods able to qualitatively and quantitatively detect multiple analytes at the same time, defined as multiplexing. This is an important advancement toward the instant gain of a large amount of information from a single analysis.[77]

Lubken and co-workers described a new sensing technology based on single-molecule encoded binary nanoswitches.[78] Figure 10A displays a micrometer-sized particle bound to a surface through a single nanoswitch. This includes three components: a single double-stranded DNA stem linking the particle to the surface, a single stem probe, and several particle probes (immobilized on the surface of the microparticle). The DNA-based nanoswitch is connected to the microparticle through the affinity complex neutravidin−biotin and to the surface through the complex between digoxigenin and its antibody, as shown in the inset of Figure 10A.

The biomolecular interaction occurs through the reversible binding of target molecules, which are picked up from the particle probe. Next, the stem probe triggers the nanoswitch because of the interaction between the stem probe and the target molecule. Each interaction exhibited a different dissociation rate in order to create the multiplexing functionality, as displayed from the different time traces reported in Figure 10A. The proposed system was able to perform a kinetic identification at the single-particle level, which means single target molecule considering the interaction mechanism. As seen in the previous section, solid-state nanopores are frequently used to perform single-molecule detection or with ultralow limit of detection ($\leq$ fM). In this regard, Sze and co-workers realized a nanopore-based platform to perform multiplexed analysis at the single-molecule level.[79] This sensing approach was based on a standard DNA translocation process mainly due to electrophoretic forces occurring in the presence of an electric field. The translocation occurred from the inner to the outer side of the nanopore. The double-stranded DNA was modified with specific recognition aptamer sequences able to target selectively α-thrombin and acetylcholinesterase. The authors demonstrated the possibility of observing differences in the ionic current due to the translocation of only DNA and DNA complexed with target proteins, namely, α-thrombin and acetylcholinesterase. This approach can be extended to n target proteins offering a tuneable sensing platform for highly sensitive multiplexed detection.

Alternatively, Pawlak and co-workers developed a protein microarray able to perform multiplexed analysis in the zeptomolar range.[80] The system is based on a planar waveguide technology where a laser light is refracted from a layer of Ta_2O_5 deposited onto a transparent glass.

A strong evanescent field, along the direction of light propagation, was created at the interface between the modified surface and the solution (penetrating for about 200 nm, similar to surface plasmon resonance). Next, the immobilized antibody would selectively interact with a certain fluorescent-labeled antigen. Thus, only the fluorescent label in the range of 200 nm from the surface (only the antigens captured) would interact with the evanescent field being then excited and detected by a CCD camera. As a proof of concept, the system was used to detect simultaneously and quantitatively interleukin-2 (IL-2), interleukin-4 (IL-4), and interleukin-6 (IL-6). The multiplexed analysis was performed by using different fluorescent labels in order to be excited at different wavelengths.

Another approach to perform single-molecule (protein) immunoassay, the so-called Simoa, was first reported by Rissin and co-workers in 2010.[23] The authors demonstrated the principle of performing a single-molecule detection by using microscopic paramagnetic beads decorated with a specific capturing antibody, which is able to form the affinity-sandwich with another antibody labeled with an enzymatic reporter capable of generating a fluorescent product and is easy to detect. This was first defined as digital ELISA. This system was able to detect the prostate-specific antigen at concentration as low as 0.4 fM, showing also calibration curves performed with high accuracy ($r^2 = 0.995$). The same concept has been reproposed by the same research team in a multiplexed approach to detect several target molecules with a sensitivity at the single-molecule level, now defined as single-molecule array. The authors were able to simultaneously detect tumour necrosis factor α, IL-6, interleukin-1α (IL-1α), and interleukin-1β (IL-1β).[82]

https://doi.org/10.1021/acs.chemrev.1c00290
Chem. Rev. 2022, 122, 4636−4699

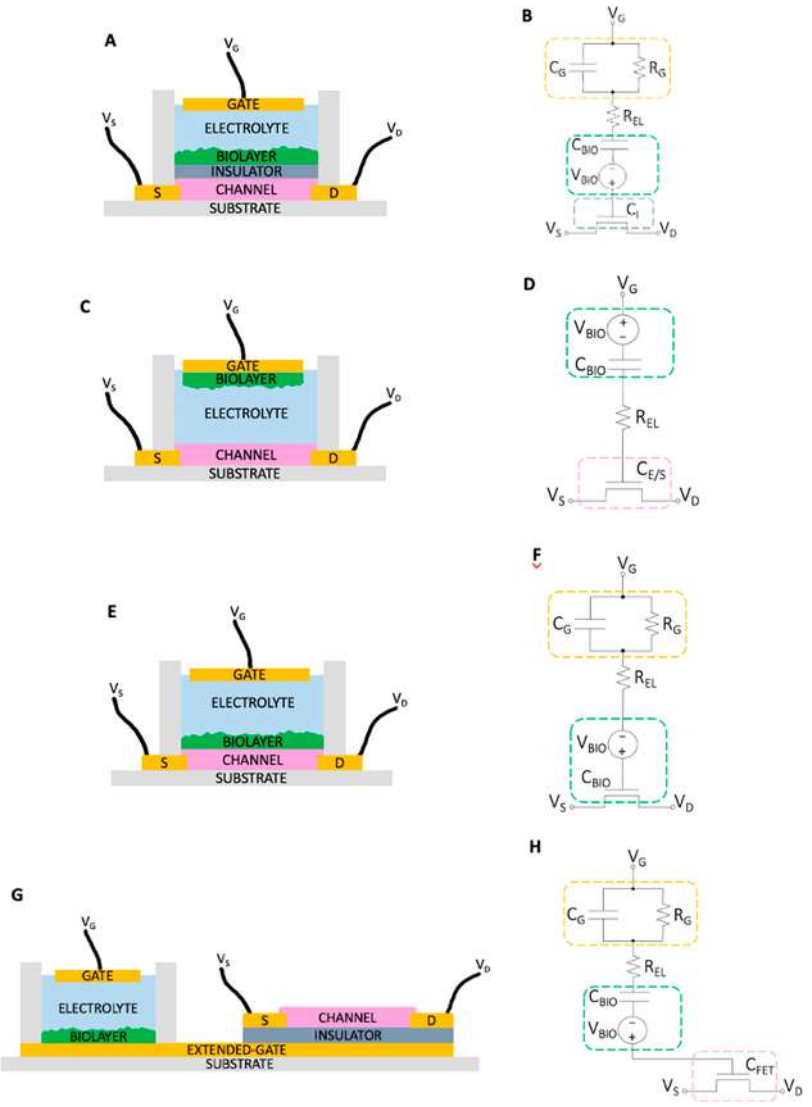

Figure 11. Architectures and equivalent circuit model of EG-FET biosensors. (A) Basic structure and (B) equivalent circuit of a biofunctionalized-insulator EG-FET. (C) Basic structure and (D) equivalent circuit of a biofunctionalized-gate EG-FET. (E) Basic structure and (F) equivalent circuit of a biofunctionalized-channel EG-FET. (G) Basic structure and (H) equivalent circuit of a biofunctionalized-extended-gate FET.

In another report, Gilboa *et al.* demonstrated the possibility of eliminating the possible assay cross-reactivity modifying the standard capturing process in a sequential process by using a magnetic field associated with paramagnetic beads.[81] The standard single-molecule immunoassay is performed by using paramagnetic beads modified with different capturing antibodies, as shown in Figure 10B. Next, the beads were directly incubated (without any magnetic separation) with the target protein, followed by the interaction with the biotinylated antibody to form the immunocomplex (*e.g.*, sandwich affinity interaction like in a normal ELISA). The modified beads were finally labeled with a redox enzyme (in this specific case, streptavidin-β-galactosidase). The single-molecule imaging is performed resuspending the beads in a fluorogenic substrate loaded in the microwells. This assay could be performed also using a sequential protein-capturing protocol by means of paramagnetic beads separated with the aid of a magnetic field, as displayed in Figure 10C.

This technology has been finally approved as a diagnostic test by the Food and Drug Administration (FDA) and is now commercialized as Simoa HD-I Analyzer, which is able to perform all the aforementioned operations in an automated mode.[83] This instrument is currently used as a validation method for new upcoming SiMoT detection systems that perform protein and genomic marker detection at the single-molecule level.

3. ULTRASENSITIVE BIOELECTRONIC DEVICES: STRUCTURES AND MATERIALS

3.1. Electrolyte-Gated-FET Sensing Devices

EG-FETs transduce and amplify the biochemical events taking place within the biolayer generating an electronic current I_D through the transistor channel. The biolayer is embedded into the transistor architecture, as for example on the gate electrode or on the semiconducting channel. The integration of a biolayer is essential as it allows the EG-FET biosensor to selectively detect the target molecule(s). The proper design optimization of the EG-FET architecture is important for enhancing the bioelectronic transduction and amplification. Depending on the specific properties of the biolayer as well as on the dimension of the biofunctionalized surface, various approaches have been

https://doi.org/10.1021/acs.chemrev.1c00290
Chem. Rev. 2022, 122, 4636−4699

proposed (see section 4). Based on the dimension of the biofunctionalized surface, *wide-field* or *large-area* and *near-field* EG-FET architectures were developed. Wide-field single-molecule approaches make use of a large-area surface, *viz.* micrometers or even millimeters wide, covered with densely packed recognition elements. Current approaches demonstrated wide-field EG-FETs biosensors with biofunctionalized insulator, gate, and channel surfaces.[84] In contrast, near-field single-molecule approaches require nanoscopic dimensions of the EG-FET because only one (or few at most) recognition element is embedded into the transistor architecture (*vide infra*). Current approaches demonstrated near-field EG-FETs biosensors with a biofunctionalized nanoscale channel or directly with a single-protein channel.[1−4] Here, we focus on the EG-FET biosensor architectures for single or few molecule detection accounting for the wide-field approaches.

3.1.1. Wide-Field EG-FET Architectures. Wide-field EG-FETs biosensors can be implemented with four fundamental structures, as schematically depicted in Figure 11. Figure 11A shows a biofunctionalized insulator EG-FET, which is based on the conventional ion-sensitive FET architecture (ISFET)[85,86] originally introduced for pH sensing with silicon transistors. In this scheme an insulating layer separates the semiconductor channel from the electrolyte. The biolayer is deposited on the insulator, which can be functionalized by means of proper chemical linkers to enhance the biolayer grafting and surface coverage. The gate electrode can be polarizable or non-polarizable, and it is in contact with the electrolyte.

The equivalent circuit of a biofunctionalized insulator EG-FET is displayed in Figure 11B. The gate is described as a capacitor C_G in parallel to a resistor R_G. The former (C_G) models polarizable gates, where charges are accumulated at the gate/electrolyte interface, and hence, an electrical double layer (EDL) is obtained, while the latter (R_G) describes nonpolarizable gates, where a redox reaction at the gate/electrolyte interface takes place. The ion transport in the electrolyte is modeled with a resistor R_{EL}, which accounts for the bulk ion concentration, gate-to-insulator/channel distance, and gate and insulator/channel geometries.[87,88] Notably, R_{EL} is very relevant during transient operation, whereas it can be neglected under steady-state operation and in the absence of parasitic leakage currents. From here on, we assume steady-state operation and R_{EL} is disregarded. The biolayer can be described as a voltage generator V_{BIO} in series with a capacitor C_{BIO}. The former (V_{BIO}) is a voltage drop accounting, for example, for charged species in the biolayer (*e.g.*, Donnan's equilibrium) and dipole effects,[25,89] while the latter (C_{BIO}) accounts for morphological and/or hydration variations of the biolayer due to conformational changes upon the biorecognition event(s).[90] The transistor channel has to be described with a proper transistor model, considering the specific charge transport properties of the semiconductor used. For the sake of simplicity, a constant electronic mobility μ is here assumed, and by solving the Poisson and continuity current equations in the case of drift-diffusion trap-free model, the electronic drain channel current results:

$$I_D = \frac{W}{L}\mu C'(V'_G - V_T)V_D \quad \text{if} \quad V'_G - V_T \geq V_D \tag{3.1}$$

$$I_D = \frac{W}{2L}\mu C'(V'_G - V_T)^2 \quad \text{if} \quad V'_G - V_T < V_D \tag{3.2}$$

where L and W are the channel length and width, respectively; C' is the electrolyte/channel capacitance per unit area; V'_G is the effective gate voltage accumulating the charge carriers in the semiconductor; V_T is the threshold voltage accounting for the interface and bulk fixed charges and Fermi energy level of the various materials stacked in the transistor architecture; V_D is the drain voltage. The source electrode is assumed biased at $V_S = 0$ V. All the various bias voltages are referred to V_S.

Focusing on the biofunctionalized insulator EG-FET architecture, C' is the insulator capacitance per unit area ($C' = C_I/A_I$, where C_I is the insulator capacitance and A_I is the insulator area on the top of the channel) and V'_G can be calculated considering the gate-electrolyte-biolayer-insulator structure, as displayed in Figure 11B. In the case of a polarizable gate electrode

$$V'_G - V_T = \frac{C_G C_{BIO}}{C_G(C_{BIO} + C_I) + C_{BIO}C_I}(V_G - V_T + V_{BIO}) \tag{3.3}$$

while in the case of a nonpolarizable gate electrode results in

$$V'_G - V_T = \frac{C_{BIO}}{C_{BIO} + C_I}(V_G - V_T + V_{BIO}) \tag{3.4}$$

Combining eqs 3.1 and 3.2 with eq 3.3 or 3.4, a simple yet informative model of a biofunctionalized insulator EG-FET is obtained. The model shows that a variation of the biolayer parameters (C_{BIO} and V_{BIO}) results in a variation of the transistor current I_D. The sensitivity is enhanced by designing $C_G \gg C_{BIO}$ and $C_G \gg C_I$ (conditions always satisfied by a nonpolarizable gate electrode). Under these conditions eq 3.3 can be approximated with eq 3.4, and I_D results:

$$I_D \cong \frac{W}{L}\mu\frac{C_I}{A_I}\frac{C_{BIO}}{C_{BIO} + C_I}(V_G - V_T + V_{BIO})V_D \quad \text{if} \quad V_{GG} - V_T + V_{BIO} \geq V_D \tag{3.5}$$

$$I_D \cong \frac{W}{2L}\mu\frac{C_I}{A_I}\left(\frac{C_{BIO}}{C_{BIO} + C_I}\right)^2(V_G - V_T + V_{BIO})^2 \quad \text{if} \quad V_G - V_T + V_{BIO} < V_D \tag{3.6}$$

On one hand, an intrinsic advantage of this approach is that the insulating layer separates the channel from the biolayer and the electrolyte, widening the range of possible semiconducting materials that can be used and preventing possible side redox reactions. Conversely, eqs 3.5 and 3.6 show how if $C_{BIO} \gg C_I$, variations of C_{BIO} upon biosensing cannot be detected, while in the case $C_{BIO} \ll C_I$, *viz.* large C_I, high-permittivity and/or thin dielectrics are required.

An alternative approach is to remove the insulator, thus putting the channel in contact with the electrolyte. This simplifies the EG-FET structure, and depending on the position of the biolayer, two different architectures can be obtained. Figure 11C shows the architecture obtained when the gate electrode is biofunctionalized. The gate can be either a self-standing electrode immersed into the electrolyte or a planar electrode fabricated on the same substrate of the transistor channel. In this architecture the gate must be a polarizable electrode. The separation between the channel and the gate electrode provides additional degrees of freedom during the biofunctionalization phase, enabling a simplified fabrication process as well as independent optimizations of the gate biofunctionalization protocol and the deposition conditions of the channel material (semiconductor contacted with the drain

https://doi.org/10.1021/acs.chemrev.1c00290
Chem. Rev. 2022, 122, 4636−4699

and source electrodes). The equivalent circuit of a biofunctionalized-gate EG-FET is displayed in Figure 11D. The biofunctionalized gate can be modeled as a voltage generator VBIO in series with a capacitor CBIO. The electrolyte resistance REL connects the gate with the channel. The EDL at the electrolyte/semiconductor interface is described by means of a capacitor CE/S. We also note this description holds in the case of both ion-impermeable and ion-permeable semiconductors, the latter used for example in OECTs.[91,92] In ion-permeable semiconducting materials, a volumetric EDL is obtained and CE/S can be calculated by multiplying the volumetric capacitance and the channel thickness. The drain current of a biofunctionalized-gate EG-FET can be related to the biological events taking place on the biolayer by considering eqs 3.1 and 3.2, where now $C' = C_{E/S}/A_S$, where A_S is the semiconductor area, and hence

$$V'_G - V_T = \frac{C_{BIO}}{C_{BIO} + C_{E/S}}(V_G - V_T + V_{BIO}) \tag{3.7}$$

The effective voltage gating the channel depends on both V_{BIO} and the voltage partition because of the series of C_{BIO} and $C_{E/S}$. Plugging eq 3.7 into eqs 3.5 and 3.6, considering eq 3.1 and eq 3.2, we obtain

$$I_D = \frac{W}{L}\mu\frac{C_{E/S}}{A_S}\frac{C_{BIO}}{C_{BIO} + C_{E/S}}(V_G - V_T + V_{BIO})V_D$$
$$\text{if} \quad V_G - V_T + V_{BIO} \geq V_D \tag{3.8}$$

$$I_D = \frac{W}{2L}\mu\frac{C_{E/S}}{A_S}\left(\frac{C_{BIO}}{C_{BIO} + C_{E/S}}\right)^2(V_G - V_T + V_{BIO})^2$$
$$\text{if} \quad V_G - V_T + V_{BIO} < V_D \tag{3.9}$$

We note that when $C_{BIO} \gg C_{E/S}$, valid for examples when a large gate electrode is used, eqs 3.8 and 3.9 show that I_D is independent of the biolayer capacitance, and the maximum sensitivity to the variation of V_{BIO} is obtained. The measurement of C_{BIO} variations requires that $C_{BIO} \leq C_{E/S}$, and when $C_{BIO} \sim C_{E/S}$ the maximum sensitivity is achieved. Interestingly, comparing eqs 3.8 and 3.9 with eqs 3.5 and 3.6 derived in the case of biofunctionalized-insulator EG-FETs, now $C_{E/S}$ plays the role of C_I, but an important advantage of the biofunctionalized-gate architecture is the possibility to easily tune C_{BIO} by means of a proper design of the gate area. In contrast, in biofunctionalized-insulator EG-FETs the area of the biolayer corresponds to the area of the insulator, and therefore, the aforementioned optimization cannot be adopted.

A third approach consists of the biofunctionalization of the semiconducting channel, and this architecture, named biofunctionalized-channel EG-FET, is displayed in Figure 11E. The main advantage is that, in principle, it is possible to electrostatically couple the biorecognition event(s) taking place in the biolayer directly to the electric charge transport layer inside the semiconductor, thus improving the bioelectronic signal transduction. A drawback of this approach is that by directly anchoring the biorecognition elements to the semiconductor, a reduced electronic transport could be obtained, and in addition, *ad hoc* methods specific for each semiconducting material have to be used. The equivalent circuit of a biofunctionalized-channel EG-FET is displayed in Figure 11F. The gate can be described by means of a capacitor C_G in parallel to a resistor R_G, accounting for polarizable and nonpolarizable electrodes, respectively. Either polarizable or nonpolarizable gate electrodes can be used. The electrolyte is modeled with a resistor R_{EL}, and the biolayer on the top of the semiconducting channel is described with a voltage generator V_{BIO} in series with a capacitor C_{BIO}. Furthermore, the drain current I_D of a biofunctionalized channel EG-FET can be related to the biorecognition events considering eqs 3.1 and 3.2 where $C' = C_{BIO}/A_S$, and assuming a polarizable gate electrode, we obtain

$$V'_G - V_T = \frac{C_G}{C_G + C_{BIO}}(V_G - V_T + V_{BIO}) \tag{3.10}$$

Plugging eq 3.10 into eqs 3.1 and 3.2, the drain current results:

$$I_D \cong \frac{W}{L}\mu\frac{C_{BIO}}{A_S}\frac{C_G}{C_G + C_{BIO}}(V_G + V_{BIO} - V_T)V_D$$
$$\text{if} \quad V_G + V_{BIO} - V_T \geq V_D \tag{3.11}$$

$$I_D \cong \frac{W}{2L}\mu\frac{C_{BIO}}{A_S}\left(\frac{C_G}{C_G + C_{BIO}}\right)^2(V_G + V_{BIO} - V_T)^2$$
$$\text{if} \quad V_G - V_T + V_{BIO} < V_D \tag{3.12}$$

Equations 3.11 and 3.12 show that optimal sensing conditions for both C_{BIO} and V_{BIO} are achieved when either a nonpolarizable gate electrode or a polarizable gate $C_G \gg C_{BIO}$ is adopted.

A fourth and last approach is displayed in Figure 11G. In this architecture, the gate of an FET is extended and put in contact with the electrolyte. This extended gate is coupled to another electrode, named gate, by means of the electrolyte. In the case of a nonpolarizable gate electrode, the biolayer is deposited on the extended gate, whereas in the case of a polarizable gate electrode, either the gate or the extended gate could be biofunctionalized.[93,94] Here we focus on the most common case of biofunctionalized floating-gate FETs, but the analysis and the design considerations can be easily extended. The equivalent circuit of a biofunctionalized extended-gate FET is displayed in Figure 11H. Although the biofunctionalized extended-gate FET architecture is different with respect to the biofunctionalized-insulator EG-FET one, under steady-state conditions R_{EL} can be neglected, obtaining an identical equivalent circuit model. As a consequence, by substituting C_I with the capacitance of the FET C_T, eqs 3.3−3.6 describe also the biofunctionalized floating-gate FETs. The important advantages of this architecture include that (i) C_T and C_{BIO} can be independently optimized and (ii) almost any FET technology can be adopted because the FET is not in contact with the electrolyte.

Table 2 summarizes the figures of merit of EG-FET biosensors clustered according to the presented architectures and operating with a LOD lower than hundreds of femtomolar. The figures of merit presented in Table 2 include the minimum and maximum concentration assayed, the assay time, the biofunctionalization time, the simplicity of the fabrication process accounting for both the transistor and the biofunctionalization methods, and the demonstration of assaying real samples. Biofunctionalized insulator EG-FETs show a minimum LOD equal to 6×10^{-17} M, which results in $\sim 10^3$ molecules assayed in 100 μL of fluid.[95] The best performance in terms of LOD are obtained for DNA detection, and IL-4 and IL-2 detection was demonstrated with a femto-molar LOD, corresponding to $\sim 10^4$ proteins assayed in 100 μL. Although this EG-FET architecture is directly derived from the conven-

https://doi.org/10.1021/acs.chemrev.1c00290
Chem. Rev. 2022, 122, 4636−4699

Table 2. Overview of the Figures of Merit of High-Sensitivity EG-FET Biosensors Clustered with Respect to the Four Presented Architectures[25−29,95,117,118]

Biosensor architecture	Disease / Application	Receptor	Target	LOD (M)	Minumum Concentration (M)	Maximum Concentration (M)	Dynamic range	Sample volume (uL)	LOD (N molecules)	Assay time (min)	Biofunctionalized material	Biofunctionalization method	Biofunctionalization time (h)	Fabrication simplicity (* = complex, *** = simple)	Real sample	Year	Ref
Biofunct. insulator EG-FET	Patau syndrome	DNA	DNA	6,00E-17	6,00E-17	1,00E-15	1	10	3,6E+02	2	Y2O3	Au nanoparticles	N.A.	**	NO	2020	191
Biofunct. insulator EG-FET	Infection	Antibodies	IL-4, IL-2	3,00E-15	1,92E-15	1,92E-07	8	20	3,6E+04	15	SiO2	GPTMS siloxane	N.A.	*	YES, cell culture medium	2020	113
Biofunct. gate EG-FET	Multiple sclerosis	Single-strand oligonucleotide	miR-182	1,00E-20	1,00E-20	1,00E-15	5	100	1	10	Au	SAM+EDC/NHS+†	23	**	NO, PBS	2020	129
Biofunct. gate EG-FET	Proof-of-concept	Antibodies	IgG	1,00E-20	1,67E-20	4,00E-15	5	100	1	20	Au	SAM+EDC/NHS	16	**	YES, diluted saliva spiked with IgG	2018	125
Biofunct. gate EG-FET	Proof-of-concept	Antibodies	IgM	2,40E-20	6,00E-21	1,00E-12	8	100	1	10	Au	SAM+EDC/NHS	25	**	NO, PBS	2019	126
Biofunct. gate EG-FET	HIV	Antibodies	HIV-1 P24	3,00E-20	2,00E-21	1,00E-18	3	100	2	10	Au	SAM+EDC/NHS	23	**	NO, PBS	2020	124
Biofunct. gate EG-FET	Inflammatory processes	Antibodies	CRP	2,50E-19	7,00E-19	7,00E-16	3	100	15	20	Au	SAM+EDC/NHS	23	**	YES, diluted saliva spiked with CRP	2019	127
Biofunct. gate EG-FET	Proof-of-concept	Antibodies	IgG	3,00E-18	6,00E-18	6,00E-11	7	100	181	10	Au	SAM+EDC/NHS	21	***	NO, PBS	2018	192
Biofunct. gate EG-FET	Cancers	Nivolumab	anti-drug antibodies	1,00E-13	1,00E-12	1,00E-09	3	N.A.	N.A.	30	Au	SAM Protein-G	7	**	NO, PBS	2021	193
Biofunct. gate EG-FET	Parkinson	Antibodies	α-Synuclein	2,50E-13	2,50E-13	2,50E-07	6	50	7,5E+06	10	Au	Protein-G	1	***	NO, PBS spiked with α-Synuclein	2020	194
Biofunct. channel EG-FET	Food spoilage	TAAR13c	Cadaverine	1,00E-16	1,00E-16	1,00E-04	12	N.A.	N.A.	1	Nickel	Lipids	14	***	Yes	2019	195
Biofunct. channel EG-FET	Duchenne muscular dystrophy	CRISPR–Cas9	DNA	1,70E-15	7,40E-14	2,80E-13	1	30	3,1E+04	15	Graphene	PBA	3	***	YES, clinical samples	2019	197
Biofunct. channel EG-FET	Inflammatory bowel	Antibodies	TNF-α	1,00E-14	1,00E-15	1,00E-12	3	N.A.	N.A.	2	CNTs	SAM+EDC/NHS	3	**	Yes, cell culture medium	2017	198
Biofunct. channel EG-FET	Odorant receptors	OR10a, OR22a, OR35a, OR7 MeSal, MeHex, E2-Hex, 4E		1,00E-14	1,00E-14	1,00E-11	3	N.A.	N.A.	300	CNTs	PBASE	2,5	**	NO, PBS	2019	199
Biofunct. channel EG-FET	Cardiovascular	Antibodies	cTnI	3,24E-14	1,00E-11	1,00E-07	4	1	2,0E+04	N.A.	ZnO	APTES+GA	3	***	NO	2017	100
Biofunct. channel EG-FET	Brain neurochemical fluxes	Aptamers	Serotonin, dopamine	1,00E-13	1,00E-14	1,00E-06	8	50	3,0E+06	1	In2O3	APTMS+TPS	19,5	***	NO, artificial cerebrospinal fluid	2020	114
Biofunct. channel EG-FET	COVID-19	Antibodies	Spike-S SARS-CoV-2	N.A.	1,00E-14	1,00E-12	2	N.A.	242	1	Graphene	PBASE	5	***	Yes, nasopharyngeal swab	2020	101
Biofunct. channel EG-FET	Cancers	Antibodies	CEA	N.A.	1,00E-13	1,00E-09	4	N.A.	N.A.	60	Graphene	Nano-BSA	3	***	NO	2019	102
Biofunct. channel EG-FET	Bladder cancer	Antibodies	NMP22	2,70E-18	1,00E-18	1,00E-13	5	30	49	10	IGZO	APTES	16,5	**	NO	2020	103
Biofunct. extended-gate FET	Mental disorders, e.g. Parkinson	Chemical molecules	Dopamine	5,23E-16	1,00E-15	1,00E-09	6	N.A.	N.A.	1	InZnO	APTES+EDC/NHS	1,5	***	YES, rat blood serum spiked with dopamin	2020	104
Biofunct. extended-gate FET	Prostate cancer	Antibodies	PSA	1,00E-15	1,00E-15	1,00E-10	5	N.A.	N.A.	N.A.	Au	SAM	32	*	NO, PBS spiked with PSA	2020	105
Biofunct. extended-gate FET	Cardiovascular	Antibodies	Troponin I	1,00E-15	1,00E-15	1,00E-11	4	N.A.	N.A.	N.A.	Au	SAM+EDC/NHS	28	*	YES, clinical human serum	2020	106
Biofunct. extended-gate FET	Prostate cancer	Aptamers	PSA	1,00E-15	1,00E-15	1,00E-12	3	100,00	6,0E+04	N.A.	Au	apta_MIP	18	***	NO, diluted plasma spiked with PSA	2016	126
Biofunct. extended-gate FET	Proof-of-concept	Biotin	Streptavidin	1,00E-13	1,00E-13	1,00E-11	2	N.A.	N.A.	1	ITO	APTES+sulfo-NHS	4	***	NO	2021	107
Biofunct. extended-gate FET	Cardiovascular	Antibodies	Troponin I	N.A.	8,00E-13	1,60E-10	2	10	N.A.	5	Au	Cysteamine	14	**	YES, human whole blood	2018	108
Biofunct. extended-gate FET	Brain injuries	Antibodies	GFAP	N.A.	5,00E-12	1,00E-09	2	N.A.	N.A.	N.A.	PS-MA-PEG	EDC/NHS	N.A.	**	NO, PBS spiked with GFAP	2017	109

tional and widely used ISFET and hence a wide range of application examples would be expected, we found only a few examples of single or few molecule detection based on this approach. This can be explained by considering eqs 3.5 and 3.6, which show that high-sensitivity operation requires a thin and high-permittivity insulator; these conditions are practically challenging to obtain and have a negative impact on the complexity and cost of the fabrication process.

A larger number of application examples are available in the case of biofunctionalized-gate EG-FETs showing a LOD as low as 10^{-20} M, which corresponds to single-molecule detection in 100 μL of fluid. Importantly, single-molecule detection was demonstrated for both genomic and protein biomarkers, including miR-182, IgG, IgM, HIV-1 P24, and CRP.[25−28] Gold is the gate material of choice for all the state-of-the-art application examples (Table 2). The reason is readily found by analyzing the functionalization methods. Gold enables the use of self-organization and self-assembly strategies based on thiol-terminated self-assembled monolayers (SAMs) for the covalent grafting of the biological recognition elements.[25−28,96−98] Activation of the SAM with EDC/NHS is typically used to improve the yield of the reaction. After this step, proteins are linked. This method has been recently extended to biotinylated single-strand oligonucleotides exploiting the strong biotin-streptavidin bonding.[28] We also stress that densely packed bioreceptors are essential for single-molecule detection with wide-field EG-FET architectures. Table 2 shows that using biofunctionalized-channel EG-FET architectures, the best LOD is 10^{-16} M, which results in hundreds of molecules assayed in 100 μL of solution.[99] The class of channel materials used include graphene,[100] carbon nanotubes (CNTs), and metal oxides.[99,101−105] Various *ad hoc* grafting primers are adopted considering the specific surface chemical properties of the channel material. By way of example, APTES and APTMS are used for grafting antibodies and aptamers to ZnO and In_2O_3, respectively, SAM with EDC/NHS and PBASE for grafting antibodies and odorant receptors to CNTs, PBASE, PBA and nano-BSA for grafting antibodies to graphene. Relevantly, there are several approaches showing fast biofunctionalization time (only 2−3 h) and assay time as fast as a few minutes (1−15 min), making them the best choice for applications where minimum time-to-results are targeted.

Finally, focusing on the biofunctionalized extended-gate FET architectures, the best LODs are in the range of 10^{-16}−10^{-15} M and the biofunctionalization time is of the order of several hours, comparable to the time showed by biofunctionalized-gate EG-FETs.[109−113] The main advantage of extended-gate FET architectures is the simple implementation. The transistor is not in contact with the electrolyte, and therefore, any solid-state low-voltage fabrication technology can be used. Moreover, both the material and the geometries of the extended gate can be easily optimized and integrated into microfluidics.[96−99,101−104,106−116]

In the following we focus on model application examples accounting for the four EG-FET architectures. Focusing on the class of biofunctionalized-insulator EG-FETs, very recently Zhang and co-workers demonstrated label-free detection of biomarkers, including DNA sequences and microvesicles (MVs) derived from HepG2 cells with limits of detections of 60×10^{-18} M and 6 particles/μL, respectively.[95] FET biosensors were fabricated with wafer-scale uniformity by using polymer-sorted high-purity CNTs. Figure 12A shows CNTs fabricated on silicon wafer. A zoomed-in view of a single transistor channel is

https://doi.org/10.1021/acs.chemrev.1c00290
Chem. Rev. 2022, 122, 4636−4699

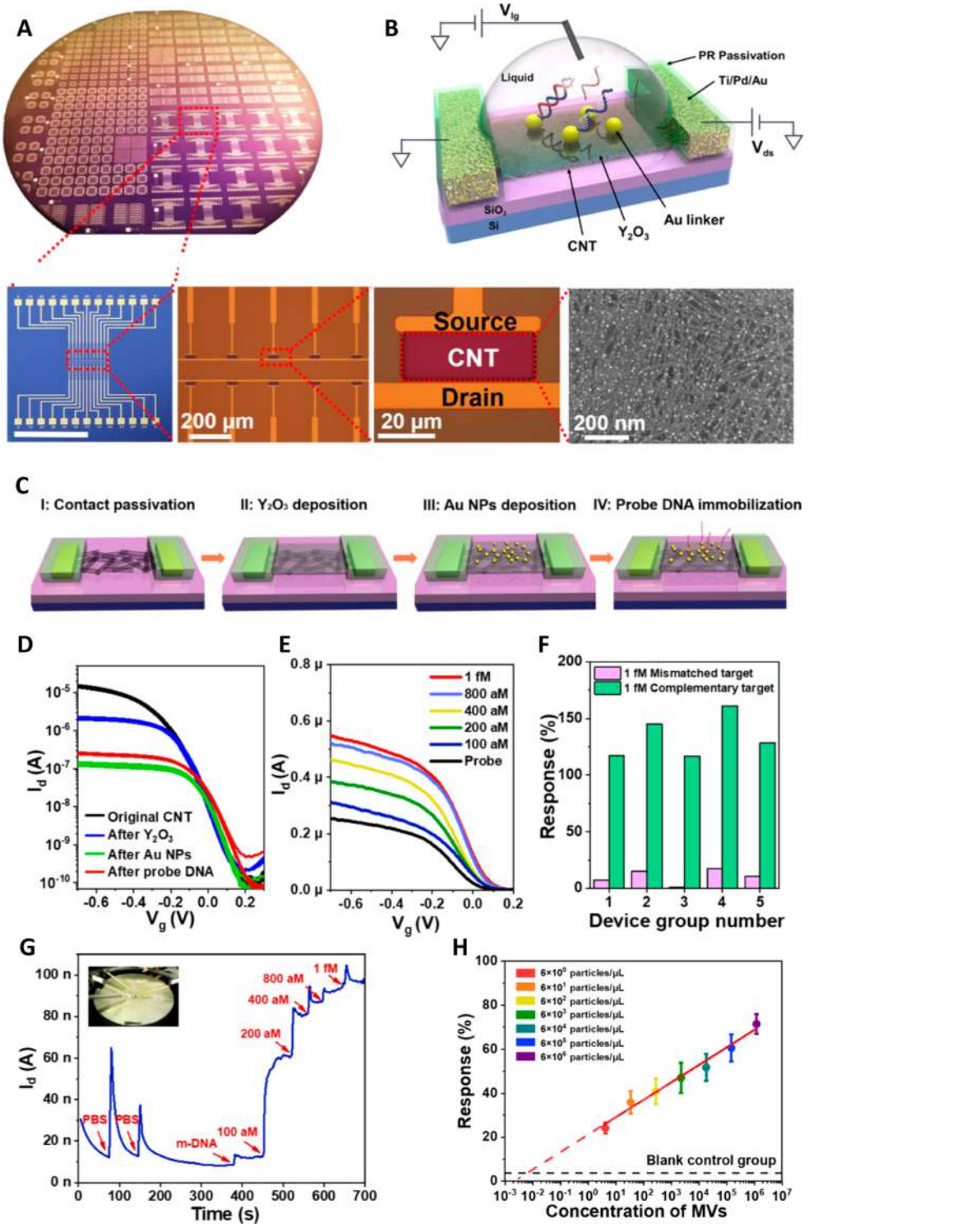

Figure 12. Application example of a biofunctionalized-insulator EG-FET architecture. (A) Biosensors fabricated on silicon substrate and optical image biosensors (scale bar is 5 mm). The channel region is also highlighted. Au NPs on the Y_2O_3/CNTs are displayed in the SEM image. (B) Schematic view of the biofunctionalized Y_2O_3/CNT EG-FET. (C) Fabrication steps of biofunctionalized-insulator EG-FETs. (D) Transfer characteristics measured at various fabrication steps. (E) Transfer characteristics at various analyte concentrations. (F) Positive and negative responses of five biofunctionalized-insulator EG-FETs. (G) Real-time response with PBS, mismatched m-DNA, and target DNA (100 aM to 1 fM). Applied voltages: $V_G = -0.1$ V and $V_D = -0.1$ V. (H) Percentage response as a function of nominal MV concentration. Reprinted with permission from ref 95. Copyright 2020 ACS Publications.

displayed. CNTs were patterned between source and drain, and the metal contacts were passivated by photoresist, thus preventing their direct contact with the electrolyte. We note that this is extremely important to reduce parasitic EDL capacitances and possible leakage currents due to faradaic side reactions. A portion of the transistor channel where Au nanoparticles (NPs) were grafted on the insulator/CNT film is shown by the scanning electron microscopy (SEM) image.

https://doi.org/10.1021/acs.chemrev.1c00290
Chem. Rev. 2022, 122, 4636−4699

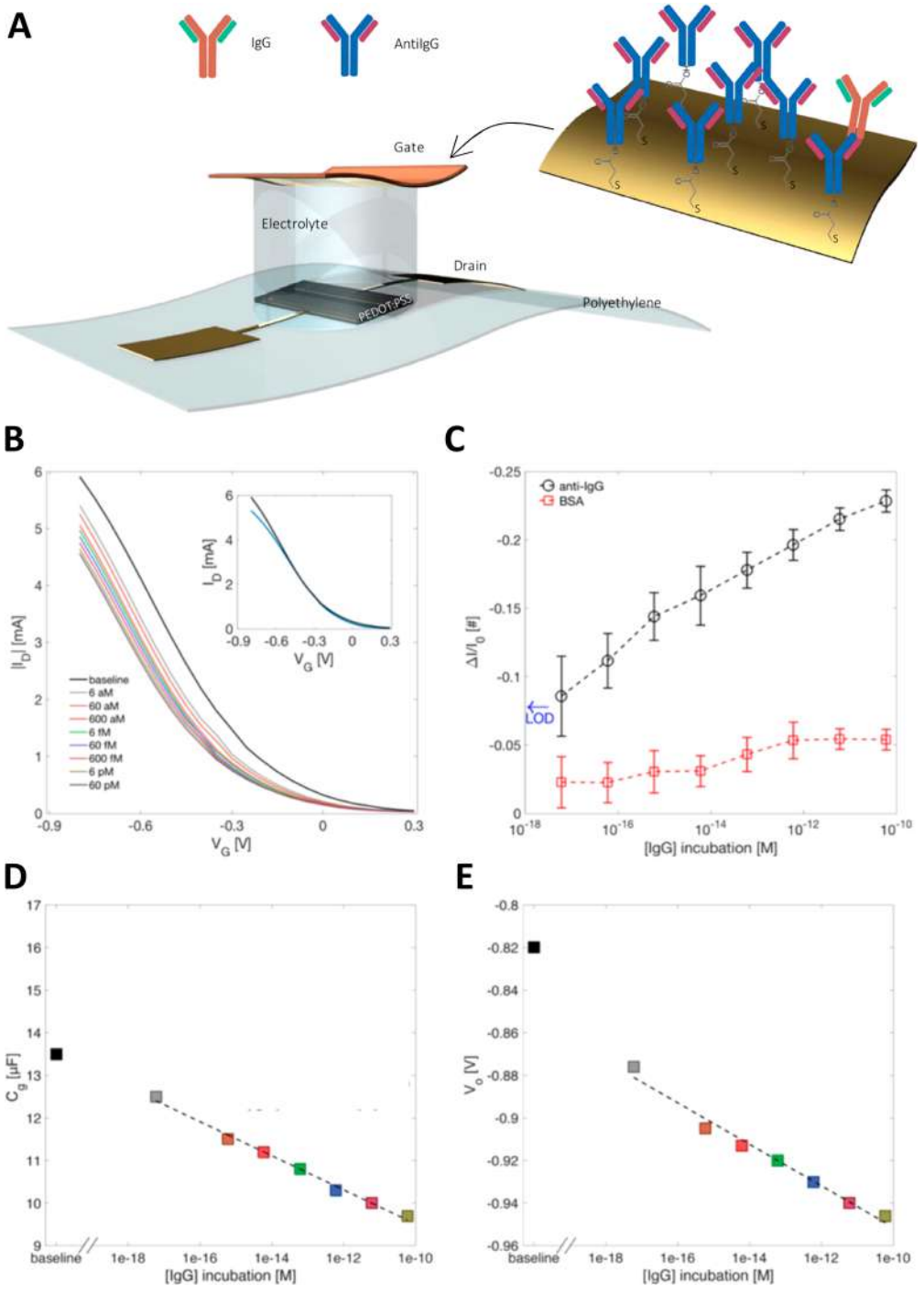

Figure 13. Biofunctionalized-gate EG-FET based on an OECT architecture. (A) OECT biosensor structure. The conductive polymer PEDOT:PSS was printed on plastic foil. The gate was obtained by depositing Au on plastic foil. Au was biofunctionalized with a SAM and the capturing IgGs. (B) Measured transfer characteristics as a function of IgG. Baseline was obtained in PBS (IgG = 0 M). Inset: Measured I_D-V_G before (black line) and after (blue line) the assay. (C) Positive response (gate: Au/anti-IgG, circles) and control experiments (gate: Au/BSA, squares) at various IgG concentrations. (D) Extracted gate capacitance (C_g) vs IgG. (E) Extracted threshold voltage shift (V_o) vs IgG. Reprinted with permission from ref 96. Copyright 2018 IOP Publishing Ltd.

Figure 12B displays the schematic structure of the biosensor. In contrast to conventional approaches where the CNT channel is functionalized with the biorecognition elements and exposed to the solution, in this approach an ultrathin Y_2O_3 film of 6 nm covers the whole CNT channel. Au nanoparticles were then deposited on the insulator and used as linkers to connect the biological recognition elements. An Ag/AgCl nonpolarizable electrode was used as gate for biasing the electrolyte solution. The main fabrication steps are shown in Figure 12C and were performed with complementary metal-oxide-semiconductor technologies, with the only exception of the gate electrode. The Y_2O_3 layer separating the channel from the biorecognition elements and the liquid environment allowed improving the reproducibility and stability of the EG-FET biosensor. The electrical characterization of 90 transistors demonstrated a yield of 100%, hysteresis-free characteristics, on/off current ratio of

https://doi.org/10.1021/acs.chemrev.1c00290
Chem. Rev. 2022, 122, 4636−4699

up to 10^5, and an average threshold voltage equal to -0.17 ± 0.017 V, and the subthreshold slope was 60−90 mV/dec. Bias stress stability tests were performed showing long-term (>1000 s) operation without appreciable degradation. In addition, the authors demonstrated that an enhanced sensor response and LOD were achieved assaying both DNA in PBS and MVs in real biofluid, despite the insulator separating the channel from the biolayer. A direct comparison of the sensing characteristics of CNT FETs biosensors with and without the Y_2O_3 insulating layer highlighted that a reduction of the drain current is displayed when the channel is exposed to the analyte. This was attributed to scattering effects and/or ion penetration into the channel material.[119,120]

In contrast, FET biosensors with a Y_2O_3 layer showed an increased current as a function of the analyte concentration, and more importantly, the current variation was larger compared to that obtained with EG-FET biosensors without an insulator. Figure 12D shows the impact of the various process steps on the electrical characteristics of CNT FETs.

The on-state drain current I_D (black line is the pristine device) drastically decreased after the growing of the Y_2O_3 film (blue line) because the dielectric capacitance was significantly lower than the EDL capacitance. The CNT FET conduction was further reduced after Au NP deposition (red line) mainly because of the reduction of the capacitance induced by Au NPs. Interestingly, while a clear reduction of the ON drain current is displayed, the subthreshold current is not affected by the aforementioned fabrication steps, indicating that neither Y_2O_3 nor Au NPs doped the channel and no interface states were introduced. After the immobilization of the DNA probes (green line), a 30 mV shift of the I_D-V_G characteristic was displayed, suggesting that the negative charge gating of the DNA probes was compensated by positive charges into the semiconductor. The measured response to the target DNA with concentration ranging from 100×10^{-18} M to 1×10^{-15} M is displayed in Figure 12E. The hybridization was performed in high-concentration 1× PBS in order to reduce the electrostatic repulsions while sensing measurements were carried out in 0.1× PBS in order to increase the Debye length.[121] Notably, the Debye length, the scale over which mobile ions screen out electric fields of fixed charges on the biomolecules, is a fundamental parameter for enhancing the sensitivity and LOD in biosensors, and it is inversely proportional to the square root of the ionic strength.[89] Hence, a typical approach to increase the Debye length is to reduce the electrolyte ion concentration. Along this direction, we have recently performed a systematic study where bioelectronic sensing measurements were performed by varying the bulk ion concentration in the electrolyte, ranging from 10^{-6} M (pure water) to 2×10^{-2} M.[25,122] The study demonstrated that sensing measurements performed in pure water, which results in a Debye length of up to 100 nm, maximize the sensitivity, and at ion concentrations greater than 10^{-2} M no response was detected.

The selectivity test displayed in Figure 12F demonstrates that the response to mismatched DNA is much lower than that obtained with complementary DNA. Real-time detection measurements were performed in order to evaluate the sensitivity, selectivity, and reliability. Figure 12G shows that when PBS solution was injected, I_D as a function of time was measured, and after about 100 s the steady-state baseline value was achieved. Injection of mismatched DNA (m-DNA) resulted in a subtle variation of I_D, indicating a negligible nonspecific binding. By contrast, when the Y_2O_3/CNT EG-FET was incubated to increasing concentrations of the target DNA, a substantial increase of I_D was obtained after 50 s. A very large increase of I_D was obtained when the Y_2O_3/CNT EG-FET was exposed to a DNA concentration equal to 200×10^{-18} M. Then, upon further increase of the target DNA concentration, a consistent increase of I_D was measured. The biosensor operation was further validated by detecting MVs obtained from human liver cancer cells (HepG2). To this aim, the sulfhydrylation aptamer sequence TLS11 was used as biorecognition element.[123,124] Figure 12H shows that an increase of the biosensor response was obtained with increasing concentrations of MV. A 6 order of magnitude dynamic range (6 to 6×10^6 particles/μL) was demonstrated. Overall, these results show that biofunctionalized-insulator EG-FETs are suitable for large-scale industrial manufacturing and provide excellent performance in terms of LOD, dynamic range, sensitivity, and stability, showing a path for single-molecule rapid detection.

Focusing on the class of biofunctionalized gate EG-FETs, state-of-the-art approaches demonstrated label-free single-molecule detection with millimeter-wide sensing surfaces. This class of EG-FETs provides the best performance in terms of LOD. Large-area few-molecule and single-molecule detection were published in 2018 by our group.[25,96] The core of this biosensing technology, named SiMoT, is the combination of the FET architecture and the cooperative effects of the densely packed bioreceptors deposited on the gate electrode. Figure 13A shows the schematic structure of a SiMoT where both the gate and the channel were fabricated on a flexible plastic substrate. In detail, we used the conductive polymer PEDOT:PSS inkjet printed on polyethylene foil as the active channel material and a gold electrode evaporated on a Kapton foil as the gate electrode.[92] We note that this is an ideal technology for the low-cost mass-production of single-molecule biosensors, opening relevant possibilities for the market exploitation of this disruptive technology. In this application example, the gate electrode was functionalized with IgG antibodies by using mixed 3-MPA/11-MUA SAMs activated with EDC and sulfo-NHS. Nonspecific adsorption was prevented by incubating the biofunctionalized electrode with ethanolamine 1 M in PBS for 1 h. The electrode was exposed to 1× PBS solutions (pH 7.4) at increasing concentrations of IgG for 10 min. After washing, the electrode was coupled to the transistor channel by using PBS as electrolyte. Typical transfer characteristics at various IgG concentrations are displayed in Figure 13B. The black curve was measured after incubation with only PBS and was taken as the baseline. The measured drain current (I_D) progressively reduced when the IgG concentration was increased, and a large variation was displayed even at the lowest concentration assayed, *viz.* 6×10^{-18} M. This concentration corresponds to only 181 molecules in the 100 μL solution assayed. The inset of Figure 13B shows the I_D-V_G characteristics measured with a first biofunctionalized gate subsequently used for the sensing measurements (black line) and a second biofunctionalized gate not exposed to the analyte (blue line). The almost perfect overlap of the characteristics confirmed the excellent stability of the biofunctionalized-gate EG-FET. The sensing response calculated as the relative variation of I_D at a given concentration with respect to the baseline I_0, *viz.* $\Delta I/I_0 = (I_D - I_0)/I_0$, is displayed in Figure 13C (black line with circles). At the minimum concentration assayed (6×10^{-18} M), the response was 9% and monotonically increased by about 3%/dec, achieving a maximum value equal to 23% at a maximum IgG concentration of 60×10^{-12} M. The biosensor response showed

https://doi.org/10.1021/acs.chemrev.1c00290
Chem. Rev. 2022, 122, 4636−4699

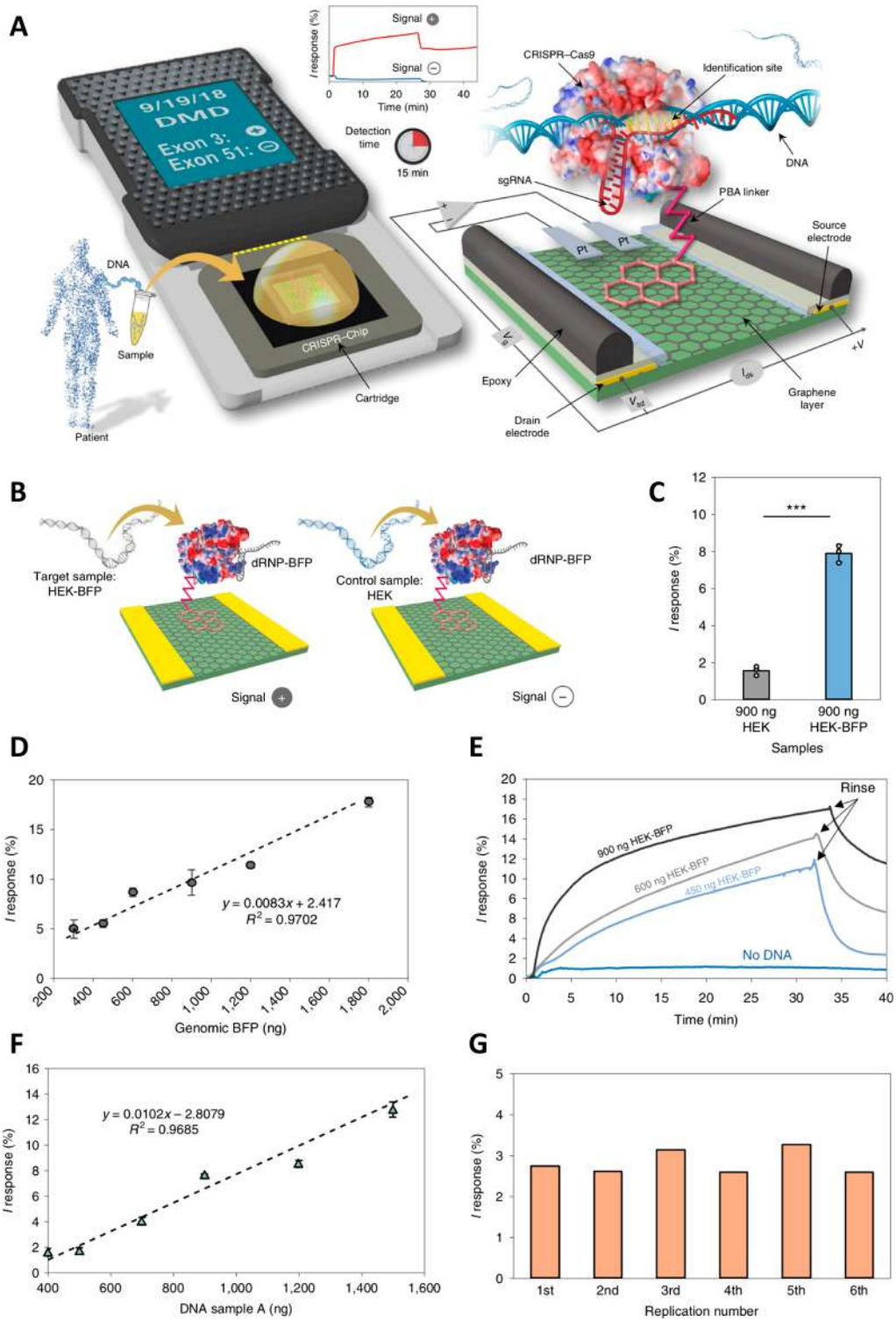

Figure 14. Application example of a biofunctionalized-channel EG-FET architecture. (A) The CRISPR-chip comprises a graphene transistor biofunctionalized with CRISPR-Cas9 for the detection of a gene without amplification. The selective binding of the target DNA to the target-specific sgRNA (named dRN) changes the electrical characteristics of the EG-FET. (B) Schematic view of dRNP-BFP-functionalized EG-FET exposed to the target (HEK-BFP) and control (HEK) samples. (C) Signal output when the biosensor is exposed to HEK and to the target HEK-BFP. (D) Output response as a function of the HEK-BFP concentration. (E) Real-time response at various HEK-BFP concentrations. (F) Response of a dRNP-DMD51-functionalized EG-FET obtained at various amounts of clinical sample. (G) Reproducibility of dRNP-DMD51-functionalized EG-FET exposed to a clinical sample. Reprinted with permission from ref 101. Copyright 2019 Springer Nature.

a dynamic range larger than 7 orders of magnitude. Mean and standard deviation of the biosensor response for each concentration were calculated from three replicates. In addition, control experiments were performed to assess the selectivity and LOD. Three biofunctionalized anti-IgG gates were exposed at increasing concentrations of BSA. The calculated mean value

https://doi.org/10.1021/acs.chemrev.1c00290
Chem. Rev. 2022, 122, 4636−4699

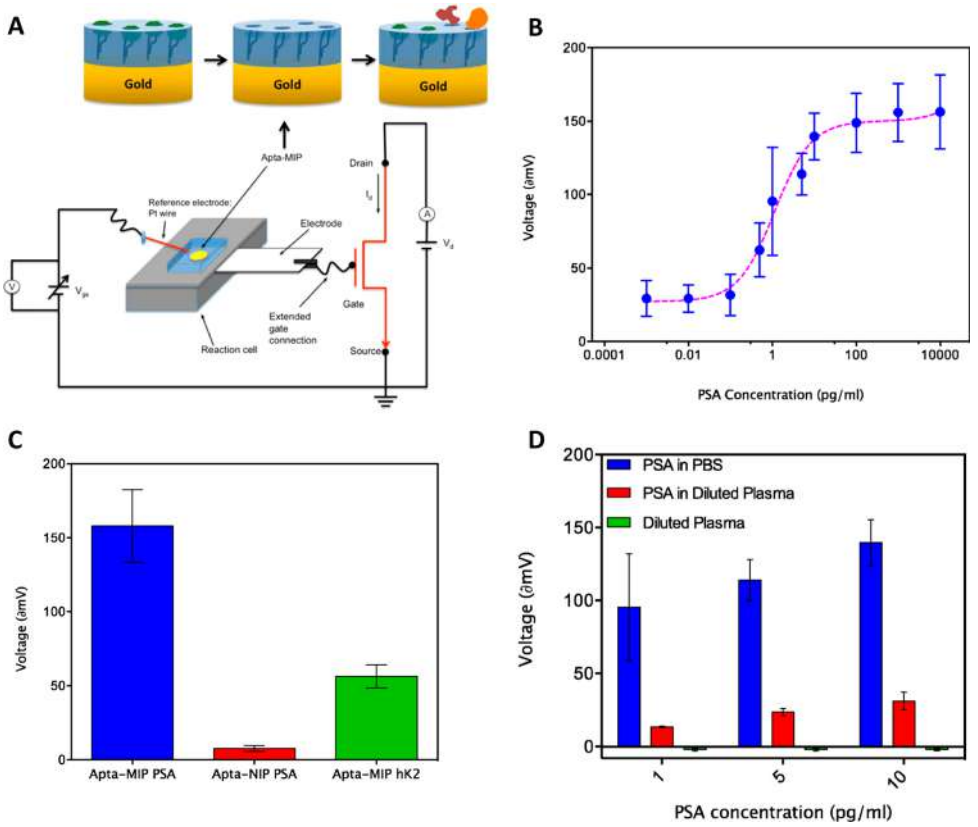

Figure 15. Application example of a biofunctionalized-extended-gate FET architecture. (A) Functionalization of a gold electrode with PSA aptamers. First, the electro-polymerization of polydopamine is used for the imprinting of the aptamer and PSA. Then, proteins are removed. Finally, the apta-MIP electrode is used in an extended-gate architecture and PSA is detected. (B) Measured (symbols) threshold voltage shift (biosensor response) at various PSA concentrations. (C) Validation of the biosensor selectivity. Response of an apta-MIP extended-gate FET incubated with PSA, *viz.* the target biomarker (blue bar); response of an apta-NIP extended-gate FET incubated with PSA (red bar); and response of an apta-MIP extended-gate FET incubated with hK2 (green bar). (D) Biosensor response when PSA is spiked in a 1000× diluted plasma. Reprinted with permission from ref 130. Copyright 2016 American Chemical Society.

and standard deviation are displayed in Figure 13C (red line with squares). A LOD level equal to 8% was obtained from the control experiments, thus proving that the sensor response at 6 × 10^{-18} M is well above the LOD. To gain more insight on the biosensor response, the transfer characteristics (I_D−V_G) at various analyte concentrations were systematically reproduced with a physical-based analytical model. The model provided the gate capacitance (C_G) and the threshold voltage (V_o) as a function of the biorecognition events occurring on the biolayer. C_G describes the EDL at the biolayer/electrolyte interface, whereas V_o depends on the electrolyte concentration, gate work function, and various physical parameters of the polymeric channel.[91] The extracted parameters C_G and V_o as a function of IgG concentration are shown in panels D and E of Figure 13, respectively. Before exposure of the biofunctionalized gate to the analyte, C_G was equal to 13.5 μF (baseline). After the incubation at 6 aM, C_G decreased by about 1 μF and V_o decreased by about 10 mV/dec. Upon further increase in the concentration, the model-based analysis showed that C_G consistently decreased by about 0.4 μF/dec and V_o consistently decreased by about 10 mV/dec. The variation of C_G was ascribed to the lowering of the biolayer permittivity due to antigen−antibody binding,[90] while the variation of threshold voltage was attributed to a variation of the work-function of the biofunctionalized gate due to an increase of the positive charges and/or dipoles reorientation.[125,126] Remarkably, attomolar LOD and *d* sensitivity were obtained thanks to the stable operation, selective response, and synergistic variation of C_G and V_o. These features further highlight that the optimal design of the biosensor architecture is of paramount importance for large-area single-molecule detection. We also note that this was the first demonstration of a biofunctionalized-gate OECT biosensor. The generality of this approach was then demonstrated by assaying at the single-molecule limit both protein and genomic biomarkers, including, for example, IgM, CRP, HIV-1 P24, and miR-182.[26−29]

Then, focusing on the class of biofunctionalized-channel EG-FET architectures, as a relevant application example the rapid detection of unamplified target genes by means of clustered regularly interspaced short palindromic repeats protein 9 (CRISPR-Cas9) immobilized on a graphene FET was recently proposed by Aran and co-workers.[101] Combining the biofunctionalized-channel EG-FET architecture with the CRISPR technology, the detection of genomic DNA containing the target gene in real clinical samples with a LOD of 1.7 × 10^{-15} M was demonstrated. Figure 14A shows a CRISPR-enhanced graphene FET, termed CRISPR-Chip, where graphene is biofunctionalized with dRNP, a Cas9 CRISPR complex.[127] The selective hybridization of the target DNA to the dRNP complex resulted in a modulation of the drain current (I_D) of the graphene FET.

Analogously to the aforementioned approaches, also in this case the output signal response is calculated as the percentage variation of I_D, and it was named *I* response, *viz.* $I = 100(I_D - I_0)/I_0$, where I_0 is the baseline. Figure 14B shows graphene FETs functionalized with dRNP-BFP molecules and exposed to

https://doi.org/10.1021/acs.chemrev.1c00290
Chem. Rev. 2022, 122, 4636−4699

various concentrations of genomic samples HEK-BFP in the range of 10−40 ng/μL. HEK genomic samples at a concentration equal to 30 ng/μL were used for the control experiments. Figure 14C shows the *I* response after exposure to 30 ng/μL of the control samples (HEK) and of the target genomic material (HEK-BFP). The mean value of the *I* response to the target HEK-BFP was 8%, while the *I* response to the control HEK was lower than 2%, proving the good selectivity. Figure 14D displays the calibration curve and provides information on the detection of HEK-BFP. From the negative control experiments a LOD of 2.3×10^{-15} M was calculated. The real-time monitoring of HEK-BFP is displayed in Figure 14E. Although a steady-state response, *viz.* a time-independent *I*, was not obtained, after about 5 min of incubation with various analyte concentrations, appreciable different responses were displayed. A total analysis time of about 15 min was estimated as the minimum time-to-results, considering incubation and washing steps. This technology was also validated in clinical settings by analyzing Duchenne muscular dystrophy (DMD)[128] mutations that result in the expression of dysfunctional dystrophin protein, which regulate the proper function of mature muscle fibers and muscle stem cells.[129] Figure 14F shows the sensitivity of CRISPR-enhanced graphene FET in the presence of DMD. Negative controls provided a LOD equal to 1.7×10^{-15} M. The current responses of the six replicates are displayed in Figure 14G and provide a relative standard deviation (RSD) of 10.6%, which shows excellent reproducibility for DNA analysis and highlights the applicability of biofunctionalized-channel EG-FET architectures in clinical contexts.

Finally, focusing on the class of biofunctionalized-extended-gate FET architectures, high-sensitivity detection of prostate-specific antigen (PSA) in human plasma was recently demonstrated by Estrela and co-workers.[130] This approach integrated hybrid synthetic receptors on a gold extended-gate electrically connected to a metal-oxide-semiconductor FET. Aptamer-PSA were immobilized on gold followed by 13 cycles of dopamine electro-polymerization. Polymeric cavities (named apta-MIP) able to selectively recognize PSA were obtained. The main steps required for the biofunctionalization of the gate electrode as well as the experimental setup are displayed in Figure 15A. The hybrid imprinting approach, being a subset of molecular imprinting, incorporate bioreceptors into the polymer cavities generating synthetic receptors. Interestingly, this approach can be generally used also for the immobilization of small molecules and antibodies.[131] In order to assess the biosensor performance, electrodes were exposed to a 1× PBS buffer solution with various PSA concentrations. Then, the electrodes were thoroughly washed and the transistor transfer characteristics were recorded. A threshold voltage shift consistent with the increase of the analyte concentration was obtained.

Figure 15B shows the threshold voltage shift measured when the PSA concentration was in the range of 10^{-3}−10^{5} pg/mL. Below 0.1 pg/mL a variation of 30 mV was measured, independent of the PSA concentration. Then, a linear response was obtained by varying the PSA concentration in the 0.1−10 pg/mL range. Above 100 pg/mL no variation of the threshold voltage was displayed, suggesting a saturation of the binding sites. The maximum response amounted to 158 ± 43 mV at a concentration of 1 μg/mL. Control experiments were performed fabricating nonimprinted "control" electrodes (apta-NIP) following the same protocol of the apta-MIP electrodes but without the PSA template. The apta-NIP sensing measurements performed in the same PSA range of concentrations showed voltage shifts 20 times lower than that obtained with the extended-gate functionalized with apta-MIP. The selectivity of the biosensor was further investigated, exposing the apta-MIP extended-gate FET to the protein hK2. Relevantly, hK2 and PSA show 80% similarity.

The voltage responses obtained with apta-MIP exposed to PSA, apta-NIP exposed to PSA, and the apta-MIP exposed to hK2 are displayed in Figure 15C. A response equal to 56 ± 14 mV was obtained at an hK2 concentration of 1 μg/mL, which is significantly lower than that obtained when incubated with PSA at the same concentration. This experiment proved the good selectivity of the biosensor. The apta-MIP extended-gate FET was further tested in human plasma spiked with PSA and covering the clinically relevant range 4−10 ng/mL.[132] Figure 15D shows the biosensor response when the PSA concentration was 1, 5, and 10 pg/mL. The response obtained when the PSA was diluted in plasma was compared with both PSA in PBS and diluted plasma without PSA. A reproducible response was obtained, although the sensitivity was lower with respect to that observed with PSA spiked in the buffer solution. The loss in sensitivity was attributed to possible protein−protein interactions, which were also observed in aptamer ELISA assays.[133] In conclusion, this application example demonstrated that the combination of the robust and simple extended-gate FET architecture with molecular imprinting approach is a viable approach for the sensitive detection of clinically relevant biomarkers. A limitation of this architecture is that state-of-the-art approaches showed a best LOD limited to the subfemtomolar range, which results in several thousands of molecules in a solution of 100 μL.

3.1.2. Stability. The operational stability of biosensors is a critical device parameter, especially considering that they operate in a liquid environment. In the case of EG-FETs, the electrolyte can be pure water, PBS, or directly real biofluids. This liquid and complex environment could result in instabilities of the transistor and an optimized design comprising the channel material, biofunctionalization strategy, gate electrode, bias conditions, device architecture, and sensing protocol is highly required. The device stability is even more important in the context of single-molecule detection because large-area EG-FET approaches rely on the combined amplification of the transistor and the cooperative effects of the densely packed biolayer. Indeed, the large amplification could also result in amplified instabilities and, as a consequence, in a reduced signal-to-noise ratio.

Current approaches are addressing the stability of EG-FETs focusing on the design of the material channel as well as on the processing conditions. Primary sources of instabilities are attributed to (i) side redox reactions due to oxygen reduction and (ii) microstructural order of the deposited material which interacts with ions into the electrolyte.[107,134−136] By way of example, conducting and semiconducting polymers are widely used as active channel materials in EG-FETs, and under device operation they can react with the molecular oxygen leading to electrochemical side-reactions. Such reactions could produce hydrogen peroxide (H_2O_2) that may contribute to the device degradation and may be harmful to the local biological environment. Side redox reactions, typically displayed in the EG-FET gate current, are a primary point of concern in the case of ion-permeable channel materials, where the whole volume of the active material can be accessed by the hydrated ions.

https://doi.org/10.1021/acs.chemrev.1c00290
Chem. Rev. 2022, 122, 4636−4699

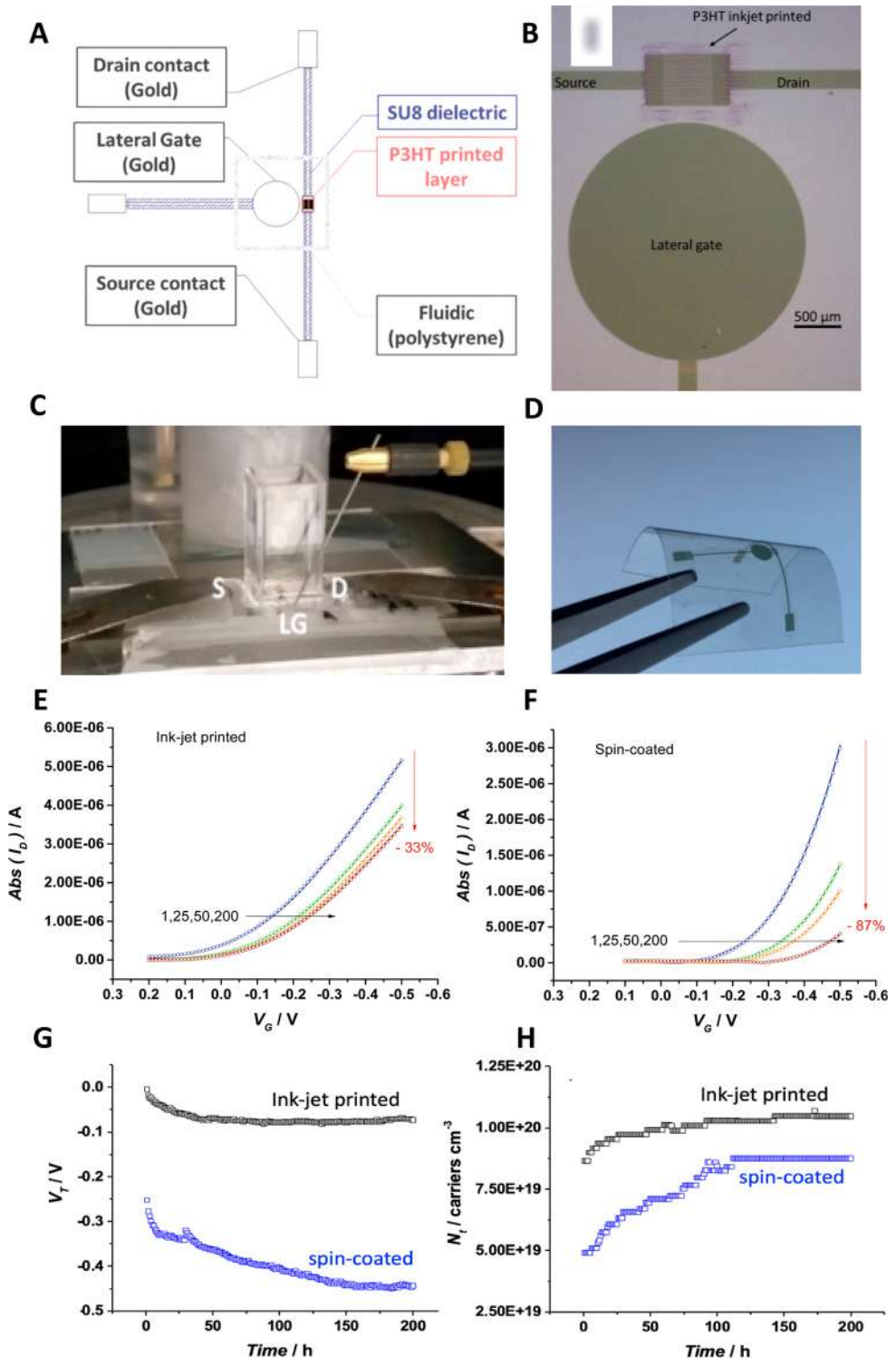

Figure 16. (A) Layout (top view) and (B) optical image of an EG-FET with lateral circular gate. (C) Experimental setup for the long-term measurements. (D) Picture of an EG-FET fabricated on plastic foil by means of photolithography and ink-jet printing. (E) Measured (symbols) and modeled (lines) transfer characteristics of an ink-jet printed EG-FET and (F) of a spin-coated EG-FET. The electrical measurements were performed according to the protocol presented by Picca and co-workers.[141] (G) Threshold voltage V_T of EG-FETs with P3HT deposited by spin-coating and ink-jet printing. (H) Total density of localized states N_t of EG-FETs with P3HT deposited by spin-coating and ink-jet printing. Reprinted with permission from ref 143. Copyright 2020 The Royal Society of Chemistry under a Creative Commons Attribution-NonCommercial 3.0 Unported License.

Researchers working in material science are actively working on the development of new organic semiconductors with improved and safer performance. Recently Giovannitti and co-workers reported donor−acceptor copolymers with reduced redox reactions during device operation.[136] Interestingly, this study explored the impact of the ionization potentials in commonly used ion-permeable polymers in order to avoid oxygen redox reactions. The stability and oxygen redox reactions of PEDOT:PSS, p(g2T-TT), and p(gPyDPP-MeOT2) were investigated, showing that larger ionization potentials reduce

https://doi.org/10.1021/acs.chemrev.1c00290
Chem. Rev. 2022, 122, 4636−4699

oxygen redox reactions and improve the operational stability of the EG-FET. The study also highlighted that the engineering of the polymer backbone is very relevant to improve the redox stability. Along this research direction, Moser, McCulloch, and co-workers found that also the molecular structure has a significant impact on water uptake in polymers and the proper engineering of ethylene glycol chains linked to the conjugated backbone of a polymer can improve the operation stability.[137] This study demonstrated that the redistribution of the pendant ethylene glycol chains in a series of polythiophenes could result in the tuning of their swelling capabilities enabling an enhancement of both the driven current and stability of electrolyte-gated transistors.

While ion-permeable polymers provide additional design variables for improving the device stability and figures of merit, their use in single-molecule biosensors is still limited because the large volumetric capacitance offered by the channel material does not allow a simple optimization of the biosensor performance. This is the reason why at the state of the art there are very few demonstrations of ultrasensitive detection with this class of materials. A more simple and effective approach is the use of organic or inorganic material channels impermeable to ions, where the EDL is installed at the electrolyte/semiconductor interface. Although at first glance the ionic-electronic interaction at the electrolyte/semiconductor interface could seem simpler than a bulk volumetric interaction, this interface defines the transistor operation and stability because of the two-dimensional nature of the charge transport in the transistor channel. Focusing for example on poly(3-hexylthiophene) (P3HT), which is one of the most widely used semiconductors for EG-FETs,[138−143] we recently investigated the stability of lateral-gate EG-FETs using P3HT as semiconducting channel material.[143] The structure of a later-gate EG-FET is displayed in Figure 16A. The gate and the interdigitated source and drain electrodes were obtained by evaporation and patterning of gold with a standard photolithographic technique. Conventional spin-coating or additive ink-jet printing were used to deposit the P3HT semiconductor. We note that the former approach is widely used because of the simplicity and uniformity, whereas the latter enables low-cost and industrial-scale fabrication. Figure 16B displays an optical image of an EG-FET with ink-jet printed P3HT. In order to operate the transistors for several days avoiding the impact of electrolyte evaporation or cell refilling in batches, a plastic well connected to a reservoir was adopted. The measurement setup is displayed in Figure 16C. A later-gate EG-FET fabricated on a plastic flexible substrate is shown in Figure 16D. In order to evaluate the operating stability, the electrical measurements were acquired with a sampling rate of 1 h and during a period of 8 days. A total amount of 200 transfer characteristics were collected for both spin-coated and ink-jet printed EG-FETs. In panels E and F of Figure 16 the I_D-V_G characteristics (symbols) at relevant cycle numbers are shown. The direct comparison of the electrical characteristics, intra- and interdevice, shows that the overall drop of I_D for the printed film was −33%, while for the spin-coated film a drop of −87% was obtained. These data were confirmed by various EG-FET replicates. To accurately estimate the EG-FET parameters, a physically based numerical model accounting for device geometries, charge transport in the organic semiconductor, and EDL formation at the electrolyte−semiconductor interface was developed. In Figure 16E,F, the transfer characteristics calculated with the model (lines) perfectly reproduce the measurements, and all 200 curves were accurately reproduced. Relevantly, the whole data set was described with a unique set of geometrical and physical parameters. Only the threshold voltage (V_T) and the total density of localized states (N_t) were dependent on the given measurement. Figure 16G,H shows the calculated V_T and N_t of ink-jet printed and spin-coated EG-FETs. The different threshold voltages are associated with the different work functions of the films. Ink-jet printed EG-FETs reached a stable operation much faster than spin-coated EG-FETs also displaying a smaller variation of both V_T and N_t. These findings suggested that ink-jet printed films led to a lower-energy disorder and an improved quality of the crystalline regions. Further analysis based on UV−vis and resonant Raman spectroscopy corroborated this picture. The different crystalline quality among ink-jet printed and spin-coated samples was eventually ascribed to the different solvents used for the semiconductor processing. Overall, these findings highlight the relevance of the device processing conditions, which can be an important and easy-to-apply route for the optimization of the biosensors' stability. Importantly, the study also investigated the shelf life of EG-FETs with printed P3HT, which is very relevant for commercial exploitation. EG-FETs stored in water and in air were investigated by means of UV−vis spectroscopy. The analysis showed that the absorption intensity of printed P3HT reduced by about 40% when the EG-FETs were stored in air, and a critical degradation of the crystalline order was also observed. By contrast, storage in water resulted in slight changes of the spectrum intensity and in a negligible degradation of the P3HT film.

Despite the great importance of the device stability, which is crucial in bioelectronics, very few contributions are available at the state of the art.[144−147] However, we positively note that this topic is triggering increasing attention, and further research should focus not only on the material design and optimal operating conditions but also on the stability analysis of the biofunctionalized surface and the development of standard procedures for assessing the biosensor stability. By way of example, along these directions the EG-FET electrical characteristics measured before and after the biosensing as well as the measured drift rate could be simple yet effective methods.[25,96,108]

3.2. Materials Used in High-Performing Bioelectronic Sensing

A plethora of different materials for EG-FETs have been studied and optimized over the past years, pointing toward higher electronic performance. Indeed, EG-FET biosensing platforms offer the advantage of monitoring many parameters of the transistor when the biorecognition element/target analyte complex formation occurs at one of the detecting interfaces. In applications where high sensitivity is required, it is of paramount importance to ensure the highest possible performance level concerning the field effect mobility (μ_{FET}), threshold voltage (V_T), source−drain on current (I_D), and on/off ratio. Later, great efforts were devoted to achieve the operational stability of the biosensor in a liquid environment for several days. Indeed, it is of utmost importance to make sure that a biosensing platform can withstand operation in water when it is directly interfaced with the biological environment to be assayed. In this perspective, novel materials and optimized device structures have been deployed, providing several interesting cases of bioelectronic platforms stable for a prolonged time while exposed to a liquid environment.[145,147,148] In this section, a

https://doi.org/10.1021/acs.chemrev.1c00290
Chem. Rev. 2022, 122, 4636−4699

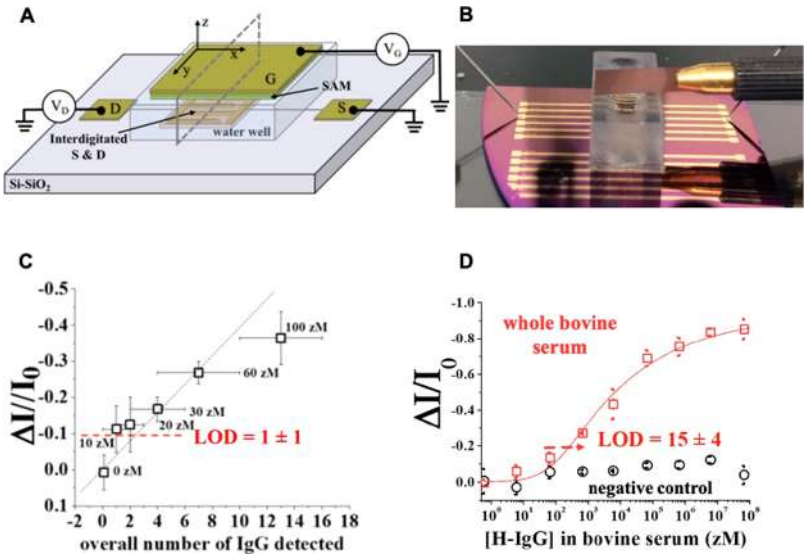

Figure 17. (A) Schematic representation and (B) picture of the SiMoT platform. (C) Dose−response curve measured upon exposure to PBS standard solutions of IgG containing from 0 to 15 ± 4 molecules. (D) Dose curve upon exposure to nominal concentrations of IgG spiked into undiluted bovine serum as red squares, from 0.6 zM to 6×10^7 zM. The selectivity of the platform is assayed exposing the sensing gate to human IgM (black circles). The Poisson distribution probability-based model is reported as a continuous red line. Reprinted with permission from ref 25. Copyright 2018 Springer Nature under Creative Commons Attribution 4.0 International License (http://creativecommons.org/licenses/by/4.0/).

bird's eye view of emerging organic as well as inorganic materials for the development of bioelectronic devices with subfemtomolar limit of detection is provided. Moreover, carbon-based semiconductors will be also reviewed. In fact, as will be detailed in the following section, they are successfully employed both as active layer or as contact materials in many bioelectronic assay.

3.2.1. Organic Materials. Organic materials represent a class of high-performing materials that are employed in bioelectronic sensors operated in liquid environments. The extended p-orbital system endows such materials with electrical conductivity. Moreover, organic materials are particularly suitable in the development of cost-effective biosensing platforms, as they are compatible with flexible substrates and large-area solution-based processing. Their mechanical properties along with long-term biocompatibility endow those materials with high compliance toward biological interfaces, being the ideal candidates for the development of biosensing devices capable of successfully operating in contact with an aqueous environment. Currently, a plethora of semiconducting polymers have been manufactured, demonstrating stable operation under ambient conditions. Remarkably, p-type stable operation in a liquid environment has been accomplished for the small molecule semiconductors sexithiophene,[149] pentacene,[150] and rubrene[151] and thiophene-based polymers, such as poly(3-hexylthiopene) (P3HT),[141,143] or poly(3,4-dioxyethylenethiophen) (PEDOT),[96,152] or OFET-based biosensor modified with 2,6-bis(4- formylphenyl)anthracene (BFPA).[153] In contrast, n-type organic semiconductors are as yet generally lower-performing than the p-type materials in terms of both charge-carrier mobility and environmental stability.[154] Recently, PEDOT film serving as a semiconducting channel for an OECT device has been engaged in the detection of immunometric interactions, returning detection limits down to the attomolar range.[96] PEDOT is porous and hydrophilic, thus enabling the ions in the electrolyte solution to pass into the bulk of the polymer. Indeed, it is possible to operate OECTs as a potentiometric capacitive coupled field effect transistor, like EG-FETs, displaying extremely high electronic and analytical performance. When this is the case, there are no conceptual distinctions between EG-FET and OECT. In fact, the electrolyte medium acts as an ion conducting material while being an electronic insulating material. Indeed, in this scenario the presence of any electroactive moieties is completely ruled out. However, the study here discussed represents an exception, because OECTs are typically proposed for electroactive compound detection, reaching nanomolar detection limits at most.[33]

P3HT represents by far one of the most studied semiconducting polymers and has been proficiently proposed in a plethora of different applications such as chemical and biological sensors,[155,125] and energetics.[156] P3HT has been engaged in the fabrication of the single-molecule with a large-transistor (SiMoT) bioelectronic device.[25] A SiMoT device is based on an EG-FET where the 0.5 cm^2 gold gate electrode is biofunctionalized[157,158] with *ca.* 10^{12} biorecognition elements. In Figure 17A,B, the schematic representation of the SiMoT platform is reported along with a picture of the EG-FET defined on a Si/SiO_2 wafer and using as gate electrode a gold film on Kapton foil. The EG-FET device comprises an electronic channel composed of source (S) and drain (D) electrodes on top of which a P3HT spin-coated film is deposited. P3HT conductivity is modulated through the gate electrode (G), and deionized water is engaged as electrolyte. These elements are immersed into a measuring well where the sensing gate is immersed too. As addressed in section 3.2.1, the operational stability of a P3HT-based EG-FET working for eight days in water has been recently demonstrated with transistors encompassing a spin-coated P3HT film deposited on a rigid Si/SiO_2 substrate as well as with a cost-effective large-area compatible ink-jet printed P3HT on plastic foil. The operational stability of printed P3HT EG-FET has been monitored for one week through electrical, optical, and Raman characterizations, and it showed that 36 h was necessary to reach the device operational stability in water. It is worth mentioning that when operational stability is reached the current drift typically observed falls in the order of few percentages per hour, thus

https://doi.org/10.1021/acs.chemrev.1c00290
Chem. Rev. 2022, 122, 4636−4699

ensuring the P3HT stability during a whole biosensing experiment. Therefore, considering a time to result of at most 2 h needed to perform a biosensing experiment, the typical P3HT current drift will follow within the noise level of the negative control experiments. Moreover, it has been demonstrated that the P3HT film can reach its operational stability upon exposure to water for about 48 h.

Such a protocol has been defined based on the observation that the pristine P3HT organic semiconductor needs to get acquainted with the water environment to reach the operational stability, even in the absence of an applied voltage. Remarkably, the SiMoT platform, based on a stable organic semiconductor, has established a world record in single-molecule detection with a label-free technique. Figure 17C displays the human-IgG immuno-assay with nominal concentrations ranging from 0 to 100 zM. Human anti-IgG is covalently attached to the gold gate and has been employed as biorecognition elements. The signals registered already at 10 and 20 zM, namely, with only 1 ± 1 particles in the 100 μL assayed volume, have been demonstrated to be beyond the LOD. Moreover, the SiMoT device is capable achieving single-molecule detection in clinically relevant body fluid as well (see Figure 17D). Different aliquots of IgG were spiked in untreated bovine serum, and the SiMoT response was registered (shown as red-squares), while human IgM was used for the negative control (back spheres). A LOD of 250 zM, being equal to 15 ± 4 proteins, has been demonstrated by the authors in real biofluids. The SiMoT platform has been successfully demonstrated to detect with single-molecule detection limits also IgM,[26] C-reactive protein in saliva,[27] HIV-P-24,[28,159] and miR-182 (a micro-RNA marker of multiple sclerosis),[29] as well as the MUC1 protein and a DNA probe for pancreatic cancer.[160] The amplification steps of such a platform need still to be experimentally demonstrated. However, a first possible mechanism has been proposed to date, based on cooperative-effects enabled by a hydrogen-bonding network residing at the sensing gate electrode. Large-area amplification effects will be thoroughly discussed in section 7 of this review.

Recently, Biscarini *et al.* demonstrated an EG-FET immunosensor, based on organic materials, to assay antidrug antibodies (ADAs) in the femtomolar range.[97] The EG-FET device is defined on a quartz glass and holds gold electrodes as the source and the drain contacts with an interdigitated geometry and a ratio of width over length (W/L) of 500 as reported in Figure 18A. The semiconducting material is a TIPS-pentacene layer. To selectivity detect the target molecules, the EG-FET embodies a gold gate functionalized with an ADA-specific biorecognition element. Specifically, Cys-protein G has been chemisorbed on the gold gate electrode using the thiol group of a modified cysteine. Protein G binds to the Fc region of antibodies. Consequently, the binding geometry of Nivolumab results in exposure of the Fab region to the liquid environment, being the docking position of ADAs. Subsequently, the gate surface is saturated with an oligoethylene glycol (11-mercaptoundecyltriethyleneglycol) self-assembled monolayer (SAM) as depicted in Figure 18A. This step aims at reducing nonspecific binding of Nivolumab and ADAs. The dose curve has been evaluated registering the transfer characteristics of the EG-FET after incubation into the ADA buffer solution (Figure 18B) demonstrating anti-Nivolumab ADA detection with a dynamic range of 4 orders of magnitude (see Figure 18C). A negative control experiment, conceived using a device with the gate electrode functionalized with infliximab and exposed to anti-Nivolumab ADAs, has been performed, registering a

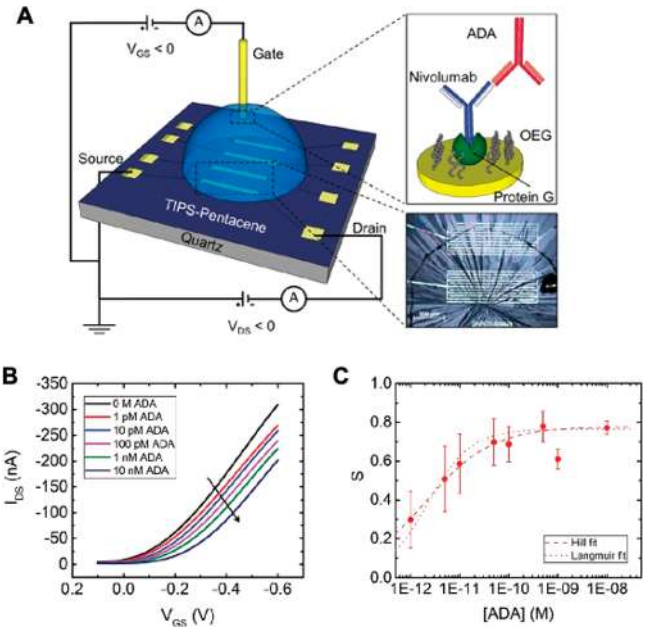

Figure 18. Schematic representation of the EG-FET device and the gate biofunctionalization protocol. (A) TIPS-pentacene is used as an organic semiconductor (in the inset is the optical microscopy picture). A PBS droplet is used as electrolyte. The zoomed-in view of the sensing gate is sketched in the of the inset. (B) Transfer characteristics registered after exposure to different concentrations of ADA, at V_{DS} = −0.2 V. (C) Semilog plot of the signal S as a function of the [ADAs] concentrations registered at V_{GS} = −0.2 V. Reprinted with permission from ref 97. Copyright 2021 The Royal Society of Chemistry under a Creative Commons Attribution-NonCommercial 3.0 Unported License.

negligible signal. A LOD as low as 100 fM has been achieved. The ultrasensitive sensing performance has been ascribed to the organic semiconductor electronic properties. Specifically, the distribution of the density of states of the semiconducting film is responsible for the exponential amplification of the subtle modification upon binding of the potential at the semiconductor/electrolyte interface. These potential variations are caused by the displacement of ions in the semiconductor/electrolyte interface due to the shift of the Fermi level of the gate ascribable to a biorecognition event.

3.2.2. Inorganic Materials. Although organic materials have exhibited so far a very high potential for the development of bioelectronic devices, the electrical performance that can be achieved with such devices is still a bit low, in comparison to a-Si in the best cases, for many potential applications.[161] In fact, even with high-purity organic semiconducting single crystals the field-effect mobilities are lower than those of polycrystalline silicon.[162] Therefore, the possibility of endowing organic bioelectronic devices with sufficiently high signal-to-noise ratio remains an intrinsic challenge for accurate monitoring. Furthermore, the shelf life and the lack of controlled doping techniques for such organic materials still represent open questions, requiring further research to be addressed. By contrast, many inorganic semiconductors display higher field-effect mobilities, excellent stability, much less aging in the air, as well as highly mature manufacturing techniques.[163,164] Consequently, almost all bioelectronic devices that reached the market to date are based on silicon microelectronics, being largely employed in almost all information infrastructure and technologies, including health-care and medical devices.[165] In

https://doi.org/10.1021/acs.chemrev.1c00290
Chem. Rev. 2022, 122, 4636−4699

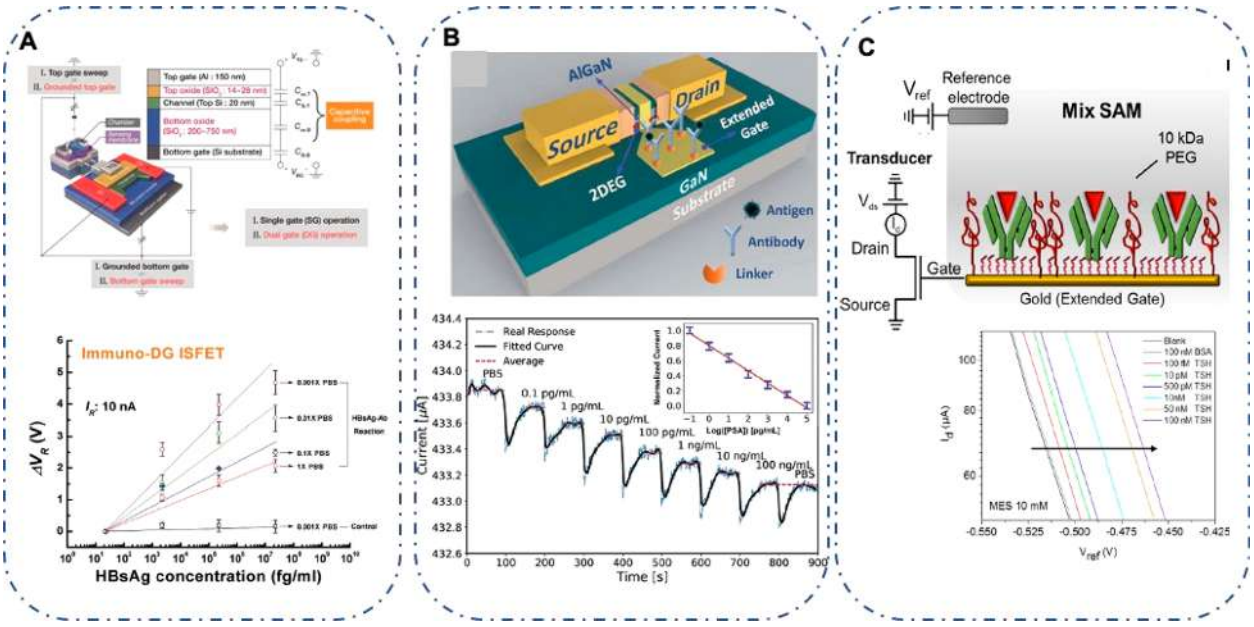

Figure 19. (A) Pictorial view of the ISFET device and a description of the dual gate (top panel) and dose response curves vs HBsAg antigen concentrations at different ionic strength of the PBS solutions. Reprinted with permission from ref 168. Copyright 2015 The Royal Society of Chemistry. (B) Pictorial diagram of the extended gate-AlGaN/GaN transistor (top panel) and PSA real-time monitoring (the red lines are the mean experimental values, while the bold black line is the fitting). Reprinted with permission from ref 169. Copyright 2017 The Royal Society of Chemistry under a Creative Commons Attribution-NonCommercial 3.0 Unported License. (C) Pictorial view of the biosensing readout circuit (top panel) and the response of the sensor exposed to BSA and different concentrations of thyroid-stimulating hormone in MES buffer (ionic strength 10 mM, pH 7). Reprinted with permission from ref 170. Copyright 2017 American Chemical Society.

broader terms, the advantages of inorganic materials rely on the availability of a wide variety of tunable architectures and the possibility to easily integrate them into fully CMOS-compatible platforms. From this perspective, several kinds of inorganic FET-based biosensors, such as Si-FET,[86] GaN high electron mobility transistors,[166] or amorphous indium-gallium-zinc-oxide (a-IGZO),[167] have been successfully proposed, showing sub-femtomolar detection limits. As an example, in a study by Lee, a self-amplified transistor encompassing a dual gate operation (ISFET) has been proposed for hepatitis B infection diagnosis through hepatitis B surface antigen (HBsAg) marker.[168] The structure of the ion-selective-FET (ISFET), reported in the top panel of Figure 19, is close to that of a MOSFET transistor, where the sensing components take the place of the MOSFET metal gate electrode and dielectric. Thus, the ISFET encompasses a transducer, represented by the FET component, and a disposable sensing counterpart. Remarkably, the sensing and the FET components have been split, to prevent any contact between the transducer and ions, that might damage some of the electronic components. The split sensing cartridge is thus termed the *extended-gate sensing device*. The transducer has been fabricated from a silicon wafer covered by a 200 nm-thick buried oxide, being the bottom gate material. The active region has been prepared by means of photolithographic standard processes. Then, the source and drain are defined by means of a phosphorus-doped poly-Si film. A thermally grown SiO_2 film is used as the top gate oxide, while the top gate electrode is made of an aluminum layer.

The extended gate sensing device has been fabricated starting from a p-type Si wafer covered by thermally grown SiO_2 (300 nm thick). A 150 nm-thick aluminum film on top of the SiO_2 wafer is used as electrode. Subsequently, the aluminum electrode was covered with a tin dioxide (SnO_2) film sensing membrane (50 nm thick) sputtered on top of it. To immobilize the anti-HBsAg capturing antibodies, the surface of the sensing membrane was immersed into a PBS (pH 7.4; 1×) buffer solution containing 150 nM of anti-HBsAg for 1 h. The unreacted sites on the surface were blocked using ethanolamine and BSA to avoid nonspecific binding. A polydimethylsiloxane chamber is then glued on top of the sensing membrane. The sensing part results in an area of about 0.5 cm^2, being conceived to host sample volumes compatible with the standards in clinical settings. The top panel of Figure 19A reports a sketch of the ISFET with the extended-gate component. The dual-gate ISFET has been proposed as a biosensing platform for detection of HBsAgs in the femtomolar to nanomolar concentration range. Importantly, by increasing the HBsAg concentration, a shift of threshold voltage toward more negative values was registered because of the surface potential change induced by the HBsAg-Ab complex formation. The following control experiment has been also designed: the surface of a sensing membrane without capturing antibodies has been exposed to HBsAg solutions. The bottom panel of Figure 19A shows the threshold voltage change registered after the incubation into HBsAg target solution, also varying the electrolyte solutions' ionic strength. The largest response has been measured by performing the sensing experiment when using the lowest ionic strength electrolyte solution, namely, 0.001× PBS, according to previous studies reported in the literature.[122] Under these conditions, a LOD of 1.5 fM has been achieved.

Recently, an extended gate-AlGaN/GaN high electron mobility transistor has been conceived by Ding *et al.* for early recognition of prostate-specific antigen (PSA).[169] A schematic illustration of the biosensing platform is shown in the top panel of Figure 19B. The structure of the extended gate-AlGaN/GaN high electron mobility transistor consists of two different main components: the sensing area and the AlGaN/GaN transistor. The gold extended gate has been functionalized according to the

https://doi.org/10.1021/acs.chemrev.1c00290
Chem. Rev. 2022, 122, 4636−4699

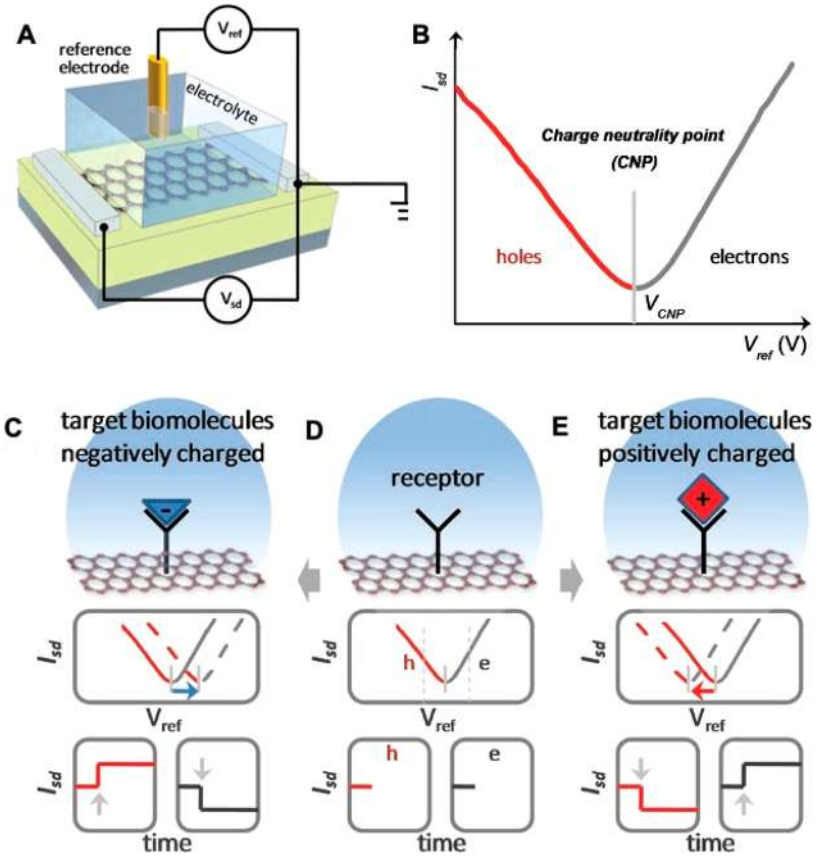

Figure 20. Schematic representation of the graphene-based biosensor sensing mechanism. (A) Sketch of an electrolyte-gated graphene FET biosensing platform. (B) Ambipolar transfer characteristic registered with a typical graphene transistor. The charge-neutrality point (CNP) marks the point of minimum current value. (C–E) Sensing mechanism of a liquid-gated graphene FET biosensor where the biorecognition elements are grafted on the graphene layer (D), as well as upon positively (E) or negatively (C) charged target analyte. Reprinted with permission from ref 173. Copyright 2017 John Wiley and Sons.

following protocol: The gate has been incubated for 6 h in deoxygenated cysteamine solution in deionized water to generate thiol–gold bonds on the gate surface. The gate has been subsequently incubated in a glutaraldehyde solution for 2 h using a lab-made reservoir. Therefore, the immobilization of PSA monoclonal antibody in the nanomolar range has been performed.

The sensing region has been designed to be large enough, bearing an area of 0.5 mm^2, to gather sufficiently high signal amplification. Indeed, the main factor enhancing the device performance has been proven to be the sensing area endowed with a dense layer of bioreceptors on the surface, thus improving the sensitivity of the assay. In the bottom panel of Figure 19B, the real-time monitoring of the drain current upon exposure to increasing PSA concentrations is reported. The fist 100 s is relevant to PBS injection, which provides the *baseline* current level. The device was further exposed to seven PSA standard solutions spanning a concentration range from femtomolar to nanomolar. During every cycle of measurements, within 60 s, the I_{DS} registers a plateau when the antibody–antigen reaction is completed. The red dashed lines in the bottom panel of Figure 19B depict the average current level reached at each steady stage. To evaluate the noise level of the blank sample, the biofunctionalized extended gate has been exposed to bare PBS solution. Interestingly, a LOD of 4 fM has been estimated, and the device showed a dynamic range of up to 6 orders of magnitude.

Another interesting approach has been recently proposed to detect thyroid-stimulating hormone with a subfemtomolar detection limit, based on an extended-gate configuration. The biosensing platform encompasses a gold sensing surface integrated with a MOSFET transducer (Figure 19C, top panel).[170] One of the main advantages offered by the extended-gate structures compared to traditional electrolyte-gated devices relies on the possibility of avoiding any contact of the transducing element with the sample solution, thus increasing the reliability of the response registered. Moreover, in this case, the transducer is far from the sensing cartridge. This endows the biosensing platform with the possibility of using the MOSFET readout component many times, whereas the sensing element is designed as a low-cost disposable cartridge. Furthermore, the use of a gold sensing interface allows exploiting the thiol-gold chemistry, being a state-of-the-art protocol for the immobilization of self-assembled monolayers (SAMs) acting as linkers for the desired biorecognition elements.[158,171] Interestingly, the biosensing platform has been validated by varying the human thyroid-stimulating hormone concentrations in MES buffer, while bovine serum albumin (BSA) has been used to collect the negative control experiment. Moreover, the sensing and negative control experiments have been performed in real biofluid, namely, undiluted horse serum spiked with different thyroid-stimulating hormone or BSA concentrations. After 20 min of incubation into the sample solutions, the stable transfer characteristics have been measured. The representative transfer

https://doi.org/10.1021/acs.chemrev.1c00290
Chem. Rev. 2022, 122, 4636–4699

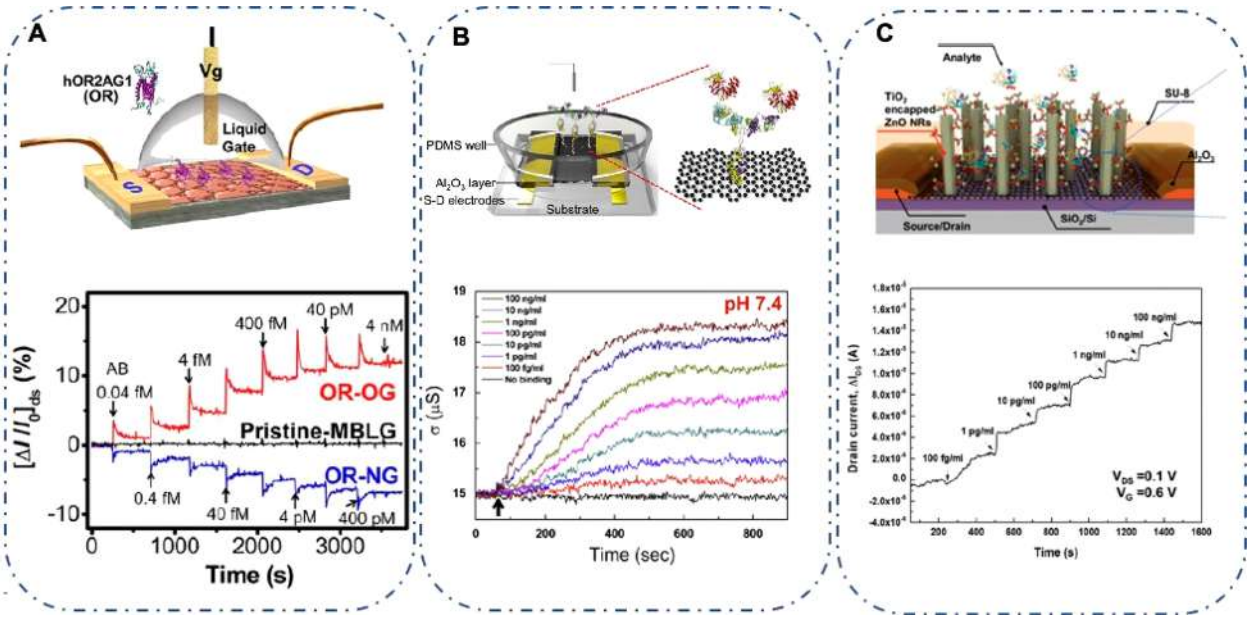

Figure 21. (A) Sketch of the graphene EG-FET bioelectronic nose (top panel) and real-time responses of the device based on olfactory receptor (OR)-conjugated p-type (OG) and n-type (NG) against the analyte concentrations in femtomolar to nanomolar range. Reprinted with permission from ref 175. Copyright 2012 American Chemical Society. (B) Illustration of reduced graphene-oxide FET biosensor (top panel) and electrical conductivity, σ, after exposure to PBS buffer and analyte solutions at each concentration of specific antigen/a1-antichymotrypsin (PSA-ACT) complex at pH 7.4 (bottom panel). Reprinted with permission from ref 177. Copyright 2013 Elsevier. (C) Pictorial illustration of a 3D channel FET biosensor (top panel) along with the real-time monitoring of the I_{DS} current upon exposure to the analyte solutions at increasing concentrations (bottom panel). Reprinted with permission from ref 178. Copyright 2015 The Royal Society of Chemistry under a Creative Commons Attribution-NonCommercial 3.0 Unported License.

curves registered upon exposure to TSH analyte concentrations in buffer solution, in the femtomolar−nanomolar range, are shown in the bottom panel of Figure 19C. The sensor has been stabilized in buffer before exposing the functionalized extended gate to the analyte solutions, resulting in a stable *baseline*. Remarkably, a LOD of 100 fM has been registered with the experiments performed in MES, while a LOD of 500 fM has been achieved in whole horse serum.

3.2.3. Graphene and Nanorods. The use of graphene in bioelectronic devices for biosensing applications has been actively pursued since 2004, when Novoselov *et al.* first demonstrated a protocol for its fabrication as well as its conducting properties.[172] The sensing mechanism, as detailed in the following, relies on the modification of the graphene electrical conductance upon selective adsorption of the target analyte on the device channel area.[173] The unique properties of graphene in comparison to other solid-state materials are related to the carbon atoms that are in a bidimensional arrangement, potentially endowing the graphene surface with high sensitivity to even subtle changes to the surroundings. The excellent electrical properties of graphene, for instance, the extraordinary mobility and low electrical noise,[174] are accompanied by the high sensitivity of graphene-based electronic biosensors.[106,173] Additionally, graphene is intrinsically chemically inert because of the absence of dangling bonds in its crystal lattice. In recent decades, all these features represented a main driving force for the huge effort to interface graphene with different biorecognition elements, *via* both covalent and noncovalent approaches. The sensing mechanism of graphene FET gated through a liquid electrolyte is exemplified in Figure 20. In the liquid-gated configuration of graphene FET, the reference electrode polarizes through the gate bias, the electrolyte solution (Figure 20A).[173] The typical electrical measurement registered with a graphene FET is shown in Figure 20B and is gathered by biasing through a constant source−drain voltage, V_{DS}, while sweeping the voltage at the reference electrode. Indeed, by varying the reference electrode potential V_{ref}, the Fermi level of the charge carriers (or in other words the electrochemical potential) can be modulated. Therefore, the charge of the carriers, flowing from source to drain, can switch from holes (red trace on the left in Figure 20B) to electrons (gray trace on the right in Figure 20B), thus endowing graphene with an ambipolar transport mechanism. Once the electron transport switches to the hole regime, the current reaches its minimum value. This is addressed as the charge-neutrality point. In a typical biosensing measurement, the biorecognition elements, responsible for the selective binding of the target molecules, are usually segregated on the graphene channel (Figure 20D, upper panel). The corresponding schematic representation of a typical I_{DS} vs V_{ref} curve registered with an electrolyte-gated FET with graphene biofunctionalization is shown in the middle panel (Figure 20D). The bottom panel of Figure 20D pictorially represents the current I_{DS} as a function of time while keeping V_{ref} constant. In the hole regime (denoted by "h") as well as in the electron regime ("e"), when a binding event between the bioreceptor and a positively charged target molecule occurs (Figure 20E), a reduction of hole carriers (consistently an enlargement of electron carriers) in the graphene arises because of the electric field. Therefore, the charge-neutrality point shifts toward more negative potentials, as suggested by the red arrow in Figure 20E. On the other hand, upon observing the real-time monitoring of the current I_{DS} (Figure 20E, bottom panel), it is apparent that the binding with positively charged target analyte generates a decrease of the I_{DS} in the hole regimen, while a current increment is registered in the electron regimen. By contrast, a target ligand baring a net negative charge (Figure 20C) produces

https://doi.org/10.1021/acs.chemrev.1c00290
Chem. Rev. 2022, 122, 4636−4699

a variation of the charge-neutrality point toward positive values while the I_{DS} increases in the hole regime. On the other hand, the binding generates a change of the charge-neutrality point becoming more negative within the electron regime, along with a decrease of the current I_{DS}.

First, a successful proof of principle of the biosensing platform encompassing a graphene liquid-gated FET was presented by Park *et al.* in 2012.[175] In this seminal paper, the authors reported a characterization of a bioelectronic nose based on bilayer graphene embedding 2AG1 human olfactory receptors, capable of selectively detecting an odorant target molecule (Figure 21A, top panel). The graphene has been achieved by chemical vapor deposition and further treated with oxygen plasma cleaning, to form a p-type film, or ammonia plasma treatment, forming an n-type one. Moreover, both treatments endow the graphene layer with a functional group suitable to chemically bind the proper biorecognition elements. Indeed, as biorecognition elements, the 2AG1-human-olfactory-receptors (hOR2AG1) have been selected to selectively bind the amyl-butyrate odorant marker. hOR2AG1 bioreceptors are grafted on top of the graphene channel material. Remarkably, about 5×10^9 olfactory receptors are deposited on the semiconducting layer. Consequently, a density of 5×10^{11} molecules per cm^{-2} is segregated on the detecting interface. A PBS solution has been used as electrolyte. The real-time monitoring of the I_{DS} current, keeping constant the reference voltage, while exposing the bioelectronic nose to increasing concentrations (40 aM to 400 pM) of the target analyte, is reported in the bottom panel of Figure 21A. The red trace is registered using the oxygen-treated graphene (p-type), whereas the blue trace is related to the ammonia-treated one (n-type), thus showing opposite responses. The black curve is registered with untreated graphene, meaning that no biorecognition elements are deposited on the biosensor detecting interface. The latter is taken as the negative control experiment. Interestingly, a linear behavior from 0.04 fM to 40 pM has been attained, followed by signal saturation for concentrations greater than 400 pM. In this case, the LOD is *ca.* 40 aM. Importantly, a response time as fast as 1 s is demonstrated. The label-free ultrasensitive detection, not requiring any pretreatment of the assayed sample, has been attributed to a morphological modification of the bioreceptors, bearing a net negative charge due to analyte/bioreceptor complex formation. According to the graphene sensing mechanism previously described (*vide supra*), this effect produces a hole accumulation in the graphene layer, thus increasing the I_{DS} current flowing in the p-type graphene transistor.

Conversely, a loss in the I_{DS} current is observed for the n-type graphene. Despite the great success of graphene-based FETS for biosensing applications, the cost-effective and large-area production of those biosensors is still limited because of the constraints of fabrication. Indeed, the difficulties in controlling the density of both defects, due to polymeric residues produced during the chemical-vapor-deposition growth of graphene, and immobilizing captured molecules on the graphene surface are the main drawbacks. To overcome those major limitations, one of the most popular approaches is the covalent modification of graphene films with oxygen functional groups, through oxidative reactions, forming graphene-oxide, widely employed since the early 1960s.[176] On the other hand, the synthetic route is based on graphite dispersion into a graphene-oxide single layer, by performing thermal or chemical reduction processes. This approach is particularly employed in large-scale production processes. The material obtained with such an approach is generally termed reduced-graphene-oxide. Reduced-graphene-oxide has been employed for the first time as an active material for an ultrasensitive biosensing application to sense prostate-specific antigen/a1-antichymotrypsin (PSA-ACT) complex biomarker. In this study, it has been demonstrated that the conductance of the reduced-graphene-oxide networks changes upon exposure to the target analyte.[177] Figure 21B (top panel) illustrates the schematic representation of the biosensor fabricated from a reduced-graphene-oxide channel. The prostate-specific antigen monoclonal capturing antibody (PSA mAb) has been grafted on the reduced-graphene-oxide channel, using a PDMS well filled with 1- pyrenebutanoic acid succinimidyl ester as a linker molecule for 2 h. After a washing step, the tailored reduced-graphene-oxide surface was exposed to PSA mAb in the nanomolar concentration range overnight and subsequently treated with ethanolamine to prevent any nonspecific binding. In Figure 21B (bottom panel) the channel conductivity (σ) versus time is reported for the reduced-graphene-oxide FET in PBS solutions at pH of 7.4, and subsequently the analyte concentration was varied in the femtomolar−nanomolar range.

The selectivity of the biosensing platform has been assessed by exposing the detecting interface to carcinoembryonic antigen biomarker in the aforementioned concentration range. Importantly, no shift in the charge-neutrality point has been registered when the detecting interface biofunctionalized with PSA mAb has been exposed to the solution containing carcinoembryonic antigen biomarkers. Remarkably, a linear shift in the charge-neutrality point with the analyte concentration is observed, along with a limit of detection as low as 1 fM and wide dynamic range of up to 6 orders of magnitude in the buffer solution. Immunosensing in human serum spiked with the analyte molecules showed the same LOD of 1 fM and a dynamic range lowered by 1 order of magnitude. The ultralow limit of detection has been tentatively attributed to the dense immobilization of the bioreceptor on the reduced-graphene-oxide surface. From the perspective of increasing the density of bioreceptors on the sensor detecting interface, a plethora of EG-FET devices encompassing two-dimensional (2D) conducting nanomaterial along with a wide-field sensing area have been demonstrated so far, achieving ultrafast detection of biomolecular interactions with subfemtomolar limit of detection.[25,97,179−181] One of the most intriguing examples of such devices is represented by the case of a 3D EG-FET with vertical, highly dense ZnO nanorods on a graphene channel being the ideal candidate for directional growth of ZnO nanorods.[178] The 3D EG-FET integrating ZnO nanorods on the graphene film has been successfully endowed with ambipolar features. The 3D EG-FET has been recommended to identify the markers of the PSA-α-1-antichymotrypsin complex. A pictorial view of the proposed biosensing device, grown on a SiO_2/Si substrate, using PSA-α-1-antichymotrypsin complex antibody as biorecognition element, is reported in Figure 21C (top panel). The responses as a function of time upon adding each target solution with different PSA-α-1-antichymotrypsin complex concentrations in the femtomolar−nanomolar range have been registered and are shown in Figure 21C (bottom panel). As the PSA-α-1-antichymotrypsin complex nominal concentrations become greater, the saturation is reached faster; for 100 fM and 100 pM, for instance, the time-response signal saturated after 64 and 44 s, respectively. Remarkably, the biosensing platform showed a dynamic range of 10^7, a LOD of ∼1 fM in PBS standard solution, whereas the LOD falls in the picomolar range in 10% diluted

https://doi.org/10.1021/acs.chemrev.1c00290
Chem. Rev. 2022, 122, 4636−4699

Table 3. Summary of the Analytical Figures of Merit of Organic, Inorganic, and Graphene-Based EG-FETs Biosensors with Subfemtomolar Detection Limits

Material	Analyte	LOD	Dynamic range	Assay of real biofluids	Time-to-result
P3HT[25]	IgG	20 zM	10^3	whole bovine serum	<1 h
PEDOT[96]	IgG	6 aM	10^8	no	<1 h
TIP-pentacene[97]	ADA	100 fM	10^4	no	few hours
Si extended-gate-ISFET[168]	HBsAg	1.5 fM	10^4	no	few hours
AlGaN/GaN high-electron-mobility transistor[169]	prostate-specific antigen	4 fM	10^6	no	<1 h
Si-MOSFET[170]	thyroid stimulating hormone	100 fM	10^3	whole horse serum	<1 h
graphene[175]	AB odorant	40 aM	10^5	no	<30 min
reduced-graphene oxide[177]	PSA-α-1-antichymotrypsin	1 fM	10^6	whole human serum	<1 h
ZnO nanorod[178]	PSA-α-1-antichymotrypsin	1 fM	10^7	10% diluted human serum	<30 min

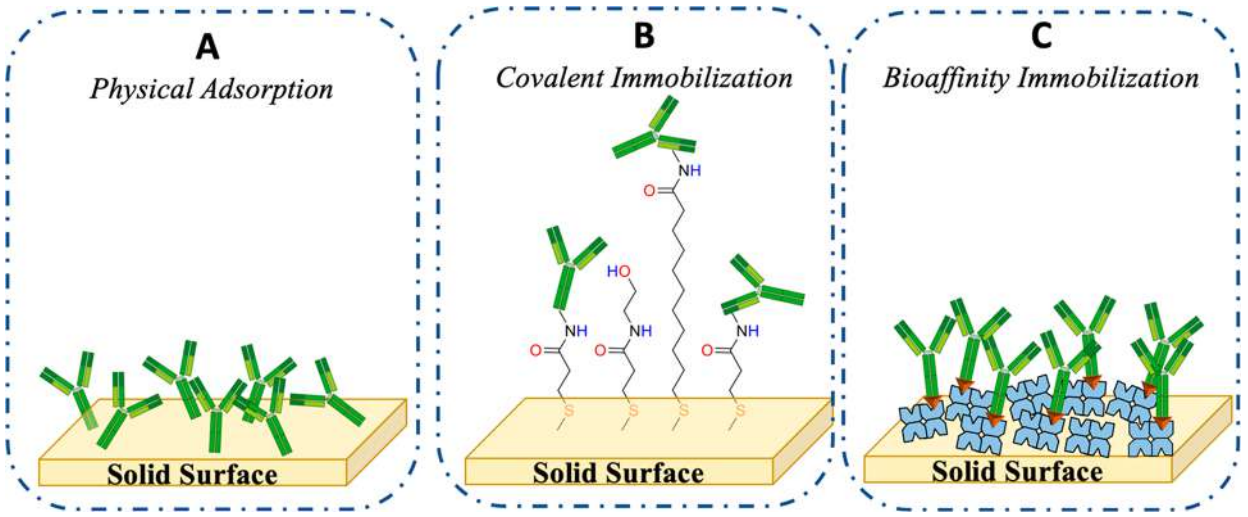

Figure 22. Schematic representation of the main categories of immobilization methods on detecting interfaces: (A) physical immobilization, (B) covalent immobilization by means of self-assembled monolayers, and (C) bioaffinity immobilization reactions.

human blood serum, and the time-to-result is 64 s when the analyte levels fall in the femtomolar range.

Table 3 summarizes all the analytical figures of merit of the EG-FETs previously discussed.

4. SINGLE-MOLECULE SELECTIVE ELECTRONIC DETECTION OF PROTEINS AND GENOMIC MARKERS

According to the US National Institute of Health, a biomarker is a measurable index of physiological or pathogenic states.[182] As extensively discussed in section 1, the opportunity to identify a single biomarker may offer new and exciting possibilities for early diagnosis of many diseases. Standard medical analysis usually foresees nucleic acids or proteins and peptides as clinically relevant markers.[183] Specifically, genomic biomarkers, in other words DNA and RNA strands, are among the most commonly employed biomarkers in a wide range of clinical applications.[184]

The use of genomic biomarkers for clinical purposes can be dated to 1999[185] when the new approach was proposed to differentiate two different forms of leukemia. Later on, a wide variety of different genomic markers was identified, allowing the discovery of oncogenes alterations and providing an important contribution to the timely diagnosis of the onset of pathological states.[186−188] On the other hand, peptide and protein biomarkers also play a pivotal role in early diagnosis of many pathological states, and it is paramount to detect them with extremely sensitive and selective technologies.[54] Moreover, protein and peptide modifications and mutations are highly important to understand biological functions and diseases. Consequently, a huge effort should be dedicated to ultrasensitive protein detection, along with the more widely employed genomic markers, now sensed with a single-copy detection limit *via* NGS.[189] However, ultrasensitive protein detection remains an extremely challenging task. Indeed, Simoa technology can sense protein markers with attomolar LODs,[23] corresponding to 10^2-10^3 proteins in a sampled volume of 100 μL, being sensitive to a lesser extent than NGS. Moreover, Simoa and NGS are benchtop systems and thus are not at all suitable in point-of-care settings. From this perspective, a bioelectronic platform based on EG-FET, capable of detecting both kinds of markers, with a LOD at the single-molecule level, is an exceptionally compelling technology to enable noninvasive early diagnosis of life-threatening progressive diseases with high societal impacts. Eventually, those technologies might enable reliable and ultrasensitive detection of pathogens too, such as viruses and bacteria. Therefore, an outline on the state of the art of EG-FETs biosensors detecting genomic markers, proteins, and pathogens with subfemtomolar LODs will be provided in section 4. Before the introduction of the most intriguing examples of EG-FET-based biosensing platforms proposed to date, some of the most used approaches to successfully embed bioreceptors into a bioelectronic platform are briefly reviewed in the following section.

https://doi.org/10.1021/acs.chemrev.1c00290
Chem. Rev. 2022, 122, 4636−4699

4.1. Biofunctionalization Strategies of a Detecting Interface

Bioelectronics are based on the integration of biotic components, for instance, proteins, DNA, or RNA, with an abiotic counterpart, such as electrodes, devices, or electronic components. From this perspective, the strategy selected to immobilize the biorecognition elements on the selected active region of the biosensor is of paramount importance. When bioreceptors are segregated into a surface, a reduction or loss of mobility always occurs. Moreover, in order to avoid any loss of the biorecognition elements' bioactivity, which might be caused by random orientation or structural deformations, the biofunctionalization protocol has to be selected and optimized to retain the conformation and functions of the bioreceptor. Importantly, the analytical quality of the data gathered with a certain biosensing platform might be adversely affected by the conditions used for the biofunctionalization procedure. When segregating a bioreceptor on a biosensor active region, the following parameters should be considered: (i) the surface chemical/physical properties, which might alter specific and nonspecific adsorption of target and nontarget molecules; (ii) the biorecognition elements' orientation, which could hamper the binding events, especially when large analytes are involved in the assay; and (iii) the surface density of the bioreceptors, affecting the sensor's analytical figures of merit. The choice of active surface material suitable for the biofunctionalization strategy is related to a particular application. As an example, the fabrication of an assay characterized by an electrical[190,191] and SPR read-out often involves the presence of a gold detecting interface.[157,192] Indeed, the use of such surfaces guarantees that the surface-confined bioreceptors hold their biofunctionality, allowing for high-throughput and reproducible assay responses. When gold detecting interfaces are involved, biofunctionalization protocols based on the thiol chemisorption are the most convenient approaches. In contrast, glass detecting interfaces are to be preferred in the case of optical readout sensors because of its transparency and low intrinsic fluorescence.[190] All the different biofunctionalization approaches developed to date can be classified into three main categories: physical, covalent, and bioaffinity immobilization techniques. Those mechanisms are pictorially represented in Figure 22. Physical immobilization is typically based on the adsorption of biomolecules on the detecting interface trough intermolecular forces, mainly hydrophobic, ionic, and/or van der Waals interactions. Depending on the biomolecules and the surface employed, one of those contributions will dominate. Such an approach is suitable to immobilize proteins on many different kinds of surfaces comprising carbon-based compounds, noble metals, or metal oxides (Figure 22A). Such a process is also largely used for DNA and protein grafting on organic semiconductor layers such as pentacene, P3HT, and PEDOT in FET devices.[193] Importantly, coupling reagents or chemical modification of the biomolecules can be completely ruled out in the case of physical immobilization. As a consequence, this approach is typically cost-effective and more rapid compared to other immobilization techniques. However, the biofilms obtained with such an approach are often poorly homogeneous, and the long-term stability of the biolayer needs to be carefully evaluated.

Alternatively, it is possible to stably segregate biorecognition elements onto solid surfaces with covalent immobilization approaches. In this case, the functional groups of the capturing molecules are chemically bound to the complementary functional groups present on a modified surface, as sketched in Figure 22B. The outcome of such approaches usually produces a detecting surface endowed with a high density of biorecognition elements. The desired functional groups on the detecting interfaces are achieved through proper chemical treatments that typically involve polymeric films or self-assembled monolayers (SAMs). Specifically, SAMs encompass a headgroup, for instance thiols, and a tail group, for instance a carboxylic or amine functional group, connected through an alkyl chain, which might hold different lengths. A wide variety of pretreated surfaces, which are commercially available, can be suited for this purpose too.[194] Covalent approaches are frequently engaged in the protein immobilization on detecting surfaces *via* available functional groups of exposed amino acids. Remarkably, covalent binding does not ensure an oriented immobilization, because a protein's anchoring can occur through many residues simultaneously. For instance, lysine residues, being the most widely used anchoring groups, are abundantly present on the exterior of proteins. This results in a multipoint anchoring on the surface, which generates a heterogeneous and nonorientated biofilm. For this purpose, among the most widely employed coupling agents, N-hydroxysuccinimide (NHS) forms stable amide bonds, which are suitable to immobilize the biorecognition element on the modified detecting interface.[171,195] After the surface activation through NHS has taken place, the detecting interface is further exposed to the protein solution, which binds to the chemical SAM through its lysine residues. The accessibility of the terminal carboxylate groups is responsible for the efficiency of the ester intermediate formation. Indeed, acid groups can generate a steric hindrance that might reduce the rate of the activation reaction, with a complete conversion of the available acid groups after several repeated reaction steps. Such an immobilization protocol is more time-consuming and might expose the protein to a harsh environment. However, this immobilization strategy endows the detecting interface with an extremely high surface coverage of densely packed bioreceptors. Therefore, covalent immobilization of biomolecules is among the most pursued approaches in bioelectronic applications. Patel *et al.*[195] proposed for the first time NHS chemistry on a SAM, investigating the impact of the availability of SAM carboxylate groups on the yield of the activation process. In their study, the authors characterized different SAMs holding chain length ranging from 3 to 11 carbon atoms, evaluating the reactivity of the resulting modified surface toward the capturing of the biorecognition elements. For this purpose, the authors investigated 3-mercaptopropionic acid (3-MPA) and 11-mercaptoundecanoic acid (11-MUA) deposited on a gold surface. Moreover, a solution prepared with a 10:1 ratio of shore and long-chain SAMs was characterized. Remarkably, the authors demonstrated that the yield of protein immobilization onto a SAM-modified surface increases using a solution comprising a mixture of SAMs with different channel length because of a lowering of the steric packing. Subsequently, the yield of the immobilization protocol varying the ratio of the mixture of shirt and long-chain SAMs was studied by Lee *et al.*[171] The amount of protein chemically bound to the SAM-modified surface has been studied in the case of mixed 3-MPA and 11-MUA solutions, with a ratio of 20:1, 10:1, and 1:1, as well as the bare long-chain SAM. The mixture encompassing a molar ratio of 10:1 has been proven to guarantee the best results in terms of bioreceptor surface coverage and kinetic parameters. Usually, the biofilm is further exposed to bovine serum albumin (BSA) to minimize the nonspecific binding.[196] Recently, such an immobilization strategy to segregate anti-immunoglobulin G and M on a Au surface has been analyzed by means of different

https://doi.org/10.1021/acs.chemrev.1c00290
Chem. Rev. 2022, 122, 4636−4699

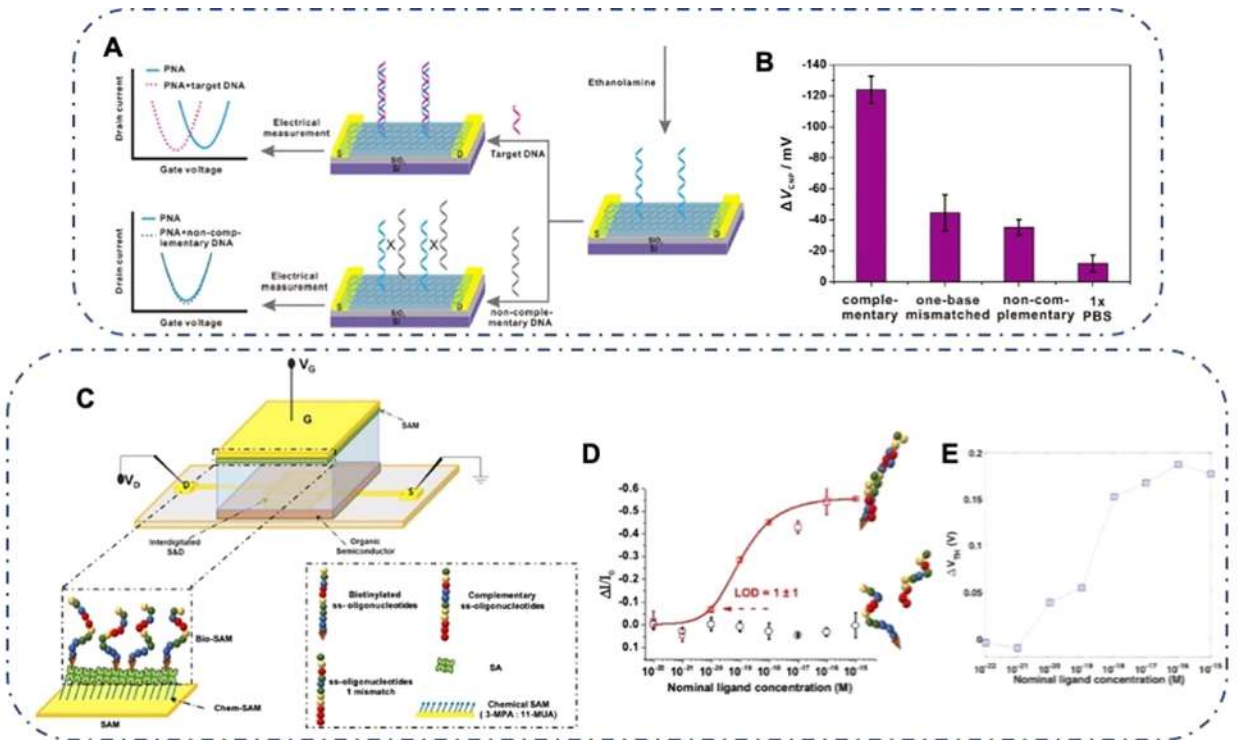

Figure 23. (A) Drawing of the reduced-graphene-oxide FET biosensing platform for ultrasensitive DNA detection. (B) Charge-neutrality point variation of the assay incubated with PBS, 1 nM noncomplementary DNA, 1 nM one-base mismatched DNA, and 1 nM complementary DNA. Reprinted with permission from ref 206. Copyright 2014 American Chemical Society. (C) Pictorial view of the SiMoT platform. (D) Relative I_{DS} current variation vs nominal concentration of the miR-182 PBS standard solutions (red squares). The response registered with the negative control experiment is shown as black circles. (E) Threshold voltage variation ΔV_T vs the miR-182 nominal concentration. Reprinted with permission from ref 29. Copyright 2020 American Chemical Society.

methods, namely, X-ray photoelectron spectroscopy (XPS), atomic force microscopy (AFM), and electrochemical surface plasmon resonance (EC-SPR).[158] XPS analysis enabled proving the high reproducibility of the covalent binding of capturing antibodies. The AFM inspection of the resulting biofilm showed nanostructures holding a thickness coherent with the nominal protein's dimensions. Those data are compatible with SPR characterization too. EC-SPR offers the possibility of monitoring *in situ* electrochemical and optical signals while each functionalization step is performed. It has been possible to evaluate the anti-IgG and anti-IgM density, demonstrating a bioreceptor coating of the sensing slide of 80% and 97%, respectively. This study supports that the covalent immobilization strategy under investigation guarantees a high-throughput and reproducible immobilization of biorecognition elements on the gold surface. Thiol groups play a pivotal role in biomolecule coupling. Indeed, the side-chain of cysteine (Cys) holds thiols as terminal groups, typically engaged in disulfide bonding. Interestingly, the coupling trough thiol groups ensures the stability of the biomolecule structures as well as the bioactivity. Multisite attachment is usually reduced, because −SH groups of proteins are less abundant than amines.[197] Maleimide chemicals can be also employed for coupling to thiols, as they react with −SH groups, resulting in a stable thioether linkage.[198] However, the biofunctionalization protocols encompassing maleimide reagents generally require the presence of organic solutions, because the compounds involved are water insoluble.[199] On the contrary, epoxy chemistry ensures the use of simple yet reliable processing, because it is particularly stable at neutral pH. Epoxy groups are usually formed on the detecting interface by means of glycidoxypropyltrimethoxysilane (GOPS), which are further linked to the capturing bioreceptors' amino groups.[200]

Bioaffinity binding approaches, shown in Figure 22C, have been widely proposed so far to attach biomolecules on a detecting interface with high density. Such techniques are based on the use of a biospecific complex of biologically active compounds.[201] In 1978 Protein A was used to achieve the oriented immobilization of IgG, being the first example of bioaffinity binding.[202] A widespread bioaffinity immobilization has been demonstrated with the biotin−avidin (or streptavidin) couple.[203] Indeed, the biotin/avidin (or streptavidin) complex formation holds an extremely high affinity constant (10^{15} M^{-1}), offering the possibility to stably bind biotinylated molecules on (strept)avidin modified surfaces, or *vice versa*. Clearly, this technique represents a simple yet particularly versatile approach for biorecognition element deposition.[204] Avidin and streptavidin are constituted by four subunits, each one encompassing a binding pocket to bind a biotin molecule. Even though both proteins hold an overall homology of 40%, the use of streptavidin is often suggested, because it reduces nonspecific binding compared to avidin. In fact, avidin, holding an isoelectric point (pI) above 10, might bind nonspecifically negatively charged molecules. On the other hand, streptavidin bears a pI of about 6. Recently, the use of genetically engineered chimeric avidin molecules adsorbed onto the detecting gold interface has been recommended too.[205] Such a strategy offers the advantage of a better yield of the biotinylated biorecognition element immobilization with respect to pristine avidin.

https://doi.org/10.1021/acs.chemrev.1c00290
Chem. Rev. 2022, 122, 4636−4699

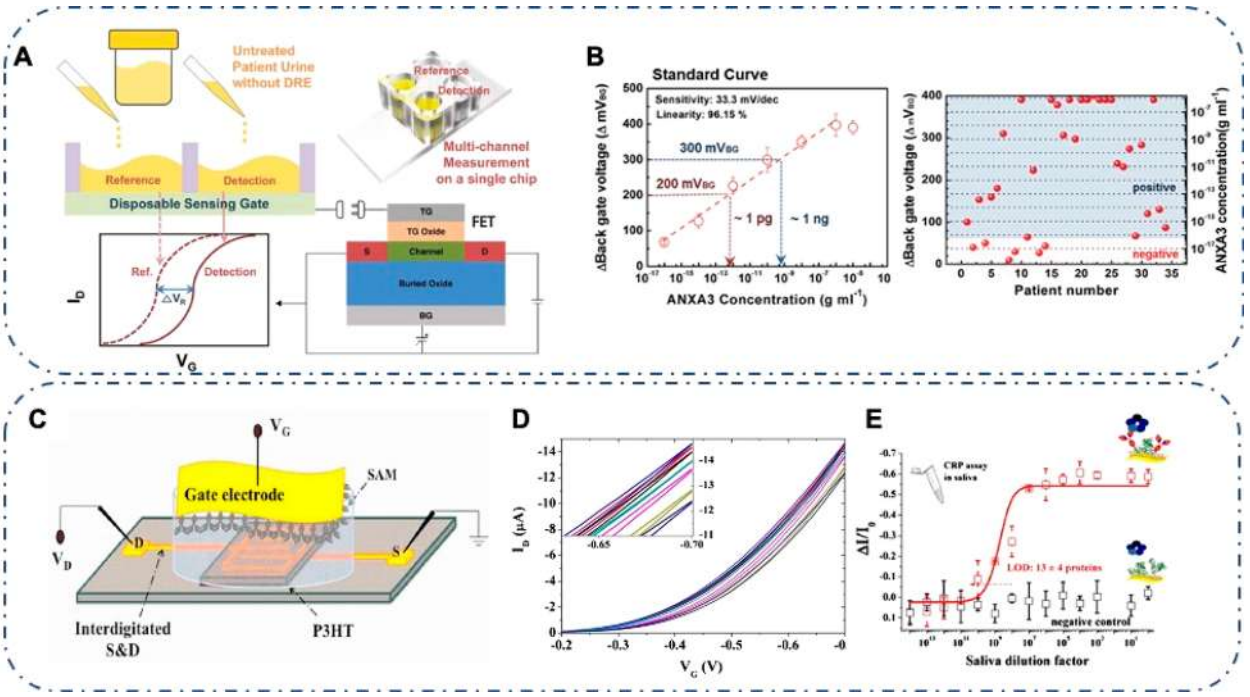

Figure 24. (A) Schematic representation of the double-gate EG-FET measurement steps for ultrasensitive prostate cancer marker detection in urine sample. (B) Dose standard curve in artificial urine spiked with annexin A3 (ANXA3) concentrations (left panel). Results of voltage shift registered with patients' urine samples along with the annexin A3 concentrations resulting from the standard curve (right panel). Reprinted with permission from ref 215. Copyright 2017 John Wiley and Sons. (C) Pictorial image of the SiMoT. (D) SiMoT sensing transfer characteristics. The transfer curve relevant to the anti-CRP incubated in PBS is reported in red. It serves as the baseline. The transfer characteristics registered upon exposure to CRP standard solution at increasing nominal ligand concentrations ranging from 6 zM (black curve) to 6×10^6 zM (dark-green curve) are shown. (E) Dose response curves registered in diluted saliva samples. The CRP/anti-CRP dose curve is reported as red shapes, while the black symbols represent the negative control experiment, registered with the BSA-functionalized gate exposed to CRP. The SiMoT modeling is represented with the red line. Reprinted with permission from ref 27. Copyright 2019 Springer Nature under Creative Commons Attribution 4.0 International License (http://creativecommons.org/licenses/by/4.0/).

4.2. Detecting Protein, DNA/RNA, and Pathogens

The most impressive examples of EG-FET-based biosensors detecting genomic markers, peptides, proteins, as well as pathogens with subfemtomolar LODs are provided in the following section. Indeed, in the past decade, a huge effort has been devoted to the development of the fast, reliable, ultrasensitive, and selective EG-FET biosensors for target biomolecule detection.

As far as genomic marker detection is concerned, a reduced-graphene-oxide-based FET biosensing platform was proposed in 2014, demonstrating the sensing of DNA *via* peptide nucleic acid (PNA)-DNA hybridization.[206] In Figure 23A the reduced-graphene-oxide-FET biosensor and its working principle are schematically depicted. The source and drain gold electrodes of the FET biosensor have been fabricated starting from a SiO_2/Si substrate by means of photolithographic and e-beam evaporation techniques. As a second step, the reduced-graphene-oxide FET biosensor has been fabricated by drop-casting the reduced-graphene-oxide on top of the active region and used as a conducting material.[207] Subsequently, 1-pyrenebutanoic acid succinimidyl ester has been grafted on the reduced-graphene-oxide surface, as the linker. Then, the PNA bioprobe has been deposited *via* covalent immobilization. Ethanolamine chemistry has been further involved to avoid nonspecific binding. Eventually, the device is exposed to the target DNA, allowing the hybridization with probe PNA to occur. The gate electrode is a silver wire used to perform the liquid-gated FET electrical measurements. The hybridization of the complementary DNA with the probe PNA triggers the n-doping of the conducting channel upon the graphene−nucleotide interaction.[208,209] The PNA-DNA hybridization is monitored by registering the change of the charge-neutrality point in the I_{DS} versus V_{ref} curve toward the left side of the graph. The negative control experiment involved the PNA-functionalized reduced-graphene-oxide FET device that was exposed to a noncomplementary DNA sequence, resulting in a zero signal. The baseline has been gathered by exposing the detecting interface to 1× PBS. Figure 23B summarizes the charge-neutrality point variation registered upon exposure of the detecting interface to PBS, non-complementary DNA, one-base mismatched DNA, and complementary DNA in the nanomolar range. Interestingly, the charge-neutrality point shifted toward more negative potentials upon exposing the biosensor from 10 fM to 1 nM of the paired DNA in the range. These data compare well with the graphene sensing mechanism described in section 3.2.3 (*vide supra*), and a LOD of 100 fM has been estimated.

Another interesting example of ultrasensitive detection of a genomic marker was reported by Torsi's group in 2020.[28] The SiMoT principle has been demonstrated to be capable of detecting genomic biomarkers too, with a single-molecule detection limit, integrating as a bioprobe a strand of oligonucleotides complementary to that of the target analyte. The ultrasensitive detection of a strand of a nucleotide sequence matching with a microRNA differentially expressed in multiple sclerosis patients, namely miR-182-5p, has been demonstrated with this assay (Figure 23C). Additionally, a negative control

https://doi.org/10.1021/acs.chemrev.1c00290
Chem. Rev. 2022, 122, 4636−4699

experiment involving a bioprobe with one single mismatch has been designed in order to evaluate the selectivity of the SiMoT platform. The gold gate electrode has been functionalized according to a protocol, well described in section 3.2 (*vide supra*) and schematically depicted in Figure 23C (bottom panel). Such a protocol encompasses a biotinylated single-strand oligonucleotide chemically bound to a mixed chemical SAM of carboxylic-terminated alkanethiols. The blue arrows in Figure 23C (bottom panel) indicates the chemical SAM; all the bioreagents involved are pictorially sketched using the cartoons in the inset on the right. The dose curve registered upon exposure of the sensing gate to increasing concentrations of miR-182 in PBS is reported in Figure 23D, in red, while the continuous trace takes into account the modeling of the experimental dose curve, detailed in section 7.[96] To assess the SiMoT selectivity, the negative control experiment has been registered as well, and the relevant data are presented in Figure 23D in black. It is apparent that the response is negligible, clearly proving the selectivity of the biosensing platform. Remarkably, the authors have also undertaken the reproducibility error evaluation, over three different SiMoT devices, achieving an error of at most 5%. This clearly indicates outstanding interdevice reproducibility. The evaluation of the response curves reported in Figure 23D allowed the demonstration of a LOD of 10 zM. In other words, a detectable signal is registered already when 1 ± 1 target miR-182 is present in the 100 μL sampled solution, with a time to result of a few hours. Relevantly, a physical based model, capable of perfectly reproducing the experimental transfer characteristics, has been proposed to extract the EG-FET threshold voltage V_T, further corroborating the modeling of the dose curves. The threshold voltage variations ΔV_T versus the analyte concentration are reported in Figure 23E, being in full agreement with the dose−response curves shown in Figure 23D.

Particular attention has been paid so far to the ultrasensitive detection of protein biomarkers in clinically relevant biofluids, which still remains an open challenge as previously stated. From this perspective, urine assays represent a particularly interesting case of study because of the extremely easy sample collection practice.[210] It has been demonstrated that urine encompasses a wide variety of markers, for instance, the markers produced by the prostate, bladder, and kidney.[211] Within the urological pathologies, prostate cancer is of the most widespread male cancers in both the United States and Europe.[212,213] In this respect, a biosensing platform capable of detecting prostate cancer markers directly in urine might represent a fast as well as noninvasive diagnostic means. Recently, a clinical study, involving 591 patients, has proposed the annexin A3 protein as a promising marker for prostate cancer, demonstrating a high degree of correlation between annexin A3 level in blood serum and cancer onset.[214] In this regard, Lee *et al.* proposed in 2017 a self-normalized urine assay based on a dual-gate FET ion-responsive device integrating a disposable sensing gate.[215] The proposed biosensor platform successfully detected annexin A3 in untreated patient urine. As shown in Figure 24A, the disposable sensing gate is separated from the transistor portion of the sensor to prevent any contamination from urine samples, resulting in an improvement of the stability of the biosensing platform. Moreover, to minimize the impact of the inhomogeneity of each different urine sample on the device's analytical figures of merit, a detection method which is also self-normalized has been suggested, encompassing the measurement of the reference signals for all inspected solutions (Figure 24A). The self-calibration of the detected response allowed the reliable evaluation of annexin A3, decoupled from the different urine surroundings. To this aim, the FET transfer characteristics have been measured in both the detection and the reference wells incubated with the same urine sample. The reference well does not host any target antibody, gathering the reference signal. Thus, two electrical signals have been registered, namely, (i) a sensing response correlated to antigen−antibody reactions and (ii) a reference level. The reference signal was subtracted from the detection signal, and this voltage difference (or shift) was taken as the sensing response, which is a function of the annexin A3 level, subtracting the spurious oscillation of the reference signal. Indeed, to this aim, a multichamber structure of PDMS is glued on top of a disposable sensing gate, as shown in Figure 24A, allowing the simultaneous measurement of two transfer characteristics (detection and reference) with the very same chip. Before assaying the annexin A3 in real patient urine, a dose−response curve for annexin A3 was registered using the artificial urine spiked with annexin A3 concentrations ranging from 3 aM to 300 nM. The dose−response curve is shown in Figure 24B (left panel). Remarkably, a LOD as low as 30 aM has been achieved. Additionally, a broad dynamic range covering almost 10 orders of magnitude of concentration has been obtained with the proposed device. To detect annexin A3 in real biofluid, 34 patients' urine samples without any pretreatment have been assayed. Figure 24B (right panel) shows the voltage shifts and the annexin A3 concentrations for the 34 patient's urine samples. Analyzing all the assayed urine samples, the authors have achieved a false negative rate of 17.64%, while the true positive rate has been found equal to 82.36%. Another remarkable example of single-protein detection in biologically relevant biofluids has been recently provided by Macchia *et al.*[27] In this paper, the SiMoT sensor has been proposed for C-reactive protein (CRP) detection sampling in 100 μL of human saliva. Among the wide variety of clinically relevant markers detectable in saliva samples, CRP has been one of the widely investigated markers to date. Indeed, it was demonstrated in the 1930s that CRP is an indicator of acute phase infection, produced by the immune-response.[216] It has a 115 kDa molecular weight, encompassing five identical subunits of 20−28 kDa each.[217,218] Although the CRP concentration in blood is currently monitored in clinical diagnosis because it is a well-established marker of systemic inflammation, the article by Macchia *et al.* represents a first study focused on CRP detection in saliva samples. Because of its nonlipophilic structure along with a considerably elevated molecular weight, the passage of CRP from the bloodstream to saliva is extremely limited.[219] Consequently, the main limitation to CRP detection in saliva is represented by the development of an ultrasensitive assay capable of tracking single molecules with high signal-to-noise ratio.[17] Before proceeding with the assay of CRP in human saliva with the SiMoT assay, the biosensing platform was validated by registering the transfer curves upon incubation of the sensing gate in CRP solutions bearing nominal concentrations in the 6 zM to 600 pM range (Figure 24D). Figure 24D shows also an inset with the sensing transfer curves with V_G in the range from −0.6 to −0.7 V, which is used to compute the SiMoT relative current changes. The PBS solution has been employed to mimic physiological conditions.

The stable baseline, shown as a red line in Figure 24D, has been taken using a sensing electrode exposed only to PBS. The red, black, and blue traces, corresponding to the gate incubation in the CRP solution at a nominal concentration of 6 zM and 60

https://doi.org/10.1021/acs.chemrev.1c00290
Chem. Rev. 2022, 122, 4636−4699

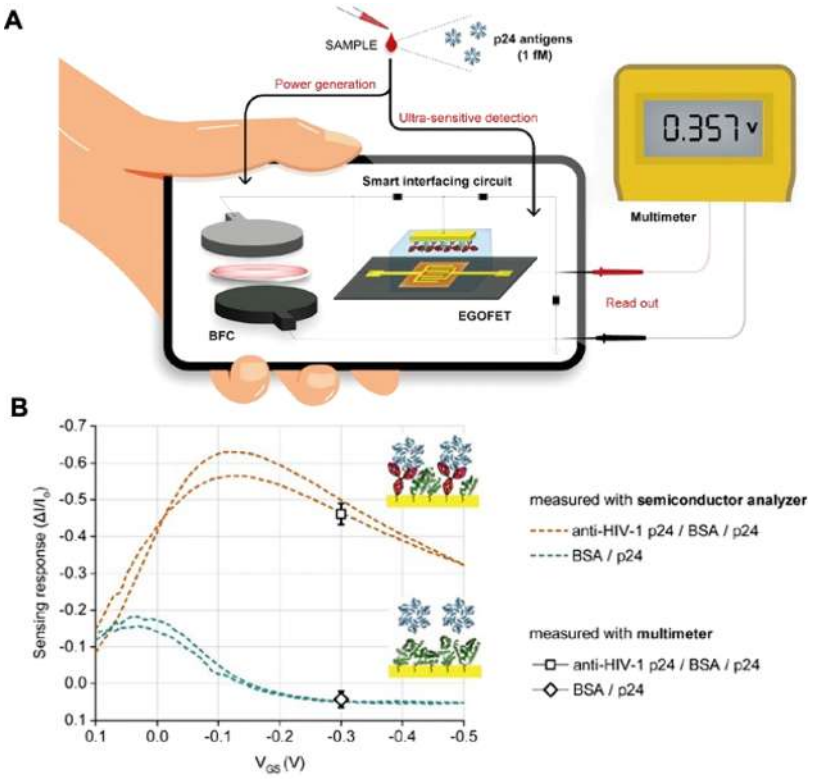

Figure 25. (A) Pictorial view of the self-powered platform encompassing an EG-FET along with the biofuel cell to be perspectively activated by the assayed sample. (B) Comparison between the relative current variation upon exposure to HIV-1 p24 antigen (1 fM) of the EG-FET operated with BFC and the values measured through a semiconductor parameter analyzer. Reprinted with permission from ref 159. Copyright 2020 Elsevier.

zM respectively, are almost overlapped. The transfer characteristics in dark cyan are related to the gate incubation step in CRP at a concentration of 6×10^2 zM. A current decrease compared to the baseline is seen upon increasing the CRP concentration, before the saturation level is reached. Furthermore, endogenous CRP proteins have been detected in diluted saliva samples. The amount of CRP in human saliva has been determined through surface plasmon resonance (SPR), finding a 7 ± 1 nM concentration of endogenous CRP in the inspected sample. According to this restul, the saliva sample was diluted in PBS by of a factor 10^{15} to remove any endogenous content of CRP from the saliva sample. The dose curve in saliva has been evaluated according to the previously described protocol. The dose curves registered are shown in Figure 24E (red shapes). Each point of the dose curves corresponds to the mean value between three replicates. The SiMoT dose curve modeling, encompassing exactly the same parameters calculated for the modeling of the dose curve in PBS, is shown as red full line. The negative control, to prove the high selectivity of the assay, has been designed to encompass the exposure of a bare bovine serum albumin (BSA) gate to the real samples. No significant response was measured. An unprecedented LOD of 13 ± 4 proteins has been evaluated.

Bioelectronic biosensors have been also successfully engaged in ultrasensitive detection of pathogens to date.[19,105,159] For instance, a platform integrating a smart interfacing circuit biased through a biofuel cell with an ultrasensitive bioelectronic sensor has been proposed to selective detect HIV-1 p24 antigen at a concentration level of 1 fM.[159] This represents a quite remarkable case, because the ultrasensitive detection of p24 protein, present on the HIV virus capsid, would be of paramount importance for a timely administration of antiretroviral therapy.[220] Indeed, from 10 to 3000 virions mL^{-1} have been demonstrated to be present in blood serum during the first phase of HIV infection, resulting in a p24 concentration of *ca.* 50 aM to 15 fM.[23] The biosensing platform proposed by Sabaté *et al.* is based on low-cost electronic components and integrates a paper-based glucose biofuel cell (BFC), making the assay completely self-powered (Figure 25A). Specifically, the proof-of-principle low-cost and self-powered assay has been obtained by interfacing a paper-based BFC with an EG-FET sensing device through the readout circuit. The sensing measurements are gathered registering the I_{DS} of EG-FET biased through an anti-HIV-1 p24 (BSA for negative control experiment) biofunctionalized sensing gate upon exposure to a PBS solution comprising a 1 fM concentration of HIV-1 p24. Reliable and stable voltages (and currents) were collected, measuring a detectable variation of the I_D current. Figure 25B shows the comparison between the sensing responses ($\Delta I/I_0$) of the EG-FET operated with BFC applying a fixed gate voltage plotted against the values measured when the device is biased with a benchtop power source, sweeping the gate potential, upon exposure to a 1 fM standard solution of HIV-1 p24 antigen. The experimental points represent the mean values along with the reproducibility errors of measurements gathered with different EG-FETs and BFCs. The $\Delta I/I_0$ relative current changes acquired in standalone operation fully agree with the data gathered using an external power generator (see Figure 25B), clearly demonstrating the reproducibility of the biosensing platform.

A recent study by Kim *et al.* reports on a graphene-based bioelectronic sensor encompassing SARS-CoV-2 spike capturing antibodies (COVID-19 FET sensor) proposed for a SARS-CoV-2 virus identification. The SARS-CoV-2 spike antibody is grafted on top of the graphene film *via* coupling agents (Figure 26A).[105] To assess the performance of the graphene FET sensor

https://doi.org/10.1021/acs.chemrev.1c00290
Chem. Rev. 2022, 122, 4636−4699

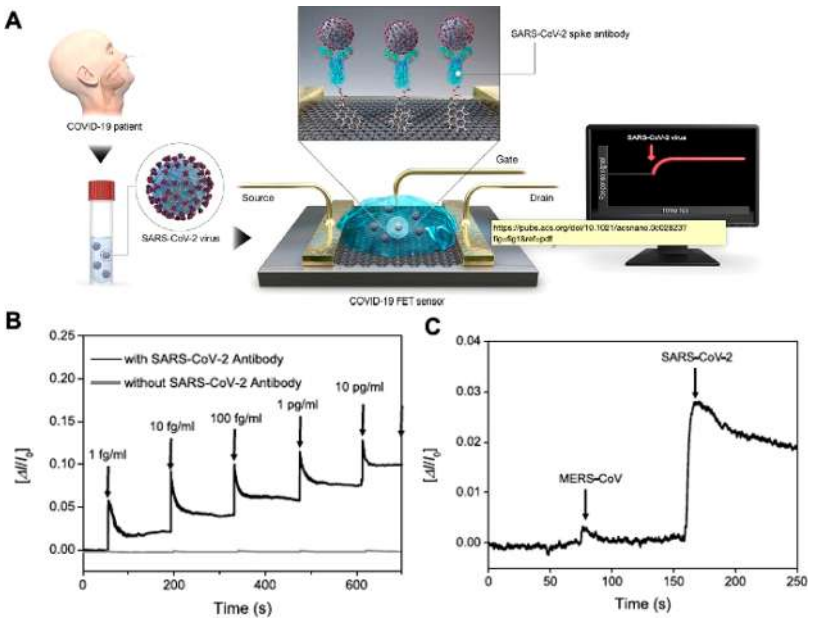

Figure 26. (A) Pictorial view of the graphene FET sensor. (B) Real-time monitoring of the source drain current upon exposure to increasing concentrations of spike S1 protein of SARS-CoV-2. (C) Selectivity of graphene FET sensor toward SARS-CoV-2 spike S1 protein compared to the response registered upon exposure to MERS-CoV spike S1 protein serving as negative control experiment. Reprinted with permission from ref 105. Copyright 2020 American Chemical Society..

against COVID-19, the real-time monitoring of the I_{DS} current upon exposure to the spike protein has been registered and is given in Figure 26B. The sensor biofunctionalized with SARS-CoV-2 capturing antibodies clearly showed a significant response in the aM range, while the sensor bearing a pristine graphene conducting film did not show any significant response after the exposure to COVID-19 patients' samples. Relevantly, the bioelectronic assay has been proven to detect target SARS-CoV-2 antigen protein with a LOD of 15 aM. In addition, the platform has been demonstrated to sense SARS-CoV-2 viral copies sampled with nasopharyngeal swabs from clinical samples. Furthermore, to assess the selectivity of the biosensing platform, the sensor was tested against the antigen protein of MERS-CoV virus, showing a negligible response (Figure 26C). This interesting study clearly proves the application of a graphene-based bioelectronic device, integrating SARS-CoV-2 spike antibody, for the ultrasensitive and selective recognition of a few SARS-CoV-2 viral copies in a clinically relevant environment.

5. CHARACTERIZING ULTRASENSITIVE ELECTRONIC INTERFACES

In this section the most relevant *in situ* spectroscopic characterization approaches to study electronic sensor devices while they operate are reviewed. To this end, two main classes of optical probes have been selected, namely, (i) surface plasmon resonance and (ii) surface-enhanced infrared absorption spectroscopy. These approaches set the groundwork to perform an independent characterization of the bioelectronic sensing devices while the sensing takes place. This will enable in-depth knowledge about not yet unraveled sensing mechanisms in large-area single-molecule bioelectronic sensors, as described in section 6.

Biosensors operating *via* large-area (typically several mm^2) transducing interfaces use a very promising approach attributable to their demonstrated single-molecule detection capability, selectivity, and compactness and the robustness of the electronic transduction. The electrical signal arises from the integrated response triggered by the selective binding events and amplified by complex collective phenomena generated at the biolayer interface. For example, in single-molecule transistor sensors, the drain−source current change is associated with the surface potential change of the biofunctionalized gate surface. However, the detailed chain of collective physical and chemical processes responsible for the huge amplification of the transduction signal, although tentatively explained by theoretical modeling (see section 7), is not supported by independent experimental evidence to date. Consequently, the improvement of reliable *in situ* and *operando* surface characterization techniques is highly desired, to assess the microscopic phenomena controlling the sensing processes and eventually guide the design of biosensors with improved performance suitable for real-world applications.

While many techniques are available for *ex situ* surface characterization, in this review we will mainly focus on *in situ* or *operando* experimental methods capable of highlighting the subtle relationships between the sensing events and the transduction phenomena. Particularly, we will focus on techniques that eventually can provide valuable insights to understand the microscopic mechanisms that starts from the interaction of a single molecule with a millimeter-wide transducing interface and result in an amplified transduced signal. To this end, we have selected two main classes of optical probes: (i) surface plasmon resonance (SPR) and (ii) surface enhanced infrared absorption spectroscopy (SEIRAS).

5.1. Surface Plasmon Resonance

Biosensors based on the shift of surface plasmon resonance (SPR) allow straight monitoring of molecular affinity bindings related to changes of mass density occurring at the sensor surface by a label-free method. The biofunctionalized active interface of the latter is immobilized on a metallic film covering the surface of an optical element.[221,222] The probe is the optical field of surface plasmons which is localized at the active device surface.

https://doi.org/10.1021/acs.chemrev.1c00290
Chem. Rev. 2022, 122, 4636−4699

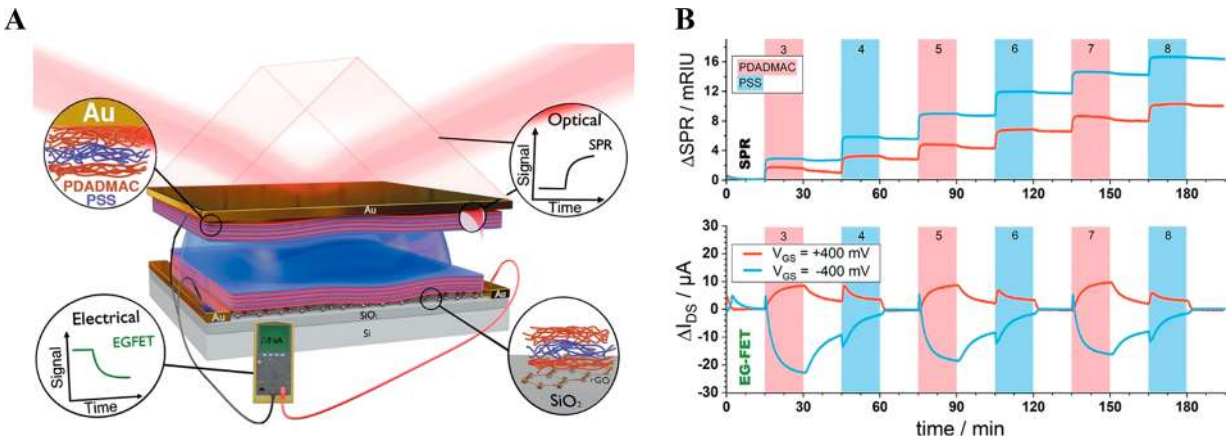

Figure 27. (A) Scheme of the dual SPR/EG-FET setup. The top Au electrode works simultaneously as (i) the SPR active surface and (ii) the gate-electrode for EG-FET transduction. (B) SPR (topmost graph) and EG-FET (bottommost graph) signals recorded *in situ* during the sequential deposition of a periodic structure of PDADMAC and PSS layers. Adapted with permission from ref 223. Copyright 2020 American Chemical Society.

The field variations are measured through changes of the local refractive index induced by the growth of self-assembled biolayers on the sensor surface.

A recent interesting advancement in the field combines optical and electronic readouts, based on SPR and EG-FET, respectively, and allows for the concurrent measurement of both mass and charge variations associated with molecular interactions that manifest as changes of either electronic or optical characteristic signals.[223] The gold layer plays a double function: it works either as the gate contact for EG-FET sensors or the optical interface for devices based on the shift of SPR (see Figure 27A). The measured detuning of the surface plasmon resonance reveals alterations of the biolayer's mass density, while the EG-FET's signal detection, which is related with chemo-electrical interactions, arises from changes of the electric field induced locally by modifications of the charge density distribution on the device surface. A theoretical model describes the relation between the mass change and the change of surface charge density during the growth of polyelectrolyte multilayers.

The efficacy of this hybrid technique is exemplified by the monitoring in real time of the layer-by-layer formation of multilayers of poly(diallyldimethylammonium chloride) (PDADMAC) and negatively charged poly(sodium 4-styrene-sulfonate) (PSS), having an average molecular weight < 100 kDa and < 70 kDa, respectively (see Figure 27B). This approach opens the way to the understanding of multifaceted processes at the solid−liquid interface, *e.g.*, non-Fickian ion diffusion, which cannot be assessed independently by the mentioned tools. In fact, an interesting exemplary outcome, showing the advantage of such a combined investigation approach is that the sole SPR would suggest that the material deposition is completed within approximately 60 s, whereas the results of EG-FET show that the charge diffusion takes a much longer time (15 min). Similar results are obtained by combining SPR and field-effect transistors exploiting reduced graphene oxide.[224]

Given the current interest in deepening the knowledge about basic physical mechanisms controlling optical and particularly electronic biosensors, it is hoped that hybrid approaches like the one described in the present section will lead to deeper insights into the fundamentals of bioaffinity reactions and will guide the development of practical immuno-sensing devices with better performance.

5.2. Surface Enhanced Infrared Absorption Spectroscopy

Vibrational spectroscopies, like infrared (IR) absorption/reflection or Raman scattering provide a wealth of information on the physical and chemical properties of materials and devices and their correlation with the molecular structure at a level comparable and often deeper than any other analytical technique. The measurement of IR or Raman spectra of the biofunctionalized interfaces of bioelectronic sensor devices allows unique identification of the constituent molecules, their relative alignment with respect to the substrate, and their local binding interactions.

Discriminating the detection of signals originating from a few molecular monolayers from the typically overwhelming background is a challenging task. Successful approaches exploit the near-field nature of surface-enhanced spectroscopies, based on either infrared absorption (SEIRAS) or Raman scattering (SERS), in which the signal enhancement occurs at the interface. In both cases the main signal amplification arises from the plasmon resonance of metal islands *via* the so-called electromagnetic enhancement mechanism.[225] When metal islands with sizes of ∼10−30 nm are illuminated by the incident radiation, localized plasmons are excited. The induced dipoles are localized at the island surface and generate a local electromagnetic field orders of magnitudes stronger than the incident one.

Experimental evidence shows that the enhancement factor of SERS is strongly peaked for values of the effective metal film thickness as thin as ∼9 nm, which corresponds to a surface structure close to the percolation threshold and disconnected metal islands.[226] Given that the enhancement rapidly vanishes for smaller and, more importantly, for larger thicknesses, this condition poses severe limitations in using SERS for *operando* monitoring of sensing events while simultaneously running electrical transduction experiments.

Instead, in the case of SEIRAS, substantial enhancement exists for connected metal films with total thickness ≥20 nm that in principle can be used as electrodes in bioelectronic sensor devices.[226]

In fact, the workhorse substrate for SEIRAS includes a metal layer structure schematically depicted in Figure 28.[227] In principle, SEIRAS may operate also *in situ* and *operando*, and therefore, the development of techniques for the simultaneous spectroscopic characterization of biofunctionalized interfaces

https://doi.org/10.1021/acs.chemrev.1c00290
Chem. Rev. 2022, 122, 4636−4699

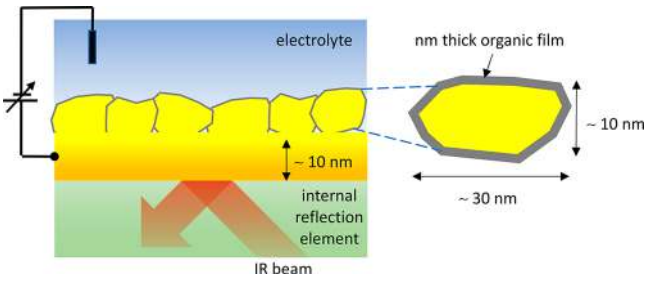

Figure 28. Schematics for simultaneous *in situ* SEIRAS and bioelectronic experiments. The ~20 nm thick nanostructured Au film produces the surface enhancement of the IR signal and can be used also as a working electrode.

associated with a transducer is attracting a great deal of attention. The biofunctionalized interfaces for SEIRAS are similar to those used for SPR. The comparison between SPR and SEIRAS shows that the latter offers the advantage of giving access to either chemical or structural information, obtained from the analysis of vibrational spectra. Hence, SEIRAS allows identifying both the nature of the adsorbed species and their structural modification upon immuno-binding.

In a first report on antibody−antigen interaction studied by SEIRAS, antibodies either for the model system glucose oxidase (anti-GOX) or for the Salmonella pathogen were immobilized on the surface of a 10 nm thick gold film deposited on a silicon wafer.[228] In the SEIRAS spectra the antibody−antigen binding was clearly revealed by the occurrence of additional bands, observable at concentrations of antigens in the range of 10^4−10^6 colonies/ml. While this work has paved the path for the investigation of immuno-assays by SEIRAS, it cannot be fully classified as an *in situ* study because the samples were removed and placed in a solution containing the antigens after recording the IR spectrum of the antibodies.

In situ time-resolved SEIRAS experiments in a solution of affinity binding between antirabbit IgG and rabbit IgG have been demonstrated.[229] The binding process caused the increase of the SEIRAS signals corresponding to the amide regions in the range of concentrations of 0.43−9.33 nM. The experimental SEIRAS configuration relies on the attenuated total reflection (ATR) scheme. This approach has distinctive advantages because it allows the enhancement of the signal-to-noise ratio and simultaneously reduces interference from concurrent signals such as those related with water or nonspecific binding molecules. The spectra and the integrated areas under the amide I and amide II spectral bands are displayed in panels a and b of Figure 29, respectively. A clear relationship between the number of captured antibodies and the integrated spectral areas is found.

An optofluidic SEIRAS platform enabling submonolayer identification of a protein prototype system comprising streptavidin on a biotinylated substrate in nanoliter volumes has been recently reported.[230] Studying the vibrational spectrum *in situ* and in real time allows assessing the kinetics of adsorption processes and receptor−ligand binding. In Figure 30A the cross-sectional scheme of the microfluidic flow cell shows the island-like structure of a gold film on a silicon substrate. The spectra of Figure 30C show the time evolution of characteristic amide I and amide II vibrational bands. Clearly, already after a time lapse of 5 min, the analysis of spectra confirms the presence of streptavidin. Using the spectral area under the amide I band as a quantitative reference for estimating the complete coverage of one monolayer of streptavidin allows estimating a LOD of (0.12 ± 0.01) pmol/cm^2 or (7.1 ± 0.3) ng/cm^2. This level is comparable to that obtained by other label-free techniques such as quartz crystal microbalance or SPR.

Besides the inherent capability of detecting protein monolayers, SEIRAS can be combined with electrochemical methodologies for *in situ* and *operando* investigations. A relevant example is shown in Figure 31, where IR differential spectra of sensory rhodopsin II (SR II) from *Natronomonas pharaonis* protein are shown as a function of the external electrical potential.[231,232] The voltage dependence of the IR spectra shows changes related with structural differences in the light-activated states and allows identifying chemical groups that play a role in protein function and conformational changes of membrane proteins that cannot be revealed by other biophysical techniques with structural sensitivity. The gold film is the working electrode in a three-electrode configuration. Because SR II is not redox active, applying an electrode potential creates a voltage drop across the SR II monolayer and the electrical double layer in a potential configuration similar to the cellular membrane one. Particularly, the intensity change of the C−O stretching bands, centered at 1757 cm^{-1}, is explained by proton movements controlled by the electric dipole direction in the external field.

In conclusion, spectroscopic methods that combine structural and electrostatic sensitivity to biochemical events like SPR and SEIRAS are paving the way to investigate *in situ* and *operando* charge-driven or dipole-driven ultrasensitive electrode interfaces at the heart of state-of-the-art bioelectronic sensors. The expected achievement is a deeper understanding of sensing and signal amplification collective phenomena, which will

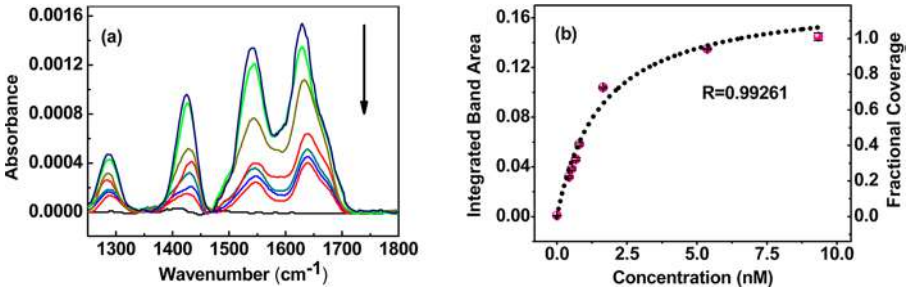

Figure 29. (a) SEIRAS spectra of a gold film bio functionalized with anti-rabbit IgG each recorded 30 min after exposure to increasing concentrations of IgG. The concentrations from bottom to top are 0.00, 0.43, 0.53, 0.67, 0.79, 1.65, 5.37, and 9.33 (nM). (b) Integrated areas of the spectral bands of panel a in the range of 1705−1465 cm^{-1} plotted as a function of the antibody concentration. The dotted curve is the best fit obtained using a Langmuir adsorption isotherm with a dissociation constant K_D = 15.7 nM. Reprinted with permission from ref 229. Copyright 2012 American Chemical Society.

https://doi.org/10.1021/acs.chemrev.1c00290
Chem. Rev. 2022, 122, 4636−4699

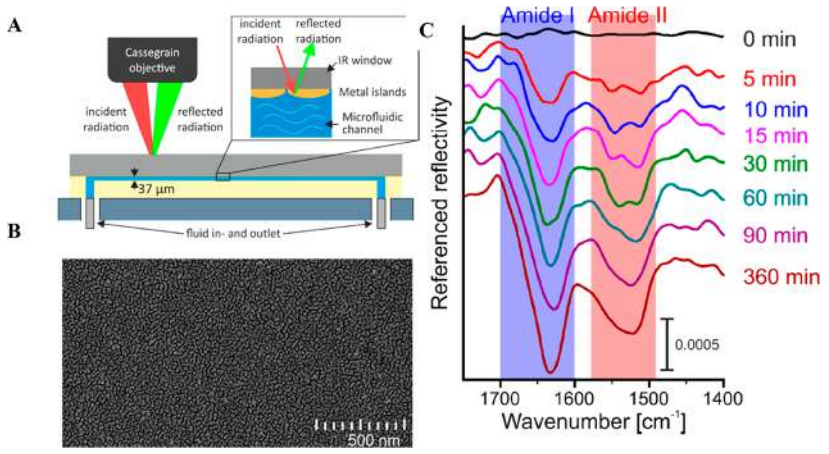

Figure 30. (A) Cross-sectional scheme of the microfluidic cell used for infrared microscopy. (B) Exemplary SEM image showing the island structure of a gold film on a silicon substrate. (C) Time evolution of *in situ* IR spectra showing the streptavidin−biotin binding after SA injection. Adapted with permission from ref 230. Copyright 2018 American Chemical Society.

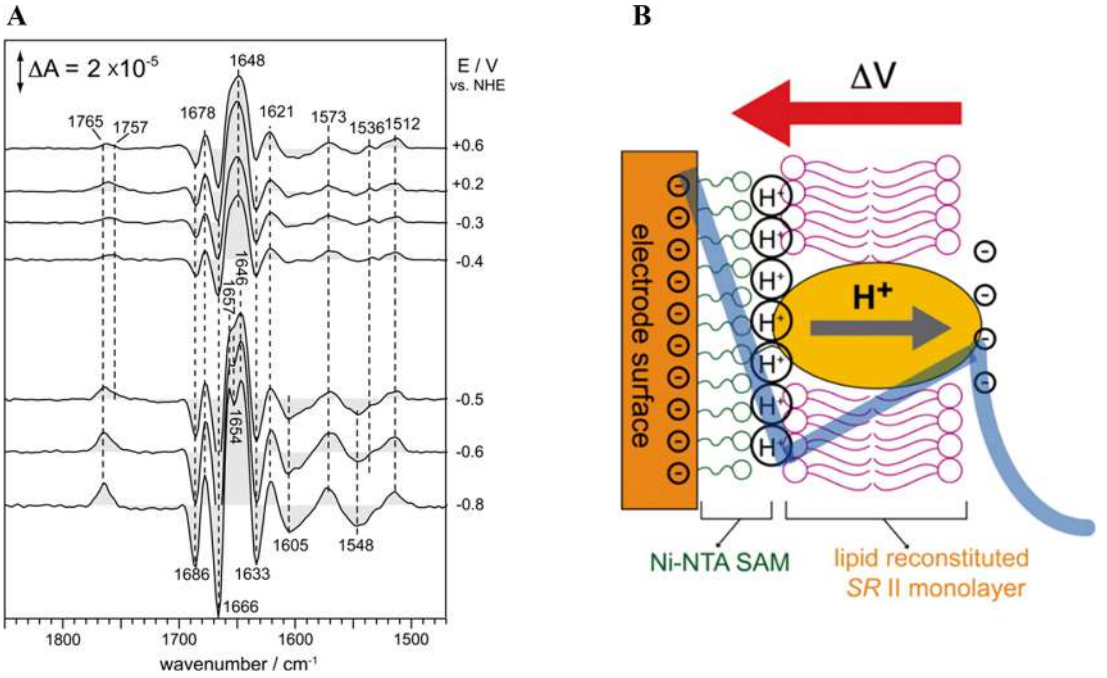

Figure 31. (A) Light-modulated differential SEIRAS spectra of one-monolayer thick rhodopsin II films as a function of an applied electrical voltage with respect to the normal hydrogen electrode (NHE). (B) Schematics of the protein film (1-monolayer-thick) close to the interface between the substrate, the film, and electrochemical double layer. The gray arrow shows the proton translocation following protein excitation by illumination. Reprinted with permission from ref 231. Copyright 2013 Elsevier.

eventually lead to the design of novel devices endowed with suitable characteristics for their widespread practical use.

6. THE ROLE OF THE SIZE OF THE DETECTING INTERFACE IN SINGLE-MOLECULE BIOELECTRONIC DEVICES

In the following an overview of some of the most peculiar aspects characterizing the single-molecule response-related mechanisms in bioelectronic detections involving micrometric and millimetric sensing interfaces are reviewed. A discussion of nanometric transducing interfaces is presented for comparison purposes. In all the examined characteristic structures the sensing mechanism is associated with an electrostatic change provoked by few a events of selective binding involving a target analyte and its affinity capturing molecule attached to a detecting surface. This shifts the electrochemical potential or equivalently the work function of the transducing electronic interface that can be the gate or the FET channel. Eventually, the transistor threshold voltage shifts too. All the devices responded on a very fast time-scale, but while the *large-area* devices can assay at ultralow concentrations (below fM), the nanometric *near-field* devices can detect only at very high concentrations (beyond pM−nM).

6.1. Analyte Brownian Diffusion at Small and Large Detecting Interfaces

As anticipated, a nanometric interface holds the advantage of assuring a high signal-to-noise ratio when it comes to the detection of a single molecule of an analyte. This is indeed a plus for signal transduction, but the effect of mass transport toward

https://doi.org/10.1021/acs.chemrev.1c00290
Chem. Rev. 2022, 122, 4636−4699

nanometric devices and the related low interaction cross section on the overall minimal detectable concentration or LOD is a limiting factor that is at the origin of the so-called *diffusion-barrier effect*. The elicited effect is elucidated in the following. A solution of a given volume comprising a number of molecules equal to $n = 1 \pm 1$ ($\sqrt{n}$ being the Poisson sampling error) in each femtoliter subvolume has a concentration of about 1 nM. Indeed, as already mentioned, a volume of 1 fL was demonstrated to be tiny enough for an enzyme and its substrate to interact in the minute time frame.[10] Hence, we can say that when a marker and a transducing nanometric interface are both confined in the same femtoliter wide volume, the probability for the marker to impinge at the interface in a few minutes is sufficiently high to grant the interaction in a reasonably short time frame. Hence, an often-undertaken approach in single-molecule *near-field* approaches is to assay a solution of the target analyte with a concentration of nanomolar or higher. This assures that a train of single-molecule interactions will take place at the nanometric interface resulting in a telegraph-noise-like signal. To deepen the discussion on this topic it is worth discussing a study that aimed to assess how much the sensitivity depends on the dimensional scale of the device, and hence it, involves sensors of different sizes (micro- to nanoscale) as well as geometries. To this end the study assesses how much the detection of biomolecules in a solution is affected by the elicited parameters and the role of mass transport.[20] Some interesting and relevant findings are summarized in Figure 32A, where a simulation describing the time needed for a target analyte that diffuses in a given volume to eventually impinge on a 200 μm wide semisphere detecting interface is shown. For a semispherical detecting interface, the accumulation function is given by

$$N(\alpha, T) = 2\pi N_A c_0 D\left(\alpha T + 2\alpha^2\sqrt{\frac{t}{\pi D}}\right) \tag{6.1}$$

with N_A being Avogadro's number, c_0 the initial concentration of the analyte in solution, and α the radius of the semisphere detecting surface; D is the diffusion constant taken as 150 μm^2 s^{-1}, typical for many biological species. Equation 6.1 addresses the important issue of estimating the minimum time required for one or more target molecules (in the solution at a given concentration) to impinge at a detecting interface. For the sake of simplicity, it assumes that every target molecule impinging on the detecting interface irreversibly binds to it. Under these circumstances the data in Figure 32A show that for a 200 μm wide interface, a concentration of 1 fM is needed to detect a few molecules in *ca.* 1 min. Equation 6.1 returns also the data plotted in Figure 32B showing the time required to accumulate a given number of binding events when semispherical transducing interfaces holding different liner dimensions are immersed in a given volume of a 1 fM solution. For dimensions below 10 μm, the αT term dominates in eq 6.1, and the accumulation (the irreversible binding) of the analyte at the detecting interface scales with α, the size of the detecting interface. The second term in the parentheses describes, at shorter times, a transient enhancement occurring at sensing interfaces that have a larger area. As is clear for a very small interface 10 nm wide that is immersed into a 1 fM solution, it can take more than a day for the first target molecule to be captured by the sensor and a few weeks to see the accumulation of 10 binding events. Therefore, to detect a single-molecule event with a small nanometric device, the inspected solution needs to have a concentration much

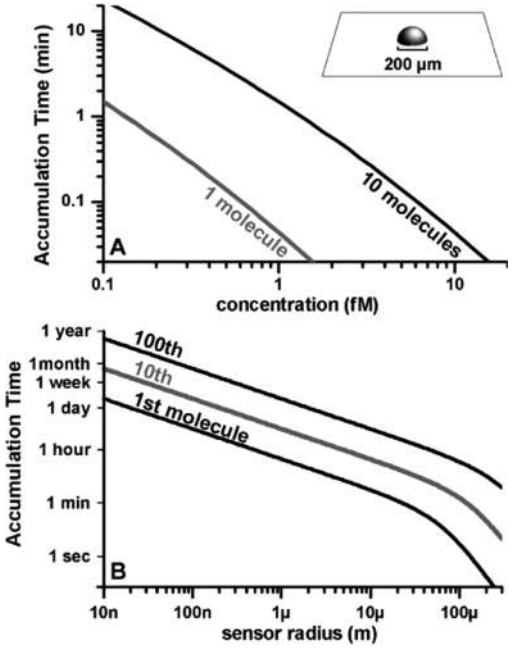

Figure 32. (A) Time needed to collect 1−10 target molecules *via* Brownian motion on a 200 μm wide semisphere detecting interface (see inset) for a diffusion constant of 150 μm^2 s^{-1}. (B) Time required for the same detecting interface to accumulate 1, 10, and 100 molecules when immersed in a one femtomolar solution of the target analyte. Reprinted with permission from ref 20. Copyright 2005 American Chemical Society.

greater than femtomolar. Timing decreases roughly linearly with the sensor dimensions up to about 100 μm, when it decreases much more rapidly. This is generally addressed as the Brownian diffusion-barrier issue plaguing label-free single-molecule detection at nanometric transducing interfaces.

The interesting behavior of the larger detecting interfaces deserves further investigation and is provided in the following section.

6.2. Nano-, Micro-, and Millimetric Bioelectronic Detecting Interfaces

As it is now clear from the systems already reviewed, the detecting interface in an ultrasensitive bioelectronic transducer can have dimensions ranging from nanometers to centimeters. In Figure 33, three examples of device structures belonging to different classes are given. Specifically, in Figure 33A a single-walled carbon nanotube one-dimensional nanoconductor acting as a high-gain field-effect transistor channel is shown. A lysozyme enzyme recognition element is conjugated to the transistor channel. The enzyme is about 7 nm wide, and hence, it is easy to be distinguished from the 1−2 nm thick carbon nanotube, by morphological investigations. It could be hence shown that only one or at most a few enzymes were attached to the transducing interface. The transistor is operated by submerging it in an electrolyte and biased *via* a gating electrode.

The sensing with this structure falls within the *near-field* approaches introduced in section 1.1. This is characterized by two main features: a high signal-to-noise ratio guaranteed by the comparable footprint of the detecting interface and the target analyte; a high interaction cross section assured only when detecting in a highly concentrated analyte (nM at least). The latter is the already introduced diffusion-barrier issue that was discussed in section 6.1. Here, this aspect is recalled highlighting

https://doi.org/10.1021/acs.chemrev.1c00290
Chem. Rev. 2022, 122, 4636−4699

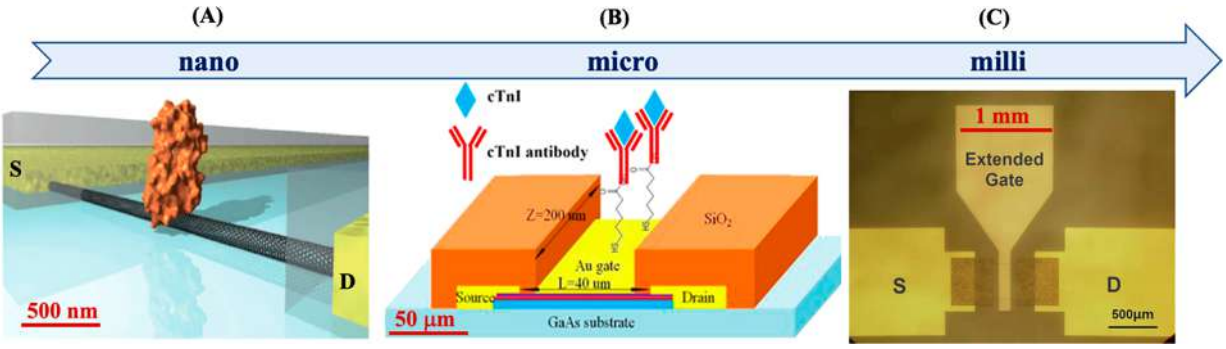

Figure 33. (A) Schematic diagram of a single lysozyme enzyme conjugated *via* a noncovalent strategy involving pyrene linkers to a carbon nanotube. It has been shown that such an immobilization procedure does not affect the enzyme activity. The partial poly(methyl methacrylate) coating of the carbon nanotube is shown in gray. (B) A field effect-transistor based on an AlGaAs/GaAs based heterostructure to detect cardiac troponin I (cTnI) is featured. The heterostructure is covered by gold that is biofunctionalized with anti-cTnI, the capturing antibody for the cardiac troponin I. (C) Structure of a 1 cm wide extended gate connected to a AlGaN/GaN high electron mobility transistor. The gate is biofunctionalized with a prostate-specific antigen PSA capturing antibodies. Panel A is adapted with permission from ref 233. Copyright 2012 American Association for the Advancement of Science. Panel B is adapted with permission from ref 166. Copyright 2020 AIP Publishing under a Creative Commons Attribution (CC BY) license (http://creativecommons.org/licenses/by/4.0/). Panel C is reprinted with permission from ref 169. Copyright 2017 The Royal Society of Chemistry under a Creative Commons Attribution-NonCommercial 3.0 Unported License.

that indeed the analyte, the peptidoglycan substrate of the lysozyme enzyme, is added to the gating electrolyte at a very high concentration of tens of μM. This assures that in each femtoliter of the solution around the lysozyme-based nanotransistor, there is plenty (about a thousand molecules) of analyte (the substrate in this case) ready to interact with the single lysozyme molecule. Under this condition, the source and drain current flowing in the carbon nanotube channel exhibits fluctuations (in fact the already introduced telegraph-noise signal, see section 1.2) that starts a few seconds after the peptidoglycan is added to the gating electrolyte solution. The single enzyme−substrate interaction takes place in a few seconds while the fluctuations develop into a two-level telegraph signal that can be statistically analyzed. The control experiments, performed in the absence of the peptidoglycan substrate or on the bare carbon nanotube transistor, show no response.[233] The analysis of the signals generated by each of the fluctuations associated with the single-lysozyme catalytic activity show that the enzyme undergoes a hinge-like movement of about 10 Å between two domains. The movement is characterized by two rates: a slower oscillation (around 90 Hz) during which the enzyme explicates its catalytic activity and a much faster one (up to 400 Hz) where no activity is present. These kinetic rates, measured thanks to the single-molecule near-field approach, are in line with those measured with single-molecule fluorescence resonance energy transfer measurements on the same system. In all, it is clear that nanometric interfaces although extremely relevant to the study of fundamental aspects of single-molecule interactions such as the two-rate catalytic activity of a single enzyme here reviewed, are however unfeasible to assay a very low-concentration solution of the enzyme's substrate.

In Figure 33B the transducer is a wider field-effect channel (*ca.* 50 μm) that can accommodate a larger number of recognition elements. Here, a high electron mobility transistor serves as a transducing element in a biosensor device for the detection of a biomarker (*e.g.*, cardiac troponin I) that can enable early diagnosis of acute myocardial infarction.[166] Specifically, an AlGaAs/GaAs heterostructure is used as channel and dielectric material. The latter outermost layer was covered by the gate contact that was biofunctionalized with the antibody for the cardiac troponin I. To immobilize the cardiac troponin I antibody, the surface was first functionalized with a self-assembled monolayer of 6-mercaptohexanoic acid, whose carboxylic moieties were activated to conjugate the cardiac troponin I antibody. The sensing mechanism, which is general and holds for many FET-based bioelectronic devices (see section 3 for more examples), involves a threshold voltage (V_T) shift associated with the electrochemical potential and work function change in the gate that in turn affects the charge concentration in the channel according to the following equation:

$$V_T = (\varphi_m - \varphi_s)/q - (Q_{ox} + Q_{ss} + Q_B)/C_0 + 2\varphi_f \quad (6.2)$$

where φ_m and φ_s are the gate metal and the channel semiconductor work functions, respectively; Q_{ox} is the charge accumulated in the dielectric, while Q_B and Q_{ss} are the charges accumulated in the depletion region within the semiconductor and at the dielectric−semiconductor interface respectively; the last term (φ_f) quantifies the doping of the semiconductor. The conjugation of the capturing biomolecules to the gate modifies its work function, and this induces or depletes extra charges in the channel shifting in turn the threshold voltage. The threshold voltage shift ΔV_T is related to the analyte concentration by a logarithmic Nernstian law. At the equilibrium, the following holds:

$$\Delta V_T = Q_A/C_0[B]_{max}\cdot[A]/([A] + K_D) \quad (6.3)$$

here Q_A is the electric charge modification associated with the analyte that is binding to the detecting interface and K_D is the equilibrium dissociation constant of the chemical or biochemical selective interaction. [A] is the concentrations of the species to be quantified (analyte) that is still in the solution at equilibrium, while $[B]_{max}$ assesses the active binding sites' maximum surface density. Thanks to the wider interface, the computed K_D is 270 fM, so the limit of detection, being smaller than this figure, is quite low, while the response time was about 30 s. In general, the FET sensing mechanism is associated with a change of the electrostatics at the detecting interface (the channel or the gate) associated with the binding, which shifts the electrochemical potential or equivalently the Fermi level of the sensing interface. In turn, the transistor threshold voltage shifts as well.

https://doi.org/10.1021/acs.chemrev.1c00290
Chem. Rev. 2022, 122, 4636−4699

In Figure 33C, the detail of the millimeter wide gate of the already introduced EG-AlGaN/GaN high electron mobility transistor sensor (see Figure 19B in section 3.2)[169] is shown. The large transducing interface is biofunctionalized with the PSA capturing antibody; here, a LOD of 4 fM has been estimated, and the device showed a dynamic range of up to 6 orders of magnitude. Moreover, the response even at the lowest concentrations is within one minute. It is a fact that large-area FET detections have been demonstrated to be rather fast in delivering their response. Besides what has already been highlighted, the following can be added: A sensor based on an AlGaN/GaN high electron-mobility transistor was shown to detect in a fast manner proteins such as Human Immunodeficiency Virus-1 Reverse Transcriptase, Carcinoembryonic Antigen, N-terminal pro b-type natriuretic peptide, and C-reactive protein, even in human serum.[234] In this device the gate surface, biofunctionalized with the antibody recognition elements, is 100 mm wide, and the detection of a solution with a concentration in the femtomolar range was completed in five minutes. The SiMoT Electrolyte-gated FETs (EG-FETs)[235] are also very high-performing millimeter-wide sensors[190,87] and they too are very selective thanks to the already mentioned biofunctionalization of the gate interface with a high density (10^{11}–10^{12} /cm^2) of recognition elements.[236,96,25] An EG-FET sensor based on a graphene channel bearing 10^{11} cm^{-2} human olfactory receptors is also proven able to detect the amyl-butyrate odorant marker down to a LOD of 40 aM responding in less than 1 s.[237] Another graphene-based EG-FET was able to detect Anthrax Toxin at a LOD of 12 aM in 200 s.[238] More recently the LOD was reduced to 10–20 zM with the SiMoT technology.[25] This is a single-molecule assay as 100 μL of a 10–20 zM solution encompasses just 1 ± 1 molecules. Also in this case trillions of recognition elements populate the millimeter-wide gate electrode and detections were possible after 10 min.[33] These results, gathered on completely different FET structures by several research groups, show that a single marker (~10 nm wide) in 100 μL (concentration of ~10 zM) can diffuse and eventually impact in the minute time scale on a millimeter-wide surface populated with trillions of recognition elements. The fast diffusion is indeed in compliance with the data discussed in section 6.1 and will be the topic of a dedicated study that is in progress.

As further support for the fact that large-area devices do behave in a comparable way, a systematic study of the dependence of a biosensor response over the dimensions of the FET transducing interface is provided in Figure 34.[239] To this end, an electrolyte-gated transistor CMOS-based technology involving channel areas ranging from 0.3 to 3 μm^2 is evaluated. The channel area is covered with a saturated density of capturing PNA biomolecules, and the transistor gate voltage shift is recorded upon complementary DNA hybridization signal. A noncomplementary strand serves in a negative control experiment. The device responses are given in Figure 34 where it is shown that complementary DNA hybridization returns a mean signal of 29.5 ± 3.7 mV, while for the negative control experiment (nonbinding DNA) a mean signal of −1.5 ± 1.9 mV is recorded. These experimental data are in good agreement with the theoretical investigation discussed in section 6.1 for the larger area devices while they do not reproduce the data on smaller devices. This is most likely because very large concentrations (in the μm range) of analytes are assayed.

Therefore, for *large-area* bioelectronic sensors (micrometer to millimeter wide) the output responses are independent of the actual sensing area and the devices can easily detect at extremely low concentration, reaching the ultimate physical limit. Conversely, the *near-field* approach engaging the nanometric interface are affected by the Brownian diffusion-barrier issues that limit the concentration assayed to be at least in the nanomolar range as will be detailed in the next section.

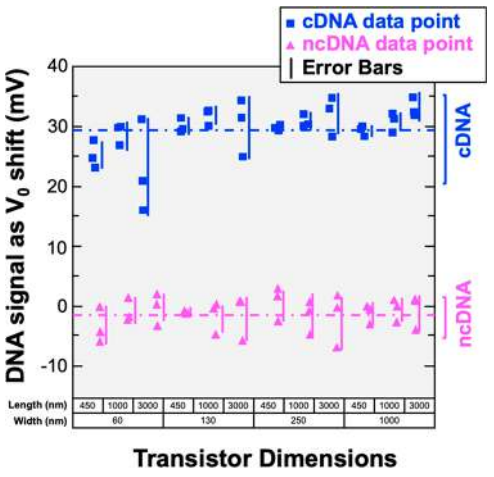

Figure 34. Sensing response as a voltage shift vs the device channel dimensions. No significant transistor dimension dependence on sensing saturated complementary DNA (cDNA) hybridization signal was observed. A negative control experiment involving a noncomplementary DNA (ncDNA) is also provided. Data taken and rearranged from ref 239.

7. AMPLIFIED RESPONSES AT LARGE-AREA TRANSDUCING INTERFACES: FROM CELLS TO BIOELECTRONIC SENSORS

It is an ingrained believe that when a single molecule impinges on a large (about μm^2 or wider) detecting interface it will affect only a negligibly small portion of the surface, and hence, the signal-to-noise ratio will be, in principle, too low to enable any detection. However, some cells can detect/track a single molecule that impinges on their 10^3 μm^2 wide surface; this occurs despite the fact that there is a factor of 10^6 between a single-molecule footprint (assumed to be 1 nm^2) and the surface area of the cell. For example, a rod cell on the retina can sense a single photon,[240] sea urchin sperm cells can track chemo-attractants at the physical limit,[241] while moths can sense a single pheromone.[242] Indeed, amplification stages are in place to make the extremely small signal detectable; those mechanisms are, however, not yet completely deciphered. For the rods sensing a single photon, the amplification seems to be associated with the signaling pathway that involves the G-protein coupling that originates an amplification encompassing the activation of the cyclic nucleotide phosphodiesterase effector enzyme. Already at this stage, ten million G-proteins are produced in a rod of a dark-adapted mouse. The production of such a huge number of G-proteins is, apparently, typical for both photo- and olfactory-receptors, which engage an amplification mechanism involving a cascade of cyclic-nucleotide-dependent systems too.[242] Sperm cells of sea urchins can detect single molecules too, but they do not rely on supramolecular assemblies of receptors cooperating in the detection of the tiny signal, nor do they use enzymatic catalytic amplification processes. Instead, sperm cells tracking the chemoattractants released in seawater by the oocyte seem to exploit the sensitivity of the cyclic nucleotide-gated K$^+$ (CNGK)

https://doi.org/10.1021/acs.chemrev.1c00290
Chem. Rev. 2022, 122, 4636–4699

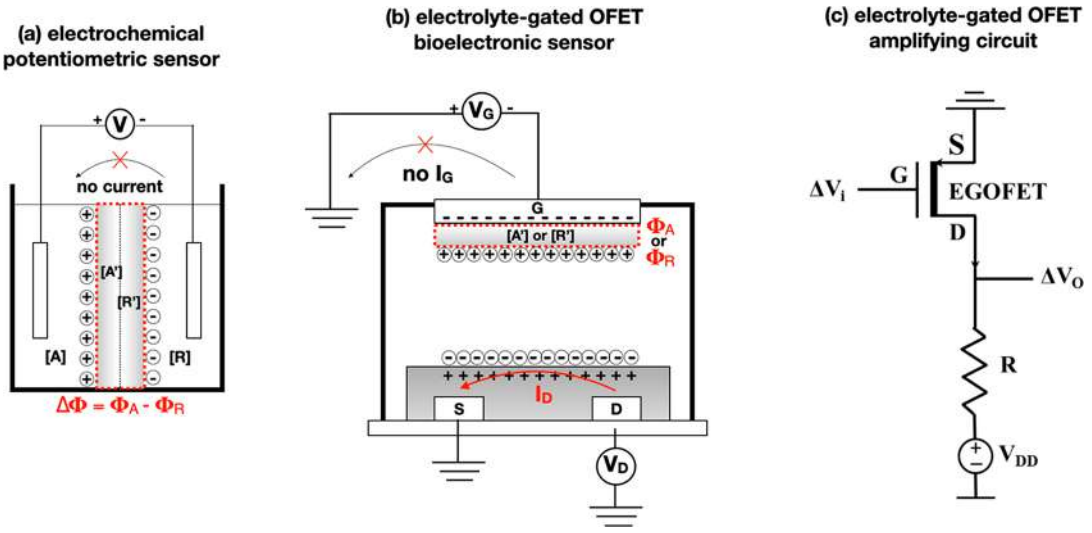

Figure 35. (a) Scheme for a standard potentiometric electrochemical sensor encompassing two electrodes with a perm-selective membrane all immersed into an ionic conducting medium. The semicell on the left comprises the analyte [A]. The semicell on the right contains a reference species [R]. The species to be detected (both the analyte and the reference one) are partitioned, according to the given equilibrium constant, between the electrolyte and the membranes, resulting in a [A′] and [R′] concentrations that are retained by the permselective membrane. (b) A schematic structure of an EG-FET sensing device with the permselective membrane grafted on the gate electrode. The electrolyte couples capacitively the gate to a FET p-type channel. (c) A p-type EG-FET (comprising an organic semiconductor; hence, it is termed EGOFET in the panel) in a very basic voltage amplifier circuit topology encompassing the FET and a loading resistance R. Reprinted with permission from ref 33. Copyright 2020 The Royal Society of Chemistry under a Creative Commons Attribution-NonCommercial 3.0 Unported License.

and CatSper channels to detect cGMP and pH, respectively.[241] The CNGK potassium ion channel is responsible for starting the electrical signal, and the process is activated by the signaling induced, also in this case, by cyclic nucleotides that convey the K^+ ions into the sperm cell flagellum. Such a K^+ influx eventually controls the flagellum's beating, directing the cell sperm toward the egg that released the chemoattractant in the first place.[243] In this case a possible amplification mechanism can be that of the changes in membrane potential that propagate along the flagellum very much like it happens in neuronal axons. The hyperpolarization triggered by the recognition event, which happens to be close to the receptor, is apparently able to propagate along the flagellum in about a millisecond, and hence, it can affect all voltage-dependent molecules, generating an amplification.[241] This mechanism seems very interesting and might provide guidance toward finding an explanation for the extremely high sensitivity of FET-based bioelectronic sensors. Moreover, while for all the mentioned cells (rods, sperm, *etc.*) that can detect at the physical limit, from photons to chemoattractants, the cell trafficking can be quite different, they all share a further peculiar feature: a large number of highly packed receptors (10^4 per μm^2) populate their surface.[244] This is indeed a characteristic that is shared by the biolayers integrated in a number of different FET-based biosensors.

Inspired by these examples that involve the large-area sensing of cells that detect at the physical limit, in the following we propose some examples of systems and mechanisms that can help us to decipher what the amplification effects could be in large-area and ultrasensitive sensors.

7.1. Electronic Amplification Effects in Field-Effect Devices

Generally speaking, a transistor bioelectronic configuration is perceived as being capable of delivering an amplified output *per se*, that is, regardless of the actual configuration and the biochemical event generating the input signal. In fact, for a signal amplification to be in place it is necessary to make sure the bioelectronic device is properly designed. This is a topic that was extensively discussed in some papers,[33,245] and here the main features connected with the amplification effects that are connate with a potentiometric EG-FET are recalled. Specifically, a systematic comparison between the main functional mechanism of an electrochemical potentiometric sensor and that of a homologous electrolyte-gated field-effect transistor is provided. It will be concluded that capacity-coupled EG-FETs working as voltage-amplifying devices can provide an amplification of the sensing output that shows a Nernstian logarithm dependence with the analyte concentration. It also provides a whole control over the quantification of the analyte.

In Figure 35a an essential version of an electrochemical potentiometric sensor comprising two electrodes immersed in an ionic conductive electrolyte is shown. When a bias V is applied, the formation of electrical-charge-double-layers (EDLs) at the electrodes/electrolyte interfaces occurs. As ions are free to drift, here is where most of the potential drops. The permselective ion membrane traps a given amount of the target analyte while enabling an ionic conductivity. This modulates the electrostatic profile, generating an equilibrium zero-current potential shift ($\Delta\Phi$) across the membrane. In this case a membrane with two parts is considered. One is in contact with the solution of the target analyte A (concentration [A]), which is partitioned into the membrane at a concentration [A′] so that at equilibrium, the electrochemical potential is Φ_A. The other side is in contact with a reference species R whose known concentration inside the membrane is [R′], and hence, the electrochemical potential is Φ_R. Eventually, $\Delta\Phi = \Phi_A - \Phi_R$.

For the sake of simplicity, the membrane here addressed is an ion-selective one. However, it can be also composed by capturing antibodies or DNA probes. These species can form stable complexes with their affinity counterparts that are the target analytes to be assayed. A net charge displacement or rearrangement that can sizably change the membrane electrochemical potential can occur also in this case. In a

https://doi.org/10.1021/acs.chemrev.1c00290
Chem. Rev. 2022, 122, 4636−4699

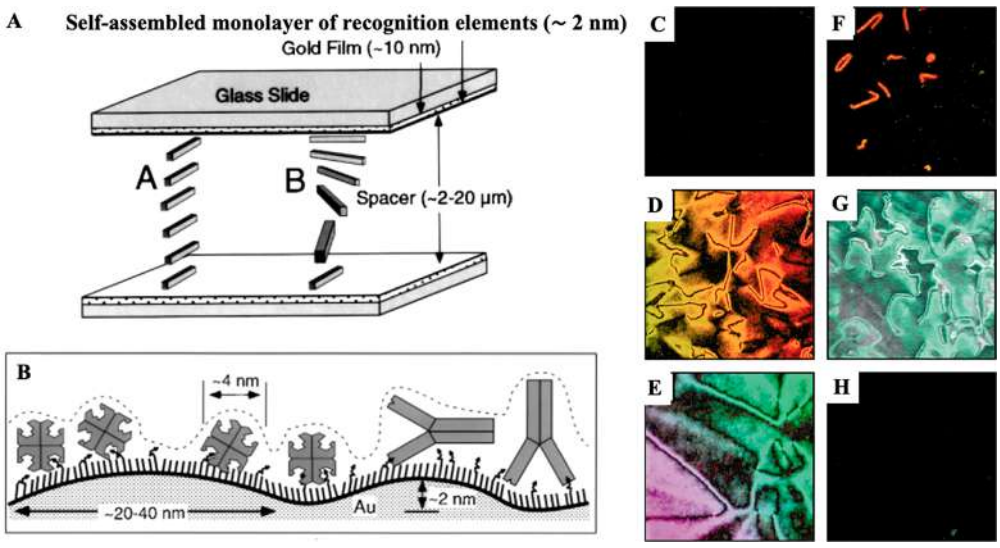

Figure 36. (A) Schematic illustration of a liquid crystal cell comprising two glass slides and a liquid crystal film sandwiched in between. The self-assembled monolayer of the biological recognition elements is covalently attached to a transparent gold layer deposited on the top glass slide. The liquid crystal film is schematically depicted by the mesogens that in the as-deposited film have a preferential orientation (structure addressed as A), whereas they become twisted (structure addressed as B) after the binding of the analyte. (B) Diagram of the change in the surface structure generated by the binding of molecules of avidin (Av) (left) or IgG (right) to their recognition elements grafted on a SAM attached on a transparent gold layer. The structure of the surface after the binding of Av and IgG is highlighted with a dotted line. Panels C through H present examples of how the liquid crystal cells turn from opaque to colored upon selective sensing when inspected under cross polarizers. See the text for details. All images are taken by positioning one of two polarizers parallel to the preferred direction of the mesogens in the films. The dimension of each image is 1.1 mm. Adapted with permission from ref 34. Copyright 1998 The American Association for the Advancement of Science.

potentiometric electrochemical sensor, the electrochemical potential shift $\Delta\Phi$ is measured and related *via* a quantitative equation to the analyte concentration [A] by the Nernst equation:

$$\Delta\Phi = (\Phi_A - \Phi_R) = \frac{k_B T}{e}(\log[A] - \log[R]) = \frac{k_B T}{e}\log[A] - \Phi_R \quad (7.1)$$

T is the temperature, and k_B is the Boltzmann constant; e indicates the elementary charge. Relevantly, the relationship between $\Delta\Phi$ and [A] holds true when $\Delta\Phi$ is measured under the equilibrium condition that neither ionic nor electronic current flows in the cell.

In Figure 35b a EG-FET device encompassing a layer of capturing elements grafted on the surface of the gate electrode (G) is featured. The FET source (S) and drain (D) contacts with a semiconducting layer form the FET channel. The I_D current induced in a FET is evaluated under a V_D bias applied at the D contact versus the grounded S contact, and the mathematical expressions for the saturation current (I_D^{sat}) reads

$$I_D^{sat} = \frac{W}{2L}\mu_{FET}C_{CDL}(V_G - V_T)^2 \quad (V_G - V_T < V_D) \quad (7.2)$$

where μ_{FET} is the FET mobility, C_{EDL} the electrical-charge-double-layer capacitance per unit area, and V_T the FET threshold-voltage; W and L are the FET channel width and length, respectively.

Upon sensing, the gates surface (electrochemical) potentials shift to Φ_A or Φ_R and the $\Delta\Phi$ shift of V_T modulates the I_D current that at fixed V_D and V_G and in the saturation region becomes

$$\Delta I_D^{sat} = \frac{W}{L}\mu_{FET}C_{CDL}[V_G - V_T + \Phi]\Delta\Phi = \beta'\Delta\Phi \quad (V_G - V_T < V_D) \quad (7.3)$$

where Φ is a function of Φ_A that is put equal to $\Phi = (\Phi_A - \Phi_R)/2$. Equation 7.3 shows the ΔI_D shift, which is measured as the sensing occurs. It scales with $\Delta\Phi$, which is the response of a potentiometric electrochemical sensor with the same features (see eq 7.1). The proportionality factor is a β' coefficient that corresponds to the FET transconductance. If we take a typical EG-FET characterized by a W/L of 10^2, a C_{EDL} of 1 μF cm^{-2}, a μ_{FET} of 10^{-2} cm^2 V^{-1} s^{-1}, which is biased at $V_G = V_D = 1$ V, a β' of approximately 1 μS can be computed, which is lower than 1. This occurs because the system is not designed as an amplifier. The point here is that an FET can deliver an amplified voltage signal only when I_D is tuned in an output voltage. To this end, a very simple amplifying circuit is given in Figure 35c. Here the input voltage (V_i) is applied to the G electrode and a load resistance R is connected between the D and the supply voltage V_{DD}. In a p-type FET V_O, taken as the output voltage, is measured at the D electrode. When the detection of the analyte occurs, the circuit input is $\Delta V_i = \Delta\Phi$ that results in a shift ΔV_O equal to $-\Delta I_D \cdot R$ where ΔI_D and hence

$$\Delta V_O = -\frac{W}{L}\mu_{FET}C_{CDL}R[V_i - V_T + \Phi]\Delta\Phi = -\beta' R\Delta\Phi \quad (7.4)$$

The amplification factor is now $a = \beta' R$. For an organic semiconductor-based EG-FET operating at voltages below 1 V, $\Delta\Phi$ is typically few millivolts, giving a ΔI_D of μA. Hence, by choosing R of about 10 MΩ, the maximum voltage amplification can be as high as 10^2–10^3, resulting indeed in an amplification $a = \beta' R$ that can reach a factor of 10^3 for an EG-FET compared to a homologous electrochemical potentiometric sensor.

https://doi.org/10.1021/acs.chemrev.1c00290
Chem. Rev. 2022, 122, 4636–4699

7.2. Amplification of an Affinity Binding by Propagation

The FET electronic amplification described in section 7.1 is relevant, but it cannot account alone for the necessary signal increase enabling the single-molecule detection at a large interface. Moreover, the FET electronic amplification *per se* enhances both the signal and the noise so it does not generally result in a sizable improvement of the LOD. Hence, other mechanisms should be brought necessarily into the play. While we have seen how cells, which are by no means nanometric objects, can sense and track a single molecule, we have also seen that amplification effects are deemed to be in place. When an enzymatic reaction is involved, the catalytic activity works in this direction. When no enzymatic reaction is there, such as in the case of the sperm cell of sea urchins, a mechanism of propagation of the single-molecule binding/tracking information along the flagellum involves voltage-dependent molecules. While experimental results for the amplification effects associated with a biochemical recognition event are not yet consolidated, two examples of propagation of the effect of a biochemical event into properly designated materials are given in the following section. The first one, proposed by the Abbott group,[34] involves mesogens in a liquid crystal, which hold a very low positional order but can align along a preferred direction. The selective binding event, occurring on a surface in contact with the liquid crystal, propagates its effect, inducing the misalignment of millions of mesogens. The second example involves a self-assembled monolayer of antibodies connected *via* a system of hydrogen bonding dipoles.[25] In this case the modeling of the self-assembled monolayer foresees that the selective binding generates a misalignment of the dipoles at the site of the binding, which propagates fueled by the gating field. These two examples could lay the groundwork to explain the extremely high sensitivity in capacitively coupled *large-area* transductions, including the FET-bioelectronics examples discussed in section 3.

7.2.1. Mesogens in Liquid Crystals. An interesting example of wide-area sensing mediated by an amplifying propagation that is triggered by a selective binding is provided by the system proposed by Abbott and co-workers.[34] Here, millimeter wide liquid crystal films are proven capable of amplifying and transducing the binding of a target analyte at a surface functionalized with a receptor, *e.g.*, biotin that binds avidin serving as target proteins. The transducing liquid crystal film is conceived in such a way that the selective binding induces a rearrangement in the liquid crystal film. This occurs *via* the reorientation of millions of mesogens molecules composing the liquid crystal per bound protein. Such an event generates a change in the macroscopic optical transmission properties all throughout the micrometer-thick liquid crystal film that upon binding turns from being opaque to becoming brightly colored. While the Abbott transducing system is not designed to detect a single molecule, it is of interest here because it was proven to involve a 10^6-amplification factor of the effect generated by a single binding event.

In Figure 36 the Abbott cell is described along with the images showing the change in the transmission optical properties of the film. Specifically, in Figure 36A the whole liquid crystal cell is schematically depicted. It was prepared by separating two gold-plated semitransparent glass substrates, separated by a micrometer-wide spacer. The liquid crystal is sandwiched between the two glass slides, and the mesogens composing the film are shown in their aligned (Figure 36A, structure A) and misaligned forms (Figure 36A, structure B). Indeed, liquid crystals are characterized by the optical anisotropy produced by the preferred self-orientations of mesogens in the nematic phase. One of the gold surfaces is modified by covalently attaching the self-assembled monolayer that is detailed in Figure 36B. The 4-cyano-49-pentylbiphenyl (5CB) liquid crystal was inserted in the spacing between the two surfaces. When the film is brought to a completely aligned *nematic* phase (structure A), the optical images (light transmitted through crossed polarizers) obtained by aligning one of the polarizers parallel to the preferred direction within the films is homogeneously black (totally opaque) showing no features. Conversely, structure B reproduces an isotropic misaligned phase, which appears very colorful when seen through two cross polarizers. Figure 36C−H presents the effect of the misalignment induced by the selective binding that propagates through the whole micrometer-wide thickness of the film and along the millimeter-wide surface.

In Figure 36B the self-assembled monolayer (SAM) deposited on a semitransparent gold comprising the recognition elements is shown. The SAM is a "mixed" one comprising biotin-$(CH_2)_2[(CH_2)_2O]2NHCO(CH_2)_{11}SH$ (BiSH) and $CH_3(CH_2)_7SH$ (C_8SH). A 27% of biotinylated species is estimated. Considering that alkanethiol chain packing on gold is about 5×10^{14} chains per cm^{-2},[246] the binding SAM surface is packed with biotin about 100 times more densely than the receptors on a cell surface. In Figure 36C the optical image generated by the light transmitted through the cell comprising a liquid crystal *ca.* 2 μm thick that is brought in its nematic phase is shown. As will be clear from the experiment shown in Figure 36E, the full nematic orientation is induced by the ordered SAM. The biotinylated SAM is attached to the top glass, and the selective binding to avidin has not occurred yet. The image shows the cell as totally and uniformly opaque. The optical image turns evenly bright when the specimen, positioned between the crossed polarizers, is rotated by 45°. In Figure 36D the biotinylated capturing SAM is exposed to a PBS solution of avidin 0.5 μM. After the binding the glass is positioned back on the cell and the anticipated colorful inhomogeneous image can be readily seen. This is explained as follows: the capturing biotinylated SAM surface before the binding holds a high degree of order that is ruined when the specific binding of avidin, occurs. Once the locally disordered surface is brought back in contact with the liquid crystal, it induces a macroscopic change in the orientations of the mesogens in the liquid crystals. The liquid crystal is now not anymore in its nematic form, and remarkably, the mesogen reorientation propagates from the surface of the film (in contact with the capturing SAM) all throughout the micrometer film thickness. In Figure 36E the cell comprises the top glass with the semitransparent gold metallization to which no SAM is attached. As the image shows no clear ordered features, it can be inferred that the liquid crystal does not perfectly self-align in its nematic phase. Hence, the SAM plays a key role in orienting the mesogens in the liquid crystal film. If the SAM is highly ordered, the liquid crystal mesogens are induced to be fully aligned; when the SAM is turned into a disordered system by the affinity binding, the mesogens are misaligned. In Figure 36F, a negative control experiment is proposed. In this case the biotinylated mixed SAM is exposed to a 0.5 μM solution of streptavidin that was previously already blocked with biotin. Because of the lack of available binding sites, such a streptavidin is not able to bind biotin anymore. The cell in this case returns a picture of a film whose mesogens are almost completely aligned. The biotinylated mixed SAM can also be used to graft capturing antibodies

https://doi.org/10.1021/acs.chemrev.1c00290
Chem. Rev. 2022, 122, 4636−4699

such as the anti-Bi-IgG that is a biotin binding species. In Figure 36G the image of the cell with the biotinylated SAMs after immersion for 5 min in 0.5 μM anti-Bi-IgG is shown. Also in this case the selective binding induces disorder. In Figure 36H the SAMs are exposed to a nonbinding antibody for 15 min (0.5 μM anti-FITC-IgG) and the order of the intact SAM is propagated to the film. These pieces of evidence clearly show that only an affinity binding holds the ability to generate a disordered feature that propagates all throughout the film of the liquid crystal. Eventually, the binding of each avidin molecule to the biofunctionalized surface is amplified because of the reorientation of millions of mesogens.

These experiments clearly show that the SAM in contact with the mesogen molecules composing a liquid crystal film can propagate their shifted orientations to regions of the liquid crystal that can be up to 100 μm from the point where the binding occurs. This long-range communication, which is possible because the mesogens are linked *via* a network of electrostatic connections, enables protein/recognition-element affinity binding occurring on a surface to be amplified as the change in the orientation propagates through micrometer-thick films of liquid crystals, changing its optical properties all the way through. Because the mesogens within a liquid crystal hold mobilities that are characteristic of a liquid, the change induced by the binding rapidly (within a few seconds) propagates from the surface, where the recognition element is, into the bulk of the film. Hence, the binding induces a local change that propagates and results in a macroscopic modification in the intensity of light transmitted through the film that can be seen with the naked eye. This approach is also label-free; it is not quantitative, but it can be suitable for on/off type assays (section 2.2) to be used as a very easy-to-operate point-of-care device working in locations remote from central laboratories.

7.2.2. Electrostatic Networks in FET-Sensing Technologies. A number of different FET-based sensors are discussed in sections 3 and 4, and their performance level is summarized in Table 2. These FET sensors are all endowed with a large-area detecting interface, and they all detect a target analyte at a low LOD falling in the concentration range of 10 zeptomolar (zM) to 1 femtomolar (fM) (10^{-20}–10^{-15} M). This means that such devices can detect a minimum number of molecules going from 1 to 10^5 molecules in 100 μL. The detection time is also in the minutes range. Moreover, the large-area FET interfaces are generally covered by receptors that are packed to the physical limit taken as 10^4 per μm^2. For example, in the case of the SiMoT technology, as many as 10^{12} recognition elements per cm^2 are in place. This means that even at a LOD of 1 fM and assuming that all 10^5 target molecules reach the detecting surface and bind to a receptor, there is a binding event involving one recognition element for every ten million (10^7) populating the detecting interface. The resulting FET signal-to-noise-ratio should be negligibly small. The FET transduction is often invoked as the only amplification effect enabling a sufficiently high response. This assumption does not withstand, however, a couple of arguments given in the following. The FET amplification factor, estimated in section 7.1 to be 10^3 for a typical large-are EG-FET, is indeed too small to account for the huge amplification needed. This is of the order of 10^7 for the assay of a 1 fM solution, but it becomes 10^{12} in the case of single-molecule detection. Even a device with a transconductance larger than that of an EG-FET, such as an electrochemical transistor,[37] does not provide alone enough amplification to enable reaching the detection of a single molecule.[31] The second argument involves the LOD definition, recalled in eq 2.4, that is evaluated as the blank average signal plus three times its standard deviation. In the most compelling experiments (see for instance Figures 12H, 13C, 17D, and 21A), the blank is taken as the signal coming from the negative control experiment. An FET transduction amplifies both the signal coming from the selective binding and the signal measured in the blank experiment. Therefore, the FET amplification factor applies to both the signal and the blank in the same way and does not, in principle, improve the signal-to-noise ratio; hence, it does not necessarily improve the LOD. From such a critical review of the data published to date in bioelectronic FET ultrasensitive detections, it can be safely stated that the search for a proof of the presence of amplification effects beyond the FET-transducing one should be actively pursued for bioelectronic FET capacitive coupled sensors in general. To this end, a possible explanation has been proposed for the SiMoT technology, but it is not limited to this technology. It involves collaborative electrostatic interaction that, at this stage, has been proven only with data modeling. Independent experimental investigations of cooperative electrostatic effects that take place in the layer of biological recognition elements are in progress, and among the possible approaches, the most promising ones are discussed in section 5.

The modeling of the SiMoT sensing data has been designed starting from the observation that cells can detect at the physical limit. The cell-trafficking processes that amplify the very small signal coming from the single biochemical recognition event occurring on their surface play a role for sure. However, it was intriguing to observe that the cells' surface was populated by a density of recognition elements as high as $10^4/\mu m^2$. This is considered among the highest possible packing for proteins attached at a surface.[244] The biofunctionalization methods discussed in section 4 often result in a very high density of recognition elements that are covalently attached to a detecting surface. In the case of the SiMoT technology, up to 10^{12} antibodies per cm^2 were attached to the gate.[158] Similarly, the density of odorant receptors attached on the graphene channel for the FET detection of odorant molecules was on the order of $10^{11}/cm^2$.[175] This is indeed equivalent to a density of $10^4/\mu m^2$, and so it can be stated that the receptors attached to the detecting interface of an ultrasensitive FET are packed at a density similar to that found on the surface of cells detecting at the physical limit. Therefore, we assumed that the conformational change induced by the biochemical binding provokes a change in the electrostatics of the capturing antibody and the overall dipole associated with it changes its orientation or equivalently becomes misaligned. We further assumed that such a localized change affects the neighboring antibodies, because of the extremely high proximity of the recognition elements on the surface, *via* a collaborative electrostatic network that was identified in the hydrogen bonds that connect the antibodies immobilized on the surface. In fact, in the specific case of the SiMoT, the antibodies are attached to a mixed self-assembled monolayer that is itself endowed with a hydrogen bonding network. This network propagates the electrostatic local change involving a huge number of recognition elements, and this affects the overall dipole moment on the gate surface. It is not ruled out at this stage that other collaborative electrostatic networks could be in place instead. The rationale for this model is general enough to encompass this possibility as well. In the following, the details of the model that was developed to decipher a plausible amplification mechanism is reviewed.[26]

For the sake of clarity, the main features of the SiMoT capturing layer are recalled in Figure 37. Here the mixed

https://doi.org/10.1021/acs.chemrev.1c00290
Chem. Rev. 2022, 122, 4636–4699

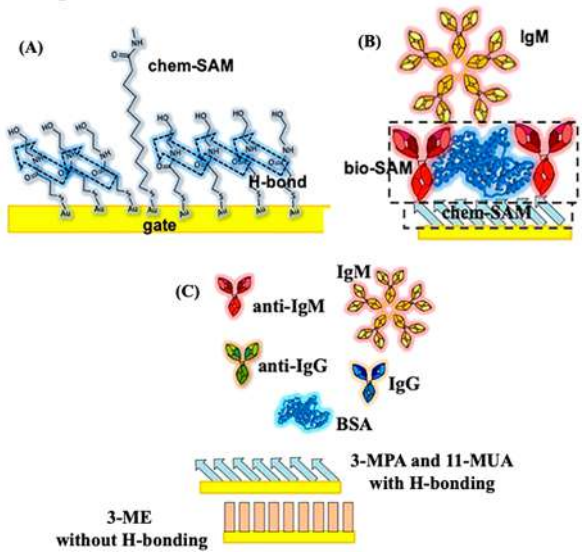

Figure 37. (a) Structure of the mixed self-assembled monolayer termed chem-SAM grafted on the SiMoT sensor gate that comprises a 3-mercaptopropionic acid (3-MPA) and 11-mercaptoundecanoic acid (11-MUA) (see section 4.1 for details). The H-bonds that electrostatically connect two chains are indicated with blue arrows. (b) View of gate covered with anti-IgM encompassing both the chem-SAM (depicted with just the blue arrows) and the bio-SAM. (c) Legend of the symbols that are used in this figure and in Figure 38 to depict the proteins used, as well as the chem-SAM bearing and not bearing an H-bond network. Adapted with permission from ref 26. Copyright 2019 American Chemical Society.

chemical SAM (chem-SAM), composed of both the 3-mercaptopropionic acid (3-MPA) and 11-mercaptoundecanoic acid (11-MUA) (10:1) whose terminal carbocyclic groups are activated with EDC sulfo-NHS and deactivated in ethanolamine, is sketched (Figure 37A). These lead to the formation of amide groups that interact *via* H-bonding that form a network. The capturing antibodies (anti-IgM in this picture) are grafted on the forming chem-SAM. Bovine serum albumin (BSA) is added afterward to minimize nonspecific binding. Anti-IgM and BSA proteins form what we term the bio-SAM that can selectively bind IgM (Figure 37B). It was proven that the strategy leads to trillions of capturing antibodies immobilized on the mixed chem-SAM most likely attached to the longer and more flexible 11-MUA.[26] In Figure 37C the sketches featuring the molecules and systems used also in Figure 38 and discussed in this section are given.

With the intent of separating the contribution to the ultrasensitive detection that is determined by the presence of the chem-SAM from that ascribable to the sole of bio-SAM, SiMoT sensing was performed with a gate encompassing a physisorbed layer of capturing molecules; that is, only the bio-SAM is present on the electrode. Specifically in this case the bio-SAM is composed of the anti-IgG capturing proteins. The sensing data involving the IgG/anti-IgG system are given in Figure 38A as red squares. As usual the error bars are the standard deviations over three replicates. Considering the noise of a negative control experiment similar to the one presented in Figure 17D, a LOD of 30 aM can be computed, which is about 10^3 molecules in 100 μL.

This LOD has being achieved also by other bioelectronic large-area devices as extensively discussed in sections 3 and 4. While this is not single-molecule detection, it is anyhow an extremely low LOD that cannot be justified by the FET amplification. Hence, it is a fact that even in physisorbed capturing protein amplification effects are in place, likely enabled by collaborative effects that are connected with electrostatic-active networks entangling the packed proteins of the biolayer. However, in this configuration a signal is measured that is 3 orders of magnitude gretaer than the LOD measured when the chem-SAM is in place.[25] Such an experiment proves that the chem-SAM seems to be essential to reaching single-molecule sensing. It also shows that the bio-SAM alone can enable very sensitive and reliable detections as well.

To determine which part of the mixed chem-SAM is really critical to achieve single-molecule sensitivity, we designed a chem-SAM in which no network of H-bonds is present. To tailor such a system the 3-MPA is replaced by 2-mercaptoethanol (2-ME). Indeed, the chem-SAM composed of a 10:1 ratio of 2-ME and 11-MUA, respectively, has no carboxylic groups on the shorter and more abundant chains. At the same time the

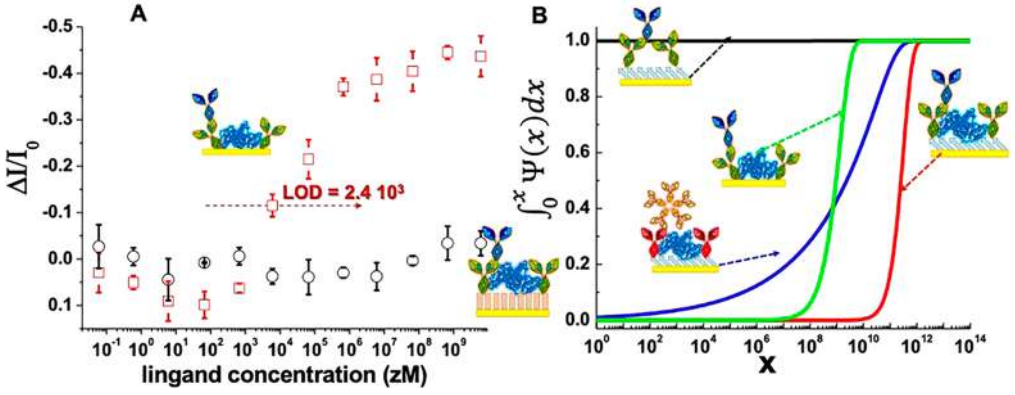

Figure 38. (A) Binding calibration curve of IgG/anti-IgG (red hollow squares) is given as the fractional decrease of I_D vs IgG concentration. The anti-IgG capturing layer is physisorbed directly on the gate surface, and BSA was added to minimize nonspecific binding. The black circles are the data measured on the SAM comprising 2-ME and 11-MUA. (B) The $\int_0^x \Psi(x)\,dx$ function vs x (binding sites in a given domain) for different capturing layer systems: red curve, mixed 3-MPA and 11-MUA chem-SAM plus anti-IgG and BSA bio-SAM to sense IgG; green curve, no chem-SAM only anti-IgG and BSA bio-SAM to sense IgG; blue curve, mixed 3-MPA and 11-MUA chem-SAM plus an anti-IgM and BSA bio-SAM sensing IgM; black curve, mixed 3-MPA and 11-MUA chem-SAM plus a sole anti-IgG bio-SAM sensing IgG. Reprinted with permission from ref 26. Copyright 2019 American Chemical Society.

https://doi.org/10.1021/acs.chemrev.1c00290
Chem. Rev. 2022, 122, 4636−4699

capturing antibodies can still be grafted on the gate surface by means of the activated 11-MUA. It was independently shown that also on this 2-ME-based mixed chem-SAM, trillions of capturing antibodies per cm^2 are grafted. As expected, because of the lack of carboxylic groups on the shorter and more abundant chains, no amide-based H-bond network is present. Figure 38A shows as black circles the detection performed with the gate bearing the 2-ME and 11-MUA mixed chem-SAM plus the bio-SAM comprising trillions of anti-IgG. It is apparent no sensing at all is seen, showing the important role of the H-bonding network for the SiMoT detection. Indeed, the hydrogen bonding network does play a critical role in the sensing, mostly when associated with the chem-SAM, but it is also worth mentioning that also the biomolecules of the bio-SAM are connected *via* a similar network. The latter can justify why even the physisorbed layer gives rather low LODs.

The first seminal works on the SiMoT technology[25,26] recognized the key relevant role of the electrostatically active H-bond network. The proposed amplification mechanism involves the presence of "domains" into which the sensing gate surface is divided. It is foreseen that for each domain the following holds: when an antigen (which is the marker analyte to be detected) interacts and binds to any one of the capturing sites (antibodies) residing in a specific domain, the whole domain switches its surface potential or equivalently its work function. This is because of the cooperative interactions entangling the capturing antibodies populating the domain, so when one of them undergoes an electrostatic conformational change the others are affected as well thanks to a propagation of the local electrostatic change. The dipoles on the SiMoT gate are likely not to be ordered as soon as the capturing layer is deposited. However, the gate field applied during the stabilization and measurement of the baseline and of the sensing curves can orient the dipoles that can gain, at this point, some degree of order. The switching of the electrostatic state of the whole domain after the propagation of the effect is also postulated to be irreversible. Hence, if any other binding occurs, within a given domain, no further shift of the work function can take place.

This rationale was turned into a mathematical model described in the following. Because the gate electrode surface is covered by a very large number of capturing proteins such as anti-IgG or anti-IgM indicated as n, the chance of finding an affinity ligand or antigen (IgM or IgG) interacting and eventually binding to a given capturing antibody, p, is very low because the number of ligands N we have that $N{\cdot}p = N/n \ll \sqrt{n}$. Hence, a number k of affinity ligands has the probability to interact with any binding sites, which is given by the Poisson distribution:

$$P_k = \frac{\lambda^k e^{-\lambda}}{k!} \tag{7.5}$$

by the same token, one of the trillion binding sites on the surface does not interact with any ligand ($k = 0$) with a probability given by

$$P_0 = e^{-r\lambda} \tag{7.6}$$

At this point let us consider that in a given domain an x number of binding sites is present. The binding probability of each one of the k affinity ligands, to either one of the x capturing sites of a selected domain, can be reasonably assumed to be mutually independent. Under these circumstances, the probability $f_0(x, \lambda)$ that any of the k ligands interacts with none of the binding sites we labeled as x is computed as the product of the probabilities that every binding site remains vacant, resulting in $f_0(x, \lambda) = \prod_1^x P_0 = P_0^x = e^{-\lambda x}$. The heterogeneity of the biofunctionalization process leads to a situation in which not all the domains comprise the same number of ligands, meaning that the domains have different sizes. The $\Psi(x)$ function (or cumulative distribution) is introduced to describe the probability that a domain is characterized by x binding sites. Therefore, the overall probability of finding a domain of binding sites that has not bound with any of the N affinity ligands present in the volume V to be assayed is given by

$$f_0(\lambda) = \int_1^n \Psi(x) f_0(x, \lambda)\mathrm{d}x = \int_1^n \Psi(x) e^{-\lambda x}\mathrm{d}x \approx \int_0^\infty \Psi(x) e^{-\lambda x}\mathrm{d}x \tag{7.7}$$

where $n = 10^{12}$ is the upper limit of integration, which is reasonably approximated to infinity and the lower one is zero. Relevantly, the $\Psi(x)$ distribution, which is unknown, is taken arbitrarily as a unimodal Γ-distribution and reads

$$\Psi(x) = \frac{x^{b-1}}{K^b} \frac{\exp\left(-\frac{x}{K}\right)}{\Gamma(b)} \tag{7.8}$$

with b being the characteristic shape and K the scale parameter correlated to the Γ-function $\Gamma(b)$ (see ref 26 for details). Equations 7.7 and 7.8 form the basis to model the $\Delta I/I_0$ SiMoT dose curves such as the one given in Figure 38A; as detailed in ref 26, the expression for the SiMoT response is hence

$$\frac{\Delta I}{I_0} = A_{sat}\left(1 - \left(1 + \frac{\sigma^2}{\overline{x}} \cdot \frac{c{\cdot}V{\cdot}N_A}{n}\right)^{-\left(\frac{\overline{x}}{\sigma}\right)^2}\right) \tag{7.9}$$

where A_{sat} is the $\Delta I/I_0$ experimental saturation level, c the analyte concentration in M, V the assayed volume, and N_A Avogadro's number; $\overline{x} = Kb$, and the variance is $\sigma^2 = bK^2$.

The interpolation of the actual sensing data (such as those given in Figure 38A) with eq 7.9 allows gathering information on the unknown distribution of the domains' size (number of x binding sites contained in each domain) on a given sensing gate. To this end, the $\int_0^x \Psi(x)\mathrm{d}x$ probability that less than x binding sites populate a domain is shown in Figure 38B as a function of x. As anticipated, the curves are built as a result of the modeling of several SiMoT dose curves with eq 7.9 that results in the relevant $\overline{x}$ and σ values. Specifically, the following dose curves, whose data are available in ref 26, have been modeled. The blue curve in Figure 37B is relevant to the IgM analyte assayed with an anti-IgM/BSA bio-SAM grafted on a 3-MPA/11-MUA chem-SAM; the red curve is relevant to the IgG protein assayed onto an anti-IgG/BSA bio-SAM also conjugated to a 3-MPA/11-MUA chem-SAM. The black curve is the IgG detected at an anti-IgG bio-SAM not comprising BSA conjugated to a 3-MPA/11-MUA chem-SAM. Last but not least, the green curve concerns the modeling with eq 7.9 of the dose curve of IgG selectively detected by an anti-IgG bio-SAM that is directly physisorbed on gold. The probability, $\int_0^x \Psi(x)\mathrm{d}x$, for the IgG sensing to occur with the anti-IgG attached as the bio-SAM (including BSA, red curve) shows an extremely high probability to find mono-dispersed giant domains comprising trillions of anti-IgG capturing sites. On the other hand, when no BSA is deposited (black curve) the domains that are found in the SAM are very much dispersed in size, so you can find also some that are

https://doi.org/10.1021/acs.chemrev.1c00290
Chem. Rev. 2022, 122, 4636−4699

constituted by only one single binding site. However, some large domains are there as well, and this explains why the LOD is low, but it is not good enough to ensure single-molecule detection. The idea is that it is probably very likely that the BSA occupies defect sites that make the SAM more compact and enhances the chances of propagating of the domino-type effect over large but not huge domains. Moreover, it also appears that if BSA is added over the actually capturing protein, the degree of electrostatic connection is improved. Interesting is the case of the physisorbed bio-SAM (green curve) as the resulting domains comprise less than 10^{10} antibodies; hence, they are quite small, and the amplification is less prominent. The case of the sensing of IgM with an anti-IgM SAM shows peculiar features when compared to a homologous IgG sensing. The selective IgM sensing results in a rather broad distribution of domain size (blue curve). Analogous to IgG sensing on anti-IgG, there is still a high chance of finding large domains (half a trillion anti-IgMs), but there is also a rather high chance of finding much smaller domains. This suggests that the anti-IgM and the anti-IgG SAMs are characterized by a very different number of defects and/or electrostatic coupling. It can be concluded on this part that the selective binding induces a work function to shift that involves the whole domain. The presence of defects can act as a discontinuity boundary that generates a disordered interdomain region that can stop the propagation and limit the size of the domain itself and hence the final level of amplification that can be reached. Because the degree of order is gate-dependent, also the level of amplification will be so. The idea here is that if the layer of biological recognition elements is highly compact and defect-free, the domain that is formed after the selective interaction with one antigen will be large and the sensing response will be high.

This mechanism was very well modeled by molecular dynamic simulations performed on an ensemble composed of almost 6500 chains to mimic the chem-SAM structure.[26] An overall area of over 10^3 nm^2 was hence covered by the modeled system, and the affinity binding is simulated by imposing a disordered conformation (H-bonds are irreversibly lost) to an about 5 nm^2 region that is a millesimal part of the total simulated area. The model is able to correctly predict that, under the applied gate field, the whole simulated area is affected by the disorder imposed. Hence, a very long-range propagation of the effect generated by a single binding event can occur. This indeed resembles very much the case of the Abbott[34] experiment previously discussed. The model further foresees that if the binding occurs while no gating field is present, the angle θ formed by the overall dipole on the electrode with the normal to the surface does not shift. Conversely, when the field is applied after the binding and the stabilization of the FET current is achieved, a θ decrease of more than 15% is observed. This proves, from one side, that the gating field is needed to trigger the collective electrostatic interactions enabling the propagation of the shift and hence of the amplification that leads to a reliable assessment of a single-binding event with a wide detecting interface. On the other side, a lowering of θ is associated with a sizable lowering of the gate surface potentials or work function. Such an occurrence is compatible with the observed direction of the threshold voltage shift.[25]

The amplification here described can qualitatively explain the high signal-to-noise ratio and also explains why the technology is not really quantitative but rather similar to the on−off technologies reviewed in section 2.2, and this is also an aspect of similarity with the Abbott technology. To better clarify the rationale of the effect that we discovered and published in 2018,[25] a pictorial representation of the dominion-like amplification effect is given in Figure 39. Here, the capturing antibodies are featured by the tiles of a dominoes game that are standing close to each other.

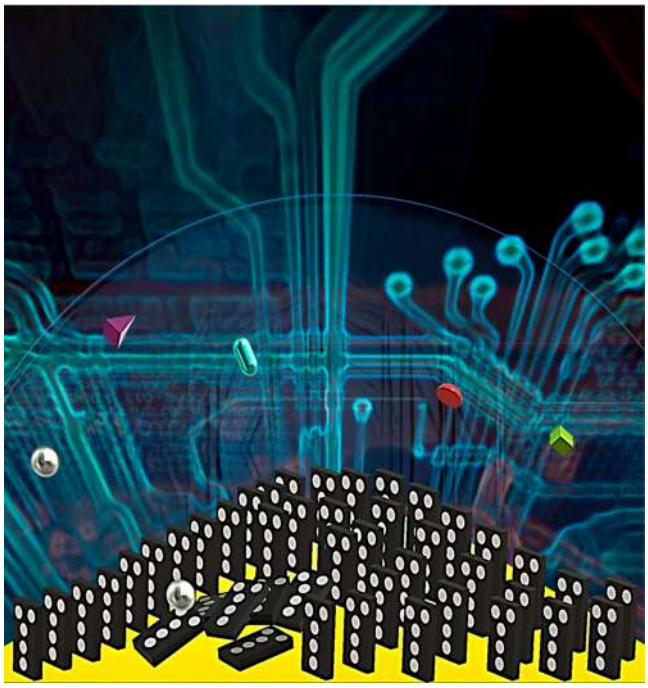

Figure 39. (A) Artistic interpretation of SiMoT large transducing gate bioelectronic sensing mechanism by Kyriaki Manoli. The capturing antibodies are featured as dominoes tiles. One bead strikes one single tile (affinity binding between one antibody and its antigen) that falls, and while doing so, it strikes others that fall also, generating a domino effect. The mechanism simulates the propagation of the gate work-function switching through a domino-like process triggered by the recognition event. Reprinted with permission from ref 26. Copyright 2019 American Chemical Society.

These tiles are immersed in a medium where a number of bead-like colored objects of different shape are present. When the silver spherical object, representing the antigen to be detected "selectively", strikes one of the tiles, this falls after the impact. While falling the tile hits other neighboring tiles that also start falling. The arrangement of the tiles changes from "standing" to "laying"; hence, the standing-to-laying shift propagates thanks to the initial event, and it is sustained by the gravitational field. Eventually a disordered region (maybe composed of tiles that are already in the laying-down arrangement) stops the propagation, hence defining the size of the domain and of the amplification effect.

In summary, the extremely high sensitivity of large-area FET bioelectronic sensors reviewed in sections 3 and 4 cannot be accounted for by considering the sole FET-type amplification. An independent amplification mechanism that affects only the signal coming from the selective biochemical binding is to be in place. An inspiration to decipher such an effect can come from nature by observing the behavior of some cells that can track a single molecule. Given the observation that some of these systems do propagate the initial binding event *via* voltage-dependent proteins, which can involve long-range interactions,[247] collaborative electrostatic effects have been inves-

https://doi.org/10.1021/acs.chemrev.1c00290
Chem. Rev. 2022, 122, 4636−4699

tigated. In this respect, it is interesting to consider the technology developed by Abbott and co-workers that is based on the reorientation of millions of mesogens, which interact *via* dipole−dipole like interactions, per single binding event. This occurs on the surface of the liquid crystal film and propagates for hundreds of micrometers, resulting in an amplified macroscopic effect. Somewhat similarly, in the model designed to demonstrate the amplification effect in a SiMoT device, hydrogen bonds are assumed to be the electrostatically active dipoles that enable the propagation of the selective binding into a domain comprising from 10^8 to 10^{12} recognition elements. This results in an amplified change of the gate work function and into a sizable shift of the FET threshold voltage. This amplification is not triggered by any of the nonselective bindings taking place in the negative control experiments. Hence, the two elicited technologies have interesting features in common: the materials enabling the transduction are formed by dipoles that are, originally, self-aligned; the affinity binding produces an input signal that generates a disorder in a very localized region of the material, this being an irreversible process; once triggered by the binding event, the disorder propagates, amplifying the output signal.

8. CONCLUSIONS AND FUTURE OUTLOOK

A comprehensive assessment of the blooming field of label-free ultrasensitive detections down to the single-molecule ultimate limit, performed with large, micrometer/millimeter wide, bioelectronic devices, is provided. The devices are capable of very-high selectivity thanks to a layer of biological elements capable of recognizimg a target analyte that is attached at one of the transistor electronic interfaces. Because the detecting surface is wide, an extremely large number of recognition elements can be grafted, resulting also in a biolayer packed with capturing proteins. The selective binding of the target molecule/marker to one of the capturing elements produces a signal that is amplified. Such mechanisms, while still elusive, have some similarities with what takes place in very different systems, such as for instance in some cells or in the liquid crystal film-based assay proposed by Abbott and co-workers. The electronic output is therefore characterized by a large signal that exceeds the level of the noise by at least three standard deviations, allowing assays at limit-of-detection values that are lower than femtomolar concentrations. The assay time-to-results can also be very short (few minutes) because such large-area transistors are not affected by the diffusion-barrier issue. The systems proposed can be applied to the detection of a number of different markers, also for progressive diseases, directly in biological fluids such as saliva or blood serum. An interesting approach is the single molecule with a large transistor (SiMoT) published in 2018 by the authors of this review. SiMoT can detect, with a limit of detection of a single-molecule, both proteins or genomic markers in real biological samples that are untreated and undiluted.

The review comprises a discussion on how to correctly operate an ultrasensitive bioelectronic sensor with the needed analytical validation strategies. It deals also with an extensive evaluation of the published ultrasensitive (limit of detections lower than fM) and single-molecule bioelectronic technologies engaging different devices from ISFETs, including extended gates, to electrolyte-gated field-effect transistors. Important aspects showing the high stability of such devices are also discussed. A very detailed overview of the different materials employed, from high electron mobility inorganic materials to organic semiconductors and graphene-based channels, is provided. To endow the devices with high selectivity, proper biofunctionalization strategies are adopted. These are reviewed along with the plethora of different target analytes that can be detected. The characterization of such high-performing electronic surfaces and interfaces is not an easy task. However, they can be crucial to help deciphering the complex sensing mechanisms with the associated amplification effects. To this end, the most relevant *in situ* and *operando* spectroscopic characterization approaches are reviewed. Among others, surface plasmon resonance and surface enhanced infrared absorption spectroscopy are discussed. Last but not least, the most relevant differences between the *near-field* and the *large-area* single-molecule label-free bioelectronic detections are also meticulously addressed.

A particular relevance is given to the description of the amplification effects that are needed to account for the sensing mechanisms enabling a significantly high signal-to-noise ratio even when the detecting interface has an area orders of magnitude larger than the footprint of the single molecules to be detected. To this end, the electronic amplification of the FET is considered along with collaborative collective electrostatic effects that generate a domino-like propagation effect. Interestingly, some cells that can track a chemoattractant with single-molecule sensitivity and amplification effects that enable the propagation of the initial input are discussed. Also interesting is the case of liquid crystal-based on−off type biodetections where the disorder induced by a binding event does propagate to the extent that a single binding elicits the electrostatic-induced disordering of a million mesogen molecules in the liquid crystals. The amplification effect is also studied in the SiMoT system, showing how dedicated molecular and biochemical Poisson statistics modeling can provide a plausible, though not yet definitive, explanation of the interesting behavior. The H-bonding network in chem-SAM is in fact supposed to enable a domino-like propagation of the single binding, but the compactness of the bio-SAM composed by a huge number of recognition elements also plays a key role.

Single-molecule large-area bioelectronics are emerging, highly innovative platforms suitable for many very relevant point-of-care applications. They are label-free and hence are fast; they can be operated directly in a biofluid such as blood serum, so they are inherently simple to be used; the measured electronic data are in a suitable digital form, and data processing and handling can be easily manage *via* apps and also cloud data storage/control systems. Furthermore, these platforms can be fabricated by mass-manufacturable technologies that are also cost-effective, large-area, and scalable. Because of all these very desirable characteristic, large-area and ultrasensitive bioelectronic sensors are expected to become very relevant in healthcare applications.

AUTHOR INFORMATION

Corresponding Author

Luisa Torsi − *Dipartimento di Chimica, Università degli Studi di Bari "Aldo Moro", 70125 Bari, Italy; Centre for Colloid and Surface Science - Università degli Studi di Bari "Aldo Moro", 70125 Bari, Italy; Faculty of Science and Engineering, Åbo Akademi University, 20500 Turku, Finland;* orcid.org/0000-0002-0798-0780; Email: luisa.torsi@uniba.it

Authors

Eleonora Macchia − *Faculty of Science and Engineering, Åbo Akademi University, 20500 Turku, Finland;* orcid.org/0000-0002-1534-7336

https://doi.org/10.1021/acs.chemrev.1c00290
Chem. Rev. 2022, 122, 4636−4699

Fabrizio Torricelli − *Dipartimento Ingegneria dell'Informazione, Università degli Studi di Brescia, 25123 Brescia, Italy*
Paolo Bollella − *Dipartimento di Chimica, Università degli Studi di Bari "Aldo Moro", 70125 Bari, Italy; Centre for Colloid and Surface Science - Università degli Studi di Bari "Aldo Moro", 70125 Bari, Italy*
Lucia Sarcina − *Dipartimento di Chimica, Università degli Studi di Bari "Aldo Moro", 70125 Bari, Italy*
Angelo Tricase − *Dipartimento di Chimica, Università degli Studi di Bari "Aldo Moro", 70125 Bari, Italy*
Cinzia Di Franco − *CNR, Istituto di Fotonica e Nanotecnologie, Sede di Bari, 70125 Bari, Italy*
Ronald Österbacka − *Faculty of Science and Engineering, Åbo Akademi University, 20500 Turku, Finland*
Zsolt M. Kovács-Vajna − *Dipartimento Ingegneria dell'Informazione, Università degli Studi di Brescia, 25123 Brescia, Italy*
Gaetano Scamarcio − *Dipartimento Interateneo di Fisica "M. Merlin", Università degli Studi di Bari "Aldo Moro", 70125 Bari, Italy; CNR, Istituto di Fotonica e Nanotecnologie, Sede di Bari, 70125 Bari, Italy*

Complete contact information is available at: https://pubs.acs.org/10.1021/acs.chemrev.1c00290

Author Contributions

§E.M. and F.T. contributed equally to this work.

Notes

The authors declare no competing financial interest.

Biographies

Eleonora Macchia (F) is senior researcher at Åbo Akademi University as PI of the project "Protein Detection at the Single Molecule Limit with a Self-powered Organic Transistor for HIV early diagnosis (ProSiT)" funded by Academy of Finland Research Council (GA#332106). She has been a postdoctoral fellow at University of Bari. She received her Ph.D. in Chemical Sciences (summa cum laude) in 2018 from the University of Bari and her Master's degree in Physics (110/110 cum laude) in 2014 from the same institution. At the age of 30 she has published 30 papers in international journals, 16 as first author, and one as corresponding author. She is coauthor of a European atent. Her works gathered over 430 Google scholar citations result in an H-index of 11. She is coauthor of three book chapters, and she participated to 18 international conferences, with 10 oral contributions and 4 posters. She has received seven scientific awards.

Fabrizio Torricelli (M) received a D.Eng. degree with honors and a Ph.D. degree in Electronics Engineering from the University of Brescia (Italy) in 2006 and 2010, respectively. From 2010 to 2012, he was appointed as a Postdoctoral Fellow at the Eindhoven University of Technology, Netherlands. He was a consultant for STMicroelectronics. Since 2019, he has been an Associate Professor at the Department of Information Engineering of the University of Brescia. His research interests include the numerical and analytical modeling of organic devices; the design of new memory and transistor architectures in silicon, metal oxide, and organic emerging technologies; and the development of electronics, bioelectronics, and biosensors based on organic electrochemical and electrolyte-gated transistors.

Paolo Bollella (M) is an Assistant Professor at University of Bari in the Department of Chemistry. Until December 2020, he was a Research Assistant Professor at Clarkson University in the Department of Chemistry and Biomolecular Science (United States). After his Ph.D., he joined the Department of Analytical Chemistry at Åbo Akademi in Turku (Finland) with a Johan Gadolin PostDoc fellowship awarded from the board of Johan Gadolin Process Chemistry Center. In October 2018, he joined the group of "Bioelectronics & Bionanotechnology" led by Prof. Evgeny Katz. In March 2019, he was awarded the Minerva Prize for Scientific Research − Merit Mention for the achievements obtained during his doctoral thesis based on the study of mediated/direct electron transfer of redox protein for biosensors and biofuel cells applications. He is the author of 62 papers in peer-reviewed international journals (Hirsch-index, 18), 3 book chapters, 1 student book, 2 proceedings, and almost 60 oral or poster contributions to national and international conferences.

Lucia Sarcina (F) has been a Ph.D. student in Chemical and Molecular Sciences at University of Bari (Italy) since December 2018. She received from the same institution her Master's degree in Material Science and Technology (110/110) in 2018, after attaining a Global Thesis study award at University of Oviedo (Spain). At the age of 27 she is coauthor of 10 publications in international journals and she has 10 international conferences contributions. She is currently working on an industrial Ph.D. project focused on the study of a standalone and disposable bioelectronic HIV sensor for point-of-care applications. She has expertise in the characterization of modified gold surfaces used as transducing systems for pathogen biorecognition.

Angelo Tricase (M) studied Chemistry and graduated summa cum laude from the University of Bari (Italy) in 2019 with a thesis on analytical characterization of electrolyte-gated-organic field effect transistor (EG-OFET) biosensors. He is currently a Ph.D. student at the University of Bari in Analytical Chemistry, and his research is focused on the study of surfaces for biosensor development, ranging from the improvement of protocols used for their preparation to the fine-tuning of the best practises for their analysis. At the age of 26 he has published two papers in well-recognized international peer-reviewed journals, such as *Frontiers in Chemistry* and *ACS Omega*. He is coauthor of a book chapter and presented four posters in national and international conferences.

Cinzia Di Franco (F) graduated in Chemistry (summa cum laude) at the University of Bari in 1999. From April 2000 to March 2003 she was employed by STMicroelectronics, Research and Development Division, as process engineer, working on single-photon avalanche photodiodes. From April 2003, she has been a researcher at CNR, Institute for Photonics and Nanotechnologies. Her research interests are in the fields of analytical chemistry, chem- and biosensors, surface microscopies, and nanomaterials. She is presently attending the Ph.D. school in Chemical and Molecular Sciences. She is the author/coauthor of more than 70 papers in peer-reviewed journals with an impact factor, chapters in international textbooks, and papers in conference proceedings publications.

Ronald Österbacka (M) has been a professor of physics at Åbo Akademi University (ÅAU) since 2005. He received his Ph.D. in Physics in 1999 from ÅAU and was a postdoctoral research fellow and an Academy Research fellow with the Academy of Finland. Österbacka is also a Presidents Visiting Fellow at the Printed Electronics Research Center at the Suzhou Institute for Nanobionics and Nanoscience (SINANO), Chinese Academy of Sciences (since 2019). He is the editor-in-chief for the IOP journal *Flexible and Printed Electronics*. Österbacka is an elected member of the Swedish Academy of Engineering Sciences in Finland and Finnish Society for the Science and Letters. Österbacka is a Knight of First Class of the Order of the White Rose of Finland, awarded by the President of Finland. He has served as a member and chair of numerous scientific boards and committees. Österbacka has coauthored more

https://doi.org/10.1021/acs.chemrev.1c00290
Chem. Rev. 2022, 122, 4636−4699

than 200 peer-reviewed articles and book chapters on electro-optical properties of disordered organic semiconductors.

Zsolt M. Kovács-Vajna (M) received his D.Eng. degree with honors from University of Bologna, Italy, in 1988. He completed a Specialization in Organization and Management at the University of Bologna in 1989. He received the Ph.D. degree in "Electronics Engineering and Computer Sciences" from the same university in 1994 based on his research activity on circuit simulation techniques and on handwritten character recognition systems. From 1989 to 1998 he was with the Department of Electronics Engineering (DEIS) in Bologna, where he was Assistant Professor and Research Associate in Electronics. In 1998 he joined the Department of Electronics Engineering (now Department of Information Engineering) of the University of Brescia, Italy, where he is full professor of Electronics. He founded the Microelectronics Laboratory. His current research interests include analog integrated circuit design, circuit simulation techniques, electromagnetic interference analysis in integrated circuits, modelling of organic devices, color theory and genetic variants, and disease association techniques.

Gaetano Scamarcio (M) is full professor of condensed matter physics, optoelectronics and nanotechnologies in the Physics Department of the University of Bari, Italy (since 2002). He received his Ph.D. in Physics in 1989 from the University of Bari. In 1989−1990 he was a research fellow at the Max Planck Institute for Solid State Physics, Stuttgart. In 1994−1996 he was a visiting scientist at Bell Laboratories of Lucent Technologies, previously AT&T, Murray Hill, NJ, United States. His research interests are in the fields of: mid-IR and THz quantum cascade lasers and their applications; optical, vibrational, and transport properties of semiconductor structures at the nanoscale; spectroscopic techniques for real-time monitoring of optoelectronic and bioelectronic devices; near-field imaging; optoelectronic sensors for mechatronics; and transistor biosensors.

Luisa Torsi (F) is professor of chemistry at the University of Bari and adjunct professor at Abo Academy University. She received her *laurea* degree in Physics and her Ph.D. in Chemical Sciences from UNIBA and was postdoctoral fellow at Bell Laboratories in the United States. She was the first woman awarded the H.E. Merck prize. She was also awarded the Distinguished Women Award by the International Union of Pure and Applied Chemistry. Recently, she was awarded also with the Wilhelm Exner Medal (2021). Torsi has authored almost 200 ISI papers, including papers published in *Science* and *Nature Materials*. Her works gathered almost 14 000 Google scholar citations resulting in an h-index of 56. Her research funding totals more €26 million, comprising several European and national contracts. Torsi is committed to role-modeling for younger women scientists. In a recent campaign, she was featured in a story of *TOPOLINO* (Italian digest-size series of Disney comics), as "Louise Torduck", a successful female scientist of the Calisota valley.

SELECTED ABBREVIATIONS

(O)FET	(organic) field-effect transistor
11-MUA	11-mercaptoundecanoic acid
2-ME	2-mercaptoethanol
3-MPA	3-mercaptoproprionic acid
a-IGZO	amorphous indium-gallium-zinc-oxide
ADAs	antidrug antibodies
anti-IgG/IgM	anti-immunoglobulin G/M
BSA	bovine serum albumin
CRP	C-reactive protein
EDC sulpho-NHS	ethyl-3-(3-dimethylaminopropyl)-carbodiimide (EDC) *N*-hydroxysulfosuccinimide sodium salt (sulfo-NHS)
EDL or CDL	electrical double layer or charge double layer
EG(O)FET	electrolyte-gated (organic) FET
ELISA	enzyme-linked immunosorbent assay
H-bond(ing)	hydrogen bond(ing)
IgG/IgM	immunoglobulin G/M
ISFET	ion-selective field-effect transistor
IUPAC	Union of Pure and Applied Chemistry
LOD	limit of detection
LOI	limit of identification
LOQ	limit of quantification
MOSFET	metal-oxide-semiconductor field-effect-transistor
NGS	next-generation sequencing
OECT	organic electrochemical transistor
PBS	phosphate-buffered saline
PCA	principal component analysis
PCR	polymerase chain reaction
POCT	point of care testing
SEIRAS	surface enhanced infrared absorption spectroscopy
Simoa	single-molecule array
SiMoT	single molecule with a large transistor
SPR	surface plasmon resonance

REFERENCES

(1) Rosenstein, J. K.; Lemay, S. G.; Shepard, K. L. Single-Molecule Bioelectronics. *Wiley Interdiscip. Rev. Nanomedicine Nanobiotechnology* **2015**, *7*, 475−493.
(2) Li, Y.; Yang, C.; Guo, X. Single-Molecule Electrical Detection: A Promising Route toward the Fundamental Limits of Chemistry and Life Science. *Acc. Chem. Res.* **2020**, *53*, 159−169.
(3) Ma, F.; Li, Y.; Tang, B.; Zhang, C. Y. Fluorescent Biosensors Based on Single-Molecule Counting. *Acc. Chem. Res.* **2016**, *49*, 1722−1730.
(4) Li, H.; Shi, W.; Song, J.; Jang, H. J.; Dailey, J.; Yu, J.; Katz, H. E. Chemical and Biomolecule Sensing with Organic Field-Effect Transistors. *Chem. Rev.* **2019**, *119*, 3−35.
(5) Deniz, A. A. Deciphering Complexity in Molecular Biophysics with Single-Molecule Resolution. *J. Mol. Biol.* **2016**, *428*, 301−307.
(6) Kumar, S.; Clarke, D.; Gerstein, M. B. Leveraging Protein Dynamics to Identify Cancer Mutational Hotspots Using 3D Structures. *Proc. Natl. Acad. Sci. U. S. A.* **2019**, *116*, 18962−18970.
(7) Rothberg, J. M.; Hinz, W.; Rearick, T. M.; Schultz, J.; Mileski, W.; Davey, M.; Leamon, J. H.; Johnson, K.; Milgrew, M. J.; Edwards, M.; Hoon, J.; Simons, J. F.; Marran, D.; Myers, J. W.; Davidson, J. F.; Branting, A.; Nobile, J. R.; Puc, B. P.; Light, D.; Clark, T. A.; Huber, M.; Branciforte, J. T.; Stoner, I. B.; Cawley, S. E.; Lyons, M.; Fu, Y.; Homer, N.; Sedova, M.; Miao, X.; Reed, B.; Sabina, J.; Feierstein, E.; Schorn, M.; Alanjary, M.; Dimalanta, E.; Dressman, D.; Kasinskas, R.; Sokolsky, T.; Fidanza, J. A.; Namsaraev, E.; McKernan, K. J.; Williams, A.; Roth, G. T.; Bustillo, J. An Integrated Semiconductor Device Enabling Non-Optical Genome Sequencing. *Nature* **2011**, *475*, 348−352.
(8) Wang, X.; Cohen, L.; Wang, J.; Walt, D. R. Competitive Immunoassays for the Detection of Small Molecules Using Single Molecule Arrays. *J. Am. Chem. Soc.* **2018**, *140*, 18132−18139.
(9) Fischer, S. K.; Joyce, A.; Spengler, M.; Yang, T. Y.; Zhuang, Y.; Fjording, M. S.; Mikulskis, A. Emerging Technologies to Increase Ligand Binding Assay Sensitivity. *AAPS J.* **2015**, *17*, 93−101.
(10) Rissin, D. M.; Walt, D. R. Digital Concentration Readout of Single Enzyme Molecules Using Femtoliter Arrays and Poisson Statistics. *Nano Lett.* **2006**, *6*, 520−523.

https://doi.org/10.1021/acs.chemrev.1c00290
Chem. Rev. 2022, 122, 4636−4699

(11) Crowley, E.; Di Nicolantonio, F.; Loupakis, F.; Bardelli, A. Liquid Biopsy: Monitoring Cancer-Genetics in the Blood. *Nat. Rev. Clin. Oncol.* **2013**, *10*, 472−484.
(12) Finoulst, I.; Pinkse, M.; Van Dongen, W.; Verhaert, P. Sample Preparation Techniques for the Untargeted LC-MS-Based Discovery of Peptides in Complex Biological Matrices. *J. Biomed. Biotechnol.* **2011**, *2011*, 245291.
(13) Engvall, E. Enzyme-Linked Immunosorbent Assay (ELISA) Quantitative Assay of Immunoglobulin G. *Mol. Immunol.* **1971**, *8*, 871−874.
(14) Walt, D. R. Optical Methods for Single Molecule Detection and Analysis. *Anal. Chem.* **2013**, *85*, 1258−1263.
(15) Rotman, B. Measurement of Activity of Single Molecules of Beta-D-Galactosidase. *Proc. Natl. Acad. Sci. United States* **1961**, *47*, 1981−1991.
(16) Hirschfeld, T. Optical Microscopic Observation of Single Small Molecules. *Appl. Opt.* **1976**, *15*, 2965−2966.
(17) Gooding, J. J.; Gaus, K. Single-Molecule Sensors: Challenges and Opportunities for Quantitative Analysis. *Angew. Chemie - Int. Ed.* **2016**, *55*, 11354−11366.
(18) Lemay, S. G.; Kang, S.; Mathwig, K.; Singh, P. S. Single-Molecule Electrochemistry: Present Status and Outlook. *Acc. Chem. Res.* **2013**, *46*, 369−377.
(19) Macchia, E.; Manoli, K.; Di Franco, C.; Scamarcio, G.; Torsi, L. New Trends in Single-Molecule Bioanalytical Detection. *Anal. Bioanal. Chem.* **2020**, *412*, 5005−5014.
(20) Sheehan, P. E.; Whitman, L. J. Detection Limits for Nanoscale Biosensors. *Nano Lett.* **2005**, *5*, 803−807.
(21) Wei, R.; Gatterdam, V.; Wieneke, R.; Tampé, R.; Rant, U. Stochastic Sensing of Proteins with Receptor-Modified Solid-State Nanopores. *Nat. Nanotechnol.* **2012**, *7*, 257−263.
(22) Sorgenfrei, S.; Chiu, C. Y.; Gonzalez, R. L.; Yu, Y. J.; Kim, P.; Nuckolls, C.; Shepard, K. L. Label-Free Single-Molecule Detection of DNA-Hybridization Kinetics with a Carbon Nanotube Field-Effect Transistor. *Nat. Nanotechnol.* **2011**, *6*, 126−132.
(23) Rissin, D. M.; Kan, C. W.; Campbell, T. G.; Howes, S. C.; Fournier, D. R.; Song, L.; Piech, T.; Patel, P. P.; Chang, L.; Rivnak, A. J.; Ferrell, E. P.; Randall, J. D.; Provuncher, G. K.; Walt, D. R.; Duffy, D. C. Single-Molecule Enzyme-Linked Immunosorbent Assay Detects Serum Proteins at Subfemtomolar Concentrations. *Nat. Biotechnol.* **2010**, *28*, 595−599.
(24) Jain, A.; Liu, R.; Ramani, B.; Arauz, E.; Ishitsuka, Y.; Ragunathan, K.; Park, J.; Chen, J.; Xiang, Y. K.; Ha, T. Probing Cellular Protein Complexes Using Single-Molecule Pull-Down. *Nature* **2011**, *473*, 484−488.
(25) Macchia, E.; Manoli, K.; Holzer, B.; Di Franco, C.; Ghittorelli, M.; Torricelli, F.; Alberga, D.; Mangiatordi, G. F.; Palazzo, G.; Scamarcio, G.; Torsi, L. Single-Molecule Detection with a Millimetre-Sized Transistor. *Nat. Commun.* **2018**, *9*, 3223.
(26) Macchia, E.; Tiwari, A.; Manoli, K.; Holzer, B.; Ditaranto, N.; Picca, R. A.; Cioffi, N.; Di Franco, C.; Scamarcio, G.; Palazzo, G.; Torsi, L. Label-Free and Selective Single-Molecule Bioelectronic Sensing with a Millimeter-Wide Self-Assembled Monolayer of Anti-Immunoglobulins. *Chem. Mater.* **2019**, *31*, 6476−6483.
(27) Macchia, E.; Manoli, K.; Holzer, B.; Di Franco, C.; Picca, R. A.; Cioffi, N.; Scamarcio, G.; Palazzo, G.; Torsi, L. Selective Single-Molecule Analytical Detection of C-Reactive Protein in Saliva with an Organic Transistor. *Anal. Bioanal. Chem.* **2019**, *411*, 4899−4908.
(28) Macchia, E.; Sarcina, L.; Picca, R. A.; Manoli, K.; Di Franco, C.; Scamarcio, G.; Torsi, L. Ultra-Low HIV-1 P24 Detection Limits with a Bioelectronic Sensor. *Anal. Bioanal. Chem.* **2020**, *412*, 811−818.
(29) Macchia, E.; Manoli, K.; Di Franco, C.; Picca, R. A.; Österbacka, R.; Palazzo, G.; Torricelli, F.; Scamarcio, G.; Torsi, L. Organic Field-Effect Transistor Platform for Label-Free, Single-Molecule Detection of Genomic Biomarkers. *ACS Sensors* **2020**, *5*, 1822−1830.
(30) Wu, Y.; Wang, X.; Li, X.; Xiao, Y.; Wang, Y. Cyclodextrin Derivatives Functionalized Highly Sensitive Chiral Sensor Based on Organic Field-Effect Transistor. *Chin. Chem. Lett.* **2020**, *31*, 99−102.
(31) Guo, K.; Wustoni, S.; Koklu, A.; Díaz-Galicia, E.; Moser, M.; Hama, A.; Alqahtani, A. A.; Ahmad, A. N.; Alhamlan, F. S.; Shuaib, M.; Pain, A.; McCulloch, I.; Arold, S. T.; Grünberg, R.; Inal, S. Rapid Single-Molecule Detection of COVID-19 and MERS Antigens via Nanobody-Functionalized Organic Electrochemical Transistors. *Nat. Biomed. Eng.* **2021**, *5*, 666−677.
(32) Nakatsuka, N.; Yang, K. A.; Abendroth, J. M.; Cheung, K. M.; Xu, X.; Yang, H.; Zhao, C.; Zhu, B.; Rim, Y. S.; Yang, Y.; Weiss, P. S.; Stojanović, M. N.; Andrews, A. M. Aptamer-Field-Effect Transistors Overcome Debye Length Limitations for Small-Molecule Sensing. *Science* **2018**, *362*, 319−324.
(33) Macchia, E.; Picca, R. A.; Manoli, K.; Di Franco, C.; Blasi, D.; Sarcina, L.; Ditaranto, N.; Cioffi, N.; Österbacka, R.; Scamarcio, G.; Torricelli, F.; Torsi, L. About the Amplification Factors in Organic Bioelectronic Sensors. *Mater. Horizons* **2020**, *7*, 999−1013.
(34) Gupta, V. K.; Skaife, J. J.; Dubrovsky, T. B.; Abbott, N. L. Optical Amplification of Ligand-Receptor Binding Using Liquid Crystals. *Science (80).* **1998**, *279*, 2077−2080.
(35) Shrivastava, S.; Trung, T. Q.; Lee, N. E. Recent Progress, Challenges, and Prospects of Fully Integrated Mobile and Wearable Point-of-Care Testing Systems for Self-Testing. *Chem. Soc. Rev.* **2020**, *49*, 1812−1866.
(36) Park, S.; Heo, S. W.; Lee, W.; Inoue, D.; Jiang, Z.; Yu, K.; Jinno, H.; Hashizume, D.; Sekino, M.; Yokota, T.; Fukuda, K.; Tajima, K.; Someya, T. Self-Powered Ultra-Flexible Electronics via Nano-Grating-Patterned Organic Photovoltaics. *Nature* **2018**, *561*, 516−521.
(37) Rivnay, J.; Inal, S.; Salleo, A.; Owens, R. M.; Berggren, M.; Malliaras, G. G. Organic Electrochemical Transistors. *Nat. Rev. Mater.* **2018**, *3*, 17086.
(38) Zhang, S.; Cicoira, F. Flexible Self-Powered Biosensors. *Nature* **2018**, *561*, 466−467.
(39) Bruen, D.; Delaney, C.; Florea, L.; Diamond, D. Glucose Sensing for Diabetes Monitoring: Recent Developments. *Sensors* **2017**, *17*, 1866.
(40) Turner, A. P. F. Biosensors: Sense and Sensibility. *Chem. Soc. Rev.* **2013**, *42*, 3184−3196.
(41) Akkilic, N.; Geschwindner, S.; Höök, F. Single-Molecule Biosensors: Recent Advances and Applications. *Biosens. Bioelectron.* **2020**, *151*, 111944.
(42) Chen, C.; Guo, Y.; Chen, P.; Peng, H. Recent Advances of Tissue-Interfaced Chemical Biosensors. *J. Mater. Chem. B* **2020**, *8*, 3371−3381.
(43) Sekretaryova, A. N.; Vagin, M. Y.; Turner, A. P. F.; Eriksson, M. Electrocatalytic Currents from Single Enzyme Molecules. *J. Am. Chem. Soc.* **2016**, *138*, 2504−2507.
(44) Ishii, Y.; Yanagida, T. Single Molecule Detection in Life Sciences. *Single Mol.* **2000**, *1*, 5−16.
(45) Leinders-Zufall, T.; Lane, A. P.; Puche, A. C.; Ma, W.; Novotny, M. V.; Shipley, M. T.; Zufall, F. Ultrasensitive Pheromone Detection by Mammalian Vomeronasal Neurons. *Nature* **2000**, *405*, 792−796.
(46) Turner, A.; Karube, I.; Wilson, G. S. *Biosensors: Fundamentals and Applications*; Oxford University Press, 1987.
(47) Grieshaber, D.; MacKenzie, R.; Vörös, J.; Reimhult, E. Electrochemical Biosensors-Sensor Principles and Architectures. *Sensors* **2008**, *8* (3), 1400−1458.
(48) Mohanty, S. P.; Kougianos, E. Biosensors: A Tutorial Review. *IEEE Potentials* **2006**, *25* (2), 35−40.
(49) Nakamura, H.; Karube, I. Current Research Activity in Biosensors. *Anal. Bioanal. Chem.* **2003**, *377* (3), 446−468.
(50) Justino, C. I. L.; Rocha-Santos, T. A.; Duarte, A. C.; et al. Review of Analytical Figures of Merit of Sensors and Biosensors in Clinical Applications. *TrAC Trends Anal. Chem.* **2010**, *29*, 1172−1183.
(51) Olivieri, A. C. Analytical Figures of Merit: From Univariate to Multiway Calibration. *Chem. Rev.* **2014**, *114*, 5358−5378.
(52) Vessman, J.; Stefan, R. I.; Van Staden, J. F.; Danzer, K.; Lindner, W.; Burns, D. T.; Fajgelj, A.; Müller, H. Selectivity in Analytical Chemistry (IUPAC Recommendations 2001). *Pure Appl. Chem.* **2001**, *73*, 1381−1386.

https://doi.org/10.1021/acs.chemrev.1c00290
Chem. Rev. 2022, 122, 4636−4699

(53) Analytical Methods Committee.. Recommendations for the Definition, Estimation and Use of the Detection Limit. *Analyst* **1987**, *112*, 199−204.
(54) Thompson, M.; Ellison, S. L. R.; Wood, R. Harmonized Guidelines for Single-Laboratory Validation of Methods of Analysis (IUPAC Technical Report). *Pure Appl. Chem.* **2002**, *74*, 835−855.
(55) Long, G. L.; Winefordner, J. D. Limit of Detection. A Closer Look at the IUPAC Definition. *Anal. Chem.* **1983**, *55*, 712A−724A.
(56) Allegrini, F.; Olivieri, A. C. IUPAC-Consistent Approach to the Limit of Detection in Partial Least-Squares Calibration. *Anal. Chem.* **2014**, *86*, 7858−7866.
(57) Union, I.; Pure, O. F.; Chemistry, A. International Union of Pure and Applied Chemistry Commission on Electroanalytical Chemistry * (IUPAC and ACS) and New Procedures for Determining the Limits of Detection and Quantification: Application to Voltammetric and Stripping A Statistical Overvie. *Pure Appl. Chem.* **1997**, *69*, 297−328.
(58) Kralik, P.; Ricchi, M. A Basic Guide to Real Time PCR in Microbial Diagnostics: Definitions, Parameters, and Everything. *Front. Microbiol.* **2017**, *8*, 108.
(59) Huber, W. Basic Calculations about the Limit of Detection and Its Optimal Determination. *Accredit. Qual. Assur.* **2003**, *8*, 213−217.
(60) Ortiz, M. C.; Sarabia, L. A.; Herrero, A.; Sánchez, M. S.; Sanz, M. B.; Rueda, M. E.; Giménez, D.; Meléndez, M. E. Capability of Detection of an Analytical Method Evaluating False Positive and False Negative (ISO 11843) with Partial Least Squares. *Chemom. Intell. Lab. Syst.* **2003**, *69*, 21−33.
(61) Jing, P.; Yi, H.; Xue, S.; Yuan, R.; Xu, W. A 'Signal on-off'Electrochemical Peptide Biosensor for Matrix Metalloproteinase 2 Based on Target Induced Cleavage of a Peptide. *RSC Adv.* **2015**, *5*, 65725−65730.
(62) Bian, X.; Guo, B.; Zhao, M.; Han, D.; Cheng, W.; Song, F.; Ding, S. An Enzyme-Free "ON-OFF" Electrochemiluminescence Biosensor for Ultrasensitive Detection of PML/RARα Based on Target-Switched DNA Nanotweezer. *ACS Appl. Mater. Interfaces* **2019**, *11*, 3715−3721.
(63) Wang, Z.; Qian, Y.; Wei, X.; Zhang, Y.; Wu, G.; Lu, X. An "on-off" Electrochemiluminescence Biosensor Based on Molecularly Imprinted Polymer and Recycling Amplifications for Determination of Dopamine. *Electrochim. Acta* **2017**, *250*, 309−319.
(64) Klein, C. J.; Foroud, T. M. Neurology Individualized Medicine: When to Use next-Generation Sequencing Panels. *Mayo Clinic Proceedings* **2017**, *92*, 292−305.
(65) Mo, F.; Wu, J.; Chen, M.; Meng, H.; Han, Q.; Fu, Y. Enzyme-Free "on-off-on" Photoelectrochemical Biosensor Based on Cascaded Quadratic Amplification Strategy for MiRNA 141 Detection. *Sensors Actuators B Chem.* **2019**, *289*, 269−276.
(66) de la Escosura-Muñiz, A.; Merkoçi, A. A Nanochannel/Nanoparticle-based Filtering and Sensing Platform for Direct Detection of a Cancer Biomarker in Blood. *Small* **2011**, *7*, 675−682.
(67) Moretti, M.; Di Fabrizio, E.; Cabrini, S.; Musetti, R.; De Angelis, F.; Firrao, G. An ON/OFF Biosensor Based on Blockade of Ionic Current Passing through a Solid-State Nanopore. *Biosens. Bioelectron.* **2008**, *24*, 141−147.
(68) Yu, R.-J.; Ying, Y.-L.; Hu, Y.-X.; Gao, R.; Long, Y.-T. Label-Free Monitoring of Single Molecule Immunoreaction with a Nanopipette. *Anal. Chem.* **2017**, *89*, 8203−8206.
(69) Garoli, D.; Yamazaki, H.; Maccaferri, N.; Wanunu, M. Plasmonic Nanopores for Single-Molecule Detection and Manipulation: Toward Sequencing Applications. *Nano Lett.* **2019**, *19*, 7553−7562.
(70) Slatko, B. E.; Gardner, A. F.; Ausubel, F. M. Overview of Next-generation Sequencing Technologies. *Curr. Protoc. Mol. Biol.* **2018**, *122*, No. e59.
(71) Lavín, Á.; Vicente, J.; Holgado, M.; Laguna, M. F.; Casquel, R.; Santamaría, B.; Maigler, M. V.; Hernández, A. L.; Ramírez, Y. On the Determination of Uncertainty and Limit of Detection in Label-Free Biosensors. *Sensors (Switzerland)* **2018**, *18*, 2038.
(72) De Vicente, J.; Lavín, Á.; Holgado, M.; Laguna, M. F.; Casquel, R.; Santamaría, B.; Quintero, S.; Hernández, A. L.; Ramírez, Y. The Uncertainty and Limit of Detection in Biosensors from Immunoassays. *Meas. Sci. Technol.* **2020**, *31*, 044004.
(73) Etchegoin, P. G.; Meyer, M.; Le Ru, E. C. Statistics of Single Molecule SERS Signals: Is There a Poisson Distribution of Intensities? *Phys. Chem. Chem. Phys.* **2007**, *9*, 3006−3010.
(74) Kalmanovskii, V. I. Construction of Calibration Curves for Methods of Analyzing Environmental Samples. *Meas. Tech.* **1998**, *41*, 288−293.
(75) Thrift, W. J.; Ragan, R. Quantification of Analyte Concentration in the Single Molecule Regime Using Convolutional Neural Networks. *Anal. Chem.* **2019**, *91*, 13337−13342.
(76) Cheng, W.-C.; Horn, T.; Zayats, M.; Rizk, G.; Major, S.; Zhu, H.; Russell, J.; Xu, Z.; Rothman, R. E.; Celedon, A. Ultra-Sensitive and Rapid Detection of Nucleic Acids and Microorganisms in Body Fluids Using Single-Molecule Tethering. *Nat. Commun.* **2020**, *11*, 4774.
(77) Van Gool, A.; Corrales, F.; Čolović, M.; Krstić, D.; Oliver-Martos, B.; Martínez-Cáceres, E.; Jakasa, I.; Gajski, G.; Brun, V.; Kyriacou, K.; et al. Analytical Techniques for Multiplex Analysis of Protein Biomarkers. *Expert Rev. Proteomics* **2020**, *17*, 257−273.
(78) Lubken, R. M.; de Jong, A. M.; Prins, M. W. J. Multiplexed Continuous Biosensing by Single-Molecule Encoded Nanoswitches. *Nano Lett.* **2020**, *20*, 2296−2302.
(79) Sze, J. Y. Y.; Ivanov, A. P.; Cass, A. E. G.; Edel, J. B. Single Molecule Multiplexed Nanopore Protein Screening in Human Serum Using Aptamer Modified DNA Carriers. *Nat. Commun.* **2017**, *8*, 1552.
(80) Pawlak, M.; Schick, E.; Bopp, M. A.; Schneider, M. J.; Oroszlan, P.; Ehrat, M. Zeptosens' Protein Microarrays: A Novel High Performance Microarray Platform for Low Abundance Protein Analysis. *Proteomics* **2002**, *2*, 383−393.
(81) Gilboa, T.; Maley, A. M.; Ogata, A. F.; Wu, C.; Walt, D. R. Sequential Protein Capture in Multiplex Single Molecule Arrays: A Strategy for Eliminating Assay Cross-Reactivity. *Adv. Healthc. Mater.* **2021**, *10*, 2001111.
(82) Rissin, D. M.; Kan, C. W.; Song, L.; Rivnak, A. J.; Fishburn, M. W.; Shao, Q.; Piech, T.; Ferrell, E. P.; Meyer, R. E.; Campbell, T. G.; et al. Multiplexed Single Molecule Immunoassays. *Lab Chip* **2013**, *13*, 2902−2911.
(83) Wilson, D. H.; Rissin, D. M.; Kan, C. W.; Fournier, D. R.; Piech, T.; Campbell, T. G.; Meyer, R. E.; Fishburn, M. W.; Cabrera, C.; Patel, P. P.; et al. The Simoa HD-1 Analyzer: A Novel Fully Automated Digital Immunoassay Analyzer with Single-Molecule Sensitivity and Multiplexing. *J. Lab. Autom.* **2016**, *21*, 533−547.
(84) Kaisti, M. Detection Principles of Biological and Chemical FET Sensors. *Biosens. Bioelectron.* **2017**, *98*, 437−448.
(85) Bausells, J.; Carrabina, J.; Errachid, A.; Merlos, A. Ion-Sensitive Field-Effect Transistors Fabricated in a Commercial CMOS Technology. *Sensors Actuators, B Chem.* **1999**, *57*, 56−62.
(86) Bhattacharyya, I. M.; Cohen, S.; Shalabny, A.; Bashouti, M.; Akabayov, B.; Shalev, G. Specific and Label-Free Immunosensing of Protein-Protein Interactions with Silicon-Based ImmunoFETs. *Biosens. Bioelectron.* **2019**, *132*, 143−161.
(87) Picca, R. A.; Manoli, K.; Macchia, E.; Sarcina, L.; Di Franco, C.; Cioffi, N.; Blasi, D.; Österbacka, R.; Torricelli, F.; Scamarcio, G.; Torsi, L. Ultimately Sensitive Organic Bioelectronic Transistor Sensors by Materials and Device Structure Design. *Adv. Funct. Mater.* **2020**, *30*, 1904513.
(88) Koutsouras, D. A.; Amiri, M. H.; Blom, P. W. M.; Torricelli, F.; Asadi, K.; Gkoupidenis, P. An Iontronic Multiplexer Based on Spatiotemporal Dynamics of Multiterminal Organic Electrochemical Transistors. *Adv. Funct. Mater.* **2021**, *31*, 2011013.
(89) Palazzo, G.; De Tullio, D.; Magliulo, M.; Mallardi, A.; Intranuovo, F.; Mulla, M. Y.; Favia, P.; Vikholm-Lundin, I.; Torsi, L. Detection beyond Debye's Length with an Electrolyte-Gated Organic Field-Effect Transistor. *Adv. Mater.* **2015**, *27*, 911−916.
(90) Mulla, M. Y.; Tuccori, E.; Magliulo, M.; Lattanzi, G.; Palazzo, G.; Persaud, K.; Torsi, L. Capacitance-Modulated Transistor Detects Odorant Binding Protein Chiral Interactions. *Nat. Commun.* **2015**, *6*, 6010.
(91) Romele, P.; Ghittorelli, M.; Kovács-Vajna, Z. M.; Torricelli, F. Ion Buffering and Interface Charge Enable High Performance

https://doi.org/10.1021/acs.chemrev.1c00290
Chem. Rev. 2022, 122, 4636−4699

Electronics with Organic Electrochemical Transistors. *Nat. Commun.* **2019**, *10*, 3044.
(92) Romele, P.; Gkoupidenis, P.; Koutsouras, D. A.; Lieberth, K.; Kovács-Vajna, Z. M.; Blom, P. W. M.; Torricelli, F. Multiscale Real Time and High Sensitivity Ion Detection with Complementary Organic Electrochemical Transistors Amplifier. *Nat. Commun.* **2020**, *11*, 3743.
(93) White, S. P.; Dorfman, K. D.; Frisbie, C. D. Operating and Sensing Mechanism of Electrolyte-Gated Transistors with Floating Gates: Building a Platform for Amplified Biodetection. *J. Phys. Chem. C* **2016**, *120*, 108−117.
(94) Wu, C. R.; Wang, S. L.; Chen, P. H.; Wang, Y. L.; Wang, Y. R.; Chen, J. C. Demonstration of the Enhancement of Gate Bias and Ionic Strength in Electric-Double-Layer Field-Effect-Transistor Biosensors. *Sensors Actuators, B Chem.* **2021**, *334*, 129567.
(95) Liang, Y.; Xiao, M.; Wu, D.; Lin, Y.; Liu, L.; He, J.; Zhang, G.; Peng, L. M.; Zhang, Z. Wafer-Scale Uniform Carbon Nanotube Transistors for Ultrasensitive and Label-Free Detection of Disease Biomarkers. *ACS Nano* **2020**, *14*, 8866−8874.
(96) Macchia, E.; Romele, P.; Manoli, K.; Ghittorelli, M.; Magliulo, M.; Kovács-Vajna, Z. M.; Torricelli, F.; Torsi, L. Ultra-Sensitive Protein Detection with Organic Electrochemical Transistors Printed on Plastic Substrates. *Flex. Print. Electron.* **2018**, *3*, 034002.
(97) Sensi, M.; Berto, M.; Gentile, S.; Pinti, M.; Conti, A.; Pellacani, G.; Salvarani, C.; Cossarizza, A.; Bortolotti, C. A.; Biscarini, F. Anti-Drug Antibody Detection with Label-Free Electrolyte-Gated Organic Field-Effect Transistors. *Chem. Commun.* **2021**, *57*, 367−370.
(98) Ricci, S.; Casalini, S.; Parkula, V.; Selvaraj, M.; Saygin, G. D.; Greco, P.; Biscarini, F.; Mas-Torrent, M. Label-Free Immunodetection of α-Synuclein by Using a Microfluidics Coplanar Electrolyte-Gated Organic Field-Effect Transistor. *Biosens. Bioelectron.* **2020**, *167*, 112433.
(99) Oh, J.; Yang, H.; Jeong, G. E.; Moon, D.; Kwon, O. S.; Phyo, S.; Lee, J.; Song, H. S.; Park, T. H.; Jang, J. Ultrasensitive, Selective, and Highly Stable Bioelectronic Nose That Detects the Liquid and Gaseous Cadaverine. *Anal. Chem.* **2019**, *91*, 12181−12190.
(100) Prattis, I.; Hui, E.; Gubeljak, P.; Kaminski Schierle, G. S.; Lombardo, A.; Occhipinti, L. G. Graphene for Biosensing Applications in Point-of-Care Testing. *Trends Biotechnol.* **2021**, *39*, 1065−1077.
(101) Hajian, R.; Balderston, S.; Tran, T.; de Boer, T.; Etienne, J.; Sandhu, M.; Wauford, N. A.; Chung, J. Y.; Nokes, J.; Athaiya, M.; Paredes, J.; Peytavi, R.; Goldsmith, B.; Murthy, N.; Conboy, I. M.; Aran, K. Detection of Unamplified Target Genes via CRISPR-Cas9 Immobilized on a Graphene Field-Effect Transistor. *Nat. Biomed. Eng.* **2019**, *3*, 427−437.
(102) Pham Ba, V. A.; Han, Y. M.; Cho, Y.; Kim, T.; Lee, B. Y.; Kim, J. S.; Hong, S. Modified Floating Electrode-Based Sensors for the Quantitative Monitoring of Drug Effects on Cytokine Levels Related with Inflammatory Bowel Diseases. *ACS Appl. Mater. Interfaces* **2018**, *10*, 17100−17106.
(103) Murugathas, T.; Zheng, H. Y.; Colbert, D.; Kralicek, A. V.; Carraher, C.; Plank, N. O. V. Biosensing with Insect Odorant Receptor Nanodiscs and Carbon Nanotube Field-Effect Transistors. *ACS Appl. Mater. Interfaces* **2019**, *11*, 9530−9538.
(104) Fathil, M. F. M.; Md Arshad, M. K.; Ruslinda, A. R.; Gopinath, S. C. B.; Nuzaihan, M. M. N.; Adzhri, R.; Hashim, U.; Lam, H. Y. Substrate-Gate Coupling in ZnO-FET Biosensor for Cardiac Troponin I Detection. *Sensors Actuators, B Chem.* **2017**, *242*, 1142−1154.
(105) Seo, G.; Lee, G.; Kim, M. J.; Baek, S. H.; Choi, M.; Ku, K. B.; Lee, C. S.; Jun, S.; Park, D.; Kim, H. G.; Kim, S. J.; Lee, J. O.; Kim, B. T.; Park, E. C.; Kim, S. Rapid Detection of COVID-19 Causative Virus (SARS-CoV-2) in Human Nasopharyngeal Swab Specimens Using Field-Effect Transistor-Based Biosensor. *ACS Nano* **2020**, *14*, 12257−12258.
(106) Zhou, L.; Wang, K.; Sun, H.; Zhao, S.; Chen, X.; Qian, D.; Mao, H.; Zhao, J. Novel Graphene Biosensor Based on the Functionalization of Multifunctional Nano-Bovine Serum Albumin for the Highly Sensitive Detection of Cancer Biomarkers. *Nano-Micro Lett.* **2019**, *11*, 20.
(107) Li, Y.; Zeng, B.; Yang, Y.; Liang, H.; Yang, Y.; Yuan, Q. Design of High Stability Thin-Film Transistor Biosensor for the Diagnosis of Bladder Cancer. *Chin. Chem. Lett.* **2020**, *31*, 1387−1391.
(108) Palit, S.; Singh, K.; Lou, B. S.; Her, J. L.; Pang, S. T.; Pan, T. M. Ultrasensitive Dopamine Detection of Indium-Zinc Oxide on PET Flexible Based Extended-Gate Field-Effect Transistor. *Sensors Actuators, B Chem.* **2020**, *310*, 127850.
(109) Yu, J.; Xu, M.; Liang, L.; Guan, M.; Zhang, Y.; Yan, F.; Cao, H. Separative Extended-Gate AlGaAs/GaAs HEMT Biosensors Based on Capacitance Change Strategy. *Appl. Phys. Lett.* **2020**, *116*, 123704.
(110) Xu, M.; Li, S.; Guan, M.; Zhang, Y.; Zeng, Y. Extended-Gate AlGaAs/GaAs HEMT for Accurate Cardiac Troponin i Antigen Detection in Clinical Human Serum. *Appl. Phys. Express* **2020**, *13*, 021003.
(111) Lee, J.; Kim, M. J.; Yang, H.; Kim, S.; Yeom, S.; Ryu, G.; Shin, Y.; Sul, O.; Jeong, J. K.; Lee, S. B. Extended-Gate Amorphous InGaZnO Thin Film Transistor for Biochemical Sensing. *IEEE Sens. J.* **2021**, *21*, 178−184.
(112) Sarangadharan, I.; Wang, S. L.; Sukesan, R.; Chen, P. C.; Dai, T. Y.; Pulikkathodi, A. K.; Hsu, C. P.; Chiang, H. H. K.; Liu, L. Y. M.; Wang, Y. L. Single Drop Whole Blood Diagnostics: Portable Biomedical Sensor for Cardiac Troponin i Detection. *Anal. Chem.* **2018**, *90*, 2867−2874.
(113) Song, J.; Dailey, J.; Li, H.; Jang, H. J.; Zhang, P.; Wang, J. T. H.; Everett, A. D.; Katz, H. E. Extended Solution Gate OFET-Based Biosensor for Label-Free Glial Fibrillary Acidic Protein Detection with Polyethylene Glycol-Containing Bioreceptor Layer. *Adv. Funct. Mater.* **2017**, *27*, 1606506.
(114) Dorfman, K. D.; Adrahtas, D. Z.; Thomas, M. S.; Frisbie, C. D. Microfluidic Opportunities in Printed Electrolyte-Gated Transistor Biosensors. *Biomicrofluidics* **2020**, *14*, 011301.
(115) Parkula, V.; Berto, M.; Diacci, C.; Patrahau, B.; Di Lauro, M.; Kovtun, A.; Liscio, A.; Sensi, M.; Samorì, P.; Greco, P.; Bortolotti, C. A.; Biscarini, F. Harnessing Selectivity and Sensitivity in Electronic Biosensing: A Novel Lab-on-Chip Multigate Organic Transistor. *Anal. Chem.* **2020**, *92*, 9330−9337.
(116) Seo, G.; Lee, G.; Kim, M. J.; Baek, S. H.; Choi, M.; Ku, K. B.; Lee, C. S.; Jun, S.; Park, D.; Kim, H. G.; Kim, S. J.; Lee, J. O.; Kim, B. T.; Park, E. C.; Kim, S. Il. Rapid Detection of COVID-19 Causative Virus (SARS-CoV-2) in Human Nasopharyngeal Swab Specimens Using Field-Effect Transistor-Based Biosensor. *ACS Nano* **2020**, *14*, 5135−5142.
(117) Rani, D.; Singh, Y.; Salker, M.; Vu, X. T.; Ingebrandt, S.; Pachauri, V. Point-of-Care-Ready Nanoscale ISFET Arrays for Sub-Picomolar Detection of Cytokines in Cell Cultures. *Anal. Bioanal. Chem.* **2020**, *412*, 6777−6788.
(118) Liu, Q.; Zhao, C.; Chen, M.; Liu, Y.; Zhao, Z.; Wu, F.; Li, Z.; Weiss, P. S.; Andrews, A. M.; Zhou, C. Flexible Multiplexed In2O3 Nanoribbon Aptamer-Field-Effect Transistors for Biosensing. *iScience* **2020**, *23*, 101469.
(119) Ko, J. W.; Woo, J. M.; Jinhong, A.; Cheon, J. H.; Lim, J. H.; Kim, S. H.; Chun, H.; Kim, E.; Park, Y. J. Multi-Order Dynamic Range DNA Sensor Using a Gold Decorated SWCNT Random Network. *ACS Nano* **2011**, *5*, 4365−4372.
(120) Kurkina, T.; Vlandas, A.; Ahmad, A.; Kern, K.; Balasubramanian, K. Label-Free Detection of Few Copies of DNA with Carbon Nanotube Impedance Biosensors. *Angew. Chemie - Int. Ed.* **2011**, *50*, 3710−3714.
(121) Liu, J.; Chen, X.; Wang, Q.; Xiao, M.; Zhong, D.; Sun, W.; Zhang, G.; Zhang, Z. Ultrasensitive Monolayer MoS 2 Field-Effect Transistor Based DNA Sensors for Screening of Down Syndrome. *Nano Lett.* **2019**, *19*, 1437−1444.
(122) Macchia, E.; Manoli, K.; Holtzer, B.; Di Franco, C.; Torricelli, F.; Picca, R. A.; Palazzo, G.; Scamarcio, G.; Torsi, L. Effect of the ionic-strength of the gating-solution on a bioelectronic response. *Proceedings to 8th International Workshop on Advances in Sensors and Interfaces, IWASI* **2019**, 221−223.
(123) Wu, D.; Yu, Y.; Jin, D.; Xiao, M. M.; Zhang, Z. Y.; Zhang, G. J. Dual-Aptamer Modified Graphene Field-Effect Transistor Nanosensor

https://doi.org/10.1021/acs.chemrev.1c00290
Chem. Rev. 2022, 122, 4636−4699

for Label-Free and Specific Detection of Hepatocellular Carcinoma-Derived Microvesicles. *Anal. Chem.* **2020**, *92*, 4006−4015.
(124) Kashefi-Kheyrabadi, L.; Mehrgardi, M. A.; Wiechec, E.; Turner, A. P. F.; Tiwari, A. Ultrasensitive Detection of Human Liver Hepatocellular Carcinoma Cells Using a Label-Free Aptasensor. *Anal. Chem.* **2014**, *86*, 4956−4960.
(125) Macchia, E.; Alberga, D.; Manoli, K.; Mangiatordi, G. F.; Magliulo, M.; Palazzo, G.; Giordano, F.; Lattanzi, G.; Torsi, L. Organic Bioelectronics Probing Conformational Changes in Surface Confined Proteins. *Sci. Rep.* **2016**, *6*, 28085.
(126) White, S. P.; Frisbie, C. D.; Dorfman, K. D. Detection and Sourcing of Gluten in Grain with Multiple Floating-Gate Transistor Biosensors. *ACS Sensors* **2018**, *3*, 395−402.
(127) Mekler, V.; Minakhin, L.; Severinov, K. Mechanism of Duplex DNA Destabilization by RNA-Guided Cas9 Nuclease during Target Interrogation. *Proc. Natl. Acad. Sci. U. S. A.* **2017**, *114*, 5443−5448.
(128) Aartsma-Rus, A.; Ginjaar, I. B.; Bushby, K. The Importance of Genetic Diagnosis for Duchenne Muscular Dystrophy. *J. Med. Genet.* **2016**, *53*, 145−151.
(129) Dumont, N. A.; Wang, Y. X.; Von Maltzahn, J.; Pasut, A.; Bentzinger, C. F.; Brun, C. E.; Rudnicki, M. A. Dystrophin Expression in Muscle Stem Cells Regulates Their Polarity and Asymmetric Division. *Nat. Med.* **2015**, *21*, 1455−1463.
(130) Tamboli, V. K.; Bhalla, N.; Jolly, P.; Bowen, C. R.; Taylor, J. T.; Bowen, J. L.; Allender, C. J.; Estrela, P. Hybrid Synthetic Receptors on MOSFET Devices for Detection of Prostate Specific Antigen in Human Plasma. *Anal. Chem.* **2016**, *88*, 11486−11490.
(131) Dechtrirat, D.; Gajovic-Eichelmann, N.; Bier, F. F.; Scheller, F. W. Hybrid Material for Protein Sensing Based on Electrosynthesized MIP on a Mannose Terminated Self-Assembled Monolayer. *Adv. Funct. Mater.* **2014**, *24*, 2233−2239.
(132) Savory, N.; Abe, K.; Sode, K.; Ikebukuro, K. Selection of DNA Aptamer against Prostate Specific Antigen Using a Genetic Algorithm and Application to Sensing. *Biosens. Bioelectron.* **2010**, *26*, 1386−1391.
(133) Balk, S. P.; Ko, Y. J.; Bubley, G. J. Biology of Prostate-Specific Antigen. *J. Clin. Oncol.* **2003**, *21*, 383−391.
(134) Picca, R. A.; Manoli, K.; Luciano, A.; Sportelli, M. C.; Palazzo, G.; Torsi, L.; Cioffi, N. Enhanced Stability of Organic Field-Effect Transistor Biosensors Bearing Electrosynthesized ZnO Nanoparticles. *Sensors Actuators, B Chem.* **2018**, *274*, 210−217.
(135) Kuo, W.-C.; Sarangadharan, I.; Pulikkathodi, A. K.; Chen, P.-H.; Wang, S.-L.; Wu, C.-R.; Wang, Y.-L. Investigation of Electrical Stability and Sensitivity of Electric Double Layer Gated Field-Effect Transistors (FETs) for miRNA Detection. *Sensors* **2019**, *19*, 1484.
(136) Giovannitti, A.; Rashid, R. B.; Thiburce, Q.; Paulsen, B. D.; Cendra, C.; Thorley, K.; Moia, D.; Mefford, J. T.; Hanifi, D.; Weiyuan, D.; Moser, M.; Salleo, A.; Nelson, J.; McCulloch, I.; Rivnay, J. Energetic Control of Redox-Active Polymers toward Safe Organic Bioelectronic Materials. *Adv. Mater.* **2020**, *32*, 1908047.
(137) Moser, M.; Hidalgo, T. C.; Surgailis, J.; Gladisch, J.; Ghosh, S.; Sheelamanthula, R.; Thiburce, Q.; Giovannitti, A.; Salleo, A.; Gasparini, N.; Wadsworth, A.; Zozoulenko, I.; Berggren, M.; Stavrinidou, E.; Inal, S.; McCulloch, I. Side Chain Redistribution as a Strategy to Boost Organic Electrochemical Transistor Performance and Stability. *Adv. Mater.* **2020**, *32*, 2002748.
(138) McMahon, D. P.; Cheung, D. L.; Goris, L.; Dacuña, J.; Salleo, A.; Troisi, A. Relation between Microstructure and Charge Transport in Polymers of Different Regioregularity. *J. Phys. Chem. C* **2011**, *115*, 19386−19393.
(139) Park, B.; Ko, D. H. Charge Transport in Ordered and Disordered Regions in Pristine and Sonicated-Poly(3-Hexylthiophene) Films. *J. Phys. Chem. C* **2014**, *118*, 1746−1752.
(140) Porrazzo, R.; Bellani, S.; Luzio, A.; Lanzarini, E.; Caironi, M.; Antognazza, M. R. Improving Mobility and Electrochemical Stability of a Water-Gated Polymer Field-Effect Transistor. *Org. Electron.* **2014**, *15*, 2126−2134.
(141) Picca, R. A.; Manoli, K.; Macchia, E.; Tricase, A.; Di Franco, C.; Scamarcio, G.; Cioffi, N.; Torsi, L. A Study on the Stability of Water-Gated Organic Field-Effect-Transistors Based on a Commercial p-Type Polymer. *Frontiers in Chemistry* **2019**, *7*, 667.
(142) Parmeggiani, M.; Verna, A.; Ballesio, A.; Cocuzza, M.; Piatti, E.; Fra, V.; Pirri, C. F.; Marasso, S. L. P3HT Processing Study for In-Liquid EGOFET Biosensors: Effects of the Solvent and the Surface. *Sensors (Switzerland)* **2019**, *19*, 4497.
(143) Blasi, D.; Viola, F.; Modena, F.; Luukkonen, A.; MacChia, E.; Picca, R. A.; Gounani, Z.; Tewari, A.; Österbacka, R.; Caironi, M.; Kovacs Vajna, Z. M.; Scamarcio, G.; Torricelli, F.; Torsi, L. Printed, Cost-Effective and Stable Poly(3-Hexylthiophene) Electrolyte-Gated Field-Effect Transistors. *J. Mater. Chem. C* **2020**, *8*, 15312−15321.
(144) Mello, H. J. N. P. D.; Dalgleish, S.; Ligorio, G.; Mulato, M.; List-Kratochvil, E. J. W. Stability Evaluation and Gate-Distance Effects on Electrolyte-Gated Organic Field-Effect Transistor Based on Organic Semiconductors. *Organic and Hybrid Sensors and Bioelectronics XI* **2018**, 45.
(145) Kuo, W.-C.; Wang, Y.-L. Investigation of Electrical Stability and Sensitivity of High Field Modulated Extended Gate FET Biosensors for MiRNA Detection. *ECS Trans.* **2019**, *89*, 3−6.
(146) Zhang, Y.; Zeng, Q.; Shen, Y.; Yang, L.; Yu, F. Electrochemical Stability Investigations and Drug Toxicity Tests of Electrolyte-Gated Organic Field-Effect Transistors. *ACS Appl. Mater. Interfaces* **2020**, *12*, 56216−56221.
(147) Cardenas, J. A.; Lu, S.; Williams, N. X.; Doherty, J. L.; Franklin, A. D. In-Place Printing of Flexible Electrolyte-Gated Carbon Nanotube Transistors with Enhanced Stability. *IEEE Electron Device Lett.* **2021**, *42*, 367−370.
(148) Roberts, M. E.; Mannsfeld, S. C. B.; Tang, M. L.; Bao, Z. Influence of Molecular Structure and Film Properties on the Water-Stability and Sensor Characteristics of Organic Transistors. *Chem. Mater.* **2008**, *20*, 7332−7338.
(149) Buth, F.; Kumar, D.; Stutzmann, M.; Garrido, J. A. Electrolyte-Gated Organic Field-Effect Transistors for Sensing Applications. *Appl. Phys. Lett.* **2011**, *98*, 153302.
(150) Cramer, T.; Kyndiah, A.; Murgia, M.; Leonardi, F.; Casalini, S.; Biscarini, F. Double Layer Capacitance Measured by Organic Field Effect Transistor Operated in Water. *Appl. Phys. Lett.* **2012**, *100*, 143302.
(151) Kergoat, L.; Herlogsson, L.; Braga, D.; Piro, B.; Pham, M.-C.; Crispin, X.; Berggren, M.; Horowitz, G. A Water-Gate Organic Field-Effect Transistor. *Adv. Mater.* **2010**, *22*, 2565−2569.
(152) Bernards, D. A.; Macaya, D. J.; Nikolou, M.; DeFranco, J. A.; Takamatsu, S.; Malliaras, G. G. Enzymatic Sensing with Organic Electrochemical Transistors. *J. Mater. Chem.* **2008**, *18*, 116−120.
(153) Sun, C.; Li, R.; Song, Y.; Jiang, X.; Zhang, C.; Cheng, S.; Hu, W. Ultrasensitive and Reliable Organic Field-Effect Transistor-Based Biosensors in Early Liver Cancer Diagnosis. *Anal. Chem.* **2021**, *93*, 6188−6194.
(154) Okamoto, T.; Kumagai, S.; Fukuzaki, E.; Ishii, H.; Watanabe, G.; Niitsu, N.; Annaka, T.; Yamagishi, M.; Tani, Y.; Sugiura, H.; Watanabe, T.; Watanabe, S.; Takeya, J. Robust, High-Performance n-Type Organic Semiconductors. *Sci. Adv.* **2020**, *6*, No. eaaz0632.
(155) Brixi, S.; Melville, O. A.; Boileau, N. T.; Lessard, B. H. The Influence of Air and Temperature on the Performance of PBDB-T and P3HT in Organic Thin Film Transistors. *J. Mater. Chem. C* **2018**, *6*, 11972−11979.
(156) Motiei, L.; Yao, Y.; Choudhury, J.; Yan, H.; Marks, T. J.; Boom, M. E. van der; Facchetti, A. Self-Propagating Molecular Assemblies as Interlayers for Efficient Inverted Bulk-Heterojunction Solar Cells. *J. Am. Chem. Soc.* **2010**, *132*, 12528−12530.
(157) Sarcina, L.; Torsi, L.; Picca, R. A.; Manoli, K.; Macchia, E. Assessment of Gold Bio-Functionalization for Wide-Interface Biosensing Platforms. *Sensors* **2020**, *20*, 3678.
(158) Holzer, B.; Manoli, K.; Ditaranto, N.; Macchia, E.; Tiwari, A.; Di Franco, C.; Scamarcio, G.; Palazzo, G.; Torsi, L. Characterization of Covalently Bound Anti-Human Immunoglobulins on Self-Assembled Monolayer Modified Gold Electrodes. *Adv. Biosyst.* **2017**, *1*, 1700055.
(159) Sailapu, S. K.; Macchia, E.; Merino-Jimenez, I.; Esquivel, J. P.; Sarcina, L.; Scamarcio, G.; Minteer, S. D.; Torsi, L.; Sabaté, N.

https://doi.org/10.1021/acs.chemrev.1c00290
Chem. Rev. 2022, 122, 4636−4699

Standalone Operation of an EGOFET for Ultra-Sensitive Detection of HIV. *Biosens. Bioelectron.* **2020**, *156*, 112103.
(160) Macchia, E.; Sarcina, L.; Driescher, C.; Gounani, Z.; Tewari, A.; Osterbacka, R.; Palazzo, G.; Tricase, A.; Kovács-Vajna, Z. M.; Viola, F.; Modena, F.; Caironi, M.; Torricelli, F.; Esposito, I.; Torsi, L. Title: Single-Molecule Bio-Electronic Label-Free Assay of Both Protein and Genomic Markers of Pancreatic Mucinous Cysts' in Whole Blood Serum. *Adv. Electron. Mater.* **2021**, *7*, 2100304.
(161) Sun, Y.; Rogers, J. A. Inorganic Semiconductors for Flexible Electronics. *Adv. Mater.* **2007**, *19*, 1897−1916.
(162) Briseno, A. L.; Tseng, R. J.; Ling, M.-M.; Falcao, E. H. L.; Yang, Y.; Wudl, F.; Bao, Z. High-Performance Organic Single-Crystal Transistors on Flexible Substrates. *Adv. Mater.* **2006**, *18*, 2320−2324.
(163) Chen, Y.; Zhang, Y.; Liang, Z.; Cao, Y.; Han, Z.; Feng, X. Flexible Inorganic Bioelectronics. *npj Flex. Electron.* **2020**, *4*, 2.
(164) Schaumann, E. N.; Tian, B. Biological Interfaces, Modulation, and Sensing with Inorganic Nano-Bioelectronic Materials. *Small Methods* **2020**, *4*, 1900868.
(165) Someya, T.; Bao, Z.; Malliaras, G. G. The Rise of Plastic Bioelectronics. *Nature* **2016**, *540*, 379−385.
(166) Luo, J.; Li, S.; Xu, M.; Guan, M.; Yang, M.; Ren, J.; Zhang, Y.; Zeng, Y. Real-Time Detection of Cardiac Troponin i and Mechanism Analysis of AlGaAs/GaAs High Electron Mobility Transistor Biosensor. *AIP Adv.* **2020**, *10*, 115205.
(167) Liang, L.; Zhang, S.; Wu, W.; Zhu, L.; Xiao, H.; Liu, Y.; Zhang, H.; Javaid, K.; Cao, H. Extended-Gate-Type IGZO Electric-Double-Layer TFT Immunosensor with High Sensitivity and Low Operation Voltage. *Appl. Phys. Lett.* **2016**, *109*, 173501.
(168) Lee, I. K.; Jeun, M.; Jang, H. J.; Cho, W. J.; Lee, K. H. A Self-Amplified Transistor Immunosensor under Dual Gate Operation: Highly Sensitive Detection of Hepatitis B Surface Antigen. *Nanoscale* **2015**, *7*, 16789−16797.
(169) Ding, X.; Miao, B.; Gu, Z.; Wu, B.; Hu, Y.; Wang, H.; Zhang, J.; Wu, D.; Lu, W.; Li, J. Highly Sensitive Extended Gate-AlGaN/GaN High Electron Mobility Transistor for Bioassay Applications. *RSC Adv.* **2017**, *7*, 55835−55838.
(170) Gutiérrez-Sanz, Ó.; Andoy, N. M.; Filipiak, M. S.; Haustein, N.; Tarasov, A. Direct, Label-Free, and Rapid Transistor-Based Immunodetection in Whole Serum. *ACS Sensors* **2017**, *2*, 1278−1286.
(171) Lee, J. W.; Sim, S. J.; Cho, S. M.; Lee, J. Characterization of a Self-Assembled Monolayer of Thiol on a Gold Surface and the Fabrication of a Biosensor Chip Based on Surface Plasmon Resonance for Detecting Anti-GAD Antibody. *Biosens. Bioelectron.* **2005**, *20*, 1422−1427.
(172) Novoselov, K. S.; Geim, A. K.; Morozov, S. V; Jiang, D.; Zhang, Y.; Dubonos, S. V; Grigorieva, I. V; Firsov, A. A. Electric Field Effect in Atomically Thin Carbon Films. *Science* **2004**, *306*, 666−669.
(173) Fu, W.; Jiang, L.; van Geest, E. P.; Lima, L. M. C.; Schneider, G. F. Sensing at the Surface of Graphene Field-Effect Transistors. *Adv. Mater.* **2017**, *29*, 1603610.
(174) Cheng, H.-C.; Shiue, R.-J.; Tsai, C.-C.; Wang, W.-H.; Chen, Y.-T. High-Quality Graphene P-n Junctions via Resist-Free Fabrication and Solution-Based Noncovalent Functionalization. *ACS Nano* **2011**, *5*, 2051−2059.
(175) Park, S. J.; Kwon, O. S.; Lee, S. H.; Song, H. S.; Park, T. H.; Jang, J. Ultrasensitive Flexible Graphene Based Field-Effect Transistor (FET)-Type Bioelectronic Nose. *Nano Lett.* **2012**, *12*, 5082−5090.
(176) Boehm, H. P.; Clauss, A.; Fischer, G. O.; Hofmann, U. Dünnste Kohlenstoff-Folien. *Zeitschrift für Naturforsch. B* **1962**, *17*, 150−153.
(177) Kim, D. J.; Sohn, I. Y.; Jung, J. H.; Yoon, O. J.; Lee, N. E.; Park, J. S. Reduced Graphene Oxide Field-Effect Transistor for Label-Free Femtomolar Protein Detection. *Biosens. Bioelectron.* **2013**, *41*, 621−626.
(178) Kim, B. Y.; Sohn, I. Y.; Lee, D.; Han, G. S.; Lee, W. Il; Jung, H. S.; Lee, N. E. Ultrarapid and Ultrasensitive Electrical Detection of Proteins in a Three-Dimensional Biosensor with High Capture Efficiency. *Nanoscale* **2015**, *7*, 9844−9851.
(179) Melzer, K.; Münzer, A. M.; Jaworska, E.; Maksymiuk, K.; Michalska, A.; Scarpa, G. Selective Ion-Sensing with Membrane-Functionalized Electrolyte-Gated Carbon Nanotube Field-Effect Transistors. *Analyst* **2014**, *139*, 4947−4954.
(180) Cui, Y.; Wei, Q.; Park, H.; Lieber, C. M. Nanowire Nanosensors for Highly Sensitive and Selective Detection of Biological and Chemical Species. *Science* **2001**, *293*, 1289−1292.
(181) Chen, R. J.; Bangsaruntip, S.; Drouvalakis, K. A.; Wong Shi Kam, N.; Shim, M.; Li, Y.; Kim, W.; Utz, P. J.; Dai, H. Noncovalent Functionalization of Carbon Nanotubes for Highly Specific Electronic Biosensors. *Proc. Natl. Acad. Sci. U. S. A.* **2003**, *100*, 4984−4989.
(182) Biomarkers Definitions Working Group. Biomarkers and Surrogate Endpoints: Preferred Definitions and Conceptual Framework. *Clin. Pharmacol. Ther.* **2001**, *69*, 89−95.
(183) Giljohann, D. A.; Mirkin, C. A. Drivers of Biodiagnostic Development. *Nature* **2009**, *462*, 461−464.
(184) Ginsburg, G. S.; Haga, S. B. Translating Genomic Biomarkers into Clinically Useful Diagnostics. *Expert Rev. Mol. Diagn.* **2006**, *6*, 179−191.
(185) Golub, T. R.; Slonim, D. K.; Tamayo, P.; Huard, C.; Gaasenbeek, M.; Mesirov, J. P.; Coller, H.; Loh, M. L.; Downing, J. R.; Caligiuri, M. A.; Bloomfield, C. D.; Lander, E. S. Molecular Classification of Cancer: Class Discovery and Class Prediction by Gene Expression Monitoring. *Science* **1999**, *286*, 531−537.
(186) van de Vijver, M. J.; He, Y. D.; van 't Veer, L. J.; Dai, H.; Hart, A. A. M.; Voskuil, D. W.; Schreiber, G. J.; Peterse, J. L.; Roberts, C.; Marton, M. J.; Parrish, M.; Atsma, D.; Witteveen, A.; Glas, A.; Delahaye, L.; van der Velde, T.; Bartelink, H.; Rodenhuis, S.; Rutgers, E. T.; Friend, S. H.; Bernards, R. A Gene-Expression Signature as a Predictor of Survival in Breast Cancer. *N. Engl. J. Med.* **2002**, *347*, 1999−2009.
(187) Hu, N.; Wang, C.; Hu, Y.; Yang, H. H.; Giffen, C.; Tang, Z.-Z.; Han, X.-Y.; Goldstein, A. M.; Emmert-Buck, M. R.; Buetow, K. H.; Taylor, P. R.; Lee, M. P. Genome-Wide Association Study in Esophageal Cancer Using GeneChip Mapping 10K Array. *Cancer Res.* **2005**, *65*, 2542−2546.
(188) Esposito, I.; Segler, A.; Steiger, K.; Klöppel, G. Pathology, Genetics and Precursors of Human and Experimental Pancreatic Neoplasms: An Update. *Pancreatology* **2015**, *15*, 598−610.
(189) Dinter, F.; Burdukiewicz, M.; Schierack, P.; Lehmann, W.; Nestler, J.; Dame, G.; Rödiger, S. Simultaneous Detection and Quantification of DNA and Protein Biomarkers in Spectrum of Cardiovascular Diseases in a Microfluidic Microbead Chip. *Anal. Bioanal. Chem.* **2019**, *411*, 7725−7735.
(190) Manoli, K.; Magliulo, M.; Mulla, M. Y.; Singh, M.; Sabbatini, L.; Palazzo, G.; Torsi, L. Printable Bioelectronics To Investigate Functional Biological Interfaces. *Angew. Chemie Int. Ed.* **2015**, *54*, 12562−12576.
(191) Torsi, L.; Magliulo, M.; Manoli, K.; Palazzo, G. Organic Field-Effect Transistor Sensors: A Tutorial Review. *Chem. Soc. Rev.* **2013**, *42*, 8612−8628.
(192) Demelas, M.; Lai, S.; Spanu, A.; Martinoia, S.; Cosseddu, P.; Barbaro, M.; Bonfiglio, A. Charge Sensing by Organic Charge-Modulated Field Effect Transistors: Application to the Detection of Bio-Related Effects. *J. Mater. Chem. B* **2013**, *1*, 3811−3819.
(193) Stoliar, P.; Bystrenova, E.; Quiroga, S. D.; Annibale, P.; Facchini, M.; Spijkman, M.; Setayesh, S.; de Leeuw, D.; Biscarini, F. DNA Adsorption Measured with Ultra-Thin Film Organic Field Effect Transistors. *Biosens. Bioelectron.* **2009**, *24*, 2935−2938.
(194) Rusmini, F.; Zhong, Z.; Feijen, J. Protein Immobilization Strategies for Protein Biochips. *Biomacromolecules* **2007**, *8*, 1775−1789.
(195) Patel, N.; Davies, M. C.; Hartshorne, M.; Heaton, R. J.; Roberts, C. J.; Tendler, S. J. B.; Williams, P. M. Immobilization of Protein Molecules onto Homogeneous and Mixed Carboxylate-Terminated Self-Assembled Monolayers. *Langmuir* **1997**, *13*, 6485−6490.
(196) MacBeath, G.; Schreiber, S. L. Printing Proteins as Microarrays for High-Throughput Function Determination. *Science* **2000**, *289*, 1760−1763.
(197) Viitala, T.; Vikholm, I.; Peltonen, J. Protein Immobilization to a Partially Cross-Linked Organic Monolayer. *Langmuir* **2000**, *16*, 4953−4961.

https://doi.org/10.1021/acs.chemrev.1c00290
Chem. Rev. 2022, 122, 4636−4699

(198) Wacker, R.; Schröder, H.; Niemeyer, C. M. Performance of Antibody Microarrays Fabricated by Either DNA-Directed Immobilization, Direct Spotting, or Streptavidin-Biotin Attachment: A Comparative Study. *Anal. Biochem.* **2004**, *330*, 281−287.
(199) Rizzi, S. C.; Hubbell, J. A. Recombinant Protein-Co-PEG Networks as Cell-Adhesive and Proteolytically Degradable Hydrogel Matrixes. Part I: Development and Physicochemical Characteristics. *Biomacromolecules* **2005**, *6*, 1226−1238.
(200) Mateo, C.; Abian, O.; Fernández-Lorente, G.; Pedroche, J.; Fernández-Lafuente, R.; Guisan, J. M.; et al. Epoxy Sepabeads: A Novel Epoxy Support for Stabilization of Industrial Enzymes via Very Intense Multipoint Covalent Attachment. *Biotechnol. Prog.* **2002**, *18*, 629−634.
(201) Turková, J. Oriented Immobilization of Biologically Active Proteins as a Tool for Revealing Protein Interactions and Function. *J. Chromatogr. B Biomed. Sci. Appl.* **1999**, *722*, 11−31.
(202) Werner, S.; Machleidt, W. Isolation of Precursors of Cytochrome Oxidase from Neurospora Crassa: Application of Subunit-Specific Antibodies and Protein A from Staphylococcus Aureus. *Eur. J. Biochem.* **1978**, *90*, 99−105.
(203) Wilchek, M.; Bayer, E. A. Introduction to Avidin-Biotin Technology. *Methods Enzymol.* **1990**, *184*, 5−13.
(204) Lehnert, M.; Gorbahn, M.; Rosin, C.; Klein, M.; Köper, I.; Al-Nawas, B.; Knoll, W.; Veith, M. Adsorption and Conformation Behavior of Biotinylated Fibronectin on Streptavidin-Modified TiOX Surfaces Studied by SPR and AFM. *Langmuir* **2011**, *27*, 7743−7751.
(205) Vikholm-Lundin, I.; Auer, S.; Paakkunainen, M.; Määttä, J. A. E.; Munter, T.; Leppiniemi, J.; Hytönen, V. P.; Tappura, K. Cysteine-Tagged Chimeric Avidin Forms High Binding Capacity Layers Directly on Gold. *Sensors Actuators B Chem.* **2012**, *171*−*172*, 440−448.
(206) Cai, B.; Wang, S.; Huang, L.; Ning, Y.; Zhang, Z.; Zhang, G. J. Ultrasensitive Label-Free Detection of PNA-DNA Hybridization by Reduced Graphene Oxide Field-Effect Transistor Biosensor. *ACS Nano* **2014**, *8*, 2632−2638.
(207) Tung, V. C.; Allen, M. J.; Yang, Y.; Kaner, R. B. High-Throughput Solution Processing of Large-Scale Graphene. *Nat. Nanotechnol.* **2009**, *4*, 25−29.
(208) Lin, C.-T.; Loan, P. T. K.; Chen, T.-Y.; Liu, K.-K.; Chen, C.-H.; Wei, K.-H.; Li, L.-J. Label-Free Electrical Detection of DNA Hybridization on Graphene Using Hall Effect Measurements: Revisiting the Sensing Mechanism. *Adv. Funct. Mater.* **2013**, *23*, 2301−2307.
(209) Manohar, S.; Mantz, A. R.; Bancroft, K. E.; Hui, C.-Y.; Jagota, A.; Vezenov, D. V. Peeling Single-Stranded DNA from Graphite Surface to Determine Oligonucleotide Binding Energy by Force Spectroscopy. *Nano Lett.* **2008**, *8*, 4365−4372.
(210) Jeong, S.; Park, J.; Pathania, D.; Castro, C. M.; Weissleder, R.; Lee, H. Integrated Magneto-Electrochemical Sensor for Exosome Analysis. *ACS Nano* **2016**, *10*, 1802−1809.
(211) Kang, B. J.; Jeun, M.; Jang, G. H.; Song, S. H.; Jeong, I. G.; Kim, C.-S.; Searson, P. C.; Lee, K. H. Diagnosis of Prostate Cancer via Nanotechnological Approach. *Int. J. Nanomedicine* **2015**, *10*, 6555−6569.
(212) Siegel, R. L.; Miller, K. D.; Jemal, A. Cancer Statistics, 2015. *CA. Cancer J. Clin.* **2015**, *65*, 5−29.
(213) Wirtz, D.; Konstantopoulos, K.; Searson, P. C. The Physics of Cancer: The Role of Physical Interactions and Mechanical Forces in Metastasis. *Nat. Rev. Cancer* **2011**, *11*, 512−522.
(214) Schostak, M.; Schwall, G. P.; Poznanovic, S.; Groebe, K.; Muller, M.; Messinger, D.; Miller, K.; Krause, H.; Pelzer, A.; Horninger, W.; Klocker, H.; Hennenlotter, J.; Feyerabend, S.; Stenzl, A.; Schrattenholz, A. Annexin A3 in Urine: A Highly Specific Noninvasive Marker for Prostate Cancer Early Detection. *J. Urol.* **2009**, *181*, 343−353.
(215) Jeun, M.; Park, S.; Kim, Y.; Choi, J.; Song, S. H.; Jeong, I. G.; Kim, C. S.; Lee, K. H. Self-Normalized Detection of ANXA3 from Untreated Urine of Prostate Cancer Patients without Digital Rectal Examination. *Adv. Healthc. Mater.* **2017**, *6*, 1700449.
(216) Meyer, M. H. F.; Hartmann, M.; Krause, H.-J.; Blankenstein, G.; Mueller-Chorus, B.; Oster, J.; Miethe, P.; Keusgen, M. CRP Determination Based on a Novel Magnetic Biosensor. *Biosens. Bioelectron.* **2007**, *22*, 973−979.
(217) Gewurz, H. Biology of C-Reactive Protein and the Acute Phase Response. *Hosp. Pract. (Hosp. Ed).* **1982**, *17*, 67−81.
(218) Pepys, M. B.; Hirschfield, G. M.; Tennent, G. A.; Gallimore, J. R.; Kahan, M. C.; Bellotti, V.; Hawkins, P. N.; Myers, R. M.; Smith, M. D.; Polara, A.; Cobb, A. J. A.; Ley, S. V.; Aquilina, J. A.; Robinson, C. V.; Sharif, I.; Gray, G. A.; Sabin, C. A.; Jenvey, M. C.; Kolstoe, S. E.; Thompson, D.; Wood, S. P. Targeting C-Reactive Protein for the Treatment of Cardiovascular Disease. *Nature* **2006**, *440*, 1217−1221.
(219) Ouellet-Morin, I.; Danese, A.; Williams, B.; Arseneault, L. Validation of a High-Sensitivity Assay for C-Reactive Protein in Human Saliva. *Brain, Behavior, and Immunity.* **2011**, *25*, 640−646.
(220) Kahn, J. O.; Walker, B. D. Acute Human Immunodeficiency Virus Type 1 Infection. *N. Engl. J. Med.* **1998**, *339*, 33−39.
(221) Englebienne, P.; Van Hoonacker, A.; Verhas, M. Surface Plasmon Resonance: Principles, Methods and Applications in Biomedical Sciences. *Spectroscopy* **2003**, *17*, 255−273.
(222) Piliarik, M.; Vaisocherova, H.; Homola, J. Surface Plasmon Resonance Biosensing. *Biosensors and Biodetection* **2009**, *503*, 65−88.
(223) Aspermair, P.; Ramach, U.; Reiner-Rozman, C.; Fossati, S.; Lechner, B.; Moya, S. E.; Azzaroni, O.; Dostalek, J.; Szunerits, S.; Knoll, W.; Bintinger, J. Dual Monitoring of Surface Reactions in Real Time by Combined Surface-Plasmon Resonance and Field-Effect Transistor Interrogation. *J. Am. Chem. Soc.* **2020**, *142*, 11709−11716.
(224) Knoll, W.; Liu, J.; Yu, F.; Niu, L.; Reiner-Rozman, C.; Köper, I. Comparing Surface Plasmon-Optical and Electronic Immuno-Sensing of Affinity Interactions—a Case Study. *Chemosensors* **2021**, *9*, 11.
(225) Osawa, M. Surface-Enhanced Infrared Absorption. In *Near-Field Optics and Surface Plasmon Polaritons Topics Appl. Phys.*; Kawata, S., Ed.; Vol *81*; Springer-Verlag: Berlin, 2001; pp 163−187.
(226) Kratz, C.; Oates, T. W. H.; Hinrichs, K. Optimization and Quantification of Surface Enhanced Infrared Absorption Using Gradient Gold Island Films. *Thin Solid Films* **2016**, *617*, 33−37.
(227) Quirk, A.; Unni, B.; Burgess, I. J. Surface Enhanced Infrared Studies of 4-Methoxypyridine Adsorption on Gold Film Electrodes. *Langmuir* **2016**, *32*, 2184−2191.
(228) Brown, C. W.; Li, Y.; Seelenbinder, J. A.; Pivarnik, P.; Rand, A. G.; Letcher, S. V.; Gregory, O. J.; Platek, M. J. Immunoassays Based on Surface-Enhanced Infrared Absorption Spectroscopy. *Anal. Chem.* **1998**, *70*, 2991−2996.
(229) Xu, J. Y.; Chen, T. W.; Bao, W. J.; Wang, K.; Xia, X. H. Label-Free Strategy for in-Situ Analysis of Protein Binding Interaction Based on Attenuated Total Reflection Surface Enhanced Infrared Absorption Spectroscopy (ATR-SEIRAS). *Langmuir* **2012**, *28*, 17564−17570.
(230) Kratz, C.; Furchner, A.; Oates, T. W. H.; Janasek, D.; Hinrichs, K. Nanoliter Sensing for Infrared Bioanalytics. *ACS Sensors* **2018**, *3*, 299−303.
(231) Ataka, K.; Stripp, S. T.; Heberle, J. Surface-Enhanced Infrared Absorption Spectroscopy (SEIRAS) to Probe Monolayers of Membrane Proteins. *Biochim. Biophys. Acta - Biomembr.* **2013**, *1828*, 2283−2293.
(232) Jiang, X.; Zaitseva, E.; Schmidt, M.; Siebert, F.; Engelhard, M.; Schlesinger, R.; Ataka, K.; Vogel, R.; Heberle, J. Resolving Voltage-Dependent Structural Changes of a Membrane Photoreceptor by Surface-Enhanced IR Difference Spectroscopy. *Proc. Natl. Acad. Sci. U. S. A.* **2008**, *105*, 12113−12117.
(233) Choi, Y.; Moody, I. S.; Sims, P. C.; Hunt, S. R.; Corso, B. L.; Perez, I.; Weiss, G. A.; Collins, P. G. Single-Molecule Lysozyme Dynamics Monitored by an Electronic Circuit. *Science* **2012**, *335*, 319−324.
(234) Chu, C. H.; Sarangadharan, I.; Regmi, A.; Chen, Y. W.; Hsu, C. P.; Chang, W. H.; Lee, G. Y.; Chyi, J. I.; Chen, C. C.; Shiesh, S. C.; Lee, G.-B.; Wang, Y. L. Beyond the Debye Length in High Ionic Strength Solution: Direct Protein Detection with Field-Effect Transistors (FETs) in Human Serum. *Sci. Rep.* **2017**, *7*, 5256.
(235) Kim, S. H.; Hong, K.; Xie, W.; Lee, K. H.; Zhang, S.; Lodge, T. P.; Frisbie, C. D. Electrolyte-Gated Transistors for Organic and Printed Electronics. *Adv. Mater.* **2013**, *25*, 1822−1846.

https://doi.org/10.1021/acs.chemrev.1c00290
Chem. Rev. 2022, 122, 4636−4699

(236) Casalini, S.; Leonardi, F.; Cramer, T.; Biscarini, F. Organic Field-Effect Transistor for Label-Free Dopamine Sensing. *Org. Electron.* **2013**, *14*, 156−163.
(237) Park, S. J.; Kwon, O. S.; Lee, S. H.; Song, H. S.; Park, T. H.; Jang, J. Ultrasensitive Flexible Graphene Based Field-Effect Transistor (FET)-Type Bioelectronic Nose. *Nano Lett.* **2012**, *12*, 5082−5090.
(238) Kim, D. J.; Park, H. C.; Sohn, I. Y.; Jung, J. H.; Yoon, O. J.; Park, J. S.; Yoon, M. Y.; Lee, N. E. Electrical Graphene Aptasensor for Ultra-Sensitive Detection of Anthrax Toxin with Amplified Signal Transduction. *Small* **2013**, *9*, 3352−3360.
(239) Gupta, M.; Santermans, S.; Du Bois, B.; Vos, R.; Severi, S.; Hellings, G.; Lagae, L.; Martens, K.; Van Roy, W. Size independent sensitivity to biomolecular surface density using nanoscale CMOS technology transistors. *IEEE Sensors Journal* **2020**, *20*, 8956−8964.
(240) Reingruber, J.; Holcman, D.; Fain, G. L. How Rods Respond to Single Photons: Key Adaptations of a G-Protein Cascade That Enable Vision at the Physical Limit of Perception. *BioEssays* **2015**, *37*, 1243−1252.
(241) Kaupp, U. B.; Alvarez, L. Sperm as Microswimmers - Navigation and Sensing at the Physical Limit. *Eur. Phys. J. Spec. Top.* **2016**, *225*, 2119−2139.
(242) Stengl, M. Pheromone Transduction in Moths. *Front. Cell. Neurosci.* **2010**, *4*, 133.
(243) Fechner, S.; Alvarez, L.; Bönigk, W.; Müller, A.; Berger, T. K.; Pascal, R.; Trötschel, C.; Poetsch, A.; Stölting, G.; Siegfried, K. R.; Kremmer, E.; Seifert, R.; Kaupp, U. B. A K^+-Selective CNG Channel Orchestrates Ca^{2+} Signalling in Zebrafish Sperm. *Elife* **2015**, *4*, e07624.
(244) Pichlo, M.; Bungert-Plümke, S.; Weyand, I.; Seifert, R.; Bönigk, W.; Strünker, T.; Kashikar, N. D.; Goodwin, N.; Müller, A.; Pelzer, P.; Van, Q.; Enderlein, J.; Klemm, C.; Krause, E.; Trötschel, C.; Poetsch, A.; Kremmer, E.; Kaupp, U. B. High Density and Ligand Affinity Confer Ultrasensitive Signal Detection by a Guanylyl Cyclase Chemoreceptor. *J. Cell Biol.* **2014**, *206*, 541−557.
(245) Ahn, J. H.; Choi, B.; Choi, S. J. Understanding the Signal Amplification in Dual-Gate FET-Based Biosensors. *J. Appl. Phys.* **2020**, *128*, 184502.
(246) Widrig, C. A.; Chung, C.; Porter, M. D. The Electrochemical Desorption of N-Alkanethiol Monolayers from Polycrystalline Au and Ag Electrodes. *J. Electroanal. Chem.* **1991**, *310*, 335−359.
(247) Barros, F.; Pardo, L. A.; Domínguez, P.; Sierra, L. M.; de la Peña, P. New Structures and Gating of Voltage-Dependent Potassium (Kv) Channels and Their Relatives: A Multi-Domain and Dynamic Question. *Int. J. Mol. Sci.* **2019**, *20*, 248.

https://doi.org/10.1021/acs.chemrev.1c00290
Chem. Rev. 2022, 122, 4636−4699